Defining the role of chromatin remodelers during forebrain development

Valerie Cardin

Department of Cellular and Molecular Medicine

Faculty of Medicine

University of Ottawa

Ottawa, Ontario, Canada

January 9th 2024

This thesis is submitted as a partial fulfilment of the

Ph.D. program in Cellular and Molecular Medicine

Abstract

Chromatin remodelers are necessary players in modifying and protecting the chromatin landscape. Aberrant expression of these complexes can lead to epigenetic regulation defects, which is a common cause of neurodevelopmental disorders. Mutations in the *BPTF* gene, encoding the largest subunit of the NURF complex, cause the newly identified disorder called Neurodevelopmental Disorder with Dysmorphic Facies and distal Limb anomalies (NEDDFL). Recent research has identified a role for Bptf in progenitor proliferation and neocortical development. Here, we aimed to enhance the coverage of *Bptf* deletion in the neural system and we hypothesized that the phenotype of the *Bptf* knockout mice will recapitulate the human phenotype and will be a better model to study NEDDFL. We showed that *Bptf* conditional KO mice have major morphological brain defects, including an abnormal cortex and malformed hippocampus. Furthermore, assessment of these mice revealed key behavioural features found in NEDDFL patients.

The ATR-X syndrome, a severe neurodevelopmental disorder with autistic-like features, is caused by mutations in the *ATRX* gene that encodes an ATP-dependent chromatin remodeling protein. Previous studies have reported that, in the absence of *Atrx*, the glutamatergic and GABAergic networks are altered, which lead us to hypothesize that alteration of the equilibrium between the excitatory and inhibitory systems play a role in the pathogenesis of ATR-X syndrome. Here, we showed that mice with *Atrx* deletion in excitatory neurons (AtrxVgKO) and inhibitory neurons (AtrxVtKO) die embryonically or shortly after birth which precluded a thorough mechanistic analysis, yet they exhibited distinct hippocampal defects. Lastly, we generated a new conditional Atrx mouse mutant (AtrxEcKO) that survived beyond birth. Using this model, I showed that loss of *Atrx* caused a hypoplastic hippocampus, hyperactive and self-

injurious behaviour that could be caused by altered myelinogenesis, axonogenesis, axonal pathfinding, cell differentiation and transcriptional regulation.

Table of Contents

List of Figures

Chapter 1

Chapter 2

Chapter 3

Chapter 4

Chapter 5

Chapter 6

Appendix

List of Tables

Chapter 2

Copyright Permission

JOHN WILEY AND SONS LICENSE TERMS AND CONDITIONS

Aug 14, 2023

This Agreement between Valerie Cardin ("You") and John Wiley and Sons ("John Wiley and Sons") consists of your license details and the terms and conditions provided by John Wiley and Sons and Copyright Clearance Center.

License Number: 5607191294546

License date: Aug 13, 2023

Licensed Content Publisher: John Wiley and Sons

Licensed Content Publication: American Journal of Medical Genetics Part A

Licensed Content Title: Clinical and hematologic aspects of the X-linked α-thalassemia/mental retardation syndrome (ATR-X)

Licensed Content Author: D. R. Higgs, A. O. M. Wilkie, M. E. P. Porteous, et al

Licensed Content Date: May 16, 2005

Licensed Content Volume: 55

Licensed Content Issue: 3

Licensed Content Pages: 12

Type of use: Dissertation/Thesis

Requestor type: University/Academic

Format: Print and electronic

Portion: Figure/table

Number of figures/tables: 5

Will you be translating?: No

Title: Defining the role of chromatin remodelers in forebrain development

Institution name: University of Ottawa

Expected presentation date: Oct 2023

Portions: Figure 2, 3, 7, 13, 14

Requestor Location: Valerie Cardin,

Publisher Tax ID: EU826007151

Terms and Conditions

TERMS AND CONDITIONS

This copyrighted material is owned by or exclusively licensed to John Wiley & Sons, Inc. or one of its group companies (each a"Wiley Company") or handled on behalf of a society with which a Wiley Company has exclusive publishing rights in relation to a particular work (collectively "WILEY"). By clicking "accept" in connection with completing this licensing transaction, you agree that the following terms and conditions apply to this transaction (along with the billing and payment terms and conditions established by the Copyright Clearance Center Inc., ("CCC's Billing and Payment terms and conditions"), at the time that you opened your RightsLink account (these are available at any time at http://myaccount.copyright.com).

Terms and Conditions

- The materials you have requested permission to reproduce or reuse (the "Wiley Materials") are protected by copyright.

- You are hereby granted a personal, non-exclusive, non-sub licensable (on a stand-alone basis), non-transferable, worldwide, limited license to reproduce the Wiley Materials for the purpose specified in the licensing process. This license, **and any CONTENT (PDF or image file) purchased as part of your order,** is for a one-time use only and limited to any maximum distribution number specified in the license. The first instance of republication or reuse granted by this license must be completed within two years of the date of the grant of this license (although copies prepared before the end date may be distributed thereafter). The Wiley Materials shall not be used in any other manner or for any other purpose, beyond what is granted in the license. Permission is granted subject to an appropriate acknowledgement given to the author, title of the material/book/journal and the publisher. You shall also duplicate the copyright notice that appears in the Wiley publication in your use of the Wiley Material. Permission is also granted on the understanding that nowhere in the text is a previously published source acknowledged for all or part of this Wiley Material. Any third party content is expressly excluded from this permission.

- With respect to the Wiley Materials, all rights are reserved. Except as expressly granted by the terms of the license, no part of the Wiley Materials may be copied, modified, adapted (except for minor reformatting required by the new Publication), translated, reproduced, transferred or distributed, in any form or by any means, and no derivative works may be made based on the Wiley Materials without the prior permission of the respective copyright owner.**For STM Signatory Publishers clearing permission under the terms of the STM Permissions Guidelines only, the terms of the license are extended to include subsequent editions and for editions in other languages, provided such editions are for the work as a whole in situ and does not involve the separate exploitation of the permitted figures or extracts,** You may not alter, remove or suppress in any manner any copyright, trademark or other notices displayed by the Wiley Materials. You may not license, rent, sell, loan, lease, pledge, offer as security, transfer or assign the Wiley Materials on a stand-alone basis, or any of the rights granted to you hereunder to any other person.

- The Wiley Materials and all of the intellectual property rights therein shall at all times remain the exclusive property of John Wiley & Sons Inc, the Wiley Companies, or their respective licensors, and your interest therein is only that of having possession of and the right to reproduce the Wiley Materials pursuant to Section 2 herein during the continuance of this Agreement. You agree that you own no right, title or interest in or to the Wiley Materials or any of the intellectual property rights therein. You shall have no rights hereunder other than the license as provided for above in Section 2. No right, license or interest to any trademark, trade name, service mark or other branding ("Marks") of WILEY or its licensors is granted hereunder, and you agree that you shall not assert any such right, license or interest with respect thereto

- NEITHER WILEY NOR ITS LICENSORS MAKES ANY WARRANTY OR REPRESENTATION OF ANY KIND TO YOU OR ANY THIRD PARTY, EXPRESS, IMPLIED OR STATUTORY, WITH RESPECT TO THE MATERIALS OR THE ACCURACY OF ANY INFORMATION CONTAINED IN THE MATERIALS, INCLUDING, WITHOUT LIMITATION, ANY IMPLIED WARRANTY OF MERCHANTABILITY, ACCURACY, SATISFACTORY QUALITY, FITNESS FOR A PARTICULAR PURPOSE, USABILITY, INTEGRATION OR NON-INFRINGEMENT AND ALL SUCH WARRANTIES ARE HEREBY EXCLUDED BY WILEY AND ITS LICENSORS AND WAIVED BY YOU.

- WILEY shall have the right to terminate this Agreement immediately upon breach of this Agreement by you.

- You shall indemnify, defend and hold harmless WILEY, its Licensors and their respective directors, officers, agents and employees, from and against any actual or threatened claims, demands, causes of action or proceedings arising from any breach of this Agreement by you.

- IN NO EVENT SHALL WILEY OR ITS LICENSORS BE LIABLE TO YOU OR ANY OTHER PARTY OR ANY OTHER PERSON OR ENTITY FOR ANY SPECIAL, CONSEQUENTIAL, INCIDENTAL, INDIRECT, EXEMPLARY OR PUNITIVE DAMAGES, HOWEVER CAUSED, ARISING OUT OF OR IN CONNECTION WITH THE DOWNLOADING, PROVISIONING, VIEWING OR

USE OF THE MATERIALS REGARDLESS OF THE FORM OF ACTION, WHETHER FOR BREACH OF CONTRACT, BREACH OF WARRANTY, TORT, NEGLIGENCE, INFRINGEMENT OR OTHERWISE (INCLUDING, WITHOUT LIMITATION, DAMAGES BASED ON LOSS OF PROFITS, DATA, FILES, USE, BUSINESS OPPORTUNITY OR CLAIMS OF THIRD PARTIES), AND WHETHER OR NOT THE PARTY HAS BEEN ADVISED OF THE POSSIBILITY OF SUCH DAMAGES. THIS LIMITATION SHALL APPLY NOTWITHSTANDING ANY FAILURE OF ESSENTIAL PURPOSE OF ANY LIMITED REMEDY PROVIDED HEREIN.

- Should any provision of this Agreement be held by a court of competent jurisdiction to be illegal, invalid, or unenforceable, that provision shall be deemed amended to achieve as nearly as possible the same economic effect as the original provision, and the legality, validity and enforceability of the remaining provisions of this Agreement shall not be affected or impaired thereby.

- The failure of either party to enforce any term or condition of this Agreement shall not constitute a waiver of either party's right to enforce each and every term and condition of this Agreement. No breach under this agreement shall be deemed waived or excused by either party unless such waiver or consent is in writing signed by the party granting such waiver or consent. The waiver by or consent of a party to a breach of any provision of this Agreement shall not operate or be construed as a waiver of or consent to any other or subsequent breach by such other party.

- This Agreement may not be assigned (including by operation of law or otherwise) by you without WILEY's prior written consent.

- Any fee required for this permission shall be non-refundable after thirty (30) days from receipt by the CCC.

- These terms and conditions together with CCC's Billing and Payment terms and conditions (which are incorporated herein) form the entire agreement between you and WILEY concerning this licensing transaction and (in the absence of fraud) supersedes all prior agreements and representations of the parties, oral or written. This Agreement may not be amended except in writing signed by both parties. This Agreement shall be binding upon and inure to the benefit of the parties' successors, legal representatives, and authorized assigns.

- In the event of any conflict between your obligations established by these terms and conditions and those established by CCC's Billing and Payment terms and conditions, these terms and conditions shall prevail.

- WILEY expressly reserves all rights not specifically granted in the combination of (i) the license details provided by you and accepted in the course of this licensing transaction, (ii) these terms and conditions and (iii) CCC's Billing and Payment terms and conditions.

- This Agreement will be void if the Type of Use, Format, Circulation, or Requestor Type was misrepresented during the licensing process.

- This Agreement shall be governed by and construed in accordance with the laws of the State of New York, USA, without regards to such state's conflict of law rules. Any legal action, suit or proceeding arising out of or relating to these Terms and Conditions or the breach thereof shall be instituted in a court of competent jurisdiction in New York County in the State of New York in the United States of America and each party hereby consents and submits to the personal jurisdiction of such court, waives any objection to venue in such court and consents to service of process by registered or certified mail, return receipt requested, at the last known address of such party.

WILEY OPEN ACCESS TERMS AND CONDITIONS

Wiley Publishes Open Access Articles in fully Open Access Journals and in Subscription journals offering Online Open. Although most of the fully Open Access journals publish open access articles under the terms of the Creative Commons Attribution (CC BY) License only, the subscription journals and a few of the Open Access Journals offer a choice of Creative Commons Licenses. The license type is clearly identified on the article.

The Creative Commons Attribution License

The Creative Commons Attribution License (CC-BY) allows users to copy, distribute and transmit an article, adapt the article and make commercial use of the article. The CC-BY license permits commercial and non-

Creative Commons Attribution Non-Commercial License

The Creative Commons Attribution Non-Commercial (CC-BY-NC)License permits use, distribution and reproduction in any medium, provided the original work is properly cited and is not used for commercial purposes.(see below)

Creative Commons Attribution-Non-Commercial-NoDerivs License

The Creative Commons Attribution Non-Commercial-NoDerivs License (CC-BY-NC-ND) permits use, distribution and reproduction in any medium, provided the original work is properly cited, is not used for commercial purposes and no modifications or adaptations are made. (see below)

Use by commercial "for-profit" organizations

Use of Wiley Open Access articles for commercial, promotional, or marketing purposes requires further explicit permission from Wiley and will be subject to a fee.

Abbreviations

5HT3aR	Ionotropic serotonin receptor 5HT3a
ADD	ATRX-DMNT3L-DNMT3A
ALT	Alternative lengthening of telomeres
ANOVA	Analysis of variance
ASI	Adult social interaction
ATRX	Alpha Thalassemia/Mental Retardation Syndrome X-Linked
BBK	Beam break assay
BRG1	Brahma-related gene 1
BRM	Brahma
CA1	Cornu ammonis 1
CA3	Cornu ammonis 3
CC	Corpus callosum
CHD	Chromodomain-helicase-DNA binding
CGE	Caudal ganglionic eminence
CoupTF1	Coup transcription factor 1
CP	Cortical plate
CSS	Coffin-Siris syndrome
Ctip2	COUP-TF-Interacting Protein 2 (Bcl11b)
DCX	Doublecortin
DG	Dentate gyrus
DMS	Dentate migratory stream
DSB	Double strand breaks

EdU	5-Ethynyl-2´-deoxyuridine
Emx2	Empty spiracles homeobox 2
EPM	Elevated plus maze
EZH2	Enhancer of zeste homolog 2
FC	Fear conditioning
Foxg1	Forkhead box g1
HIRA	Histone regulator A
Hb H	Hemoglobin H
HPC	Hippocampus
IF	Immunofluorescence staining
INO80	Inositol requiring 80
ISWI	Imitation switch
Lhx2	LIM homeobox protein 2
MAZ	Multipolar cell accumulation zone
MGE	Medial ganglionic eminence
MRN	MRE11-RAD50-NBS1
MWM	Morris water maze
MZ	Marginal zone
NBS	Nicolaides-Baraitser syndrome
NDD	Neurodevelopmental disorder
NEC	Neuroepithelial cell
NEDDLF	Neurodevelopmental disorder with dysmorphic facies and distal limb anomalies

NeuN	Neuronal nuclear protein
Ngn2	Neurogenin2
Ntng1	Netrin G1
Ntng2	Netrin G2
NOR	Novel object recognition
OF	Open field
PAD	PML-associated domain
PanNET	Pancreatic endocrine tumour
PARP1	Poly (ADP-ribose) polymerase 1
Pax6	Paired Box 6
PB	Phenotyper box
PML	Promyelocytic leukemia protein
PML-NBs	PML nuclear bodies
PP	Preplate
PRC2	Polycomb Repressive Complex 2
PTM	Post-translational modification
PV	Parvalbumin
RBR	RNA binding region
RGC	Radial glial cell
RR	Rotarod
Satb2	Special AT-rich sequence Binding protein 2
SENP	SUMO-specific protease
SP	Subplate

Sp8	Transacting transcription factor 8
Sst	Somatostatin
STR	Simple tandem repeats
SVZ	Subventricular zone
VIP	Vasoactive intestinal peptide
VNTR	Variable number tandem repeats
VZ	Ventricular zone
SWI/SNF	Switch/sucrose-non-fermenting
Tbr1	T-Box Brain Transcription Factor 1
Tbr2	T-box Brain Protein 2
VZ	Ventricular zone
WB	Western blot
WBS	William-Beuren syndrome

Significant contributions

Dr Binnaz Yalcin from the University of Bourgogne in France performed the volumetric analysis shown in Figure 5.4.

David P. Cook significantly helped with the analysis of the RNA sequencing dataset shown in Figure 5.12 and 5.13.

Alex John Cordova Albayay performed the Golgi Cox staining shown in Figure 5.15.

Acknowledgements

To Dr David Picketts, you are such an amazing, caring and generous supervisor. I want to thank you for your guidance and support over the last seven years. You gave me confidence and I really appreciate that you trusted my ideas and let me run with it.I sincerely thank you for pushing me to be my best and to believe in me.

Next, I want to thank previous and current members of the Picketts' lab. You guys made it fun to come to the lab every day and welcomed my crazy personality with open arms. To Keqin Yan, my mom in the lab, who is an incredible selfless human. I am grateful for all the time you spend teaching me new techniques in the lab and being present no matter the situation. You have made me laugh when I needed it, listened to me complain and always made me feel like love. You have been a mentor to me and I owe you so much for that. You will always have a special place in your crazy girl's heart.

À ma maman, papa et frère, merci de m'avoir supporté à travers toutes ces années. Je n'aurai jamais été capable de passer au travers sans vous. Vous me montrer constamment à quel point vous être fiers de moi et ça vaut tout l'or du monde. To my friend who are a second family to me. Lauren, Tom, Pascale, Khalid, Ben, Rose, David, Dave and Andrea you are the most amazing group of friends that I could even ask for. I thank you for being there to wipe my tears and take shots with me when it was rough. I love you guys so much!

Lastly to Cedrik, who has been with me through it all. I dedicate my thesis to you. You were always there to comfort me when I cried for the millionth time and telling me that everything would be fine. Even though you keep saying you "don't know brain stuff", your outside view always gave me another useful perspective. Thank you for being there for me and Je t'aime Peplou.

Chapter 1: General Introduction

1.1 Neurodevelopment

1.1.1 Early embryonic development

Embryonic development is a complex, cooperative and methodical process that is tightly regulated by a plethora of signaling factors and gene expression changes [1]. Shortly after implantation, the gastrulation process begins with the formation of the primitive streak. This transient structure expresses multiple signaling molecules that define the anterior-posterior axis and gives rise to the three primary germ layers; the endoderm, mesoderm and ectoderm. These germ layers are the precursors to all the organs and peripheral tissues of the embryo. Of interest for this thesis, the nervous system derives from the ectodermal cells [2].

The neural plate is the thickened portion of the ectoderm layer that folds onto itself during neurulation to create the neural tube [2]. The anterior region of the neural tube can be subdivided into the prosencephalon, mesencephalon and rhombencephalon, which are the precursors of the forebrain, midbrain and hindbrain respectively [3]. The prosencephalon undergoes rapid growth by embryonic day eight (E8) and is further divided into the diencephalon and telencephalon. The diencephalon gives rise to the thalamic regions and the retina whereas the telencephalon separates along the dorsoventral axis into the dorsal pallial (neocortex) and ventral subpallial (basal ganglia and amygdala).

1.1.2 Neocortical development

Neocortical formation begins around E8.5 with the expression of the transcription factor *Forkhead box g1* (*Foxg1*) by the neuroepithelial cells (NECs) [4]. During this period, *Coup transcription factor 1* (*CoupTF1*), *Empty spiracles homeobox 2* (*Emx2*), *Paired box 6* (*Pax6*), *LIM homeobox protein 2* (*Lhx2*) and *Transacting transcription factor 8* (*Sp8*) are expressed in a gradient manner in the rostrocaudal and dorsoventral axes to guide neuroprogenitors to their respective positions [5-9]. Within the dorsoventral axis, *Emx2*, *Pax6* and *Lhx2* are the key transcription factors that specify the neocortical identity [3]. The neuroepithelial progenitors, located in the dorsal ventricular zone (VZ), undergo symmetric division generating more NECs (Figure 1.1) [10]. Then, around E9.5-10.5, NECs begin to differentiate into radial glial cells (RGCs). RGCs are neural progenitors that serve as a scaffold for neuronal migration [11]. They are easily identified by their characteristic radial bipolar morphology. They are characterized by a short apical endfoot located on the surface of the VZ, a soma in the VZ and a long basal process that expands throughout the entire thickness of the neocortex. Initially, RGCs use symmetric division to generate two identical daughter cells. At later stages, they undergo asymmetric division, which produces one RGC for self-renewal and either a postmitotic neuron or an intermediate progenitor cell (IPC) [3]. RGCs expressed the transcription factor *Pax6*, which initiate neurogenesis and regulates the switch between symmetric and asymmetric division [12]. The differentiation of RGC to IPC triggers the expression of the transcription factor *T-box brain gene 2* (*Tbr2*) and the cessation of *Pax6* expression. The pro-neural gene *Neurogenin2* promotes the transition from RGC to IPC by initiating the *Tbr2* expression in IPCs and repressing *Pax6* in RGCs [13, 14]. IPCs start to appear at the onset of peak neurogenesis (E11.5) [11]. Once generated in the VZ, IPCs migrate radially to the subventricular zone (SVZ), a proliferative region that lies above the VZ [15]. IPCs have a limited proliferative potential, thus they mostly divide symmetrically to generate two postmitotic neurons [11]. Occasionally, they produce two identical IPCs that will go on to form neurons. Collectively, RGCs and IPCs comprise the progenitor pool of the developing neocortex.

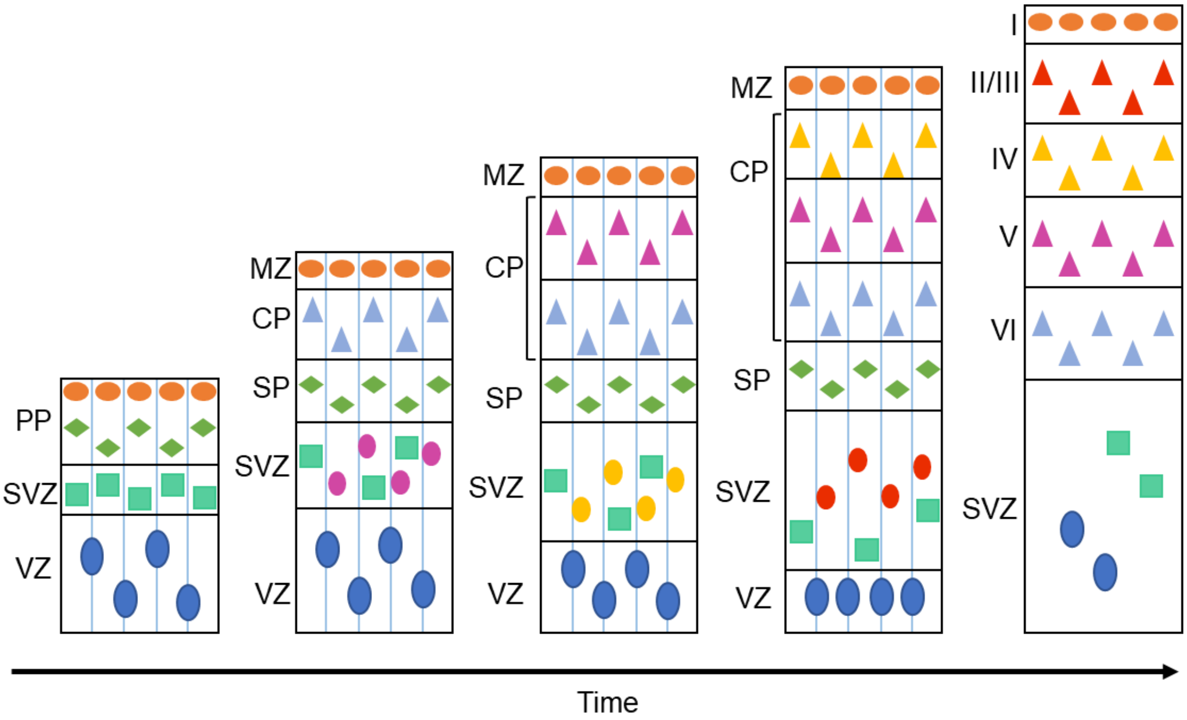

<u>Figure 1.1: Inside-out layer formation of the neocortex</u>

The first wave of postmitotic neurons generated by the RGCs (blue ovals) and the IPCs (turquoise squares) migrate upward to form the PP. The second wave of newborn neurons (blue triangles) migrate through the SVZ and split the PP into the MZ (Cajal-Retzius neurons, orange ovals) and the SP (green diamonds) to form the CP. The subsequent neurons generated in the SVZ (purple, yellow and red ovals) migrate up to expand the CP in an inside out manner (purple, yellow and red triangles). Thus, the later-born neurons migrate radially past the existing layers. The right panel represents the 6 layers of the neocortex. RGC, radial glial cell; IPC, intermediate progenitor cell; PP, preplate; VZ, ventricular zone; MZ, marginal zone; CP, cortical plate; SP, subplate; SVZ, subventricular zone.

Adapted from Tan X and Song Hai Shi 2013 [11]

Once they have acquired their progenitor's identity, *neurogenin1/2* and *Ascl1* are expressed to control and facilitate their differentiation [16]. *Neurogenin1/2* expression favors the differentiation of RGCs and IPCs toward a glutamatergic neuronal identity [16, 17]. On the other hand, *Ascl1* expression specify a GABAergic identity [18].

At E10.5, the newly generated neurons form a layered structure called the preplate (PP). Then, the PP is split into the marginal zone (MZ), which is the most superficial layer, and the subplate (SP) located above the SVZ (Figure 1.1) [19]. The MZ, also called layer I in the postnatal cortex, is mostly populated by Cajal-Retzius neurons [3]. They secrete reelin, a large glycoprotein, that interacts with the extracellular Matrix to guide the radial migration of cortical neurons to their respective layer [20]. The MZ is also a corridor during the tangential migration of GABAergic neurons [21]. On the other hand, the subplate is a transient structure containing some of the earliest born neurons and it is an important regulator of cortical development and plasticity [22]. Around E11.5, the newly-born excitatory neurons migrate to the cortical plate (CP); a structure that develops between the MZ and the subplate [19].

The cortical lamination is a well-organized process that takes place in the CP for the excitatory projection neurons. Interestingly, the cortex is formed in an inside out manner with the earliest born neurons (layer V and VI) located at the bottom of the CP [3]. The late born neurons (layer II-IV) migrate radially and sequentially past layer V and VI to the top of the CP (Figure 1.1, right panel). Layer VI is the deepest layer and has the most diverse morphological cell types [23]. It contains multiform neurons as well as small and large pyramidal neurons. These neurons send their projections to the thalamus and are known to express *Tbr1* [3]. Layer V neurons are large pyramidal neurons that extend their axonal projections to the basal ganglia, spinal cord and brain stem [24]. Furthermore, 20% of layer V neurons send their axons across the *corpus callosum* (callosal projections) [25]. The neurons in this layer are characterized by their expression of *Ctip2*. Layer IV of the neocortex is populated by different types of spiny and pyramidal neurons [26]. These cells mainly integrate the thalamic inputs into the cortical network and are known to express the transcription factor *Foxp1* [27]. Lastly, layer II/III are populated by stellate and pyramidal neurons. These neurons send their axonal projection to the *corpus callosum* and/or the anterior commissure, which are crucial to ensure proper communication between the two hemispheres [25]. Layer II/III neurons express the transcription factors *Cux1*, *Cux2* and *Satb2* [3]. Interestingly, the mouse neocortical layer II and III are merged whereas in humans they are distinct layers. The transcription factors expressed by each cortical layer are closely regulated by one another and are crucial to specify laminar fates. In layer VI, *Tbr1* represses *Ctip2* to specify the identity of the neurons. Once the neuron has migrated to layer V, *Ctip2* will repress *Tbr1* allowing the production and the differentiation of those neurons into their final identity. Similarly, *Satb2* represses *Ctip2* in order to generate layer II/III neurons. This intricate and controlled repression circuit allows for the sequential differentiation of cortical projection neurons as they migrate to their respective laminar position [28].

The cortex is comprised of 70-80% of glutamatergic neurons and 20-30% of GABAergic neurons [29]. Together, they form highly elaborate, interconnected and dynamic microcircuits. The main role of cortical excitatory neurons is to propagate signals whereas the cortical interneurons are responsible for shaping and modulating the network dynamics. In contrast to excitatory projection neurons, there is a large diversity of neocortical interneurons, which is necessary in order to have a malleable system [30]. It includes variation in their morphology, connectivity, firing patterns, gene expression and neurochemistry. Interneurons are classified into three major groups; parvalbumin (PV), somatostatin (Sst) and the ionotropic serotonin receptor 5HT3a (5HT3aR), which is subdivided into vasoactive intestinal peptide (VIP) positive and negative. The origin of neocortical inhibitory neurons as well as their migration to their final position differ from the excitatory neurons. Ventral telencephalic progenitors give rise to the inhibitory neurons in the ganglionic eminences, which is part of the subpallium. More specifically, ~60% of inhibitory neurons originate from the medial ganglionic eminence (MGE) and ~30% from the caudal ganglionic eminence (CGE) [31-33]. PV and Sst cortical interneurons are made in the MGE whereas VIP neurons come from the CGE [3]. The subpallium, similar to the dorsal telencephalon where excitatory cortical neurons are generated, has a VZ with radial progenitors and a SVZ containing basal progenitors [34]. Most interneurons are generated between E11 and E17 and tend to settle in the same cortical layer as excitatory neurons born at the same time [3]. Neurons born in the MGE are typically born earlier and migrate tangentially to the deep cortical layers [35]. On the other hand, neurons from the CGE are born later and migrate to the upper cortical layers. Interestingly, cortical inhibitory neurons sense the ambient GABA and glutamate levels, which stimulates their mobility towards the cortex, and rely on neurotransmission to terminate their migration to their target position [36].

1.1.3 Hippocampal development

The hippocampus is a cortical structure that consists of the *Cornu Ammonis* 1, 2 and 3, also known as CA1, CA2 and CA3, and the dentate gyrus (DG) [37]. The presence of the CA2 hippocampal region in human is unquestionable, however the separation between CA2 and CA3 in other species remains controversial [38]. Even though they are part of the same structure, neurons populating CA1, CA3 and DG have differences in their migration patterns and origin.

CA1 pyramidal neurons are generated between E12 to E18 in mice [39]. While most CA1 pyramidal neurons are generated in the VZ, a small portion are produced by basal progenitors in the SVZ. Newly born neurons move above the VZ in a region called the multipolar cell accumulation zone (MAZ). Here, they transform into multipolar cells and start migrating upwards to the intermediate zone (IZ) located above the MAZ. At this stage, they extend and retract their multiple processes to migrate and sense their environment [40]. Interestingly, the length of time CA1 neurons spend with a multipolar morphology is dependent on their birthdates. Neurons born at E12-E13 are only staying in a multipolar state for a day as they migrate to the IZ [39]. On the other hand, neurons born at E15-E16 keep their morphology for three-four days as they accumulate in the MAZ before moving to the IZ. Time-lapse imaging has shown that CA1 neurons in the IZ move obliquely first, then migrate radially to the hippocampal plate, which is the future pyramidal layer of the CA1 region, by following the tracks of radial fibers. CA1 pyramidal neurons continue to populate the pyramidal layer until the CA1 region is fully formed.

The CA3 pyramidal neurons originate from the VZ between E14 and E18 in mice [37]. Once generated, they travel above the VZ and acquire a multipolar morphology [40]. It is at this stage that they start expressing the glutamate receptor subunit KA1, which is a marker for CA3 neurons. Interestingly, KA1 is expressed in a cell-autonomous manner, which means that the final destination of the CA3 pyramidal neurons is determined during the multipolar stage in the VZ [41]. CA3 pyramidal neurons accumulate in the MAZ for four days before starting their migration to their respective location. It is thought that the prolonged sojourn of CA3 pyramidal cells is due to the neurons waiting to make a connection with the DG granule cells [42]. Unlike the CA1 region, the CA3 hippocampal region has a neurogenic gradient where the oldest neurons are located near the CA1 regions and the youngest are near the DG [43].

The DG progenitors are located in a restricted region of the medial pallium called the DG neuroepithelium [42, 44]. At E13.5, the DG neuroepithelium is referred as the primary dentate VZ, or primary Matrix. By E15.5, a portion of the newly generated progenitors migrate out of the primary Matrix towards the pial side of the cortex [37]. This process is referred to as the dentate migratory stream (DMS) and forms the secondary Matrix (Figure 1.2). This Matrix is comprised of proliferating progenitors and immature granule cells. Once the cells have reached the end of the DMS, they accumulate in a new germinative pool called the tertiary Matrix. Here, dentate granule cells first form the outer portion of the supra-granular blade, which is the top blade of the DG. Once formed, they move on to the outer shell of the infra-granular blade and, by E17.5-E18.5, a prototype of the DG is observed [45]. Within the first two postnatal weeks, the majority of the dentate granule neurons are generated from the tertiary Matrix. The DG is generated in an outside-in gradient, which means that the oldest cells are located at the periphery and the youngest are deeper closer to the hilus [42]. Postnatally, neural stem cells are positioned in the subgranular zone (SGZ), which is one of the two adult neurogenic niches. The mature DG is composed of three layers, namely the granule cell layer, molecular layer and the polymorph layer [46]. The molecular layer contains the dendrites of granule neurons whereas the polymorph layer contains their axons.

Overall, hippocampal microcircuits are highly interconnected networks of neurons that are crucial for learning, memory consolidation, stress response and more. Anatomical and functional abnormalities are often associated with neuropsychiatric disorders, neurodevelopmental disorders and even post-traumatic stress disorders [37].

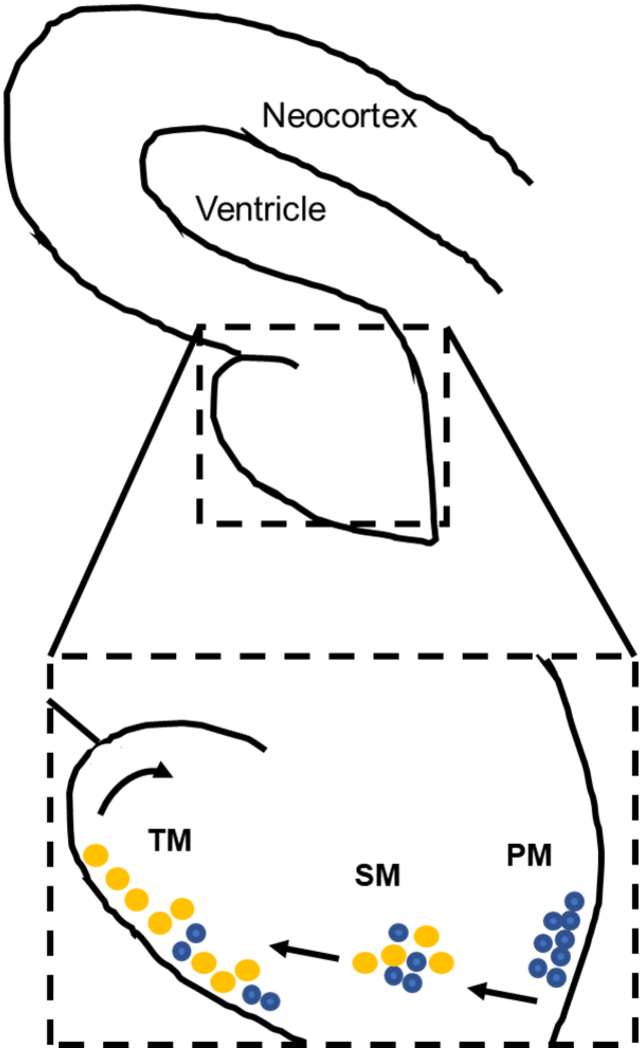

Figure 1. 2: Schematic of the dentate migratory stream during hippocampal development

Newly generated progenitors (blue circles) from the primary Matrix (PM) migrate to the secondary Matrix (SM). They continue to proliferate as they are migrating to generate either a daughter cell or an intermediate progenitor (yellow circles) The progenitors continue their migration toward the tertiary Matrix (TM) where they will form the outer portion of the supra-granular blade first and then they will form the outer shell of the infra-granular blade.

Adapted from Hayashi K et al. [37]

Therefore, any impairments during its developmental can lead to severe pathological conditions including epilepsy, learning and memory disabilities.

1.2 Chromatin and nucleosome organization

1.2.1 Chromatin structure

The human genome is extremely complex and its linear length represents a topological challenge, as it measures close to two meters long [47]. Extraordinarily, it is contained within each cell nucleus, which only has a diameter of ~10μm. Therefore, the process of DNA packaging is crucial for the cell architecture and needs to be meticulously organized. Chromatin remodelers are specialized proteins and/or complexes that cooperate with other chromatin factors to modify the chromatin landscape to expose or conceal specific DNA regions [48].

Chromatin is a highly dynamic structure that works in conjunction with a plethora of proteins to regulate DNA accessibility for transcription, recombination, replication and DNA repair. There are two types of chromatin that have distinct locations and functions. Euchromatin is the decondensed form of chromatin found in the distal arms of the chromosomes [49]. It is considered the transcriptionally active form of chromatin. Euchromatin is loosely dispersed in the nucleus during interphase and is replicated throughout the S phase. Heterochromatin is the portion of the genome that remains condensed and is largely concentrated at the pericentromeric regions of the chromosomes and at telomeres [50]. It is considered the transcriptionally inactive form of chromatin. In the nucleus, heterochromatin is observed at the periphery and is replicated towards the end of S phase.

The fundamental repeating subunit of chromatin is the nucleosome. It is an octamer that consists of two copies of the four canonical histones, namely H3, H4, H2A, H2B, around which 147 bp of DNA is wrapped [51, 52]. Alternatively, nucleosomes can be constructed from histone variants. They can differ from the core histones by a few amino acids or by the addition of larger domains [52]. Variants confer specific biochemical properties to the nucleosome, specialize small or large regions of chromatin and can alter higher-order chromatin structure [53]. For example, some histone variants are involved in the regulation of transcription, others have a temporal distribution and/or tissue-specific localisation [53]. Each nucleosome is linked to another by 10 to 50 bp of DNA, referred as linker DNA arms, depending on the organism and the cell type. Core histones, linker DNA arms and their binding protein linker histone H1 form the chromatosome [54, 55]. The positioning and spacing of the nucleosomes are specific to the regulation of the locus of interest.

Histone exchange is a dynamic process that is crucial and needs to be meticulously regulated. The initiation of histone exchange is facilitated by the weakening of both the histone-DNA interactions and the histone-histone interactions. This can be achieved by the addition of post-translational modifications (PTMs) on histones, by altering nucleosome assembly by histone chaperones or by the ATP-dependent chromatin remodelers [52]. Multiple enzymes can add PTMs to amino acids found on the histones. They can phosphorylate, acetylate, methylate, ubiquitinate and sumoylate the histone tails and globular domains to regulate cellular outcomes [56]. Histone writers, erasers and readers are specific proteins that either add, remove or recognize PTMs [57]. Furthermore, PTMs can facilitate the recruitment of other proteins to the chromatin by forming docking sites [58]. They are often referred as epigenetic changes since they can alter gene expression without modifying the DNA sequence.

Histone phosphorylation occurs on serine, threonine and tyrosine residues located on all 4 histone tails. It is a transient and dynamic event that can be triggered by extracellular signals, DNA damage or entry into mitosis [59]. Histone phosphorylation leads to the specific binding of reader proteins and can change the affinity of reader or writer proteins of other PTMs.

Histone acetylation is also a dynamic process regulated by two large families with antagonizing actions, namely the histone acetyltransferases (HATs) and histone deacetylases (HDACs) [60]. The addition of acetyl groups onto lysine residues neutralizes their positive charge, which prevents the formation of higher-order chromatin structure. Therefore, acetylation is associated with relaxed chromatin and increased accessibility for transcription factors. Oppositely, deacetylation favors a more compact chromatin state and transcriptional repression [61]. In agreement with this, hyperacetylated histone H3 is found in heavily transcribed regions whereas hypoacetylated histone H3 is found in heterochromatin [62]. Furthermore, acetylated histones can be binding sites for bromodomain proteins, which promote transcription [60]. Examples of common acetylated histone marks are H3K4, H3K9, H3K27, H3K79 and H4K20 [63]. In yeast, it is found on more than 40% of all histone H3 and is involved in transcriptional regulation and DNA repair [64, 65].

Methylation can occur either on lysine or arginine residues. Interestingly, there is an added level of complexity since lysine can be mono-, di- or tri-methylated and arginine can be mono- or di-methylated [66, 67]. Contrary to phosphorylation and acetylation, methylation does not alter the charge of the histone protein. It is possible that histone methylation alters the architecture of the chromatin but, due to the relatively small size of the methyl group, it most likely creates specialized binding sites for regulatory proteins [68]. Therefore, histone methylation acts more like a signal for effector molecules that recognize a specific methylated mark [69]. There are known methylated marks on histones that dictates the sub-location within chromatin. For example, H3K9me3 is enriched at the pericentric region whereas H3K27me3 is found on the inactive X-chromosome [70-72]. Oppositely, methylated H3K4, H3K79 and H3K36 are associated with regions on euchromatin that are transcriptionally active [68, 72].

The last two PTMs are the histone ubiquitination and sumoylation, which differ greatly from the other PTMs. Histone ubiquitination involves the covalent binding of a 76-amino acid protein, ubiquitin, via the sequential actions of three enzymes, E1 activating, E2 conjugating, and E3 ligase enzymes [73]. These complexes determine the degree of ubiquitination, either mono- or poly-ubiquitylated, and which lysine residues are targeted. There are two well-characterized ubiquitylated marks found on histone H2A and H2B. H2BK123ub1 is mainly implicated in transcriptional initiation and elongation whereas H2AK119ub1 is involved in gene silencing [74, 75]. Histone sumoylation is closely related to ubiquitination as it involves the small ubiquitin-like modifier (SUMO). Similarly, it is covalently bound to lysine residues through the actions of E1, E2 and E3 enzymes. Both of these PTMs are dynamic processes that can be reversed by the action of either a deubiquitinase or a SUMO-specific protease (SENP) [76, 77].

Histone chaperones are histone-binding proteins that help with histone storage, transport, turnover, nucleosome assembly and PTMs [78]. Contrary to ATP-dependent chromatin remodelers, they destabilize nucleosomes in an ATP-independent manner by using the spontaneous movement of the DNA [52]. Although some histone chaperones share similar binding sites, they are recruited at different locations and have different purposes. For example, deposition of histone variant H3.3 by histone regulator A (HIRA) complex is mainly found in regions with active transcription [79]. HIRA was also linked with the activation and/or long-term maintenance of gene expression patterns [80]. Oppositely, histone H3.3 can be deposited in telomere and pericentric heterochromatin by the histone chaperone complex comprised of Death-domain-associated protein (DAXX) and the chromatin remodeler ATRX [81]. Thus, the coordination between all chromatin-associated proteins needs to be tightly regulated to ensure genome integrity [78].

1.2.2 Chromatin remodelers and their association with neurological diseases

Chromatin remodelers use the energy from ATP hydrolysis to restructure the nucleosomes by weakening the histone-DNA interactions [82]. This process can be achieved by moving, evicting or modifying the composition of the nucleosomes. These dynamic modifications on the chromatin allow for DNA replication, repair and regulation of gene transcription [83]. Chromatin remodelers share similar properties to successfully alter the chromatin landscape. They all have an ATPase domain, part of the SNF2 family of DNA helicases, that is required to bind and hydrolyze ATP and a subunit that modulates the activity of the ATPase. Also, they contain multiple associated subunits and/or domains that provide specificity to binding partners. They can interact with specific histone subunits, DNA sequences, PTMs and other chromatin-associated proteins or transcription factors [84]. The association of different ATPases with multiple combination of subunits gives rise to a distinct set of chromatin-remodelling complexes that are recruited in a context-specific manner [85].

ATP-dependent chromatin remodelers can be classified into five families; SWI/SNF (switch/sucrose-non-fermenting), ISWI (imitation switch), CHD (chromodomain-helicase-DNA binding), INO80 (inositol requiring 80) and ATRX (Alpha Thalassemia/Mental Retardation Syndrome X-Linked) [82, 86]. Each family will be discussed in the following sections.

1.2.2.1 SWI/SNF

The SWI/SNF family of chromatin remodelers is the largest and the most well-studied [87]. There are two different ATPase proteins found in the mammalian SWI/SNF complex that provide the catalytic activity of these complexes, Brahma (BRM) and Brahma-related gene 1 (BRG1) [85]. These ATPase subunits are mutually exclusive, thus only one of them can be found in Brahma/BRG1 associated factor (BAF) complexes at a time. Within the ATPase subunits, there is at least one bromodomain that is responsible for the recognition of acetylated residues in the histone tails [88]. Additionally, a highly conserved group of proteins (BAF47, BAF155 and BAF170) is responsible to maintain the integrity of the complex and is crucial for the chromatin remodeling process [89]. The subunit composition of BAF complexes contributes to the target specificity and is associated to cell-lineage specific functions [90, 91]. SWI/SNF complexes can slide and catalyze the ejection/insertion of nucleosomes. First, the complex binds to specific nucleosomal DNA sequences, which weakens the DNA-histone interactions. Then, using the ATPase activity of the BRG1 or BRM subunits, a DNA loop is formed and propagated around the octamer to facilitate nucleosome sliding. The displacement of nucleosomes exposes genomic DNA, which enables the binding of transcription factors and, ultimately, the transcriptional regulation of specific gene loci [48]. Interestingly, genome-wide studies have revealed that BAF complexes are enriched at promoter regions and super-enhancers of active genes associated with cell proliferation and differentiation [92-94]. SWI/SNF remodelers play central roles in neurodevelopmental processes. In embryonic stem cells (ESCs) BAF complexes are required to maintain the pluripotency [95]. In neural progenitors, it plays a critical role to establish and maintain neural fate and functionality [96].

Multiple neurodevelopmental disorders (NDDs) are associated with mutations in the SWI/SNF family of chromatin remodelers [87]. The Coffin-Siris syndrome (CSS) is an NDD characterized by intellectual disability, distinct facial features and abnormal development of the fifth finger [97]. Mutations in the BAF250B subunit are the most frequent mutations observed in CSS [98]. However, mutations in BAF47, BAF57, BRG1 and BAF250A have also been detected. Similarly, mutations in the *BRM* gene cause a more severe variant of the CSS called Nicolaides-Baraitser syndrome (NBS). Patients with NBS have intellectual disability, epileptic seizures, microcephaly and brachydactyly. Furthermore, alteration of SWI/SNF complexes have been linked to Autism Spectrum Disorder (ASD). Indeed, whole genome sequencing of ASD patients has identified mutations in BAF155, BAF170, BAF180 and BAF250B [99].

1.2.2.2 ISWI

The ISWI proteins were first identified in *Drosophilia* as the ATPase subunits of the nucleosome remodeling factor (NURF) complex [100, 101]. It is characterized by two key motifs, an N-terminal ATPase domain that provides the energy for the remodeling activity and a C-terminal HAND-SANT-SLIDE (HSS) domain that binds to the N-terminal tail of histone H4 and to linker DNA [102-104]. In mammals, SNF2H (*SMARCA5*) and SNF2L (*SMARCA1*) are the two homologs that act as the catalytic subunits of multiple ISWI complexes [105]. SNF2H is transiently expressed during embryogenesis and early postnatal development in proliferating cells [105]. Oppositely, SNF2L is highly expressed postnatally and during adulthood in post-mitotic cells. In mammals, there are eight different ISWI complexes that have been identified: NUcleosome Remodeling Factor (NURF), ATP-utilizing Chromatin assembly and remodeling Factor (ACF), CHRomatin Accessibility Complex (CHRAC), Remodeling and Spacing Factor complex (RSF), Nucleolar Remodelling Complex (NoRC), WSTF–ISWI

CHromatin remodeling complex (WICH), CECR2-containing Remodeling Factor complex (CERF) and SNF2H-cohesin. The core of each complex consists of an ATPase protein (SNF2H or SNF2L) and one regulatory subunit (ACF1, WSTF, TIP5, BPTF, CECR2, RSF1 or BAZ2B) [106]. Unlike the ISWI complexes, CHRAC and NURF contains three subunits instead of one. Contrary to other families of ATP-dependent chromatin remodelers, ISWI remodelers can only slide nucleosomes to expose or hide the genomic strand [82]. The NURF complex contains the catalytic subunit SNF2L, the regulatory protein BPTF, which is one of the two proteins described in this thesis, and two closely related subunits called RBAP46 and RBAP48 [107]. High levels of NURF were reported in the brain and the ability to regulate the transcription of *Engrailed*, suggesting a role for the complex in brain development [108]. Further information about BPTF will be discussed in section 1.3.

The Williams-Beuren syndrome is an NDD characterized by intellectual disability, growth delay, motor defects, epilepsy and dysmorphic facial features [109]. Affected individuals are missing 17 to 28 genes on chromosome 7, which includes the *WSTF* gene encoding a subunit of the WICH complex [104]. Another NDD caused by alteration of a subunit of an ISWI remodeler is the NEurodevelopmental Disorder with Dysmorphic Facies and distal Limb anomalies (NEDDFL) [110]. NEDDFL is caused by mutations in the *BPTF* gene and is further discussed in section 1.3.

1.2.2.3 CHD

The CHD family of ATP-dependent chromatin remodelers is characterized by two signature motifs, namely the tandem chromodomain located in the N-terminal region and a central SNF2-like ATPase domain [111]. Interestingly, the chromodomain facilitates chromatin interactions by binding to DNA, RNA and methylated histone H3 [112]. The CHD family contains nine members that are divided into three groups according to the presence or absence of additional domains: CHDI, CHDII and CHDIII [113]. The first sub-family, which includes the Chd1 and Chd2 proteins, have a DNA-binding domain located in the C-terminal region. They are directly involved in nucleosome assembly and spacing to regulate gene transcription [107]. The second sub-family harbours a pair of PHD Zinc-finger-like domains rather than the DNA-binding domain found in CHDI [111]. The Chd3, Chd4, and Chd5 proteins are the catalytic subunits of the Nucleosome Remodeling Deacetylase (NuRD) complex. The NuRD complex is mostly associated with gene repression. It can directly interact with methylated histones, transcription factors and histone deacetylases (Hdac1 and Hdac2) to remove the histone PTMs. The third CHD sub-family, which Chd6 to Chd9 are part of, is more diverse and less studied than the others [114]. The classification was made based on the functional motifs found in the C-terminal regions that alter the function of the Chd6-9. However, not all members of the CHDIII sub-family share the additional domains.

Mutations in CHD chromatin remodelers have a wide spectrum of effects. For example, mutations in CHD2 have been discovered in patients with ASD, developmental delay, intellectual disability and epileptic seizures [115]. Also, haploinsufficiency of the *CHD7* gene is the main cause of CHARGE syndrome (Coloboma of the eye, Heart defects, Atresia of the choanae, Retardation of growth and/or development, Genitalia and/or urinary abnormalities, and Ear abnormalities and deafness) and is found in patients with Kallmann syndrome [116, 117]. *In vitro* studies found that some *CHD7* mutations led to a defect in nucleosome remodelling, thus directly associating CHARGE syndrome with chromatin remodelling defects [118].

1.2.2.3 INO80

The INO80 family consists of the INO80 complex and the SWR subfamily, which includes the SWR SNF2-related CREB-binding protein activator protein (SRCAP) and TIP60/P400 [107]. Unlike the other chromatin remodelers, the INO80 family is characterized by the addition of a conserved insertion in the ATPase domain, which is responsible for the presence of two RuvB-like helicases, Rvb1 and Rvb2, in the various complexes [119]. Although the INO80, SRCAP and TIP60/P400 have a few subunits in common, the additional subunits within the complex confer different roles in chromatin remodeling, nucleosome modification, and gene regulation. The INO80 complex is often associated with the establishment of nucleosome spacing, nucleosome eviction, remodelling and the exchange of histone variant H2A.Z [120-123]. Also, it has been shown that INO80 is required for embryonic stem cell renewal and to establish pluripotency [85]. On the other hand, SWR complexes are specialized in the deposition of histone variant H2A.Z [119]. The SRCAP complex has been associated with the eviction of the canonical histone H2A to replace it by the histone variant H2A.Z [121]. On the other hand, the TIP60/P400 complex can acetylate the core histones H2A, H3, and H4 and other signaling molecules to modulate specific cellular responses [124, 125]. Particularly, it can recognize DNA damage sites and promotes the remodelling of chromatin flanking the site to an “open” state to facilitate the access of the repair machinery to the double strand DNA break to repair it [107]. This process is accomplished by the acetylation of histone H4 and the exchange of histone H2A [126].

Multiple syndromes and pathologies have been associated with mutation in the INO80 and SWR complexes. For example, mutations in TIP60 has been linked with a syndrome that causes individuals to have short stature, cerebral malformations, seizures, global developmental delay and intellectual disability [127]. Similarly, SRCAP complex mutations have been identified as the cause for Floating-Harbor syndrome, which is characterized by a short stature, language deficits, intellectual disability and dysmorphic features [128].

1.2.2.4 ATRX

ATRX is the other protein of interest of this thesis. Briefly, ATRX was first discovered as the cause of X-linked alpha thalassemia mental retardation (ATR-X) syndrome (see section 1.4.5) [129]. Similarly to the other families of chromatin remodelers, ATRX has a C-terminal ATPase domain of the SNF2 family [130]. It is also characterized by an N-terminal ATRX-DMNT3L-DNMT3A (ADD) domain that is comprised of a PHD- and GATA-zinc finger module which functions to bind to the H3K9 methylated histone tails. ATRX is also known to interact with the histone chaperone DAXX to deposit the histone variant H3.3 at telomeric and pericentric heterochromatin [81]. Further information regarding its structure, interactions and function are described in section 1.4.

1.3 Bromodomain PHD transcription factor (BPTF)

1.3.1 Protein structure and characterization

The Bptf protein was first isolated from embryo extracts of *Drosophilia melanogaster* [131]. It was named NURF301 as it was the largest subunit of the NURF complex at 301kDa. On the other hand, the full-length *BPTF* gene was identified through a cDNA database search for new bromodomain-containing genes [132]. The human BPTF protein is approximately 300 kDa in size and is the largest subunit of the NURF chromatin remodeling complex.

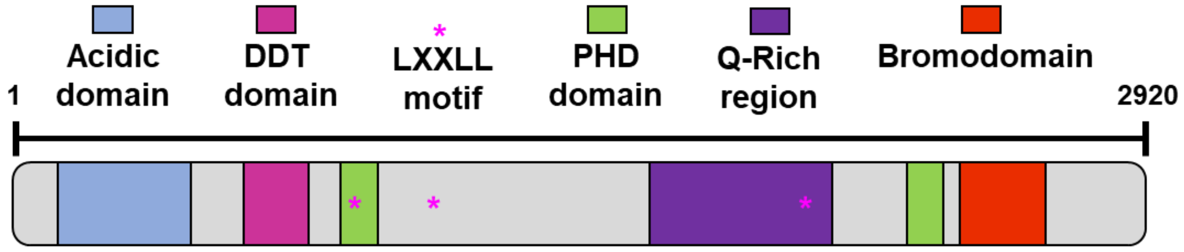

Figure 1.3: BPTF protein

Schematic representation of the domain organization of the *Homo Sapiens* BPTF protein (2920 amino acids). Each domain is represented with different colours. The location of the LXXLL nuclear receptor-binding motifs are depicted as pink asterisks.

The protein structure of BPTF is characterized by specific motifs at the N- and C-terminal regions (Figure 1.3). It is also noted that BPTF contains 3 LXXLL nuclear receptor-binding motifs as well as a glutamine-rich region [133]. However, the functions of those regions are not well understood. The N-terminus contains an acidic domain, a DDT domain, which has DNA-binding abilities, and a PHD domain [134]. The C-terminal region contains another PHD domain adjacent to a bromodomain [133]. This PHD domain can detect methylated marks on the lysine 4 residue of histone H3 (H3K4me2/3) to promote nucleosome remodelling by the NURF complex [135]. Interestingly, its affinity declines as the number of methyl groups decreases. The bromodomain was shown to recognize and interact with multiple acetylated marks on histone H4, namely K12ac, K16ac and K20ac [136]. In the presence of the H3K4me3 mark within the nucleosome, the specificity of the bromodomain for K16ac is significantly increased. Also, it was reported that the bromodomain can transiently bind to histone variant H2A.Z [137].

1.3.2 Previous studies

Multiple studies have been conducted to elucidate the function of *Bptf* in different cell types. It was reported that *Bptf* is required for the self-renewal of mammary stem cells and their differentiation into mammary epithelial cells (MECs) [138]. In the absence of Bptf, an uncharacterized MEC type is generated and is associated with upregulation of apoptotic pathways. Genome-wide analysis revealed an increase in chromatin accessibility of regulatory regions located near apoptosis- and cell cycle-related genes when BPTF was deleted. Bptf has also been shown to be involved in immune cell maintenance. For example, it is essential for thymocyte maturation, T-cell homeostasis and the development of Treg cells in the periphery [139, 140].

Bptf implication in cancer has recently gained importance. Indeed, it was reported that overexpression of Bptf was noted in non-small-cell lung cancer, hepatocellular carcinoma and colorectal cancers [141-143]. In melanoma, Bptf overexpression is associated with a poor survival outcome [144]. It was demonstrated that Bptf regulates *BCL2*, *BCL-XL*, and *CCND2*, which are key genes promoting tumorigenesis. Another study showed that Bptf forms a complex with the transcription factor c-MYC to promote tumorigenesis [145]. In mouse embryonic fibroblast, Bptf is essential for c-MYC-driven proliferation, the transition from G1 to S-phase and for preventing replication stress. Furthermore, it was reported that in absence of Bptf, DNA accessibility at c-MYC target genes is reduced and c-MYC recruitment to chromatin is impaired [146]. This ultimately leads to a reduction in cell proliferation and increased replication stress [145, 147]. Disruption of the Bptf-c-MYC complex could potentially be used as a therapy in c-MYC-driven tumours [133].

In mice, *Bptf* is essential for embryonic development [148]. Embryos with loss-of-function mutations of *Bptf* do not survive past E7.5-E8.5. Microarray analysis revealed that many essential markers for early embryonic tissue differentiation were altered in the mutant embryos. Also, *Bptf* was identified as a co-activator of Smad-dependent genes in embryonic stem (ES) cells. Multiple genes within this pathway require *Bptf* for their partial or full activation. In the absence of *Bptf*, ES cells show significant defects in the differentiation of ectoderm, mesoderm and endoderm. Thus, Bptf is vital for the early stages of embryonic development.

1.3.3 Neurodevelopmental Disorder with Dysmorphic Facies and distal Limb anomalies

Neurodevelopmental Disorder with Dysmorphic Facies and distal Limb anomalies (NEDDFL) is a newly identified syndrome caused by loss-of-function or missense mutations of one of the *BPTF* alleles [110]. Upon discovery, 11 unrelated individuals were diagnosed with NEDDFL, seven of which are males and four are females [110, 149]. Common features are developmental delay observed in 11/11 patients, intellectual disability 11/11, speech delay 11/11, microcephaly 8/10, dysmorphic features 10/11 and motor delay 9/11. Interestingly, one of the individuals was previously diagnosed with Silver-Russell syndrome, which shares similar features with NEDDFL. Thus, it is possible that other individuals with comparable features have been misdiagnosed and that the number of patients with NEDDFL is greater than what is reported. Recently, 25 new cases were discovered with additional features including seizures, scoliosis, mild ophthalmologic defects and brain abnormalities [150].

It is thought that NEDDFL results from the haploinsufficiency of *BPTF* causing an increase in neuronal cell death [110]. Our lab previously generated a forebrain-specific *Bptf* knockout (cKO) using the *Emx1* Cre driver to study the pathogenesis of NEDDFL in a mouse model [151]. It was reported that the *Bptf* cKO mice has severe forebrain hypoplasia associated with a reduction in intermediate progenitor cells, increased apoptosis and a prolonged cell cycle length within proliferating progenitors. The reduced brain size is consistent with patients who present with microcephaly. Also, RNA-sequencing analysis revealed that specific pathways involved in neurogenesis and neuronal differentiation were dysregulated. However, more research on this syndrome is required and more characterization is needed to fully understand the extent of the pathogenesis and how closely it mirrors the human syndrome.

1.4 ATRX

1.4.1 Protein structure

ATRX is a large gene that spans over 300 kb on chromosome Xq13.3-21.1 [129, 130]. It is comprised of 40 exons and is differentially spliced to generate 24 protein-coding transcripts (http://vega.archive.ensembl.org), including two transcripts of well-characterized protein variants. These two transcripts are the full-length ATRX and a truncated isoform called ATRXt. Full-length ATRX is the most abundant protein variant, contains 36 exons and encodes a protein of 285 kDa in size. On the other hand, ATRXt is the second most common ATRX transcript and encodes a 200 kDa protein [152]. The ATRXt isoform arises from the failure to splice out intron 11 causing a premature stop in the translation and the absence of the ATPase/helicase domain.

ATRX is an ATP-dependent chromatin remodeler (Figure 1.4). In the literature, it is either considered to be part of the SWI/SNF family or is classified as an orphan member [130, 153]. ATRX has a C-terminal ATPase domain of the SNF2 family, which is used to generate energy to remodel nucleosomes [130]. This domain consists of two highly conserved RecA-like lobes that are required for the ATPase activity [153]. Unlike the other members of the SWI/SNF family that randomly reposition a nucleosome relative to a specific DNA sequence [154], ATRX participates in triple-helix DNA displacement similar to the DNA repair protein Rad54 [155]. The other domain essential for ATRX function is the ADD domain. The ADD domain is subdivided into three components: an N-terminal GATA-like finger, a PHD-like domain, and a C-terminal α-helix [156, 157]. The primary role of the ADD domain is to bind to specific modifications of the N-terminus of the histone H3 tail.

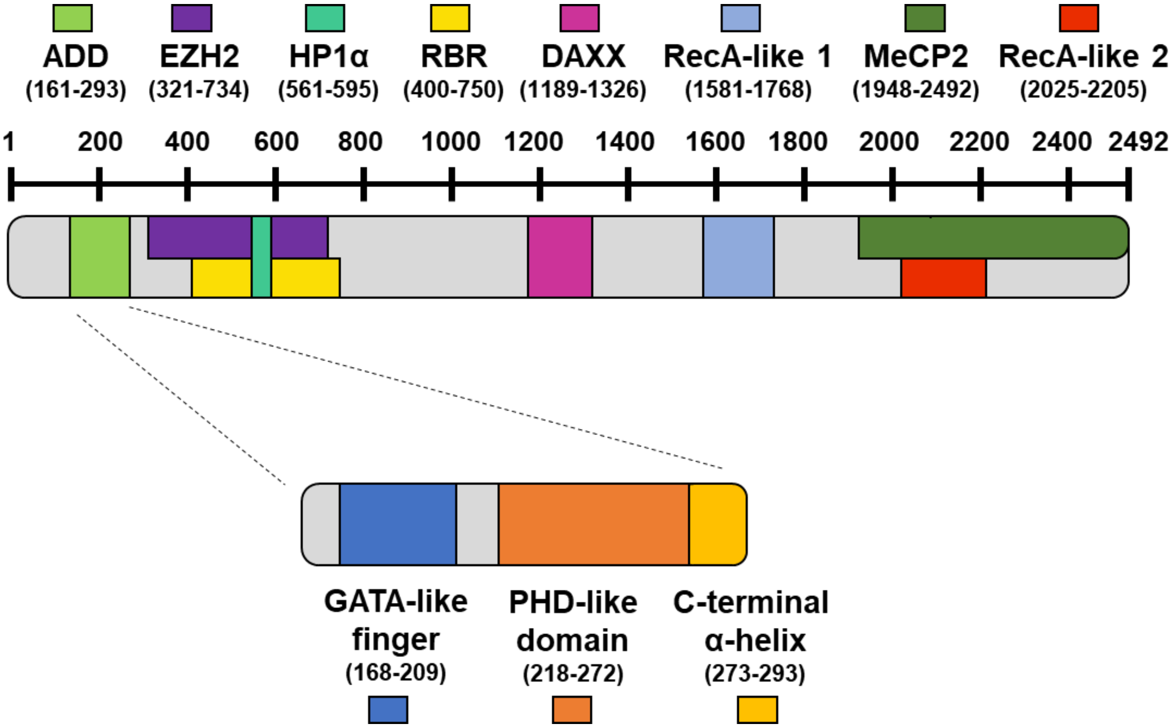

Figure 1.4: ATRX protein

Schematic representation of the domain organization of the ATRX protein with the corresponding amino acids. All the domains, except for the ADD and helicase domains which are functional domains, are protein interaction domains. Each domain is represented with different colours and the amino acids involved are noted. The ADD domain is enlarged to show the GATA-like finger, PHD-like domain and C-terminal α-helix. The ATPase domain is comprised of the RecA-like1 and RecA-like 2 motifs.

Adapted from Valenzuela M et al. [158].

The histone post-translational modifications (PTMs) recognized by the ADD domain is a combinatorial mark of H3K9me3 and H3K4 [159, 160]. It can also recognize the combinatorial mark H3K9me3S10ph [161]. H3K9me3 recognition module allows ATRX to sense methylation states of H3K9 and H3K4, which dictate the binding capacity of ATRX to the H3K9me3 modification (e.g. H3K4me3 prevents ATRX from binding to the nucleosome).

1.4.3 Interacting partners and molecular function

ATRX is localized to pericentromeric and telomeric heterochromatin throughout the cell cycle [162]. It interacts with specific histone PTMs directly via its ADD domain, or indirectly by associating with secondary interacting proteins, such as HP1α or MeCP2 [163, 164]. HP1α interacts with H3K9me3 through its chromodomain and recruits ATRX to these sites via an LxVxL binding site located between the ADD and ATPase domains [161]. Mutations within the motif significantly impair ATRX localization to heterochromatin [160]. MeCP2 interacts with ATRX through the C-terminal helicase domain of ATRX. Also, ATRX localization to heterochromatin is disrupted in the absence of MeCP2 [164-166]. Interestingly, the N-terminal fragments of ATRX localize to heterochromatic loci in an MeCP2-independent manner whereas the C-terminal localization is dependent on the MeCP2 interaction, thereby suggesting that multiple mechanisms can recruit ATRX to heterochromatin [164].

Examination of the binding sites of ATRX on heterochromatin showed specific patterns of simple tandem repeats (STRs), variable number tandem repeats (VNTRs) and long terminal repeats of endogenous retrovirus sequences of family K (ERVK) [167]. The STRs DNA sequences have a high GC content and are prone to forming a secondary DNA structure known as a G-quadruplex (G4 DNA). The formation of G4 DNA is presumed to be an obstacle to the movement of enzymes along the DNA strand, impacting DNA replication and transcription, and presenting a source of genetic instability [168]. The role of ATRX in preventing G4 DNA formation is thought to promote some of the phenotypes observed in the ATR-X syndrome. One of the features of the ATR-X syndrome is the α-thalassemia blood disorder. It was reported that patients sharing the same ATRX mutation can have different levels of α-globin [167]. ATRX binds to a VNTR sequence upstream of the HBM gene. The authors found a positive correlation between the size of the VNTR sequence and the severity of the α-thalassemia. Indeed, the longer the size of the VNTRs, the more HbH inclusions were found in the red blood cells, which correspond to a more severe phenotype. It was inferred that longer VNTR sequences increases the probability of G4 DNA formation that ultimately alters HBM expression.

Outside of these heterochromatin interactions, ATRX has a key interacting partner: the histone chaperone death domain-associated protein (DAXX). Together, they form a histone chaperone complex for the deposition of histone H3.3 in repetitive regions of the genome, including telomeres, where deposition of H3.3 with the H3.3K9me3 mark is critical for telomere maintenance [169-171]. In fact, telomere structure is maintained by a positive feedback loop. H3.3K9me3 recruits more ATRX-DAXX complexes that will deposit more H3.3 that will be targeted for trimethylation on its K9 residue [171, 172]. Mutations in the ATRX-DAXX-H3.3 pathway are prevalent in cancers characterized by alternative lengthening of telomeres (ALT), which is a telomerase-independent pathway to prevent the shortening of telomeres [173]. Activation of the ALT pathway is typically found in pancreatic endocrine tumours (PanNETs), gliomas, neuroblastomas and sarcomas and is associated with a positive prognosis in most cancers [174-177].

Aside from telomeres, ATRX-DAXX protects normally-silenced repetitive sequences, including retrotransposons [172]. ATRX-DAXX loading of histone H3.3 into these regions prevents DNA secondary structure formation, which stalls replication and transcription and can promote inappropriate recombination to occur at these sequences [172]. ATRX is also localised to multiple interstitial heterochromatin sites and imprinted alleles where it has a role in the regulation of transcription [166, 178, 179]. Under normal condition, the ATRX-DAXX complex deposits H3.3 preferentially to the methylated allele of imprinted differentially methylated regions (DMRs) to silence them. In the absence of ATRX, deposition of H3.3 fails leading to the loss of the H3K9me3 modification at imprinted DMRs, loss of repression and aberrant expression of these genes [178]. Conditional deletion of *Atrx* using *Foxg1*-Cre showed that some imprinted genes were upregulated in the forebrain and that impairment of the imprinting process leads to multiple intellectual disability syndromes [166, 180, 181]. In a mouse model with a human ATRX mutation, the $ATRX^{\Delta E2}$ mice, DNA microarray analysis revealed that the *Xlr3b* gene, an imprinted gene involved in the regulation of dendritic spine morphogenesis and synapse assembly, was upregulated in the absence of *Atrx* [182, 183]. They showed that ATRX binds directly to the G4 DNA found within the *Xlr3b* gene and regulates its expression by recruiting DNA methyltransferases. The overexpression of *Xlr3b* leads to the inhibition of dendritic transport of the CamKII-α mRNA causing synaptic dysfunction.

Another study showed that ATRX can bind within the gene bodies at repetitive sequences that have a high H3.3 occupancy and high probability of forming G4 DNA [184]. They showed that in absence of ATRX, the progression of the RNA polymerase II (RNApolII) at the ancestral pseudoautosomal region (aPAR) is impeded at these sites due to G4 DNA formation leading to incomplete transcript formation. Of interest, the autism susceptibility gene

Neuroligin 4 accumulates RNApolII within its gene body leading to a significant reduction of its expression.

During the neuronal differentiation process, dramatic changes to the chromatin landscape are required to repress or activate specific genes. In embryonic stem cells, SOX2 forms a complex with OCT4 to maintain pluripotency [185]. In mature neurons, ATRX associates with SOX2 at neuronal promoters to increase the expression of nearby genes [186]. The localization of ATRX-SOX2 correlates with increased active enhancer marks H3K7ac and H3K4me1. These results highlight a new regulatory role for ATRX during neuronal differentiation.

Furthermore, it was suggested that DAXX recruits ATRX to promyelocytic leukemia protein (PML) nuclear bodies (PML-NBs), thus regulating the cellular localization of ATRX [158]. PML-NBs are dynamic structures present in the nucleus of most cells [187]. They are formed by a shell of PML protein that are transiently and/or permanently associated with over 100 proteins, including the DAXX/ATRX complex and histone H3.3 [188-190]. PML-NBs are implicated in the regulation of multiple cellular processes such as the cell cycle, apoptosis, gene expression, stress and DNA damage response [158]. It was previously demonstrated that PML-NBs can be found in specific heterochromatic regions such as telomeres [191]. Due to the localization of the DAXX/ATRX/H3.3 complex at PML-NBs, it was suggested that the complex was responsible for the deposition of PML-NBs to specific chromatin regions [189]. Interestingly, in the absence of the PML protein, the deposition of H3.3 by DAXX/ATRX to PML-associated domains (PADs) on heterochromatin is significantly impaired. Also, there is a shift in chromatin states of PADs favoring H3K27me3 instead of H3K9me3. H3K27me3 is a well-known repressive epigenetic mark that is placed by the Polycomb Repressive Complex 2 (PRC2) [192].

ATRX is critical to maintain genome integrity during cell replication and prevent replication stress [193, 194]. During cell replication, it is recruited to the site of DNA damage and associates with the MRE11-RAD50-NBS1 (MRN) complex, which is an important player in DNA damage recognition and double strand break (DSB) processing [195, 196]. In embryonic mouse brains, Atrx deletion causes defects in mitotic progression in neuroprogenitors and abnormal chromosome congression and segregation [197]. Other studies revealed that ATRX deletion leads to defects in replication fork progression resulting in a prolonged S-phase, inability to maintain telomere structure, increased DSBs and mitotic catastrophe [194, 195, 198-200]. Furthermore, the accumulation of DNA damage and fork degradation triggers the activation of poly(ADP-ribose) polymerase 1 (PARP1) by the neural progenitors to promote fork protection and ultimately cell survival [200].

Lastly, it is well known that ATRX is an RNA-interacting protein. It binds to Xist, a long non-coding RNA (lncRNA) on the inactive X chromosome (Xi), to regulate the enrichment of the histone methyltransferase complex PRC2 and facilitate stable heterochromatin formation [201]. Also, ATRX is involved in X chromosome inactivation through its direct interaction with Enhancer of zeste homolog 2 (EZH2), the catalytic subunit of PRC2 (Figure 1.4). Recently, the RNA binding region (RBR) on ATRX was discovered [202]. It is located within the N-terminal region. Interestingly, deletion of the RBR significantly impairs the ATRX-RNA interactions and partially compromises the localization of ATRX to chromatin. Thus, ATRX localization to chromatin is partially dependent on its RNA interaction.

1.4.4 Morphology and cellular studies

It was previously shown that the mutations that cause the ATR-X syndrome are functional hypomorphs [203]. However, it is still unclear how these mutations can cause intellectual disability and other neurological defects. Several ATRX knockout mouse models have been generated over the years, which all result in early lethality. Indeed, global ATRX knockout mice using the *GATA-1-Cre* diver die around embryonic day 9.5 due to a defect in the formation of the extraembryonic trophoblast [204]. On the other hand, conditional ATRX knockout in the forebrain using the *Foxg1*-Cre knock-in line induces premature cell death during corticogenesis and death of the animal by P1 [205, 206]. Also, these animals show loss of proliferating neural progenitors that caused hypocellularity in both the cortex and hippocampus. More specifically, there is a reduction in dentate granule cells, pyramidal cells of upper cortical layers, and GABAergic interneurons, disrupting the ratio of excitatory and inhibitory signals [207]. It is important to note that the *Foxg1*-Cre line was shown to have a highly variable Cre activity pattern, abnormal behavioral response, and congenital hypoplasia in the *corpus collosum* [208]. Here, the Cre recombinase was knocked-in to one of *Foxg1* allele, thus the mice were heterozygous for FOXG1. Therefore, not all the phenotype observed in the Atrx knockout animals using the Foxg*1*-Cre driver can be attributable to the loss of Atrx since they have a compound mutation. To account for this caveat, another forebrain-specific ATRX knockout was generated using the *Nestin-Cre* driver [205]. Similarly, these mice died at P1, were smaller in size and have a reduced caudal-medial cortex. Overall, the phenotype of *Atrx*$^{f/y}$*;Nestin-Cre* mice was comparable to *Atrx*$^{f/y}$*;Foxg1-Cre* mice but less severe.

To avoid these limitations, the retina has been used to study the role of ATRX, as the retina is a well-characterized structure with development similar to the CNS [209].

Additionally, ocular defects were found in 25% of ATR-X syndrome patients [210]. Interestingly, ATRX is important for the survival of amacrine and horizontal cells postnatally and this critical period coincides with light-induced synaptic organization [210]. However, it is unclear whether the cell death is due to a developmental defect caused by the absence of ATRX, or a light-induced phenomenon. Further investigation showed that retinal interneuron survival requires a non-cell autonomous ATRX activity, suggesting a maturation or cell connection defect [211]. Also, many subtypes of these retinal interneurons displayed an altered morphology and reduced number, suggesting that ATRX is required for normal retinal function [210].

Furthermore, quantitative RT-PCR showed altered expression of excitotoxicity-related genes, like *Gad67* and *GluR1*, in the retina of conditional ATRX knockout mice [211]. Interestingly, impairment in the glutamatergic system in the brain was observed in mice with a human ATRX mutation resulting in hypomorphic expression ($ATRX^{\Delta E2}$). These animals expressed ATRX protein at 30% levels but survived through adulthood and have behavioral deficits [212]. Dendritic spines of pyramidal neurons in medial prefrontal cortex (mPFC), but not hippocampal CA1 neurons, showed an altered morphology following ATRX deletion in this model [212].

Recently, an Atrx conditional knockout mouse has been generated using the αCaMKII-Cre driver [213-215]. Here, *Atrx* ablation occurs postnatally in forebrain excitatory neurons, avoiding the early lethality previously mentioned. Both male and female knockout mice have deficits in odor discrimination but no social deficits, stereotypies, and repetitive behaviours, which are often observed in autism [214]. Further examination revealed a male-specific long-term spatial learning and memory deficit associated with structural hippocampal defects [215]. The *Atrx* knockout male had fewer synaptic vesicles and an enlarged postsynaptic area at the

CA1 apical dendrite-axon junctions. Next-generation sequencing showed that *Atrx* ablation in excitatory neurons of male mice results in an aberrant expression of synapse-related genes. Also, it was demonstrated that *Atrx* directly binds to the miR-137 sequence, which is a microRNA found in presynaptic terminals that has been implicated in neurotransmitter release. Lastly, electrophysiology experiments revealed that *Atrx* knockout males had impairments in hippocampal synaptic transmission [213]. Thus, Atrx is required in excitatory neurons for adequate hippocampal synaptic transmission and plasticity.

1.4.5 ATR-X syndrome

1.4.5.1 Discovery: α-thalassaemia syndrome

The ATR-X syndrome was first reported in 1981 by Weatherall et al. [216]. The research group described three families with northern European origin in which a son had severe intellectual disability and hemoglobin H (Hb H) disease. Hb H disease is a blood disorder resulting from a reduction in the synthesis rate of the α-chains of hemoglobin and an accumulation of β-chains. This leads to the formation of β_4 molecules (Hb H) instead of the normal $\alpha_2\beta_2$ molecules. The Hb H precipitates in the red blood cells which leads to their premature hemolysis causing anemia. Hb H disease is a type of α-thalassaemia syndrome, in which molecular defects lead to the suppression of the α-chain synthesis.

ATR-X syndrome is a neurodevelopmental disorder associated with mutation in the ATRX gene [129]. There is a wide range of clinical features observed in patients and the severity of those features is variable. In the following sections, we will discuss the patients' phenotype.

1.4.5.2 Neurological features

The first neurological features observed in ATR-X affected males is the microcephaly that develops postnatally despite a normal head circumference at birth. A comprehensive study used the MRI and CT scans of 27 patients with *ATRX* mutations or ATR-X syndrome to assess the neuroradiologic features [217]. They classified the brain anomalies they found in five categories; 1) nonspecific brain atrophy (17/27); 2) white matter abnormalities, especially around the trigones (11/27); 3) widespread and scattered white matter abnormalities (1/27); 4) delayed myelination (4/27); and 5) severe and rapidly progressive cortical brain atrophy (1/27). Other studies have shown either hypoplasia, and partial or complete agenesis of the *corpus callosum* [218-220]. Seizures have been reported in approximately one third of ATR-X patients and most of those seizures are tonic/clonic or myoclonic in nature [218, 221-225]. Parents often report jerking movements that resemble seizures but they are not associated with epileptiform activity on EEG. As the affected children grow older, there is a tendency for spasticity.

1.4.5.3 Anatomical features

ATR-X syndrome patients share distinct facial features that are used, in combination with other symptoms, for the diagnosis. It is thought that most of the facial anomalies are caused by facial hypotonia [226]. Generally, the distance between the eyes is increased, while the nose is small, triangular and uplifted (Figure 1.5). Also, affected males have mid-face hypoplasia, upswept frontal hair line and their tongue protrudes causing significant drooling. Many affected subjects have skeletal abnormalities and some of them are due to hypotonia and immobility. Indeed, it was reported that 91% of ATR-X syndrome patients have relatively mild skeletal abnormalities [218].

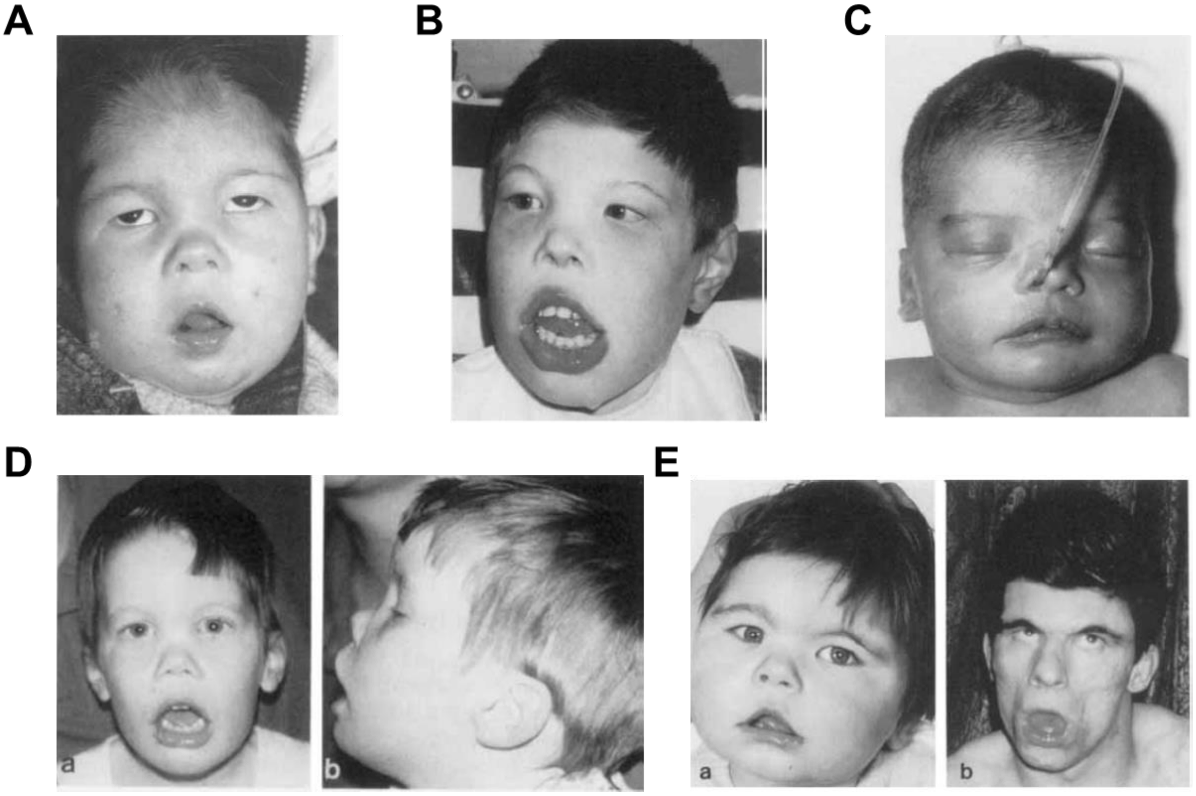

Figure 1.5: Anatomical abnormalities shown in ATR-X syndrome patients.

A) Subject is 1.5 years old; facial abnormalities, positional deformity of the feet, severely hypotonic, lethargic with a poor suck, occasional myoclonic jerks and delay in his motor development. B) Subject is 13 years old; facial abnormalities; feeding difficulties from birth, cleft of the soft palate, walk without assistance and no speech. C) Subject is 14 days old; abnormal facial appearance, hypotonia, difficulties feeding, several cardiovascular defects. D) Subject is 4 years old; facial abnormalities, micropenis, hypotonia, psychomotor delays, no speech, no language comprehension and brain atrophy. E) Same subject at 1.5 years old (left panel) and 23 years old (right panel); severe developmental delays, facial anomalies, skeletal abnormalities of the lower limbs, able to walk, no speech, poor language comprehension and episodes of agitation and headbanging. Adapted from Gibbons et al. [6] with permission from John Wiley and Sons.

Growth delays is common as well as short stature in 2/3 of the affected males. These skeletal abnormalities lead to motor delays and/or deficits and in worst cases the subjects are wheelchair bound.

Genital abnormalities are found in 80% of affected children and their severity is highly variable. In some cases, the phenotype is very mild and presents as undescended testes or deficient prepuce. Other subjects have a micropenis, hypospadias or even ambiguous female external genitalia [222, 227]. In more severe cases, the male pseudohermaphrodites are raised as female. These subjects have no Mullerian structures, dysgenetic testes and streak gonads. Commonly, the puberty is delayed and, sometimes, is completely arrested in some subjects.

1.4.5.4 Behavioral features

It is important to note that no systematic study of behaviour has been conducted for ATR-X syndrome. Thus, most of the behavioural phenotypes of the subjects are anecdotal. Nevertheless, all reports taken together are generating a thumbnail sketch of the mannerisms [228, 229] that could be useful for diagnostic purposes. Parents report that their children have a happy demeanor and experience a wide range of emotions that are appropriate to the circumstances. Many individuals with ATR-X syndrome are affectionate towards their caregivers and appreciate physical contacts [226]. Occasionally, some patients will exhibit autistic-like behaviours that include eye contact avoidance and little interest and/or recognition of people around them. In this situation, patients appear to be in a world of their own with little contact with reality. Aggressive behaviours, including hair pulling, pinching and scratching, are common behaviours that can be observed towards siblings. Affected individuals experience episodes of hyperactivity where they become highly agitated and vocal. These occurrences are accompanied with screams that can last for days as well as head banging and other self-injurious behaviours.

Lastly, affected males exhibit choreoathetotic movements, which are defined as rapid (chorea) and slow (athetosis) involuntary movements. In the case of ATR-X syndrome patients, they frequently put their fingers into their mouths and, on occasion, induce vomiting. Unfortunately, other involuntary movements are related to self-injuries. Repetitive stereotypic behaviours can be found in most ATR-X syndrome males. They vary between pill-rolling and hand flapping to spinning around on one spot while gazing into a light. These behaviours are commonly shared in several autism spectrum disorders and neurodevelopmental disorders, which can lead to misdiagnosis.

1.4.5.5 Gastrointestinal features

Infantile hypotonia is a very common symptom associated with severe sucking difficulties [226]. Consequently, a feeding tube is often required for many weeks to ensure proper nutrition. Several children develop persistent feeding problems that ultimately leads to malnutrition and require the use of a feeding gastrotomy. In early childhood, recurring vomiting, gastroesophageal reflux, regurgitating, abdominal distention and chronic constipation have been recognized as common complications [218, 230].

1.4.5.6 Diagnostic criteria

To this day, there are no definitive diagnostic criteria that have been set for ATR-X syndrome. Nevertheless, there are typical features that are common among affected individuals; severe intellectual disabilities, severe expressive language disorders, distinctive facial traits, genital abnormalities and α-thalassaemia blood disorder. Based on these clinical features and blood tests, ATR-X syndrome can be suspected at birth or early childhood. However, a definitive diagnostic can only be obtained by sequencing the *ATRX* gene to identify mutations.

1.5 Inhibitory/excitatory balance in Autism spectrum disorders

Autism spectrum disorder (ASD) encompasses a large number of intellectual disability disorders that share common symptoms (e.g. Epilepsy and hyperactivity) [231]. In most cases, a reduction in GABAergic signaling has been observed in the brains of autistic patients [232]. Based on various studies, a new theory emerged suggesting that an increase in the inhibitory to excitatory neuron ratio leads to hyper-excitability of cortical circuits in ASDs [233]. This could explain the changes in GABAergic inputs and the epileptic episodes found in autistic patients. Contradictory findings, however, have shown a reduction in the ratio is modified in ASD [234]. The discrepancy in these findings may arise from single genes that are mutated in ASD and are responsible for a large number of fundamental cellular processes. Thus, alteration of these genes has complex effects in multiple cell types and can give rise to changes in excitation or inhibition altering network activity.

1.6 Hypothesis and specific objectives

Aberrant epigenetic regulation is now recognized as a common cause of neurodevelopmental disorders, yet many syndromes remain poorly understood. Chromatin remodelers are critical players in modifying and protecting the chromatin landscape. Mutations in Bptf, the largest subunit of the NURF complex, causes the newly identified disorder called Neurodevelopmental Disorder with Dysmorphic Facies and distal Limb anomalies (NEDDFL).

It was previously reported that Bptf is important for progenitor proliferation and neocortical development [151]. By enhancing the coverage of *Bptf* deletion in the neural system, we hypothesized that the phenotype of the *Bptf* knockout mice will recapitulate the human phenotype and will be a better model to study NEDDFL.

Mutations in the chromatin remodeler Atrx is known to cause the ATR-X syndrome, a severe neurodevelopmental disorder with autistic-like behaviours [226]. Studies have reported that in the absence of Atrx, the glutamatergic and GABAergic network are altered [206, 207, 211-215]. Therefore, we hypothesized that alteration of the equilibrium between the excitatory and inhibitory systems play a role in the pathogenesis of ATR-X syndrome. We generated two different *Atrx* conditional mouse mutants to characterize specific neuronal populations.

Lastly, multiple studies have generated Atrx knockout models to elucidate Atrx function. However, none of them have successfully deleted Atrx embryonically in post-mitotic cells without early postnatal lethality. Thus, individually, they do not represent strong models of the ATR-X syndrome. We generated a new conditional Atrx mouse mutant to dissect the function of *Atrx* in the developing brain and to provide a better understanding of the development of intellectual disabilities in ATR-X syndrome.

To address these hypotheses, we examined the following specific objectives:

1. Generate and perform a Behavioral characterization of the Bptf; *Nestin*-Cre mice
2. Generate and characterize mice ablated for Atrx in specific excitatory and inhibitory neuronal populations
3. Generate and characterize mice ablated for Atrx in the developing forebrain using the *Emx1*-Cre driver.

Chapter 2: Material & Methods

2.1 Transgenic mice

2.1.1 Animal Husbandry

Mice were housed in the Animal Care and Veterinary Services (ACVS) facility of the University of Ottawa. The University of Ottawa Animal Care Committee approved all animal studies and experimental procedures in accordance with guidelines established by the Canadian Council of Animal Care. Mice were maintained under a 12-hour light/dark cycle with food and water *ad libidum*.

2.1.2 Mouse lines

2.1.2.1 *Atrx* loxP line

The *Atrx*$^{\mathrm{fl/fl}}$ mice were generated by our lab in collaboration with A. Smith (University of Edinburgh, Edinburgh, United Kingdom). These mice have two loxP sites flanking exon 18 of the *Atrx* gene, which contains the ATP binding pocket [205]. Excision of exon 18 by Cre recombinase creates a frameshift and leads to the inactivation of the full-length ATRX protein while leaving the ATRXt isoform intact. *Atrx*$^{\mathrm{fl/fl}}$ mice were kept on a C57BL/6 background.

2.1.2.2 *Bptf* loxP line

The *Bptf*$^{\mathrm{fl/fl}}$ mice were generated by the research group of Dr. Wu at Johns Hopkins University [148] and donated to our lab by Dr. Camila dos Santos from the Cold Spring Harbor Laboratory [138]. These mice have two loxP sites flanking exon 2 of the *Bptf* gene. Deletion of exon 2 results in a frame shift which leads to a loss of function variant. *Bptf*$^{\mathrm{fl/fl}}$ mice were kept on a C57BL/6 background.

2.1.2.3 Cre driver lines

The first Cre driver line we used, was the *Nestin*-Cre line that were bred to the *Bptf*$^{f/f}$ line. *Nestin* is expressed in the central and peripheral nervous system starting at E7.5 [235]. These mice were kept on a mixed background of C57BL/6 and 129sv.

Three Cre recombinase expressing mouse models were used to breed with the *Atrx* floxed line to generate three distinct conditional *Atrx* knockouts. The *Vglut2*-IRES-Cre mice were purchased from The Jackson Laboratory (stock #028863) to target the ablation of *Atrx* in a subset of excitatory neurons. The mice were generated by inserting the Cre recombinase gene preceded by the internal ribosomal entry sequence (IRES-Cre) downstream of the *Vglut2* stop codon [236]. Thus, the Cre recombinase expression is driven by the endogenous *Vglut2* gene. These mice were backcrossed for eight generations on a C57BL/6 background.

The *Viaat*-Cre mice were purchased from The Jackson Laboratory (stock #017535) and bred with C57Bl/6 mice for 10 generations to generate a pure C57Bl/6 background. To generate these mice, a homology arm (A box) containing the regulatory elements of the *Viaat* gene linked to a Cre recombinase cassette was introduced 5’ of the *Viaat* sequence by homologous recombination [237]. Thus, *Viaat* expression is directly driving the transcription of Cre recombinase.

The *Emx1*-IRES-Cre mice were purchased from The Jackson Laboratory (stock #005628) to generate a forebrain-specific *Atrx* knockout. The mice were generated by inserting IRES-Cre sequence downstream of the *Emx1* stop codon [238]. Consequently, *Emx1* endogenous expression is driving the expression of the Cre recombinase. These mice were kept on a C57BL/6 background.

2.1.2.4 Tdtomato reporter line

The TdTomato, also called Ai14, mice were a kind gift from Dr. Jing Wang at the University of Ottawa. These animals were bred with the *Vglut2*-IRES-Cre and *Viaat*-Cre mice to document the expression of the Cre recombinases using the TdTomato reporter gene.

2.1.3 Genotyping

Ear or tail clips were added to a lysis buffer containing 0.95 N NaOH and 7.6 mM EDTA at a pH of 8 and placed into a PCR thermocycler (Eppendorf Mastercycler EP Gradient 96 well thermal cycler) at 90° C for 60 minutes. The reaction was stopped by the addition of neutralization buffer containing 0.97 M Tris-HCl pH 8.1.

The genotyping PCR was performed as follows: 3 minutes of denaturation at 95°C, then 32 cycles of denaturation at 95°C for 15 seconds, followed by annealing between 52-62°C (depending on the primer pairs) for 15 seconds and elongation at 72°C for 30 seconds. Then, fourr minutes of elongation at 72°C was done. The samples were ran on a 1% agarose gel for visualization. The list of primers used can be found in table 2.1. Briefly, SRY and Fabp1 primers were used for determining sex and Cre primers were used to detect all Cre driver lines by amplifying the coding region.

Table 2.1: List of primers used for genotyping

Gene	Primer	Sequence
Sry	Sry-F	TTGTCTAGAGAGCATGGAGGGCCATGTCAA
	Sry-R	CCACTCCTCTGTGACACTTTAGCCCTCCGA
Fabp1	Fabp1-F	TGGACAGGACTGGACCTCTGCTTTCCTAGA
	Fabp1-R	TAGAGCTTTGCCACATCACAGGTCATTCAG
Cre	Cre-F	ATGCTTCTGTCCGTTTGCCG
	Cre-R	CCTGTTTTGCACGTTCACCG
Atrx	Atrx-F	GGTTTTAGATGAAAATGAAGAG
	Atrx-R1	TGAACCTGGGGACTTCTTTG
	Atrx-R2	CCACCATGATATTCGGCAAG
Bptf	Bptf flox-F	GGCACTTGCATGATCTGTTGTCACCCG
	Bptf flox-R	TTCTACATGGCCAGCCATGTCCAGGCC

2.2 Behaviour tests

2.2.1 General procedure

Prior to testing, mice were handled every other day and their cages were changed. During the testing period, only the water bottles were changed. All the behaviour tests were scheduled with at least one rest day between each other. Mice were kept under the normal 12-hour light cycle and had access to food and water *ad libidum*.

2.2.2 Beam Break assay

Each mouse is placed in a novel cage surrounded by a metal frame equipped with horizontal beams of infrared red detectors (Micromax analyzer). When the mouse moves, the photocell analyzer records the interruption in the beam. The number of beam breaks and locomotor activity are recorded over 48 hours (Micromax, Omni-tech Electronics Inc., Columbus, OH) [239].

2.2.3 Phenotyper box

The phenotyper box is a home cage simulator where multiple parameters are recorded automatically allowing long-term data collection. The chambers consist of clear Plexiglas boxes (Noldus Information Technology PhenoTyper) with an overhead camera linked to the mouse tracking software EthoVision (Ethovision 14, Noldus Information Technologies, Leesburg, VA, USA). The fully automated cages are designed to measure parameters such as locomotion, feeding, drinking and exploration. Each testing chamber is equipped with water bottle, nest box and food chamber. For our protocol, we video recorded the mice over a period of 72 hours [239].

2.2.4 Rotarod

The mouse is placed on a rotating textured rod (Ugo Basile) and the speed is gradually increased to 45 rpm reaching maximum speed within 60 seconds. The test is concluded once the mouse falls off the rod, does a 360° rotation around the rod or after five minutes. Each mouse has four five-minutes trials per day for three consecutive days. There is a 10-minute inter-trial interval in the home cage [239-241].

2.2.5 Open field

The open field arena is a 45-cm square box made of opaque white plastic (custom-built by Canus Plastics Inc.). There is overhead illumination (300 lux) and a camera linked to the Ethovision tracking program (Ethovision 14, Noldus Information Technologies, Leesburg, VA, USA) records the activity of the mouse. During testing, the mouse is allowed to freely move in the arena for a duration of 10 minutes [239, 242, 243]. The time spent in the centre of the box, time spent in the four corners and distance traveled are the main measurements of this test.

2.2.6 Elevated plus maze

The apparatus consists of two 6- cm wide and 75 cm long arms intersected in the centre at a perpendicular angle (Noldus, Wageningen, The Netherlands). The first arm is an open platform and the second arm is closed with 20 cm high walls. The junction between the two arms is open allowing the mouse to freely move in the maze. An overhead illumination (100 lux) and a camera linked to the Ethovision tracking program (Ethovision 14, Noldus Information Technologies, Leesburg, VA, USA) records the mouse movements. The test starts when the mouse is placed in the centre of the maze and ends after 10 minutes [244-247]. Time spent in the closed arms, time spent in the open arms and distanced travelled are measured during this test.

2.2.7 Morris water maze

Morris water maze is the most commonly used test to evaluate spatial learning and memory in mice. In this paradigm, a pool of 132 cm in diameter (Med Associates Inc. and Maze Engineers) is filled with tap water and non-toxic white paint. A hidden platform of 10 cm in diameter is located 24 cm away from the edge of the pool and one cm from the surface. Visual cues are placed on the walls of the testing room. In our protocol, each mouse is randomly placed in the pool from four starting locations and is given one minute to find the platform. Each mouse has four trials per day for seven consecutive days. On day eight, the platform is removed from the pool and the time spent in the target quadrant is measured. The mouse is tracked by an overhead camera linked to the Ethovision 14 software.

2.2.8 Fear conditioning

The fear conditioning test is used to evaluate learning and memory. The testing chambers are Phenotyper boxes (see 2.2.3) equipped with grid shock floors (Med Associates Inc.). The camera from within the Phenotyper box records the mouse’s behaviour, which is then analyzed with the Ethovision 14 software. The fear conditioning test takes place on three consecutive days.

The first day is the training day. The mouse is placed in the testing box for a total of six minutes. After the first two minutes, the mouse goes through the following training session: 30 second tone, two second foot shock and 1-minute rest. This sequence is repeated three times.

The second day corresponds to the contextual memory. The mouse is loaded into the same Phenotyper box as day one for a six-minute trial while its freezing time is measured. No shock is applied.

The third day is the “cue” day. The mouse is placed in a modified Phenotyper box with triangular walls, vanilla scent and a different lighting. After the first three minutes, the same tone as day one is played but without any shock. The mouse freezing time is recorded.

2.2.9 Nest building

In the nest building test, a square nestlet material is added to the bottom of a clean cage. Then, each mouse is loaded into their respective cage and allowed to build a nest for 16 hours (5pm to 9am). The following day, the mice are returned to their home cage and the nestlets are scored based on specific criteria (Table 2.2) [239, 248, 249].

2.2.10 Splash test

Four cages with bedding are positioned in front of a camcorder (Handycam by Sony). Each mouse is sprayed twice on the back with water. The test begins when the mouse is placed in one of the cages and allowed to groom for a duration of 10 minutes (Figure 2.1). Latency to groom and total grooming time are manually scored.

2.2.11 Marble burying

The marble burying test is separated into two trials; habituation and the burying steps. In the habituation step four rat cages are filled with 10 cm of woodchips. Then, mice are loaded in the cages and allowed to explore for five minutes. After the habituation, the mice are put back in their home cage for five minutes. Meanwhile, 20 marbles are evenly placed on top of the woodchip bedding (Figure 2.2). Following the inter-trial, the mice are loaded once again in the testing cages for 30 minutes. The number of buried marbles is manually scored at the end.

Table 2.2: Scoring system for nest building test

Score	**Description**
1	Nestlet not noticeably touched (>90% intact)
2	Nestlet partially torn up (50-90% intact)
3	Nestlet mostly shredded; not identifiable nest site: <50% intact, <90% within a quarter of the cage floor area.
4	An identifiable, flat nest: >90% of nestlet is torn up, material gathered into a nest within a quarter of the cage floor area. Nest is flat - walls higher than mouse body height (curled up on its side) on less than 50% of its circumference.
5	A (near) perfect nest: >90% of nestlet is torn up, nest is a crater with walls higher than the mouse body height on more than 50% of the circumference.

Figure 2.1: Schematic of the splash test.

A The mouse is sprayed twice on its back with water and **B** put back in its cage allowing grooming time for 10 minutes.

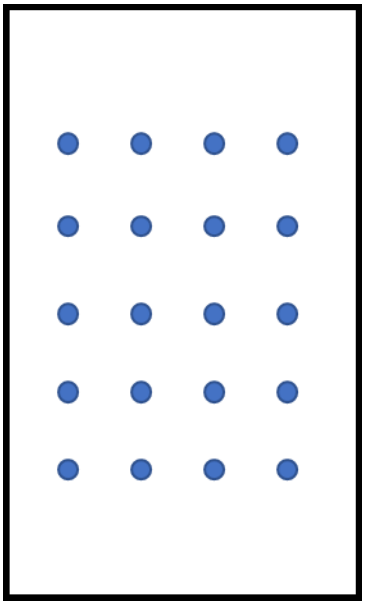

Figure 2.2: Schematic of marble arrangements

Top view of the mouse cage containing the marbles (blue).

2.2.12 DigiGait

The DigiGait is an apparatus that analyzes the gait of rodents (DigiGait treadmill system by Mouse Specifics). It is comprised of a transparent treadmill suspended above a camera that tracks and captures images of the mouse’s paws (Figure 2.3). The mouse is loaded onto the treadmill in a clear Plexiglass box to contain the mouse on the belt. The speed of the belt is set at 18cm/s and three-second long videos are captured for the analysis. Then the videos are analyzed using the Digigait Analysis software.

Figure 2.3: Picture of the DigiGait

The mouse is loaded in the clear plexiglass container on the top of the belt. The settings are located on the blue panel.

2.3 Histology

2.3.1 Tissue collection

2.3.1.1 Embryo fixation

An intraperitoneal (IP) injection of EdU was administered to the pregnant female at gestational day 16.5 followed by a 1-hour waiting period. Then, the pregnant female was put to sleep using CO_2 and the embryos were collected. The head of all the embryos were dissected and placed in a fixating solution of 4% paraformaldehyde (PFA) for 24 hours. A tail sample was taken for later genotyping. Fixed brains were immersed in a 30% sucrose solution with 0.3% sodium azide for one week to ensure cryoprotection. Following that, brains were fast frozen in methyl-butane at -60°C and stored at -80°C.

2.3.1.2 Adult mouse perfusion

Postnatal day 40 and 60 (P40 and P60) mice were anesthetized using CO_2 and their thoracic region was opened to expose the heart. Transcardiac perfusion of cold PBS was used to flush the blood followed by 4% PFA to fix the tissues.Whole brain was dissected and stored in 4% PFA solution for one hour. Once fixed, brains were placed in a 30% sucrose with 0.3% sodium azide for 1 week and fast frozen in -60°C methyl butane.

2.3.2 Cryostat sectioning

Brains were transferred to a HM525X cryostat set at -28°C for 1 hour prior to sectioning. Optimal cutting temperature (O.C.T.) compound (Fisher Scientific; 23-730-571) was used as an embedding medium. Brains were sectioned coronally at a 20µm thickness and mounted on Superfrost Plus (Fisher Scientific, 22-037-246) microscope slides. Slides were stored at -20°C.

2.3.3 Nissl staining

Cortical and hippocampal brain sections mounted on microscope slides were rehydrated in a series of baths containing 95% ethanol for 10 min, 70% ethanol for 1min 50% ethanol for one min and 2x water five min. The rehydrated sections were stained in a 0.25% cresyl violet solution for 15 min and then washed twice with water for three mins. The stained slides were then dehydrated in 50% ethanol two min, dip in 70% ethanol+0.5% acetic acid, 95% ethanol for two min and xylene 30 min.

2.3.4 Volumetric analysis

Neuroanatomical studies were carried out using four AtrxEcKO mice (Emx1-cre) at 16-weeks of age compared to four littermate WT animals. Mouse brain samples were fixed in 4% buffered formalin for 48 hours, before paraffin embedding and sectioning at 5µm thickness using a sliding microtome (Microm HM 450). One sagittal section was defined, previously described in Collins et al. 2018 [250], at lateral 0.60 mm, double-stained (Luxol Fast Blue for myelin and Cresyl violet for neurons) and scanned at cell-level resolution using the Nanozoomer whole-slide scanner 2.0HT C9600 series (Hamamatsu Photonics, Shizuoka, Japan). A total of 40 brain morphological parameters, made of area and length measurements, were taken blind to the genotype using scripted routines and manual segmentation on ImageJ. These measurements included 22 brain parameters: 1) the total brain area; 2) the primary and secondary motor cortices; 3) the pons; 4) the cerebellar area, the internal granular layer of the cerebellum and the medial cerebellar nucleus; 5) the lateral ventricle; 6) the *corpus callosum*; 7) the thalamus; 8) the caudate putamen; 9) the hippocampus and its associated features; 10) the fimbria of the hippocampus; 11) the anterior commissure; 12) the stria mEdUllaris; 13) the fornix; 14) the optic chiasm; 15) the hypothalamus; 16) the pontine nuclei; 17) the substantia nigra; 18) the fibers of the pons; 19) the granular retrosplenial cortex; 20) the dorsal subiculum; 21) the inferior colliculus; and 22) the superior colliculus.

2.3.5 Immunofluorescence staining

Microscope slides containing brain coronal sections were dried at room temperature for one hour and washed three times for five minutes using PBS. Then, the slides were transferred into a plastic staining jar containing the antigen retrieval solution (sodium citrate buffer). The container was microwaved for 10 minutes (power level 1) and cooled down on the bench for 30 minutes. Brain sections were outlined using an immuno pen (Agilent, cat # s2002) and washed once with PBS. Then, the sections were blocked using 10% horse serum for one hour at room temperature. The antibody solution was prepared using the 10% horse serum and the appropriate antibody dilution (Table 2.3). Following the blocking step, the antibody was added on the slide overnight at 4°C. The following day, the slides were washed three times with PBS and incubated with the secondary antibody (Table 2.4) for one hour at room temperature.

Table 2.3: List of primary antibodies used for immunofluorescence staining

Antibody	Host	Dilution	Company	Catalog #
ATRX	Rabbit	1:1000	Santa Cruz	SC-15408
Calretinin	Rabbit	1:400	Millipore	AB5054
Ctip2	Rat	1:300	Abcam	Ab18465
DCX	Guinea pig	1:500	Millipore	AB2253
MAG	Mouse	1:500	Millipore	MAB1567
Math2	Rabbit	1:300	Abcam	Ab85824
NeuN	Mouse	1:300	Millipore	MAB377
Ntng1	Mouse	1:50	Santa Cruz	SC-271774
Ntng2	Rabbit	1:1000	Gift from Dr Shigeyoshi Itohara, RIKEN Center for Brain Science	
Pax6	Rabbit	1:200	BioLegend	901301
Prox1	Mouse	1:200	Millipore	MAB5654
Satb2	Mouse	1:300	Abcam	Ab51502
Tbr1	Rabbit	1:100	Abcam	Ab31940
Tbr2	Rabbit	1:200	Abcam	Ab23345

Table 2.4: List of secondary antibodies used for immunofluorescence staining

Antibody	Host	Dilution	Company	Catalog #
Alexa Fluor 488	Mouse	1:500	Invitrogen	A-21202
Alexa Fluor 488	Rat	1:500	Jackson	712-545-150
Alexa Fluor 594	Rabbit	1:500	Cederlane	711-585-152
Alexa Fluor 647	Mouse	1:500	Invitrogen	A-3571

Following the three washes, DAPI was added to the slide (1:25 000 in PBS) for 15 minutes. The slides were mounted using Dako (Agilent, cat # s3023) and sealed using nail polish.

2.3.6 Microscopy and image processing

Microscope slides with immunofluorescence staining were imaged using the widefield upright Zeiss AxioImager M2 microscope and the Zen imaging software. We used the z-stack with extended focus module to capture all the layers of cells within the sample. The tiling option was used to take wide field of view using the 20x objective. The tiles were than stitched to generate an image. Next, the images were deconvoluted using the Autoquant software and manually quantified using Image J (Fiji).

2.4 Protein and RNA

2.4.1 Protein extraction

Cortex and hippocampus were dissected and homogenized in RIPA buffer (50mM Tris-HCl pH 7.5, 1% NP-40, 1% Triton-X-100, 150mM NaCl, 12mM Na-deoxycholate, 0.05% sodium dodecyl sulfate (SDS), 2mM EDTA, 1mM DTT) containing a protease inhibitor cocktail (Sigma cat# P8340) using a homogenizer. The lysates were incubated at 4ºC for 30 minutes on a shaker and centrifuged at 12,000 rpm in a temperature-controlled centrifuge set at 4ºC for 10 minutes. The supernatants were transferred to clean tubes and the protein concentrations were determined using a Bio-Rad protein assay dye reagent (cat #5000006) and a spectrometer to read absorbance at 595nm.

2.4.2 Immunoblotting

Aliquots containing 20 mg of protein extracts were denatured in a heat block set at 92°C for five minutes. Samples were loaded on 8% polyacrylamide gels and run for 90 minutes at 50 milliamps (mA) in SDS running buffer (25mM Tris-HCl, 192mM glycine and 0.1% SDS). Next, the gels were transferred to polyvinylidene fluoride (PVDF) membranes at 100 volts for 90 minutes in transfer buffer (39mM glycine, 48mM Tris-HCl and 20% methanol). Antibody solutions were prepared using 5% BSA and the appropriate antibody concentrations. The membranes were probed with the primary antibody solution overnight at 4°C on a rocker. Upon the removal of the primary antibody, the membranes were washed three times using TBS-T (150 mM NaCl, 50mM Tris, pH 7.4, 0.05% Tween 20, pH 7.4) for five minutes at room temperature. The HRP-conjugated secondary antibodies were added to the membrane at the appropriate concentrations in 5% BSA and incubated for 1 hour at room temperature. The secondary antibodies were removed and the membrane was washed 3 times with TBS-T. Protein visualisation was done using the Clarity Western ECL Substrate (Bio-Rad, cat# 1705061) according to the manufacturers guidelines. The treated membranes were exposed to X-ray films and developed.

2.4.3 RNA extraction

We dissected the hippocampi from P60 *Atrx*; *Emx1*-Cre mice and flash froze the tissue using liquid nitrogen. We followed the RNA extraction protocol from Invitrogen. Briefly, samples were transferred into clean tubes with 1ml of TRIzol, homogenized using a homogenizer and incubated on ice for five minutes to permit complete lysis. We added 200µl of chloroform to each tube, incubated them for two minutes and centrifuged for 15 minutes at 12 000 × g at 4°C. The aqueous phase was removed and transferred to a clean RNA-free tube.

We precipitated the RNA by adding 500µl of isopropanol to the samples, incubated them for 10 minutes on ice and centrifuged them for 10 minutes at 12 000 × g at 4°C. We removed the supernatant and resuspended the pellet with 1 ml of 75% ethanol and centrifuged for five minutes at 7500 × g at 4°C. The supernatant was removed and the extra ethanol was allowed to evaporate for 10 minutes on the bench. The RNA pellet was resuspended using 50µl of RNase-free water and incubated in a heat block set at 55°C for 10 minutes. The concentration was determined by using a nanodrop and samples were stored at -80°C.

2.4.4 cDNA synthesis

The collected RNA was treated using the Invitrogen™ DNA-free™ DNA Removal Kit (Cat# 10729525). Briefly, 2 µg of RNA, 1 µl of DNase, 2 µl of 10x buffer and HPLC water were mixed and incubated for 30 minutes at 37°C. The mix was centrifuged and the supernatant was collected. The cDNA synthesis was done by mixing 15 µl of 500 ng of RNA with 1 µl of random primers (300 ng/µl) and incubating at 70°C for 5 minutes. The reverse transcription procEdUre was done using the RevertAid RT Reverse Transcription Kit (Thermofisher, cat# K1691) according to the manufacturer’s protocol. In summary, 5 µl of 5x buffer, 0.6 µl of RNase out, 1 µl of dNTPs (25 mM), 1 µl of reverse transcriptase and 1.4 µl of HPLC water were added to the 16 µl mixture. Samples were incubated at 25°C for 5 minutes, followed by 42°C for 1 hour and lastly 70°C for 15 minutes. Samples were diluted 1:10 using HPLC water and stored at -20°C.

2.4.5 Quantitative real-time PCR

A master mix was prepared using 17.5 µl of 2X SYBR green advantage qPCR Premix (Clontech, cat# 639676), 11.9 µl of HPLC water, 3.5 µl of cDNA and 2.1 µl of the appropriate primers (10 µM). Triplicates wells were loaded with 10 µl of master mix in a 96-well qPCR plate. Then, the plate was loaded on an Applied Biosystems 7500 Real-Time Fast PCR thermocycler. The qRT-PCR was performed as follows: initial 5-minute hold at 50°C, followed by 10 minutes of denaturation at 95°C, then 40 cycles of denaturation at 95°C for 15 seconds, followed by annealing and extension at 60°C for 60 seconds. The relative mRNA levels were calculated using the ΔΔCT method and normalized using the ribosomal 18S specific primers. The primer list can be found in table 2.5.

2.4.6 Library preparation and sequencing

The RNA was extracted as previously described in section 2.4.3 and purified using the ThermoFisher PureLink RNA Mini Kit (cat #12183018). We used four WT and four AtrxEcKO P60 hippocampus samples that we sent for sequencing to Genome Quebec (Montréal). The following section was performed by the sequencing facility. RNA concentration was determined using a NanoDrop Spectrophotometer ND-1000 (NanoDrop Technologies, Inc.) and the integrity of the RNA was assessed using the Agilent 2100 Bioanalyzer (Agilent Technologies). They generated the library using 250 ng of RNA and performed an mRNA enrichment using the NEBNext Poly(A) Magnetic Isolation Module (New England BioLabs). The cDNA synthesis was done using the NEBNext RNA First Strand Synthesis and NEBNext Ultra Directional RNA Second Strand Synthesis Modules (New England BioLabs). The following steps to the library preparation was done using the NEBNext Ultra II DNA Library Prep Kit for Illumina (New England BioLabs). The library quantification was performed using the Quant-iT™ PicoGreen® dsDNA Assay Kit (Life Technologies) and the Kapa Illumina GA with Revised Primers-SYBR Fast Universal kit (Kapa Biosystems). The LabChip GX analyzer (PerkinElmer) was used to determine the average fragment size.

Table 2.5: List of primers used for qRT-PCR

Primer	Sequence (5’ to 3’)
Ntng1-forward	TTTGGGCTCAATCCATGATCG
Ntng1-reverse	TGTTGTTCCAGTCTTACACTCAC
Ntng2-forward	ATGGATAGCCGCCTTACATCA
Ntng2-reverse	CCCCAACCCTTCCCTATTTGTG
Neurog2- forward	AACTCCACGTCCCCATACAG
Neurog2-reverse	GAGGCGCATAACGATGCTTCT
Unc13c-forward	AGTTACCGAGTTGCTATCGCC
Unc13c-reverse	GCTGCTCCTTAGCTCATTGAA
Ntn5-forward	TGACCCTGCGTTTCTGCAC
Ntn5-reverse	CGGCCTCTTACTCCAGTGG
m18S-forward	AGTCCCTGCCCTTTGTACAC
m18S-reverse	GATCCGAGGGCCTCACTAAAC
COUP-TF1-foward	TCCCATCGAAACTCTCATCC
COUP-TF1-reverse	AGTGGGCTGCTCTTGTTCC
CXCR4-foward	ATGGAACCGATCAGTGTGAGT
CXCR4-reverse	TGAAGTAGATGGTGGGCAGG

The resulting library was normalized, denatured and diluted to 200 pM and neutralized with hybridization (HT1) buffer Lastly, ExAMP was added and the clustering was performed on an Illumina cBot. The flowcell was run on a HiSeq 4000 for 2x100 cycles (paired-end mode). We used the HCS HD 3.4.0.38 as the Illumina control software and RTA v. 2.7.7 for the real-time analysis. The bcl2fastq2 v2.18 program was used to demultiplex samples and generate fastq reads.

2.4.7 Bioinformatic analysis

Transcript reads were quantified and mapped using Kallisto (v0.45.0) with the GRCm38 transcriptome reference and the -b 50 bootstrap option [251]. Then, we used Sleuth, which is an R package, to construct general linear models for the log-transformed expression of each gene across genotypes. The significant variables for each gene was tested using the Wald's test followed by the Benjamini-Hochberg false discovery rate method to adjust the p-values to q-values. Significant genes were defined as genes with a q-value < 0.05 and the effect size (beta coefficient of the regression model) cut-off of |b|>0.25 was also used for each data set. Also, we performed Gene Ontology analysis on the differentially expressed genes (DEGs) using the R package gProfileR and Disease Gene Ontology using DOSE [252].

2.6 Data collection and statistical analysis

The behaviour data was collected from different cohorts and comprising a minimum of four independent experiments that resulted in n>15 for most genotypes. Data from independent experimental cohorts were compared with each other to ensure consistency. All the statistical analysis and graphs were generated using Graphpad Prism 8 software. Error bars on all graphs represent Standard Error of Mean (SEM). We calculated the P-value between two groups using the two-tailed student's t-test analysis. We used a one-way analysis of variance (ANOVA) followed by the Tukey's test for multiple comparisons when more than two groups were compared. Lastly, two-way ANOVA along with a Tukey Post-hoc test was used when comparing more than two groups with two variables. Statistical significance was determined by a p-value of ≤ 0.05. In graphs, asterisks were used to represent different p-value results (* $p < 0.05$, ** $p < 0.01$, *** $p < 0.001$, **** $p < 0.0001$).

For the histological studies, multiple brain samples from independent litters were collected. We used four different animals per genotype for the immunofluorescence staining. Specific to the analysis of cortical layers, three different cortical regions were quantified per mouse and averaged.

Chapter 3: Characterization of the *Bptf*; Nestin-Cre mice

3.1 Introduction and rationale

Mutation in the *Bptf* gene is associated with a neurodevelopmental disorder called NEurodevelopmental Disorder with Dysmorphic Facies and distal Limb anomalies (NEDDFL) [110]. NEDDFL patients exhibit various degrees of intellectual disability, motor deficits, developmental delay and specific limb and facial characteristics.

Our lab has previously generated a conditional knockout mouse model, *Bptf*; *Emx1*-Cre, to determine the effect of *Bptf* deletion in the brain [151]. These mice survive to adulthood but were smaller in size when compared to WT animals. Interestingly, these mice had severe cortical hypoplasia, prolonged cell cycle and increased cell death that ultimately led to reduced neuronal output.

The mouse model we are using in this chapter is the *Bptf*; *Nestin*-Cre mice. *Nestin*, also called neuroepithelial stem cell protein, is a type VI intermediate filament, which is a critical component of the cytoskeleton. It is mainly expressed in the neural progenitors of the central and peripheral nervous system [253]. We generated this model to enhance the coverage of *Bptf* deletion in the neural system in comparison to the *Emx1*-Cre driver that targets only excitatory neurons within the forebrain. Previously, a preliminary study conducted in our lab showed that the *Bptf* knockout (*Bptf* NcKO) mice died embryonically or at birth on a pure C57BL/6 background. Knowing that the NEDDFL patients are heterozygous, we wanted to examine the brain and behavioural phenotype of the heterozygous *Bptf*; *Nestin*-Cre mice.

While generating the *Bptf*; *Nestin*-Cre hetereozygotes, we noted that animals from all genotypes were generated, including *Bptf* NcKO mice which were surviving past P0. After further investigation, we found that the offspring were no longer on a pure C57BL/6 background but rather a mixed background of C57BL/6 and Sv129s. Therefore, we decided to characterize both *Bptf* NcKO and Het mice.

3.2 *Bptf* NcKO mice survive to adulthood with major morphological brain defects

To generate the *Bptf* conditional knockout mouse, we used two mouse lines. First, we used the *Bptf*$^{fl/fl}$ mice, which have two loxp sites flanking exon 2 of the *Bptf* gene (Figure 3.1 A) [148]. In the presence of Cre recombinase, exon 2 is excised creating a frame shift that results in a loss of function allele. We bred these mice to the second mouse line, *Nestin*-Cre$^{+/-}$ mice, where the expression of Cre recombinase is driven by the *Nestin* promoter. The expression of *Nestin* begins at E7.75, which means that we are deleting the *Bptf* gene in the early stages of neurodevelopment [235].

We wanted to test the viability of the mice, therefore we made a survival curve with the WT, Het and *Bptf* NcKO mice (Figure 3.1 B). We monitored survival for 100 days because NEDDFL is not a degenerative disease and the physical and biological manifestations of the disease were predicted to remain constant over time. We found that we lost 27 of 43 *Bptf* NcKO pups before weaning age and two between 40-50 days. 14 *Bptf* NcKO mice survived to the end of the 100 day monitoring period. Interestingly, we only lost two Hets and one WT at postnatal day 0 (P0). At the end of the experiment, we had 52 Hets and 36 WT animals. Although we were able to get several *Bptf* NcKO mice past P21, *Bptf* deletion in neural progenitors leads to a high mortality rate (67%; 29/43).

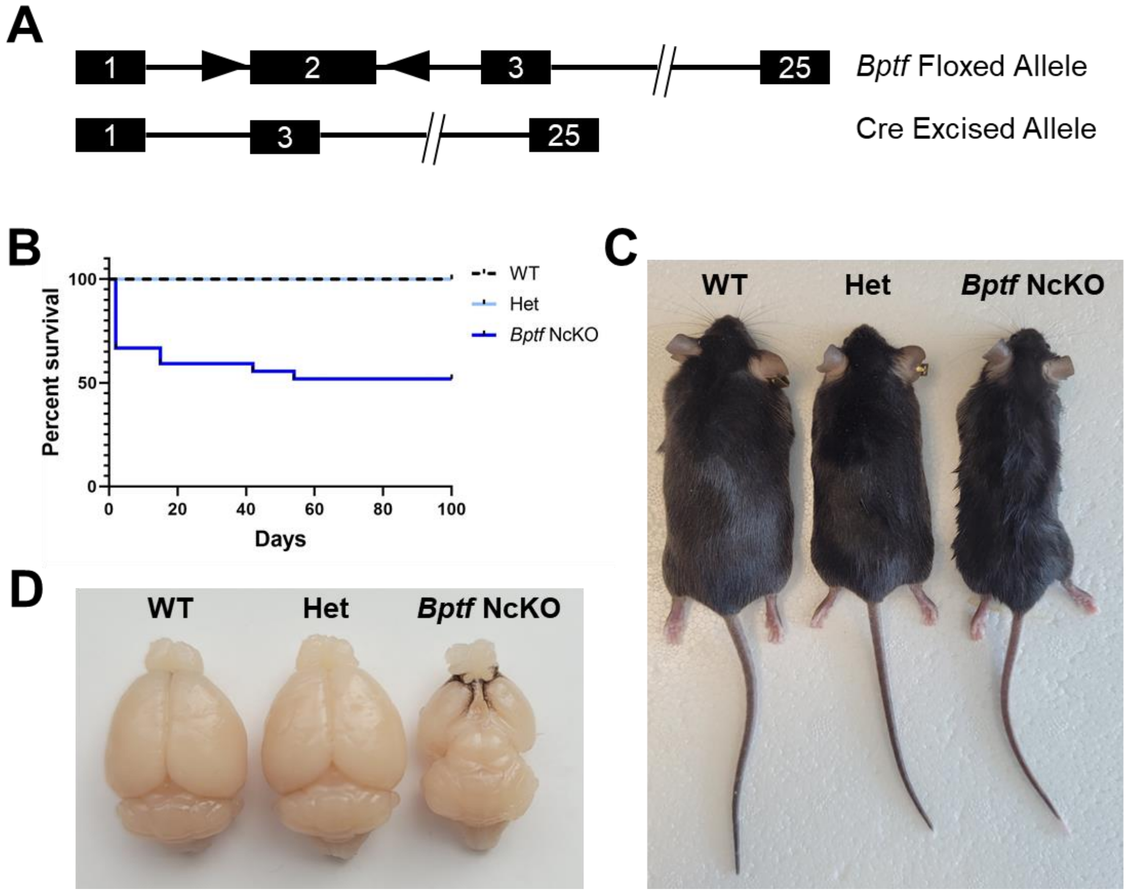

Figure 3.1: Characterization of the *Bptf*; *Nestin*-Cre mice

A Schematic of the *Bptf* floxed allele and the *Cre* excised allele. **B** Survival curve showing the percent survival of WT, Het and *Bptf* NcKO mice up to 100 days. Data represent means. n=37 (WT), n=54 (Het), n=43 (*Bptf* NcKO). **C** Bodies and **D** brains of P100 WT (left), Het (middle) and *Bptf* NcKO (right) mice.

Next, we visually compared the WT, Het and *Bptf* NcKO mice (Figure 3.1 C-D). We noticed that the WT and Het mice were similar in size and the gross morphology of their brains were comparable. On the other hand, *Bptf* NcKO mice were smaller compared to the WT animals. Interestingly, we noticed that the *Bptf* NcKO mice had consistently a dirty coat suggesting inefficient grooming and/or lack of grooming behaviour (Figure 3.1 C). This subject will be further discussed in section 3.7. The next striking phenotype we observed in the *Bptf* NcKO mice was the overall brain morphology. We noted that they had a smaller brain and, most evidently, severe cortical hypoplasia (Figure 3.1D).

To better visualize the brain defects, we did a Nissl stain using brain sections of P90 animals. The first striking difference we observed was that the brains of BPTF NcKO mice were half the size of the other two groups (Figure 3.2 A). Furthermore, the coronal section allowed us to clearly see the cortical hypoplasia. We examined the hippocampus of the three groups because NEDDFL patients have intellectual disability, which is mainly linked to this brain region. We noted no change between the WT and Het mice (Figure 3.2 B). However, the hippocampus of BPTF NcKO mice were indiscernible.

Taken together, we can conclude that *Bptf* deletion in neural progenitors causes severe brain morphological defects and the death of 50% of the animals by the weaning age.

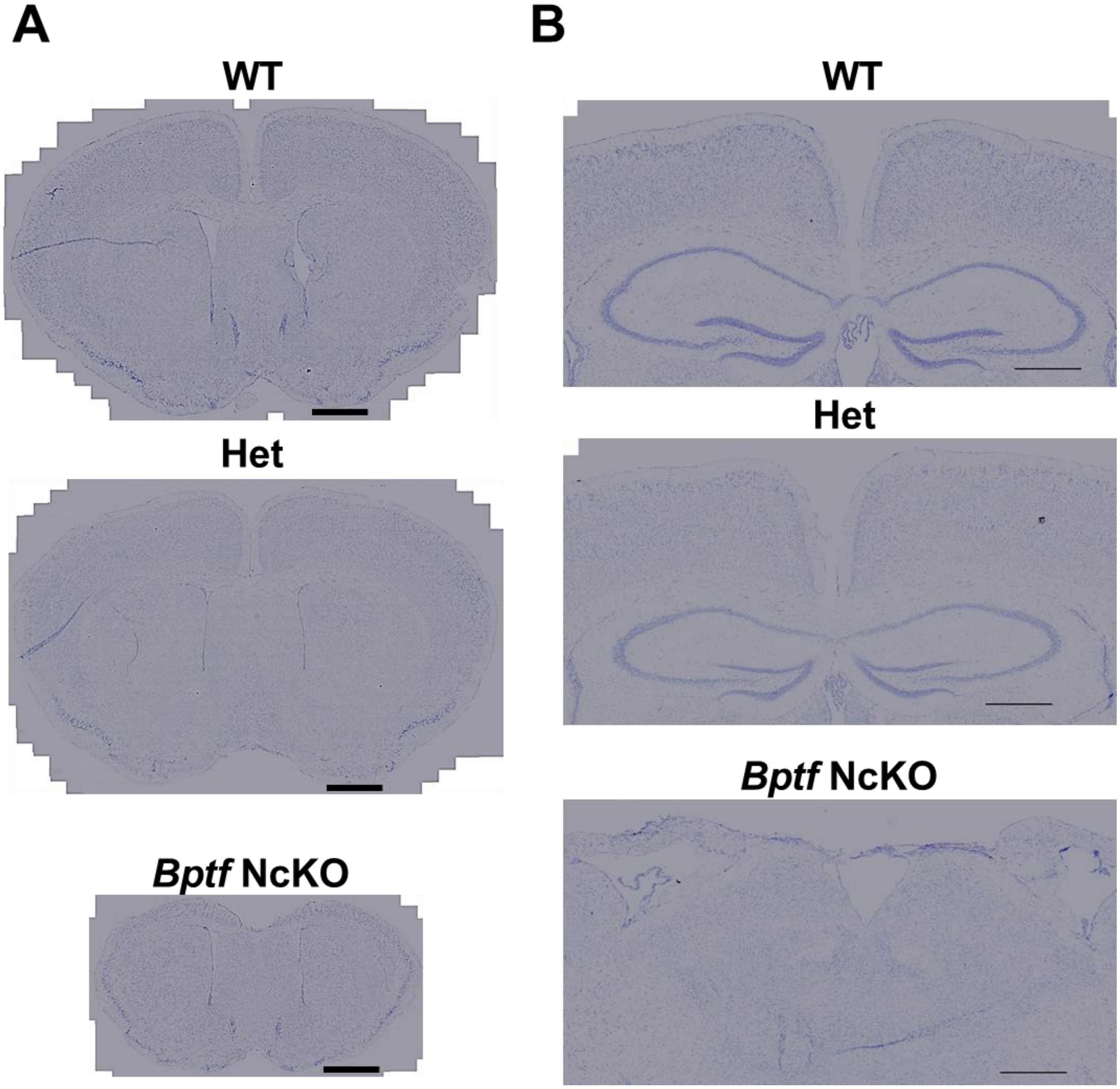

Figure 3.2: *Bptf* NcKO mice have severe brain defects

Nissl stain was performed on P90 WT, Het and *Bptf* NcKO coronal sections. **A** Whole brain coronal sections and **B** hippocampal regions are shown. Scale bars represent **A** 500µm and **B** 300µm.

3.3 *Bptf* deletion in neuronal progenitors affects cortical lamination and hippocampal formation

The significant brain morphological alterations we observed directed us to examine the neocortical cell types and their laminar location. We performed IF staining on P0 brain coronal sections using Satb2, Ctip2 and Tbr1 to label layer II-IV, V and VI respectively (Figure 3.3). The most noticeable effect of *Bptf* deletion was the thinning of the cortex. We quantified the total number of cells using DAPI and did not find any significant change (WT: 406.4 cells ± 25.56; Het: 412.7 cells ± 23.66; *Bptf* NcKO 346.9 cells ± 22.60; n=3). However, we observed that the cells were more densely packed and, sometimes, overlapped in the *Bptf* NcKO mice, which suggested a migration defect.

To quantify the proportion of neurons expressing a laminar layer marker, we restricted the counts to their respective layers and normalized them to the total number of cells. We found no significant change in the percentage of Satb2+ cells in layer II-VI (WT: 31.81% ± 1.721; Het: 31.16% ± 1.550; *Bptf* NcKO 36.97% ± 1.630; n=3). Interestingly, compared to the Het and WT littermates the *Bptf* NcKO mice showed no clear distinction between the cells in layer V and VI. Therefore, an approximation of the layers was made to quantify both Ctip2+ and Tbr1+ cells. We found no significant change in the percentage of Ctip2+ cells in layer V (WT: 8.927% ± 0.4984; Het: 9.025% ± 0.4750; *Bptf* NcKO 6.700% ± 0.7202; n=3). However, we observed a significant reduction in the percentage of Tbr1+ cells in layer VI (WT: 27.72% ± 1.469; Het: 26.07% ± 0.5150; *Bptf* NcKO 16.03% ± 0.2307; n=3). It is important to note that almost all Tbr1+ cells were also expressing Ctip2 in the *Bptf* NcKO mice. These results suggest that *Bptf* NcKO mice do not have a lamination defect but rather a differentiation defect in cortical progenitors.

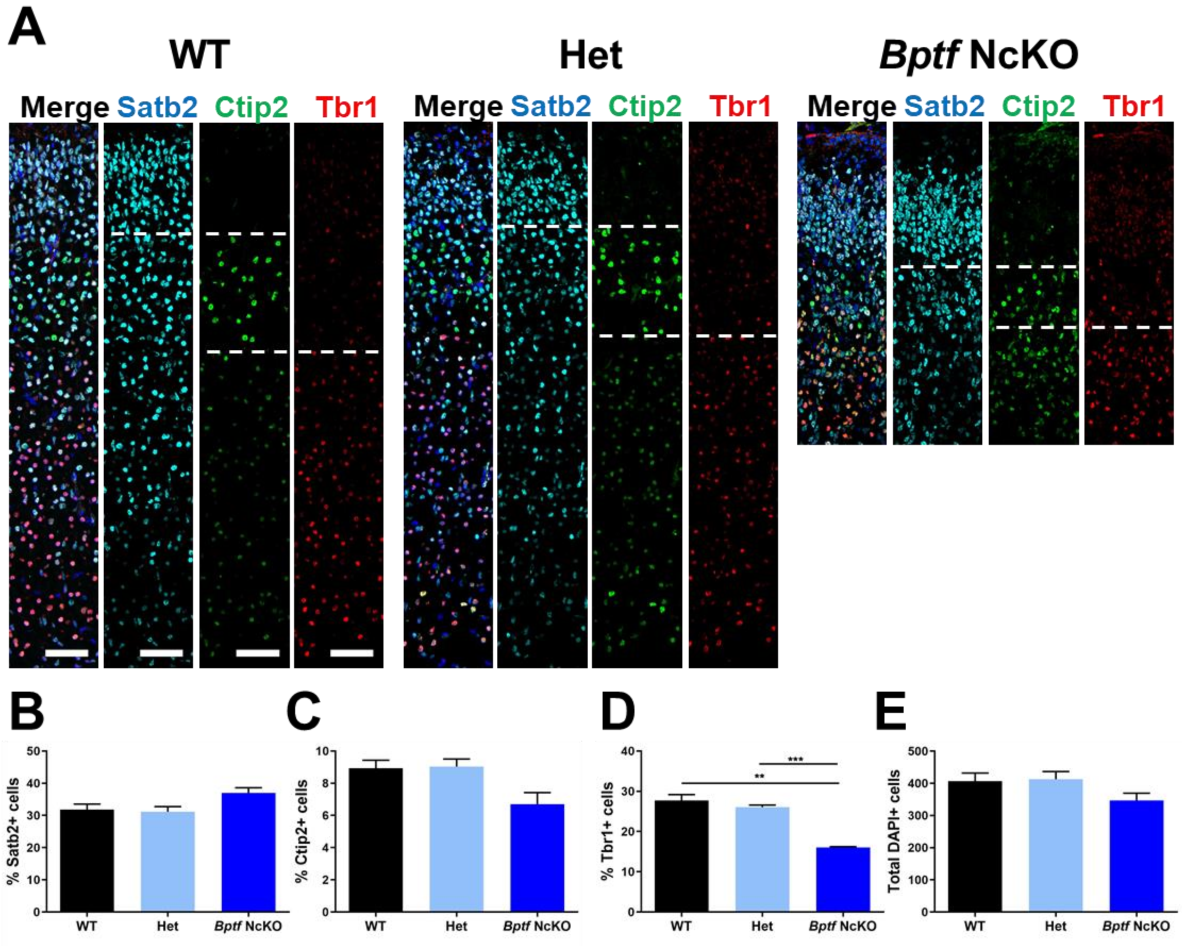

Figure 3.3: *Bptf* NcKO mice shows a thinner cortex and reduction in deep layer cells

A P0 coronal sections were used to do immunofluorescence staining. Satb2 (cyan), CTIP2 (green) and Tbr1 (red) were used to label layer II-IV, layer V and layer VI respectively. Quantification of **B** Satb2, **C** CTIP2, **D** Tbr1 and **E** DAPI. Scale bar, 50μm. Data represent means ± SEM. n=3. ** $p < 0.01$, *** $p < 0.001$.

In section 3.2, we showed that the hippocampus of P90 *Bptf* NcKO mice was missing. Here, we wanted to determine whether they had a hippocampus at an earlier age and characterize it. We performed IF staining on P0 coronal sections using NeuN to label mature neurons (Figure 3.4A). First, the general structure of the hippocampus was unchanged in the WT and Het animals. Interestingly, *Bptf* NcKO mice did have a hippocampus. However, it was significantly smaller and the organization of the mature neurons was altered. In fact, instead of lining the outside border of the hippocampus, the mature neurons of BPTF NcKO mice were scattered throughout the entire structure.

The analysis of the hippocampus was separated by subregions; CA1, CA3 and dentate gyrus (DG). We began by counting the number of DAPI+ cells in each subregion and found a significant decrease in all three sections of *Bptf* NcKO mice (WT: CA1 556.33 cells ± 74.48, CA3 679 cells ± 99.035, DG 711.667 cells ± 88.35; Het: CA1 cells 452.333 ± 39.405, CA3 668 cells ± 38.974, DG 669 cells ± 52.205; *Bptf* NcKO: CA1 204.667 cells ± 12.454, CA3 238.667 cells ± 37.356, DG 318.667 cells ± 48.528; n=3) (Figure 3.4C). There was no change observed in the Het animals. Next, we quantified the number of NeuN+ cells per subregion and normalized it to the total number of cells within that subregion. We found a significant increase in the percentage of NeuN+ cells in the CA1 and CA3 region of Het mice and in CA1 of *Bptf* NcKO mice (WT: CA1 17.267% ± 2.43, CA3 37.443% ± 2.521, DG 47.68% ± 0.824; Het: CA1 37.973% ± 5.626, CA3 55.523% ± 2.889, DG 31.253% ± 4.755; *Bptf* NcKO: CA1 36.057 %± 4.646, CA3 45.17% ± 7.869, DG 43.947% ± 6.864; n=3) (Figure 3.4B).

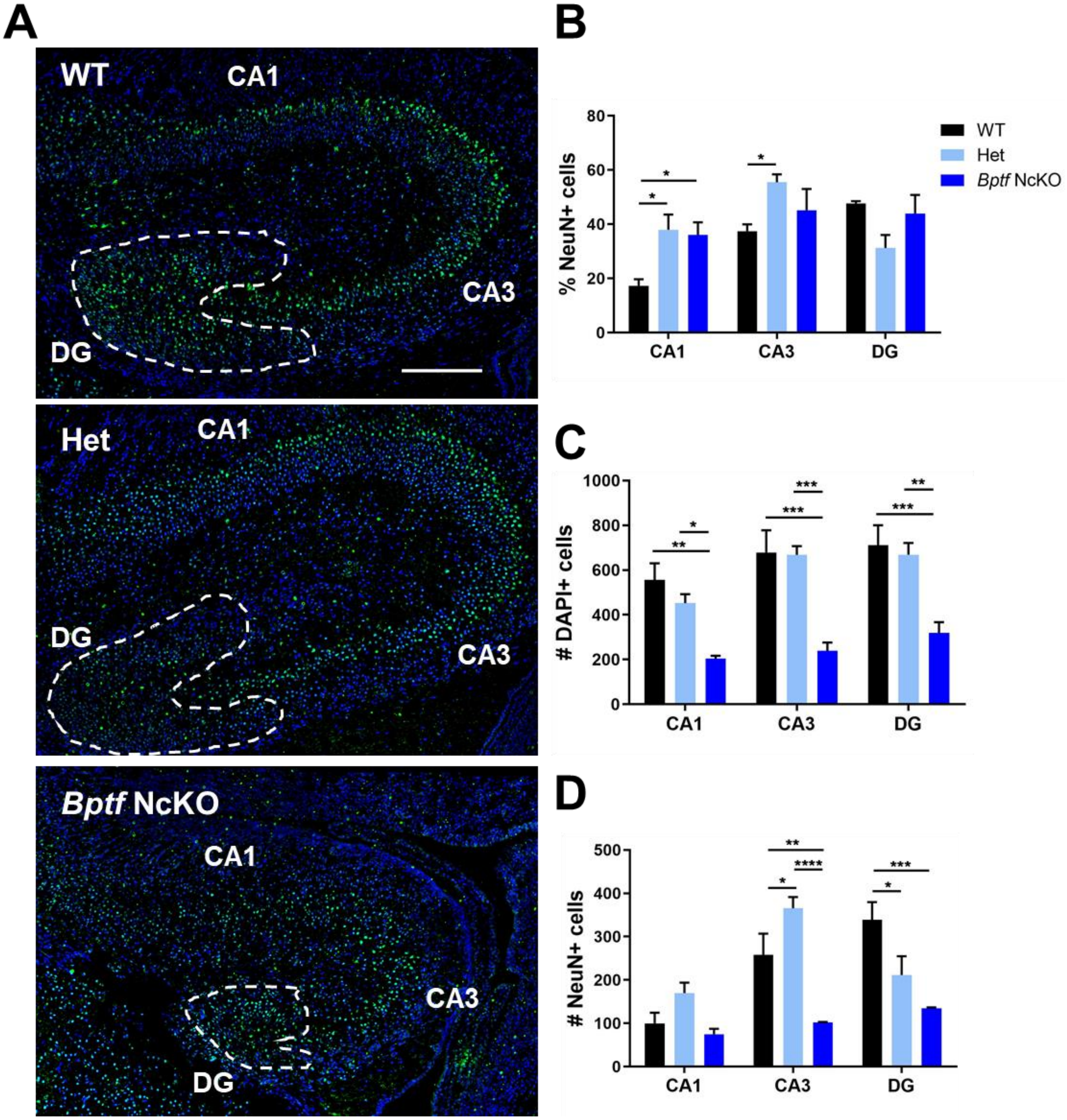

Figure 3.4 *Bptf* NcKO mice show a smaller HPC and a reduction in mature neurons.

A P0 coronal sections were used to do immunofluorescence staining using NeuN (green) and DAPI (blue). CA1, CA3 and DG (outlined in white) of WT and *Bptf* NcKO are shown. **B** Percentage of NeuN+ cells, **C** Number of DAPI+ cells and **D** Number of NeuN+ cells were assessed. Scale bar, 100µm. Data represent means ± SEM. n=3. * $p < 0.05$, ** $p < 0.01$, *** $p < 0.001$, **** $p < 0.0001$.

Furthermore, we wanted to include the number of NeuN+ cells per hippocampal regions to show the striking difference in mature neurons (WT: CA1 99.667 cells ± 24.768, CA3 258 cells ± 48.748, DG 339 cells ± 40.772; Het: CA1 169.667 cells ± 24.251, CA3 365.667 cells ± 25.828, DG 211.333 cells ± 43.322; *Bptf* NcKO: CA1 74.667 cells ± 12.811, CA3 102.333 cells ± 0.882, DG 134.333 cells ± 2.333; n=3) (Figure 3.4D).

These results suggest that *Bptf* is required in cortical and hippocampal progenitors for the proper expansion of the cortex and the development of the hippocampus.

3.4 *Bptf* NcKO mice display motor deficits

The severe cortical hypoplasia previously observed led us to hypothesize that *Bptf* NcKO mice may have motor deficits since it appears that the motor cortex is affected. We started a battery of behaviour tests to examine the motor behaviour including mobility, fatigue resistance, coordination and overall locomotor activity.

The first test we performed was the Beam Break (BBK) assay. Here, the mouse is placed in a stress-free home cage-like environment for 48 hours and its movements are recorded. We found that *Bptf* NcKO mice had significantly more beam breaks throughout the 48-hour period than the WT and Het mice (Figure 3.5 A). Interestingly, the total ambulatory time was not changed across the 3 groups of mice (Figure 3.5 B). During the night, the total movement time was significantly increased in the *Bptf* NcKO mice (Figure 3.5 C), which encompasses ambulatory time and any other type of movements. Lastly, *Bptf* NcKO mice travelled more distance at the beginning of the test and sporadically during the 48-hour period.

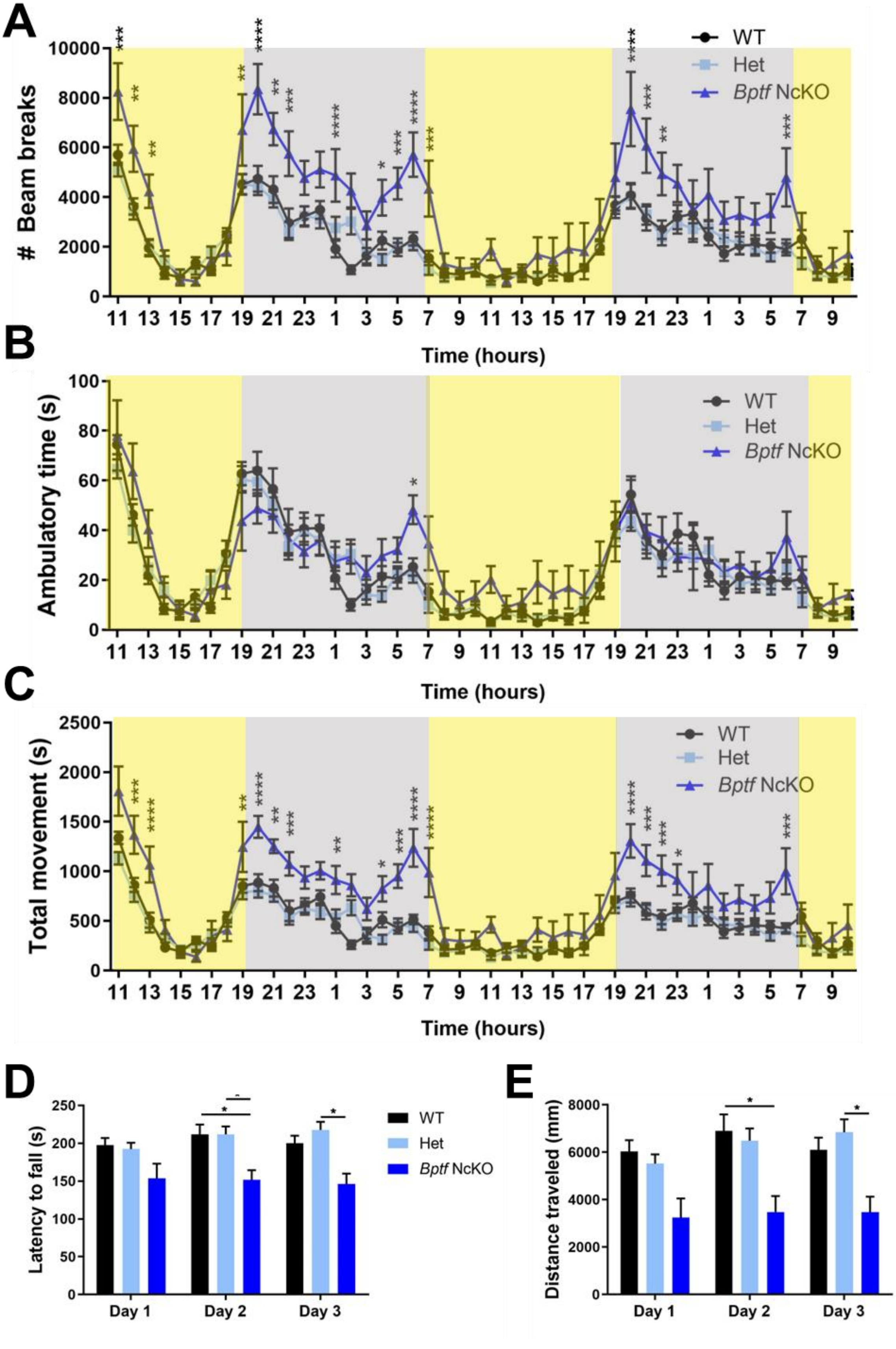
A
Beam breaks
0
2000
4000
6000
8000
10000
WT
Het
Bptf NcKO
11 13 15 17 19 21 23 1 3 5 7 9 11 13 15 17 19 21 23 1 3 5 7 9
Time (hours)
B
Ambulatory time (s)
0
20
40
60
80
100
WT
Het
Bptf NcKO
11 13 15 17 19 21 23 1 3 5 7 9 11 13 15 17 19 21 23 1 3 5 7 9
Time (hours)
C
Total movement (s)
0
500
1000
1500
2000
2500
WT
Het
Bptf NcKO
11 13 15 17 19 21 23 1 3 5 7 9 11 13 15 17 19 21 23 1 3 5 7 9
Time (hours)
D
Latency to fall (s)
0
50
100
150
200
250
Day 1
Day 2
Day 3
WT
Het
Bptf NcKO
E
Distance traveled (mm)
0
2000
4000
6000
8000
Day 1
Day 2
Day 3

Figure 3.5 *Bptf* NcKO mice have higher baseline activity level and show motor deficits. **A** The number of beam breaks, **B** ambulatory time and **C** total movement were measured during the beam break assay. The X axis represents the time of the day. The 12-hour light/dark cycle is depicted as the yellow and grey rectangles, respectively. **D** The latency to fall and the **E** distance traveled were measured during the rotarod test. The values plotted for each day are an average of the 4 trials. Data represent means ± SEM. * $p < 0.05$, ** $p < 0.01$, *** $p < 0.001$, **** $p < 0.0001$. n=17 (WT), n=20 (Het), n=5 (*Bptf* NcKO).

These results showed that *Bptf* NcKO mice have a higher activity baseline than the WT and Het mice, which are not significantly different from one another.

The next test performed was the rotarod. The mouse needs to utilize its coordination and endurance to stay on the rotating rod. Each mouse is tested four times a day on three consecutive days. We found that *Bptf* NcKO mice were falling more quickly on day two and day three than the WT and Het mice (WT: Day1 197.705s ± 9.255, Day2 211.471s ± 13.237, Day3 199.838s ± 10.236, n=17; Het: Day1 192.375s ± 8.446, Day2 211.675s ± 10.591, Day3 217.563s ± 10.898, n=20; *Bptf* NcKO: Day1 153.688s ± 19.237, Day2 151.563s ± 12.847, Day3 146.125s ± 13.770, n=4) (Figure 3.5 D,E). Similarly, we found that *Bptf* NcKO mice travelled approximately half of the distance of WT and Het mice (WT: Day1 6028.138mm ± 484.530, Day2 69433mm ± 696.048, Day3 6102.156mm ± 511.698, n=16; Het: Day1 5523.471mm ± 387.809, Day2 6491.519mm ± 511.568, Day3 6840.738mm ± 551.406, n=20; BPTF NcKO: Day1 32.537mm ± 806.229, Day2 3474.767mm ± 676.782, Day3 3472.493mm ± 652.919, n=4). These results suggest that *Bptf* NcKO mice have locomotor deficits when presented with a complex motor function task.

The last motor function test we performed was the DigiGait. It uses red light reflection to capture multiple paw-related data to analyze the gait of the animal. The first measurement that interested us was the swing (Figure 3.6 A). It corresponds to the time the paw was not in contact with the belt.

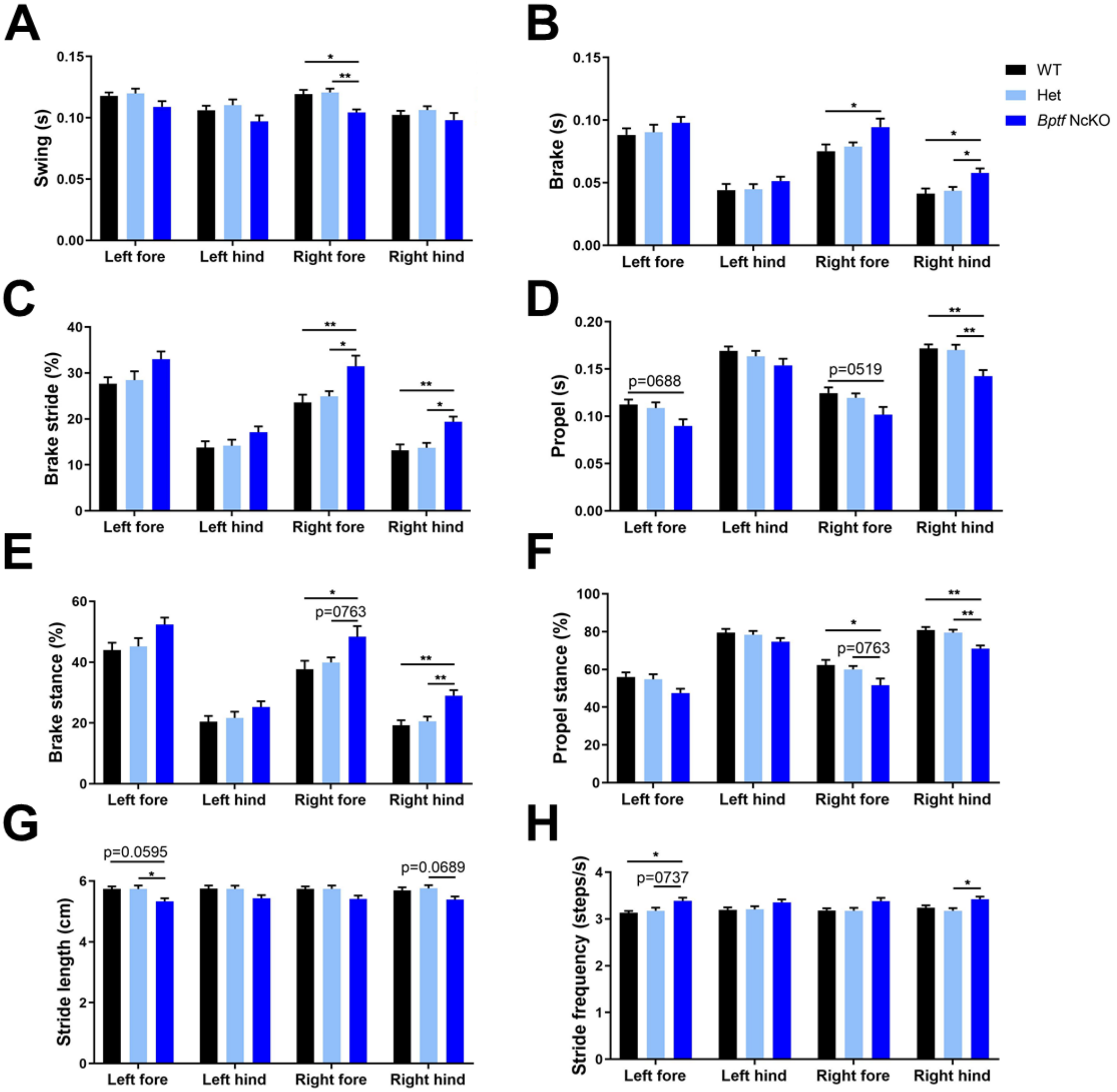

Figure 3.6: *Bptf* NcKO mice have gait impairments.

A The swing, **B** brake, **C** brake stride, **D** propel, **E** braked stance, **F** propel stance, **G** stride length and **H** stride frequency were measured during the DigiGait test. Each paw was processed individually. Data represent means ± SEM. * $p < 0.05$, ** $p < 0.01$, n=15 (WT), n=19 (Het), n=9 (*Bptf* NcKO).

We found that the right fore paw of *Bptf* NcKO mice spent significantly less time swinging when compared to the WT and Het mice (WT: Left fore 0.118s ± 0.003, Left hind 0.106s ± 0.004, Right fore 0.119s ± 0.004, Right hind 0.102s ± 0.003, n=15; Het: Left fore 0.120s ± 0.004, Left hind 0.110s ± 0.005, Right fore 0.121s ± 0.003, Right hind 0.106s ± 0.003, n=19; *Bptf* NcKO: Left fore 0.109s ± 0.005, Left hind 0.097s ± 0.005, Right fore 0.104s ± 0.003, Right hind 0.098s ± 0.006, n=9). In agreement with this result, we found that the brake time, which is the time between the initial paw contact with the belt to the maximum paw contact, was significantly increased for both right fore and right hind paws in *Bptf* NcKO mice (WT: Left fore 0.088s ± 0.005, Left hind 0.044s ± 0.005, Right fore 0.075s ± 0.005, Right hind 0.041s ± 0.004, n=15; Het: Left fore 0.090s ± 0.006, Left hind 0.045s ± 0.004, Right fore 0.079s ± 0.003, Right hind 0.044s ± 0.003, n=19; *Bptf* NcKO: Left fore 0.098s ± 0.005, Left hind 0.051s ± 0.003, Right fore 0.094s ± 0.007, Right hind 0.058 ± 0.004, n=9) (Figure 3.6 B).

When we analyzed the total stride, we found that the *Bptf* NcKO mice had a higher percentage of the stride that was for the braking phase for both right fore and hind paws (WT: Left fore 27.633% ± 1.440, Left hind 13.767% ± 1.397, Right fore 23.593% ± 1.681, Right hind 13.140% ± 1.300, n=15; Het: Left fore 28.453% ± 1.927, Left hind 14.163% ± 1.310, Right fore 24.905% ± 1.130, Right hind 13.721% ± 1.052, n=19; *Bptf* NcKO: Left fore 33.011% ± 1.679, Left hind 17.111% ± 1.288, Right fore 31.489% ± 2.285, Right hind 19.378% ± 1.132, n=9) (Figure 3.6 C).

The next measurement that was interesting was the propulsion phase, which is the time the paw was in maximum contact with the belt (Figure 3.6 D). We found that the right hind paw of *Bptf* NcKO mice had significantly less propel time than the WT and Het mice (WT: Left fore 0.112s ± 0.005, Left hind 0.169s ± 0.005, Right fore 0.125s ± 0.006, Right hind 0.172s ± 0.004, n=15; Het: Left fore 0.109s ± 0.006, Left hind 0.164s ± 0.006, Right fore 0.120s ± 0.005, Right hind 0.170s ± 0.006, n=19; *Bptf* NcKO: Left fore 0.090s ± 0.007, Left hind 0.154s ± 0.007, Right fore 0.102s ± 0.008, Right hind 0.142s ± 0.006, n=9).

The next phase of the stride we analyzed was when the paw is in contact with the belt, referred as stance (Figure 3.6 E-F). First, we analyzed the percentage of the stance phase when the paw is in braking phase. The right fore and hind paws of *Bptf* NcKO mice had a significantly higher braking stance percentage than WT and Het mice (WT: Left fore 43.993% ± 2.436, Left hind 20.433% ± 1.888, Right fore 37.740% ± 2.753, Right hind 19.220% ± 1.691, n=15; Het: Left fore 45.247% ± 2.673, Left hind 21.663% ± 2.040, Right fore 39.921% ± 1.678, Right hind 20.553% ± 1.583, n=19; *Bptf* NcKO: Left fore 52.422% ± 2.246, Left hind 25.267% ± 1.910, Right fore 48.356% ± 3.542, Right hind 29.044% ± 1.768, n=9). Second, we investigated the percentage of the stance phase when the paw was in propulsion phase. Once again, we found that the right paws of *Bptf* NcKO mice had a lower percentage of propel stance (WT: Left fore 56.007% ± 2.436, Left hind 79.567% ± 1.888, Right fore 62.260% ± 2.753, Right hind 80.787% ± 1.693, n=15; Het: Left fore 54.753% ± 2.673, Left hind 78.337% ± 2.040, Right fore 60.079% ± 1.678, Right hind 79.447% ± 1.583, n=19; *Bptf* NcKO: Left fore 47.578% ± 2.246, Left hind 74.733% ± 1.910, Right fore 51.644% ± 3.542, Right hind 70.956% ± 1.768, n=9).

The last paw measurements we performed were the stride length and frequency (Figure 3.6 G-H). We observed a smaller stride length in *Bptf* NcKO left fore (WT: Left fore 5.740cm ± 0.081, Left hind 5.753cm ± 0.100, Right fore 5.740cm ± 0.085, Right hind 5.693cm ± 0.097, n=15; Het: Left fore 5.737cm ± 0.116, Left hind 5.742cm ± 0.104, Right fore 5.742cm ± 0.111, Right hind 5.758cm ± 0.103, n=19; *Bptf* NcKO: Left fore 5.333cm ± 0.100, Left hind 5.433cm ± 0.105, Right fore 5.411cm ± 0.112, Right hind 5.389cm ± 0.102, n=9). In agreement with that, we found a higher stride frequency in *Bptf* NcKO mice for the left fore and right hind paws (WT: Left fore 3.133 steps/s ± 0.040, Left hind 3.193 steps/s ± 0.056, Right fore 3.180 steps/s ± 0.048, Right hind 3.240 steps/s ± 0.051, n=15; Het: Left fore 3.174 steps/s ± 0.067, Left hind 3.205 steps/s ± 0.065, Right fore 3.174 steps/s ± 0.065, Right hind 3.174 steps/s ± 0.058, n=19; *Bptf* NcKO: Left fore 3.89 steps/s ± 0.068, Left hind 3.356 steps/s ± 0.063, Right fore 3.378 steps/s ± 0.074, Right hind 3.422 steps/s ± 0.057, n=9).

Taken together, we found that the *Bptf* NcKO mice have gait impairments. Their paws spent more time in contact with the belt and less time swinging or in propulsion phase. This suggests that the *Bptf* NcKO mice have a harder time swinging and moving their paws during a stride. Furthermore, to keep up with the belt set speed, they make smaller strides and increase their frequency.

3.5 Repetitive behaviours are observed in *Bptf* NcKO mice

In our battery of behaviour tests, we wanted to assess anxiety. First, we performed the open field (OF) test (Figure 3.7 A-B). It is based on the mouse's conflicted inclination to explore a novel environment and its fear of brightly lit open spaces. First, we observed no change between the WT and Het mice in their time spent in the centre (WT: 25.99s ± 3.308, n=19; Het: 18.24s ± 2.716, n=24), time spent in the four corners (WT: 272.7s ± 13.44, n=19; Het: 294.9s ± 8.187, n=24) and distance travelled (WT: 4071mm ± 202.2, n=19; Het: 3997mm ± 159.0, n=24).

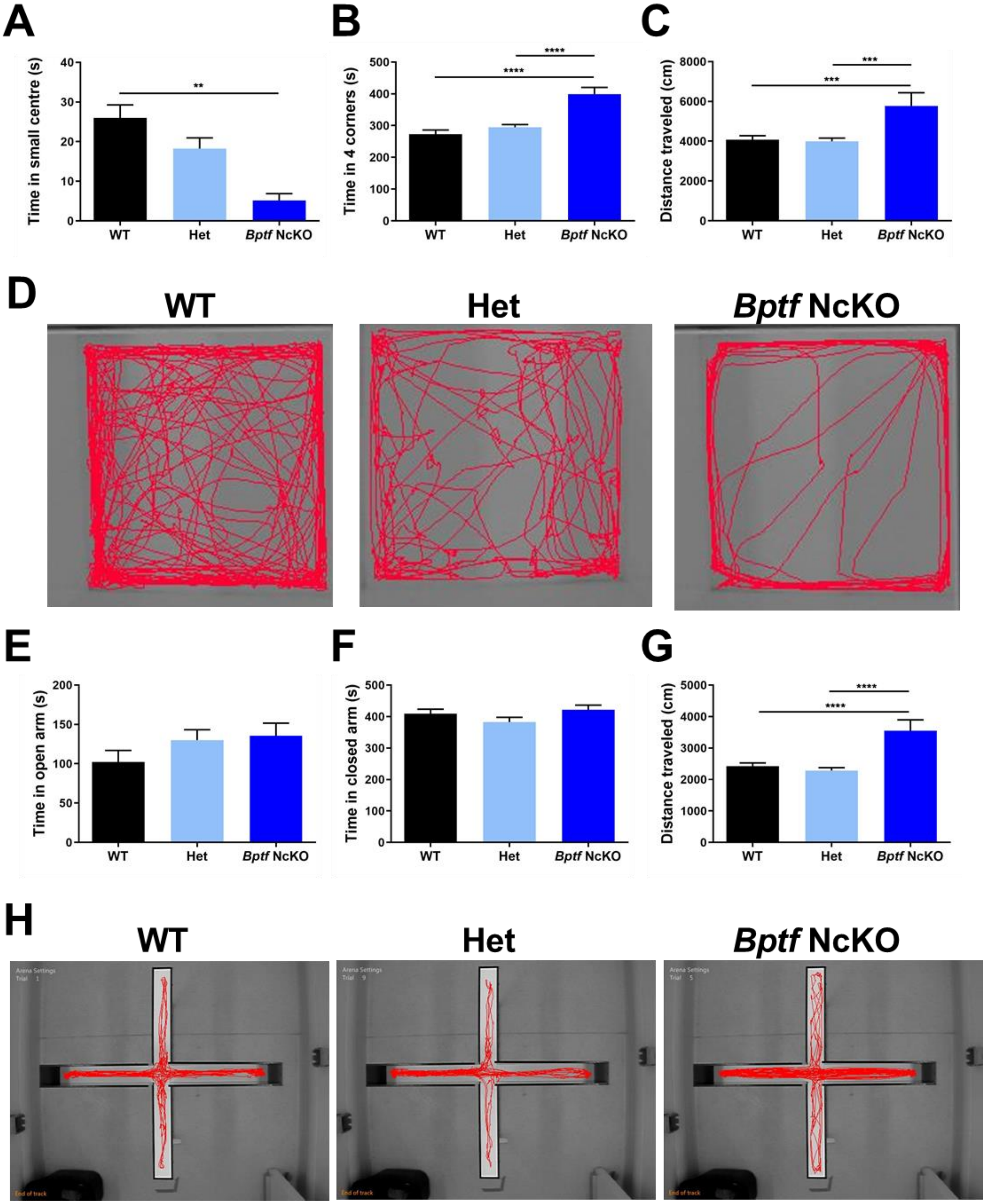
A
Time in small centre (s)
40
30
20
10
0
**
WT
Het
Bptf NcKO
B
Time in 4 corners (s)
500
400
300
200
100
0
****
****
WT
Het
Bptf NcKO
C
Distance traveled (cm)
8000
6000
4000
2000
0
***
***
WT
Het
Bptf NcKO
D
WT
Het
Bptf NcKO
E
Time in open arm (s)
200
150
100
50
0
WT
Het
Bptf NcKO
F
Time in closed arm (s)
500
400
300
200
100
0
WT
Het
Bptf NcKO
G
Distance traveled (cm)
5000
4000
3000
2000
1000
0
****
****
WT
Het
Bptf NcKO
H
WT
Het
Bptf NcKO

Figure 3.7 *Bptf* NcKO mice have no anxiety phenotype.

A Time in the small centre, **B** Time in the 4 corners and **C** distance traveled were measured during the OF test. **D** Representative tracking data of the mice for each genotype. **E** Time in the open arm, **F** time in the closed arm and **G** distance traveled were measured during the EPM test. **H** Representative tracking data for mice of each genotype**.** Data represent means ± SEM. ** $p < 0.01$, *** $p < 0.001$, **** $p < 0.0001$. n=17-19 (WT), n=20-24 (Het), n=5-9 (*Bptf* NcKO).

In contrast, we noticed that the *Bptf* NcKO mice spent significantly less time in the centre of the OF (BPTF NcKO 5.138s ± 1.739, n=5), more time in the four corners (*Bptf* NcKO 399.3s ± 20.90, n=5) and overall were moving more than the WT and Het mice (*Bptf* NcKO 5775mm ± 664.1, n=5). Normally, these results would lead us to the conclusion that *Bptf* NcKO mice have an anxiety phenotype. However, based on the mouse tracks during the test, we saw that the *Bptf* NcKO mice were continuously running along the periphery of the OF arena in a tight line, which is reminiscent of a stereotypical behaviour. Therefore, we decided to perform a second test, the elevated plus maze (EPM), to assess the possible anxiety phenotype (Figure 3.7 C-D).

The EPM test is based on the notion that mice prefer dark closed places rather than bright open places. In this paradigm, the mouse is conflicted by the desire of exploring the new environment and the safety of the closed arm. We saw no change in the time spent in the open arms (WT: 102.3s ± 14.56, n=16; Het: 130.0s ± 13.26, n=20; *Bptf* NcKO 135.6s ± 16.00, n=9) and closed arms (WT: 408.8s ± 14.73, n=16; Het: 382.7s ± 15.13, n=20; *Bptf* NcKO 421.3s ± 14.95, n=9) across all the groups. However, the *Bptf* NcKO mice had an increased distance travelled (WT: 2429mm ± 99.57, n=16; Het: 2287mm ± 91.75, n=20; *Bptf* NcKO 3551mm ± 345.3, n=9), which was consistent with the previous test.

Thus, we concluded that the *Bptf* NcKO mice did not have an anxiety phenotype, but rather experienced stereotypical movements that were further tested in later sections. Also, we found no anxiety phenotype in Het mice.

3.6 *Bptf* NcKO mice have learning and memory deficits

The first test we used to assess the learning and memory ability of our mice was the Morris water maze (MWM). Here, the mouse needs to learn to find a hidden platform under the surface of the water by using visual cues positioned on the walls of the testing room. For our protocol, we trained the mice to locate the platform for seven consecutive days. On the eighth day (probe day), the platform was removed and we calculated the time spent in the target quadrant. We found that the WT and Het mice spent a comparable amount of time in the target quadrant (WT: 30.55s ± 2.560, n=19; Het: 29.18s ± 2.501, n=24) (Figure 3.8A). However, the *Bptf* NcKO mice spent significantly less time in the target quadrant when compared to the WT and Het mice (BPTF NcKO 8.222s ± 2.371, n=5). Also, we compared the distance traveled to verify that each cohort of mice were swimming around and not just floating and we found no significant difference (WT: 1314mm ± 87.23, n=19; Het: 1183mm ± 78.05, n=24; *Bptf* NcKO 1131mm ± 134.7, n=5) (Figure 3.8B). These results suggest that the *Bptf* NcKO mice were not impaired in their ability to swim but did not learn the location of the hidden platform.

The second test we used to assess the learning and memory skills of the mice was the cue and contextual fear conditioning. Here, an aversive stimulus, foot shock, is associated with a neutral context and neutral tone. Following the training sessions, the neutral stimulus, context or auditory cue, triggers the same behavioural reaction as would the aversive stimulus (Figure 3.8G). We measured the fear of the neutral stimulus by recording the mouse freezing time, which is the typical mouse response in reaction to fear. On day one, we measured the percentage of mobility time for six minutes to determine if there were any discrepancies between the groups and we found no change (WT: 88.49% ± 2.411, n=19; Het: 92.97% ± 1.607, n=24; *Bptf* NcKO 95.89% ± 2.133, n=5) (Figure 3.8D).

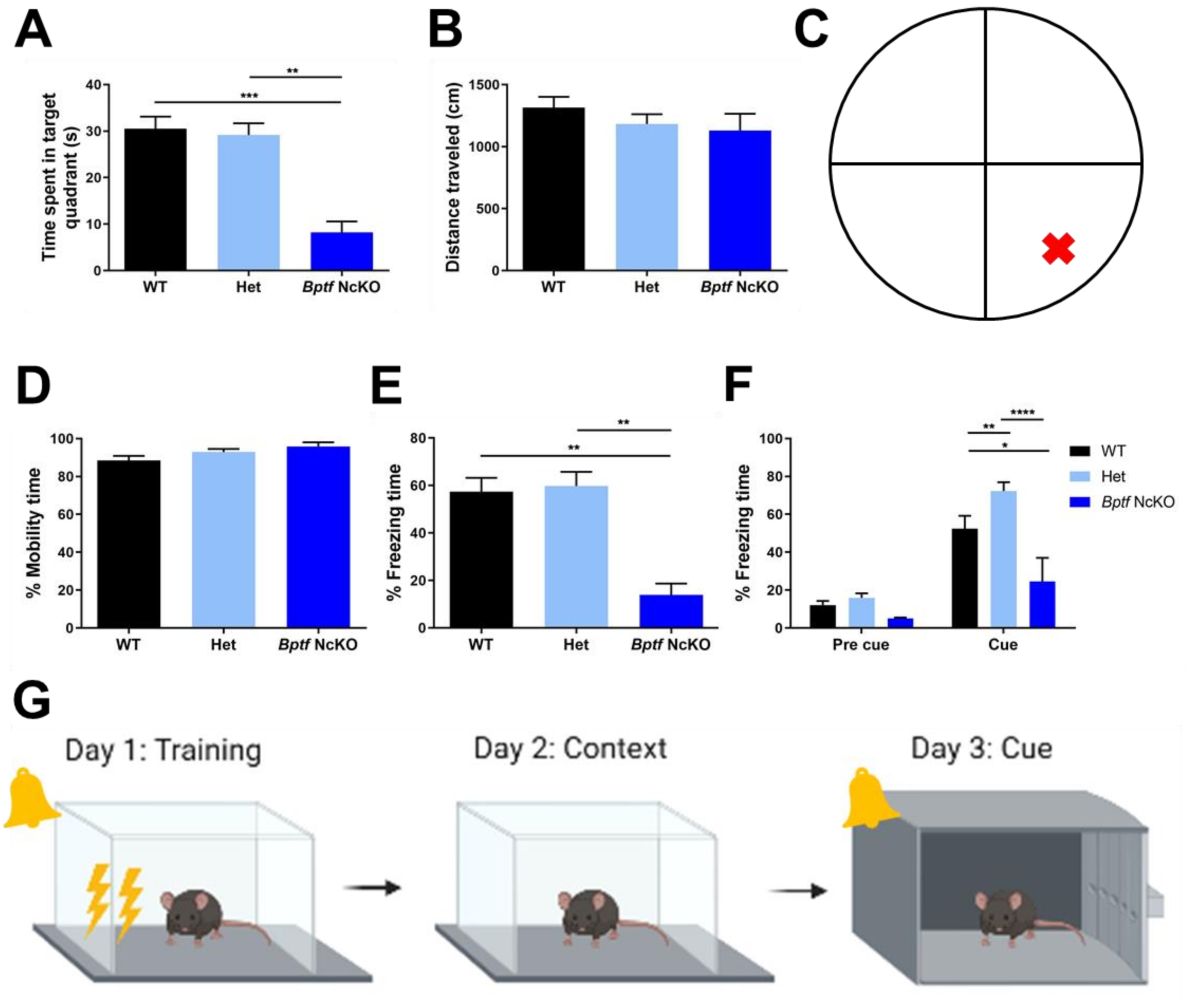

Figure 3.8: *Bptf* NcKO mice have learning and memory deficits.

A Time spent in the target quadrant and **B** distance traveled were measured during the MWM test. **C** Schematic of the MWM apparatus. The pool is separated into 4 quadrants and the hidden platform is depicted as the red cross. **D** Percentage of mobility time on day 1, **E** percentage freezing time on day 2 and **F** percentage of freezing time on day 3 were measured during the fear conditioning test. **G** Schematic of the fear conditioning. On day 1, the mouse is trained to associate a foot shock (yellow lightnings) with a tone (yellow bell)/environment. On day 2, the mouse is assessed of whether they associated the foot shock with the environment. On day 3, the environment is changed and the mouse is assessed to determine if they associated the cue with the foot shock. Data represent means ± SEM. * $p < 0.05$, ** $p < 0.01$, *** $p < 0.001$, **** $p < 0.0001$. n=19 (WT), n=24 (Het), n=5 (*Bptf* NcKO).

This means that all the mice had a similar activity baseline during the training period. On day two, we tested whether the mice made the association between the foot shock and the neutral context, which was the surrounding environment, without the auditory tone. We found that the WT and Het mice spent significantly more time freezing than the *Bptf* NcKO mice (WT: 57.45% ± 5.801, n=19; Het: 59.75% ± 6.006, n=24; *Bptf*NcKO 13.93% ± 4.790, n=5) (Figure 3.8E). This suggested that the WT and Het mice made the association between the aversive stimulus and the neutral context but not the *Bptf* NcKO mice. On day three, we wanted to determine if the mice associated the foot shock with the neutral auditory cue in the absence of the familiar context. Here, the environment was completely changed; the shape of the cage, the scent in the cage, the light parameters, surrounding sounds and the person administering the test were modified. Pre cue, no change was observed in mice movements across all cohorts. Following the cue, both WT and Het mice froze longer than *Bptf* NcKO mice (WT: Pre cue 12.161% ± 2.120, Cue 52.464% ± 6.768, n=19; Het: Pre cue 15.987% ± 2.284, Cue 72.285% ± 4.700, n=24) (Figure 3.8F). Interestingly, the tone triggered a minor freezing response in *Bptf* NcKO mice, but it was significantly smaller to the WT and Het mice (*Bptf* NcKO: Pre cue 5.085% ± 0.477, Cue 24.537% ± 12.537, n=5). This suggested that only the WT and Het mice associated the foot shock with the context and the tone.

In summary, *Bptf* NcKO mice were not able to use spatial cues to learn the location of a hidden platform during the MWM test. Also, they were incapable to make the association between an aversive stimulus with a neutral stimulus. Thus, BPTF NcKO mice have strong learning and memory deficits. Interestingly, the Het mice displayed a comparable behaviour to those of WT mice. Thus, we were not able to find any learning and memory deficits in Het mice.

3.7 *Bptf* NcKO mice show difficulty initiating conscious voluntary movements

All our mice were randomly group housed at weaning age. Interestingly, we noticed a certain behaviour when *Bptf* NcKO mice were housed together without a WT or Het mouse in the cage. Following a cage change, the nest material remained untouched. That led us to question whether the *Bptf* NcKO mice exhibit the fundamental behaviour that a typical mouse display.

First, we performed the nest building test to confirm our previous observation. Nest building is a daily activity that is complex and considered a spontaneous behaviour. It requires several coordinated actions including digging, carrying, fraying, sorting and fluffing of nest material. For this test, we loaded each mouse in a clean cage, provided a square of nestlet material and let them build their nest for 16 hours. Each nest was scored using specific criteria (Table 2.2). The WT and Het mice were able to make at least a flat nest, which corresponded to a score of 4, and in some cases would make a near perfect nest (WT: 4.313 ± 0.1983, n=16; Het: 4.200 ± 0.1170, n=20) (Figure 3.9 A-B). The *Bptf* NcKO mice did not even touch the nestlet material (*Bptf* NcKO 1.000 ± 0.000, n=9). These results showed that the *Bptf* NcKO mice are incapable of building their own nest and did rely on other mice to build it in their home cage.

Second, we wanted to assess the digging and burrowing ability, thus we chose the marble burying test. In this paradigm, mice are presented with 20 glass marbles laying on top of woodchip bedding. The number of buried marbles after 30 minutes is manually scored. The WT mice fully buried seven marbles on average (Figure 3.9 C-D). The Het mice only buried four and the *Bptf* NcKO mice did not bury any of the glass marbles (WT: 7.000 marbles ± 0.8619, n=15; Het: 4.250 marbles ± 0.8172, n=20; *Bptf* NcKO 0.000 marbles ± 0.000, n=9).

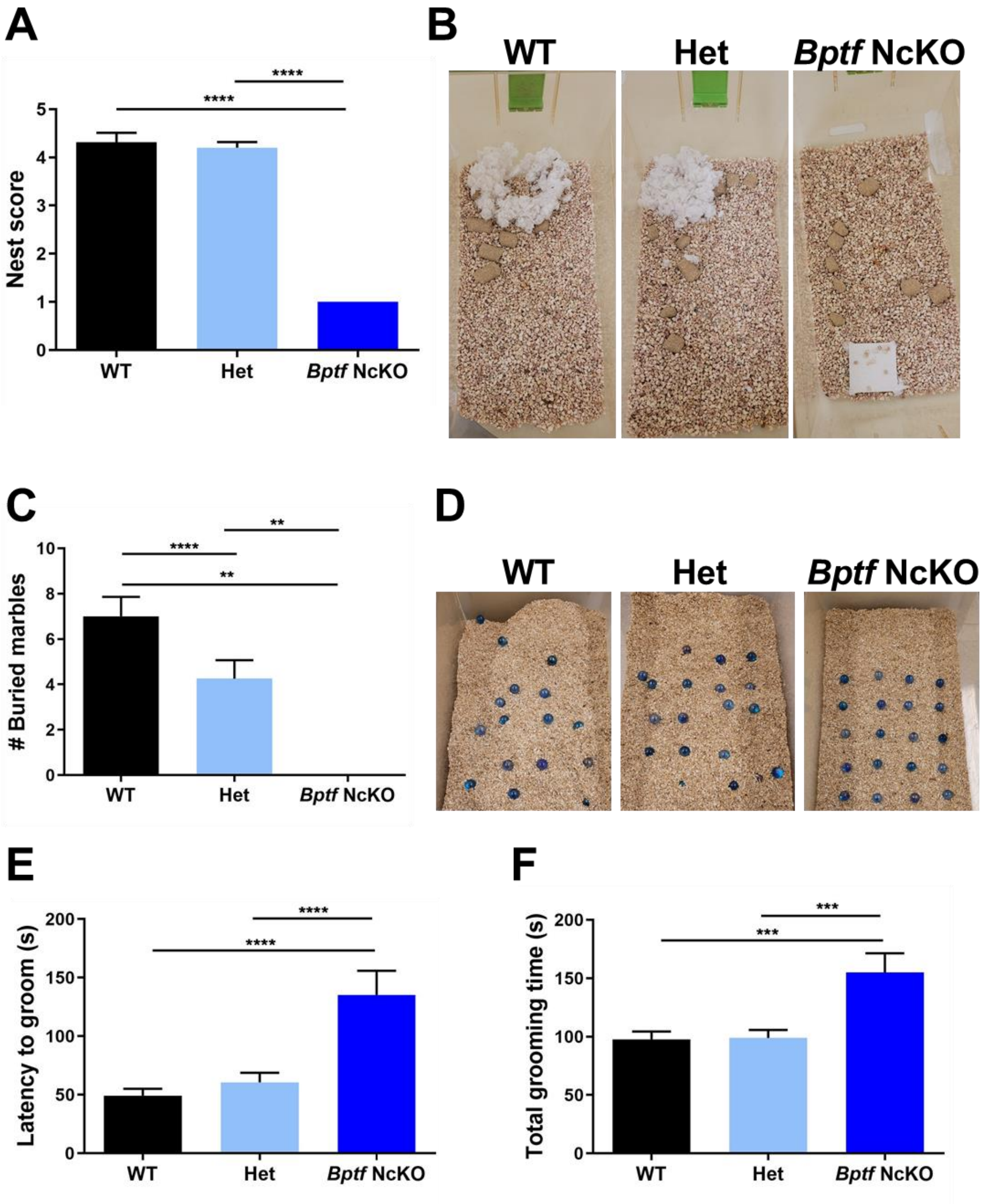
A
Nest score
0
1
2
3
4
5
****
****
WT
Het
Bptf NcKO
B
WT
Het
Bptf NcKO
C
Buried marbles
0
2
4
6
8
10
****
**
**
WT
Het
Bptf NcKO
D
WT
Het
Bptf NcKO
E
Latency to groom (s)
0
50
100
150
200
****
****
WT
Het
Bptf NcKO
F
Total grooming time (s)
0
50
100
150
200
***
***
WT
Het
Bptf NcKO

Figure 3.9: *Bptf* NcKO mice are lacking innate behaviour

A Nest score was given to the mice nestlet during the nest building test. **B** Representative image of the nestlet of each genotype after the 16-hour period. **C** The number of buried marbles was measured during the marble burying test. **D** Representative image of the marbles' arrangement following the 30-minute trial. **E** Latency to groom and **F** total grooming time were measured during the splash test. Data represent means ± SEM. ** $p < 0.01$, *** $p < 0.001$, **** $p < 0.0001$. n=16 (WT), n=20 (Het), n=9 (*Bptf* NcKO).

Furthermore, we noticed that the WT and Het mice made substantial digging pits whereas none of the *Bptf* NcKO mice dug. Based on the repetitive behaviour found in section 3.5, we expected the *Bptf* NcKO mice to bury more marbles.

However, due to their motor deficits observed in section 3.4, it was fair to assume that they would have difficulty digging since it is a complex movement and requires multiple coordinated actions.

The final test we performed to examine the innate behaviour of our mice was the splash test, also called the grooming test. Here, the mice are sprayed with a water solution on their back and loaded into a clean cage placed in front of a camcorder for 10 minutes. The time spent grooming and latency to first grooming session were manually scored. First, we observed that *Bptf* NcKO mice spent significantly more time grooming than the WT and Het littermates (WT: 97.81s ± 6.572, n=16; Het: 98.95s ± 6.813, n=20; *Bptf* NcKO 155.1s ± 16.30, n=9) (Figure 3.9F). Second, the latency to groom was also increased in the *Bptf* NcKO mice (WT: 49.27s ± 5.860, n=16; Het: 60.55s ± 8.283, n=20; *Bptf* NcKO 135.2s ± 20.68, n=9) (Figure 3.9E).

Furthermore, we noticed that *Bptf* NcKO mice were unstable during grooming. They easily lost their balance and had to lean against the wall of the cage for support. During the test, the WT and Het mice dug, buried their nose in the bedding and were grooming. On the other hand, *Bptf* NcKO mice were running around the periphery of the cage, similar to their behaviour in the OF test. At the end of the 10-minute trial, both WT and Het animals were completely dry but *Bptf* NcKO mice were still wet. Thus, *Bptf* NcKO mice had a longer and inefficient grooming session.

Taken together, these results suggest that *Bptf* NcKO mice have strong deficits in initiating conscious voluntary movements, which are critical for innate behaviours.

3.8 Summary of Findings

We generated *Bptf*; *Nestin*-Cre mice to specifically delete the *Bptf* gene in neural progenitors. We found that approximately 50% of *Bptf* NcKO mice survive past weaning age and they had severe developmental deficits. They were overall smaller in size and had severe brain malformations. We observed that a considerable portion of the cortex did not develop and that their hippocampus was not noticeable by P90. Interestingly, we did not find any obvious change in the heterozygous mice.

Next, we examined the cortical layers to determine whether there was any defect at a cellular level. We found that the cortex of the *Bptf* NcKO mice were approximately 50% thinner and that the number of deep layer neurons were significantly reduced. Also, we observed that the cells within the cortex were more tightly packed than in the WT or Het mice.

At P0, *Bptf* NcKO animals had a small and unorganized hippocampus. Using DAPI counts, we found that all the hippocampal regions in *Bptf* NcKO mice were significantly smaller when compared to the WT and Het mice. Furthermore, the number of mature neurons in CA3 and DG were significantly reduced.

Subsequently, we wanted to characterize the behaviour of *Bptf*; *Nestin*-Cre mice. We started by assessing the motor function using the BBK, RR and DigiGait. We found that *Bptf* NcKO mice were breaking more beams during the BBK and that the total movement was increased at certain points during the day. Since the ambulatory time was not significantly different, we associated these increases to grooming behaviours. Moreover, we found that *Bptf*

NcKO mice had a lower a latency to fall during the RR, which meant they had motor deficits. During the DigiGait, we found that *Bptf* NcKO mice had gait impairments that translated into a difficulty propelling their paws to initiate a stride, smaller stride length and increased stride frequency. We found no abnormality in the Het mice in any of the motor function tests.

The next set of behaviour tests we performed was to assess the learning and memory ability of our *Bptf*; *Nestin*-Cre mice. During the MWM, we found that *Bptf* NcKO mice were unable to use the spatial cues to learn the location of the hidden platform following the 7-day training period. Furthermore, they were incapable of associating an aversive stimulus to a neutral stimulus during the FC test. They did not memorize that in a specific context or environment they received a foot shock. Also, they did not learn that the auditory cue preceded a foot shock. The Het mice did learn the location of the hidden platform and did make the association of the aversive stimulus with the neutral stimulus. Thus, we can conclude that *Bptf* NcKO mice have severe learning and memory deficits.

The last behavioral assessment we did was to examine the fundamental behaviour of the *Bptf*; *Nestin*-Cre mice. We found that *Bptf*NcKO mice were unable to build a nest, did not bury any marbles, did not dig and had difficulties grooming themselves. These results suggest that the *Bptf* NcKO mice have dyspraxia. Dyspraxia is defined as the partial loss of the ability to plan, organize and coordinate movements [254]. Praxis deficits are most commonly found in patients with strokes, neurodegenerative disorders and neurodevelopmental disorders including autism spectrum disorders [255-257].

Chapter 4: Characterization of mice ablated for Atrx in specific neuronal populations

4.1 Introduction and rational

Mutations in the *Atrx* gene are the primary cause of the ATR-X syndrome and they are also frequently found in patients with an autism spectrum disorder (ASD) diagnosis [258-260]. ASDs are characterized by impairments in social interactions and repetitive and stereotypical behaviours. They can also include intellectual disabilities, hyperactivity and epilepsy [231]. Rett syndrome is classified as an ASD and shares common symptoms and features with the ATR-X syndrome [261]. Furthermore, both syndromes are caused by mutations in genes encoding chromatin-interacting proteins. Rett syndrome is associated with mutations in the *MECP2* gene, which encodes a nuclear protein that binds methylated DNA and is essential in the reorganization of chromatin landscape.

Animal studies showed that *Mecp2* removal in inhibitory neurons, using the Cre-driver *Viaat*, recapitulates numerous features of Rett syndrome patients, and *Mecp2* knockout mice [237]. Interestingly, *Mecp2* ablation in excitatory neurons (*Vglut2*-Cre) also showed specific Rett syndrome characteristics that were very distinct from the ones found in the *Mecp2;Viaat-Cre* mice [262]. Consequently, it is possible to tease out the contributions of the excitatory and inhibitory neurons to the phenotype of Rett syndrome.

The lack of information surrounding the ATR-X syndrome and the implication of the glutamatergic/GABAergic system in ASDs led us to hypothesize that alteration of the equilibrium between these two systems play a role in the pathogenesis of ATR-X syndrome.

4.2 Generation and initial characterization of *Atrx; Vglut2*-Cre and *Atrx; Viaat*-Cre mice

In this chapter, we used two conditional *Atrx* knockout (KO) mouse models to tease out the contribution of the inhibitory and excitatory network to the ATR-X syndrome's phenotype. We used *Atrx*$^{fl/fl}$ mice, which have exon 18 flanked by two loxp sites. When Cre recombinase is expressed, it results in the excision of exon 18 (as shown in Figure 4.1A), the inactivation of the ATPase activity, and an overall reduction in Atrx transcript and protein levels [205]. The first model used was the *Atrx; Vglut2*-Cre that we generated by crossing *Atrx*$^{fl/fl}$ mice to *Vglut2*-IRES-Cre mice (Figure 4.1B). The second model used was the *Atrx; Viaat*-Cre that we obtained by crossing *Atrx*$^{fl/fl}$ mice to *Viaat*-Cre mice (Figure 4.1C). Here, our goal was to compare *Atrx*; *Vglut2*-Cre (AtrxVgKO) and *Atrx*; *Viaat*-Cre (AtrxVtKO) with WT littermates for any differences in brain development. Since ATRX is an X-linked gene and mutations primarily show phenotypes only in males, we chose to limit our analysis to male mice in this chapter. To assess viability, we recorded the genotypes of all births from both mouse lines to discover that the Mendelian ratios were skewed (Figure 4.1D). AtrxVtKO and AtrxVgKO mice should represent 25% of all births. However, we observed a reduction of ~50% of conditional KO (cKO) mice born. Of these mice, between 65 and 72% died at birth or embryonically. The cKO pups that were alive at birth died within a few hours and we saw no obvious cause of death for either mouse line. Due to the early lethality, all further characterization of these two transgenic mouse lines was performed at P0.

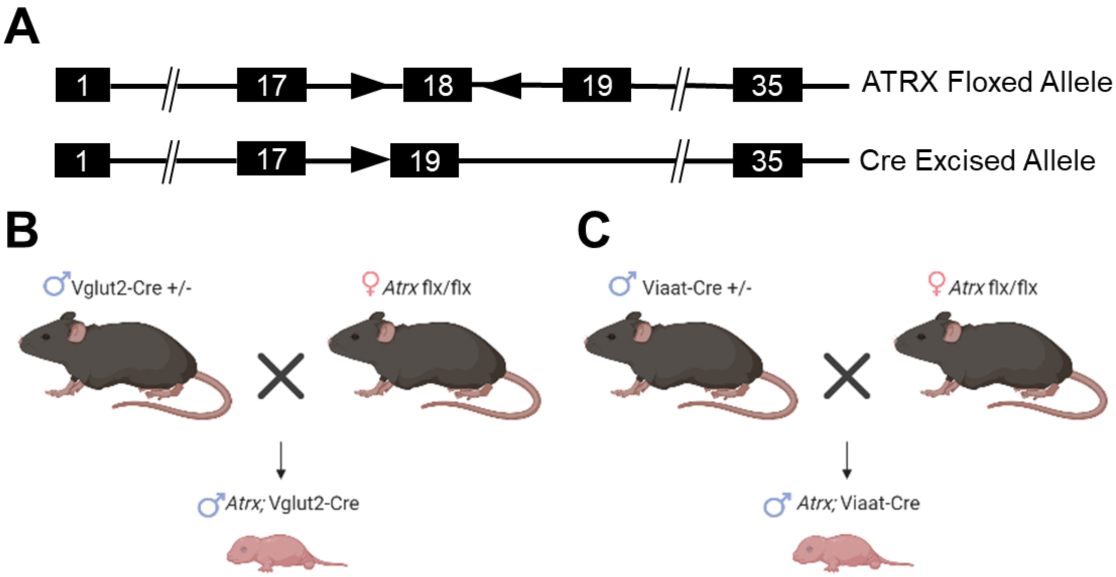

D

	# pups alive ♂ at P0		# pups dead ♂ at P0	
	WT	**KO***	**WT**	**KO***
***Atrx;* Vglut2-Cre**	26	5	0	9
***Atrx;* Viaat-Cre**	21	3	0	8

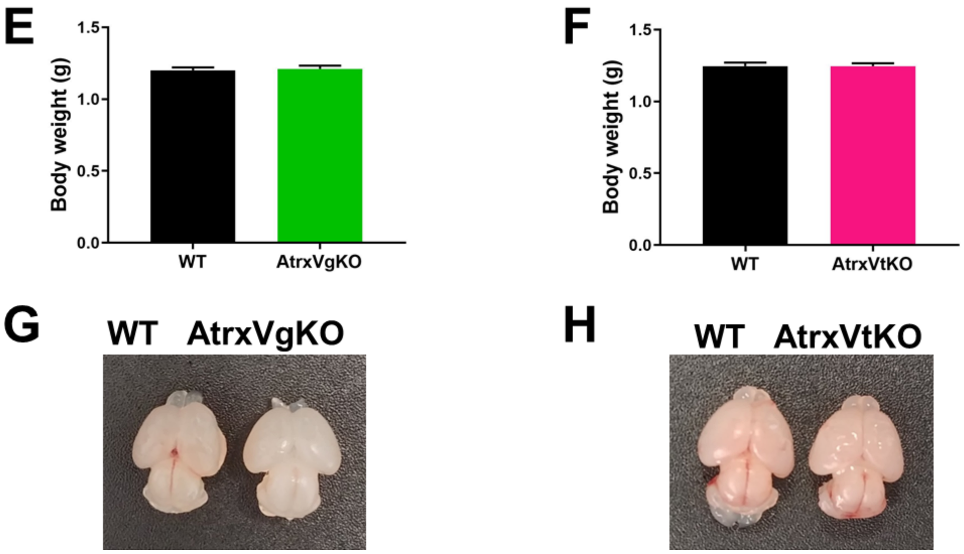

Figure 4.1: Characterization of *Atrx;Vglut2*-Cre and *Atrx;Viaat*-Cre mice

A Schematic of the *Atrx* floxed allele and the *Cre* excised allele. Breeding schemes of **B** *Atrx;Vglut2*-Cre and **C** *Atrx;Viaat*-Cre mice. **D** Table showing the number of males that were born alive and stillborn. *Pups only survived for a few hours. Body weight at P0 for **E** *Atrx;Vglut2*-Cre and **F** *Atrx;Viaat*-Cre mice. P0 brains of **G** *Atrx;Vglut2*-Cre and **H** *Atrx;Viaat*-Cre mice. Data represent means ± SEM. n=10.

We weighed the pups and found no significant differences in mass across all genotypes and mouse lines (WT: 1.2g ± 0.02108; AtrxVgKO: 1.210g ± 0.02322; n=11) (WT: 1.245g ± 0.02473; AtrxVtKO: 1.245g ± 0.02073; n=10) (Figure 4.1E-F). We dissected the P0 brains of WT, AtrxVgKO and AtrxVtKO mice and we saw no gross morphological difference between the genotypes (Figure 4.1 G-H).

To confirm the proper expression of our Cre drivers, we crossed the *Vglut2*-Cre and the *Viaat*-Cre lines to a tdtomato reporter mouse line, also called Ai14. When bred together, a stop cassette preceding the reporter gene is excised allowing for expression of the fluorescent protein as a marker of Cre+ cells. The vesicular glutamate transporter 2 (VGLUT2) is highly expressed at embryonic and postnatal stages in the cortex and hippocampus [263, 264]. We found that the tdtomato reporter was highly expressed in all cortical layers at P0 (Figure 4.2A). Also, we saw that it was strongly expressed in the hippocampus, which was consistent with previously published data [262]. The vesicular inhibitory amino acid transporter (VIAAT) is widely expressed in the central nervous system during embryogenesis [265]. We found that the expression pattern of tdtomato in the cortex was sparse and consistent with the literature (Figure 4.2B) [237, 266]. We saw that it was highly expressed inside the hippocampus and at a lower level at its periphery. We conclude that the two Cre lines are driving expression of Cre recombinase in a pattern similar to the known endogenous expression for each gene.

Next, we used P0 coronal sections and Nissl staining to visualize the hippocampus of *Atrx;Vglut2*-Cre and *Atrx;Viaat*-Cre mice to determine whether they had morphological defects (Figure 4.3). We noted that both AtrxVgKO and AtrxVtKO mice had a hippocampus formation and that the sub-regions, namely CA1, CA3 and DG, were also present.

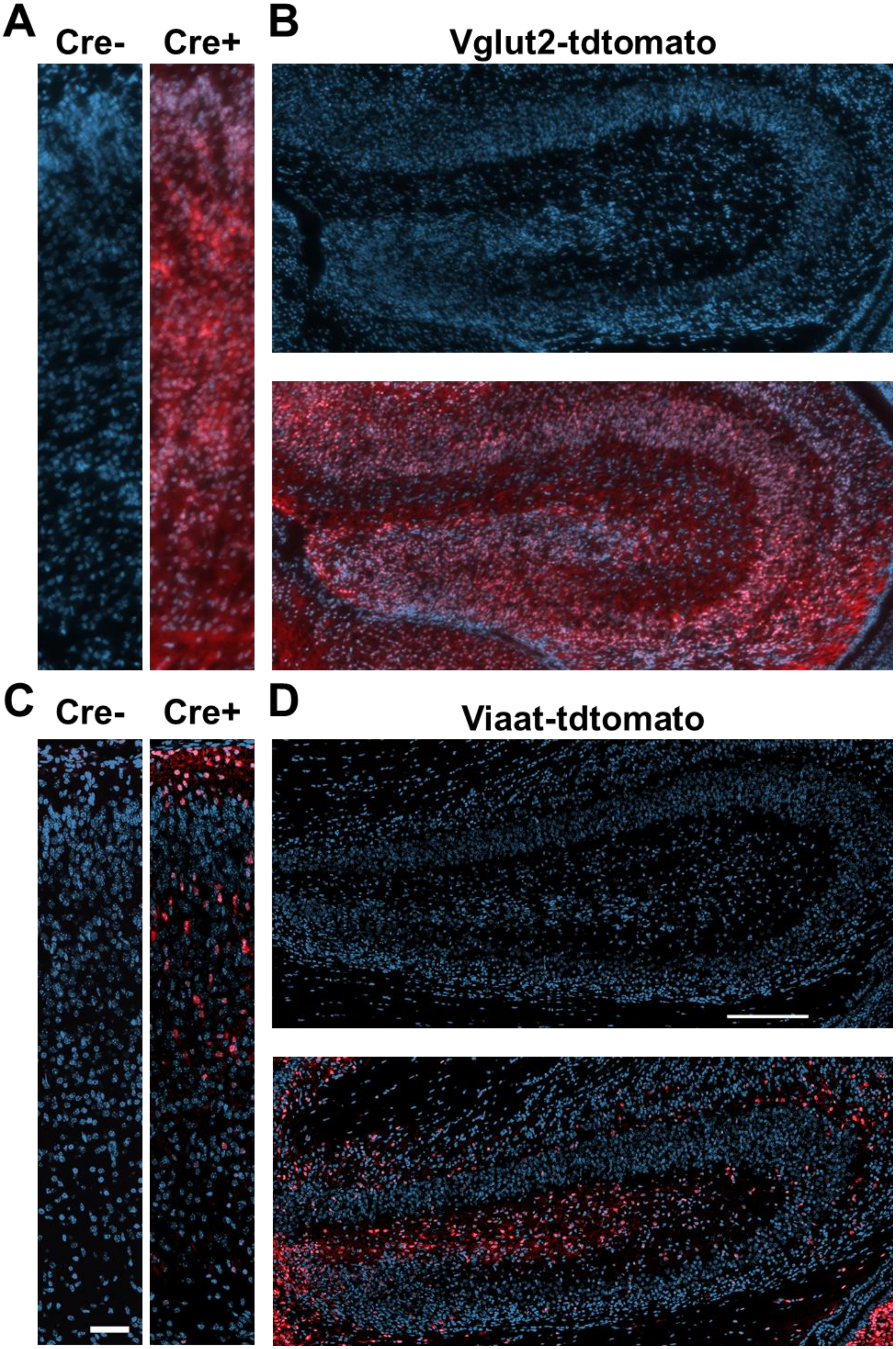
A
Cre-
Cre+
B
Vglut2-tdtomato
C
Cre-
Cre+
D
Viaat-tdtomato

Figure 4.2: Expression of the tdtomato reporter in Vglut2-Cre and Viaat-Cre mice

P0 coronal sections of **A-B** Tdtomato; Vglut2-Cre and **C-D** Tdtomato; Viaat-Cre mice stained with DAPI (blue). **A, C** Cortex and **B, D** hippocampus are shown. Scale bar, 50µm for cortex and 200µm for hippocampus.

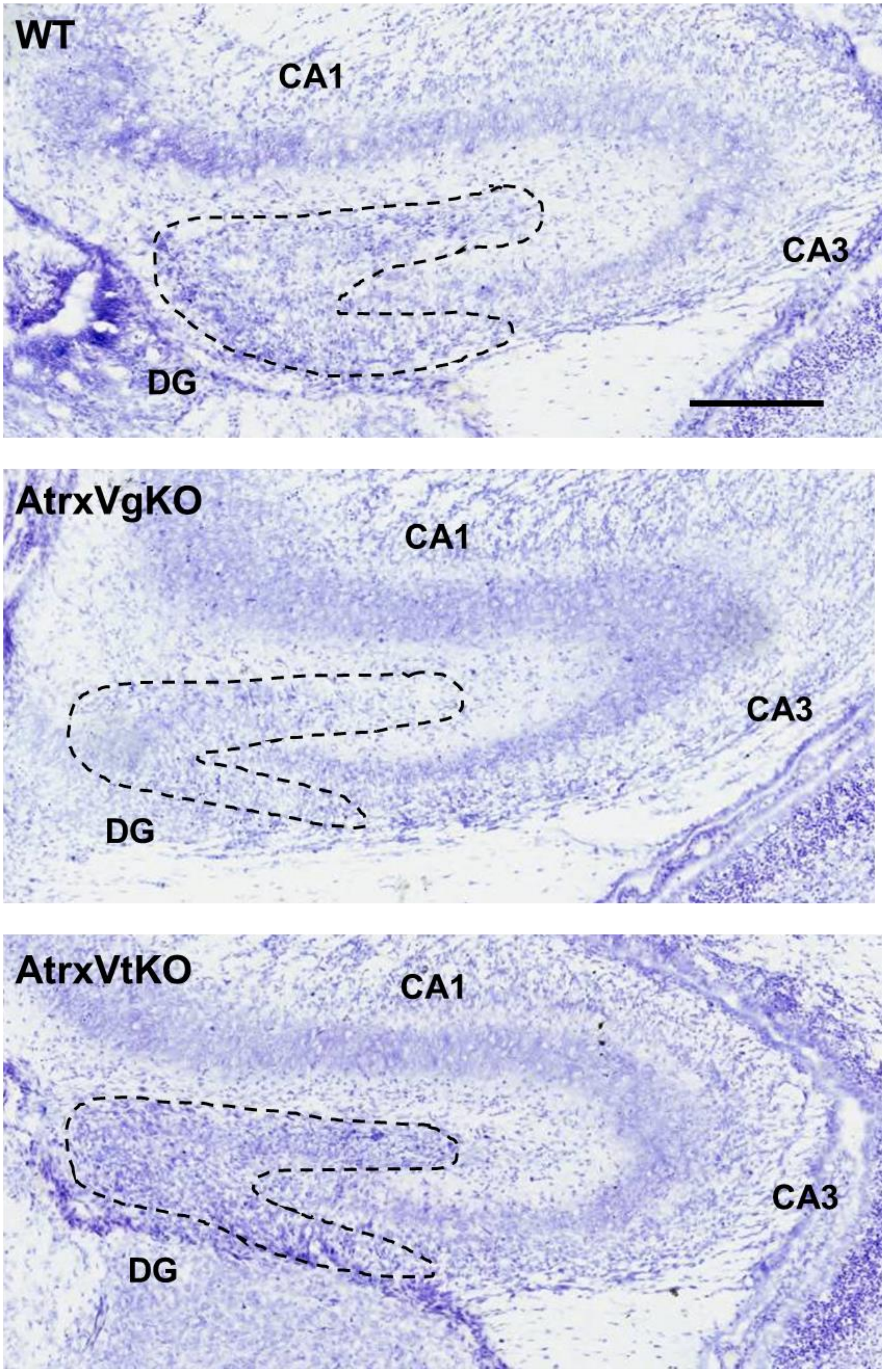
WT
CA1
CA3
DG
AtrxVgKO
CA1
CA3
DG
AtrxVtKO
CA1
CA3
DG

Figure 4.3: *Atrx* deletion in excitatory and inhibitory neurons does alter the gross morphology of the hippocampus.

P0 coronal sections of WT (top), AtrxVgKO (middle) and AtrxVtKO (bottom) were used for Nissl stain. CA1 and CA3 hippocampal regions were identified on each image. The dentate gyrus (DG) was outlined in a dotted black line. Scale bar, 100µm.

We observed no gross structural differences in the hippocampus at P0 in either mutant mouse line.

In summary, we generated two mouse models to tease out the involvement of the excitatory and inhibitory neurons in the phenotype of ATR-X syndrome. We found that both AtrxVgKO and AtrxVtKO mice died at birth or shortly after birth with no apparent cause.

4.3 Cortical layer lamination is not affected by *Atrx* deletion in excitatory neurons

The first mouse model we examined was the *Atrx*; *Vglut2*-Cre mice. Although we did not observe any obvious differences in brain size, we wanted to determine whether AtrxVgKO mice had cortical abnormalities. We used P0 coronal sections to perform IF staining using Satb2, Ctip2 and Tbr1 antibodies to label layer II-V, V and VI neurons, respectively (Figure 4.4). We counted three identical regions within one side of the cortex from each animal (n=3 mice/genotype) to get an accurate representation. Each layer marker was quantified within its own layer limits and normalized to the total number of cells. We did not find any change in cortical thickness nor in total number of cells (WT: 557.3 cells ± 8.212; AtrxVgKO 586.0 cells ± 88.16; n=3). Furthermore, we did not find any difference in the percentage of Satb2+ (WT: 36.44% ± 1.000; AtrxVgKO% 34.15 ± 1.396; n=3), Ctip2+ (WT: 9.767% ± 0.6566; AtrxVgKO 9.273% ± 1.032; n=3) and Tbr1+ cells (WT: 31.34% ± 1.467; AtrxVgKO 30.73% ± 1.506; n=3). We also noted that the signal of Tbr1 in layer VI was fainter in AtrxVgKO mice and that there were cells strongly expressing Ctip2 in layer VI. This could be the result of cells not switching the expression of Ctip2 for Tbr1 in layer VI [28].

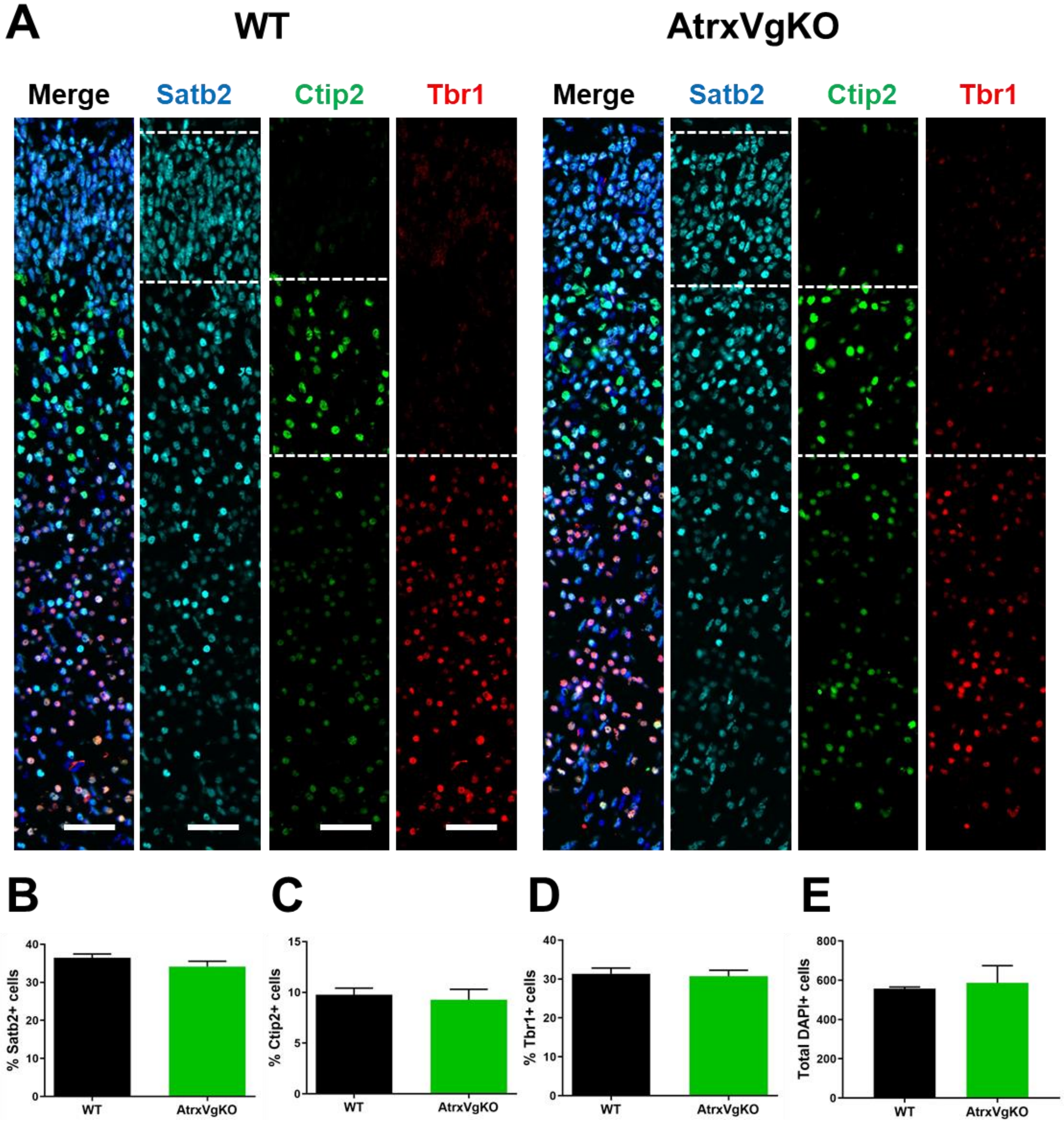

Figure 4.4: *Atrx* deletion in excitatory neurons does not impact the cortical layers

A P0 coronal sections were used for immunofluorescence staining. Satb2 (cyan), Ctip2 (green) and Tbr1 (red) antibody staining are shown with nuclei counterstained with DAPI (Blue) were used to label layer II-V, layer V and layer VI neurons, respectively. Quantification of marker positive cells for **B** Satb2, **C** CTIP2, **D** Tbr1 and **E** DAPI. Scale bar, 50µm. Data represent mean ± SEM. n=3.

These results suggest that *Atrx* deletion in excitatory neurons does not significantly influence cortical lamination although some fate changes may be occurring given the reduced expression level of Tbr1 and increased expression of Ctip2 within layer VI.

4.4 *Atrx* deletion in excitatory neurons leads to a reduction in mature neurons in some hippocampal regions

As previously shown in section 4.2, the hippocampus of AtrxVgKO mice had morphological defects. Briefly, we saw a shortened CA1 region and a thinner CA3 region. Here, we determined whether the hippocampal neurons were affected by *Atrx* deletion in excitatory neurons. We used IF staining to visualise and quantify the number of mature neurons in different hippocampal regions, namely CA1, CA3 and DG (Figure 4.5). Firstly, we examined the total number of cells in each region and we found no difference (WT: CA1 815.250 cells ± 116.102, CA3 842.750 cells ± 39.926, DG 1292 cells ± 121.269; AtrxVgKO: CA1 797.500 cells ± 159.652, CA3 823.750 cells ± 122.395, DG 968.250 cells ± 165.853; n=4). Also, the overall size of the hippocampi was comparable. Next, we quantified the number of mature neurons using the NeuN marker. We found that the percentage of NeuN+ cells in CA1 and CA3 were significantly reduced in AtrxVgKO mice (WT: CA1 44.803% ± 1.369, CA3 60.638% ± 2.700, DG 70.973% ± 3.269; AtrxVgKO: CA1 21.195% ± 1.657, CA3 46.515% ± 4.418, DG 64.615% ± 2.597; n=4). In the CA3 region of AtrxVgKO mice, there was only a small line of positive cells on the outside edge. However, the magnification of this region showed us that multiple cells expressed the marker but had a fainter signal. We also saw this characteristic in the CA1 region.

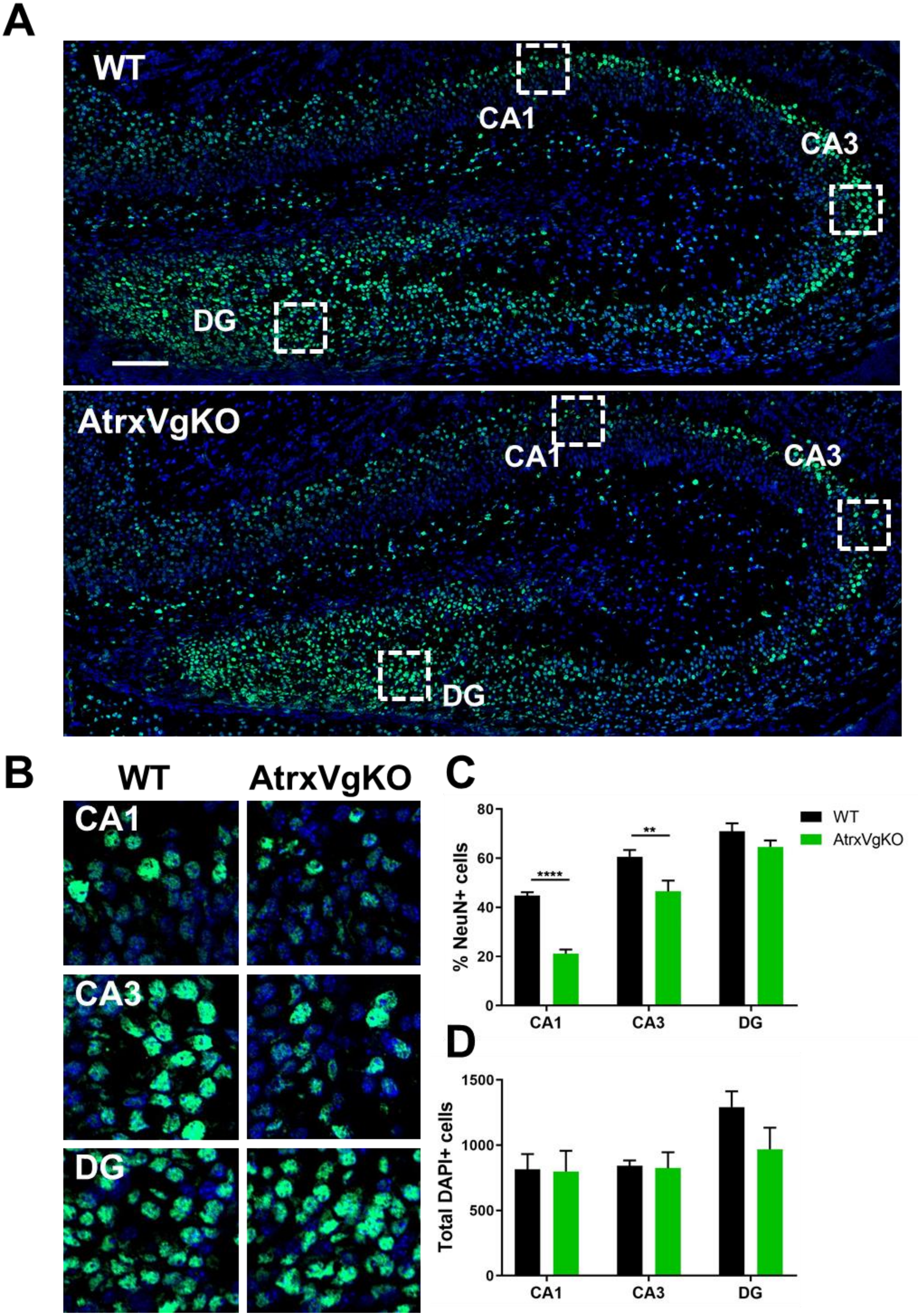
A
WT
CA1
CA3
DG
AtrxVgKO
CA1
CA3
DG
B
WT
AtrxVgKO
CA1
CA3
DG
C
% NeuN+ cells
80
60
40
20
0
****
**
CA1
CA3
DG
WT
AtrxVgKO
D
Total DAPI+ cells
1500
1000
500
0
CA1
CA3
DG

Figure 4.5: AtrxVgKO mice have less neurons in some hippocampal regions

A P0 coronal sections were immunostained for mature neurons using a NeuN (green) antibody and nuclei were counterstained with DAPI (blue). **B** Magnified images of CA1, CA3 and DG (white squares) of WT and AtrxVgKO are shown. **C** Percentage of NeuN+ cells and **D** Number of DAPI+ cells were assessed. Scale bar, 100µm. Data represent means ± SEM. $n=4$. ** $p < 0.01$, **** $p < 0.0001$.

Interestingly, there was no effect of *Atrx* deletion in excitatory cells on the number of mature neurons in the DG. These results were consistent with our previous observations (Figure 4.3 middle).

Lastly, we decided to examine the number of intermediate progenitors. We used P0 coronal sections that we stained using Tbr2 (Figure 4.6A). We saw no difference in the overall shape of the DG and location of the Tbr2+ cells. Upon quantification, we found no change in the number of intermediate progenitors (WT: 210.3 cells ± 8.090; AtrxVgKO: 212.0 cells ± 11.59; n=4) (Figure 4.6B).

Taken together, these results suggested that *Atrx* was needed in glutamatergic cells to generate mature neurons in CA1 and CA3 hippocampal regions. Since there is a similar number of cells within those regions and that we can see a faint NeuN signal, it is possible that these cells are taking longer to differentiate into mature neurons. Also, *Atrx* ablation in excitatory cells did not impact the progenitor pool at P0.

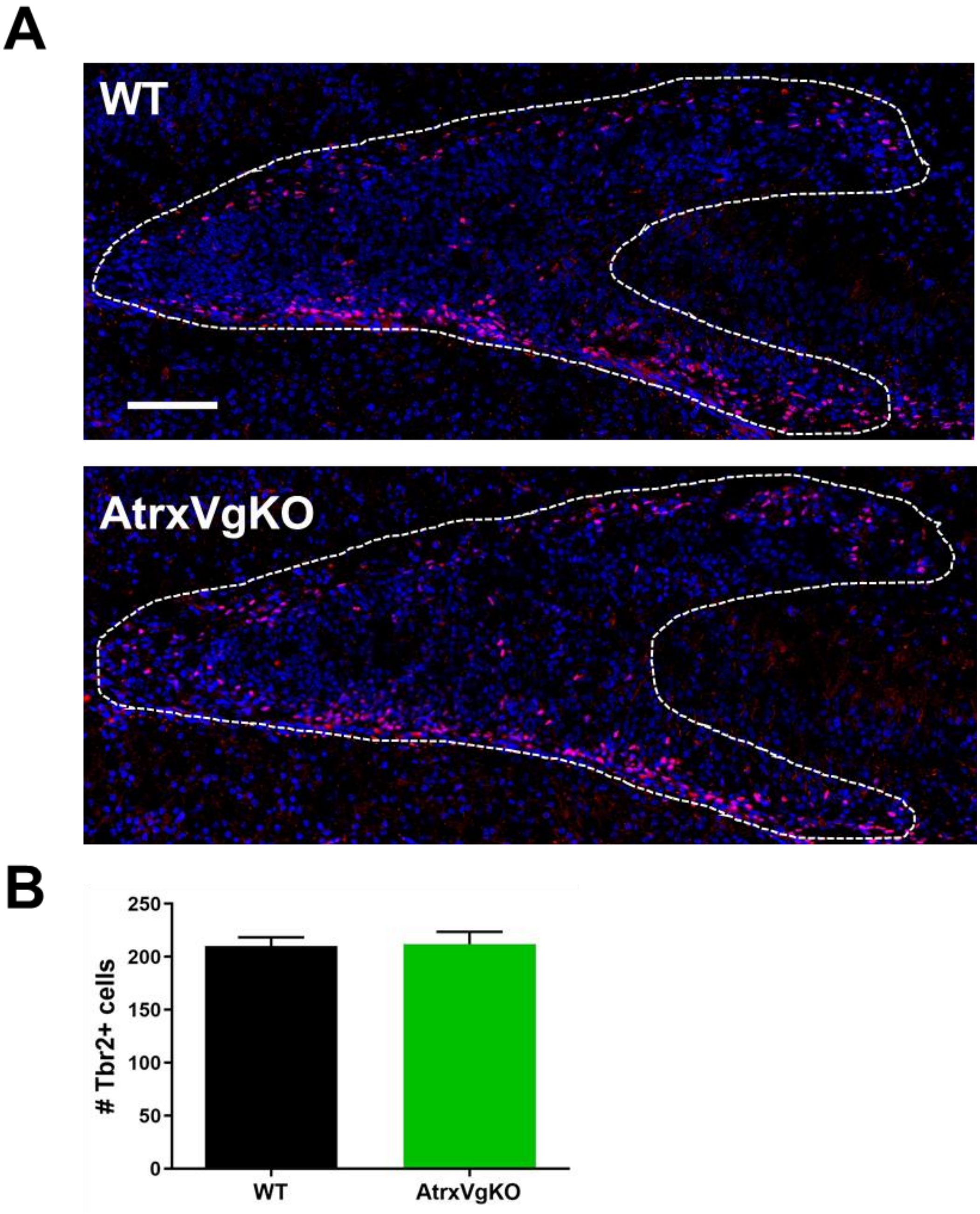

Figure 4.6: AtrxVgKO mice have normal number of intermediate progenitors in the DG

A IF staining was performed on P0 coronal sections using a Tbr2 (red) antibody and counterstained with DAPI (blue). DG (outlined in white) of WT and AtrxVgKO are shown. **B** Number of Tbr2+ cells was assessed. Scale bar, 200µm. Data represent means ± SEM. n=4.

4.5 AtrxVtKO mice show no defect in cortical lamination

The following sections of this chapter were performed using the *Atrx*; *Viaat*-Cre mice. Here, we wanted to determine the outcome of deleting *Atrx* in inhibitory neurons. We analyzed the cortical layers using P0 coronal brain sections. We did IF staining and labeled layer II-V, V and VI using Satb2, Ctip2 and Tbr1antibodies, respectively (Figure 4.7). The quantification was done as previously mentioned in section 4.3. We found no change in the percentage of Satb2+ (WT: 35.60% ± 2.329; AtrxVgKO 31.68% ± 1.002; n=3), Ctip2+ (WT: 8.767% ± 1.136; AtrxVgKO 8.343% ± 0.7831; n=3) and Tbr1+ cells (WT: 28.57% ± 2.768; AtrxVgKO 26.19% ± 1.933; n=3) when we compared the WT to the AtrxVtKO mice. Also, we found no difference in the total number of cell nuclei (WT: 538.0 cells ± 10.44; AtrxVgKO 534.3 cells ± 29.61; n=3) and cortical thickness. Of note, we also compared the total number of cells of AtrxVtKO with AtrxVgKO mice and found no difference.

These results suggest that cortical lamination was not affected by *Atrx* deletion in inhibitory neurons.

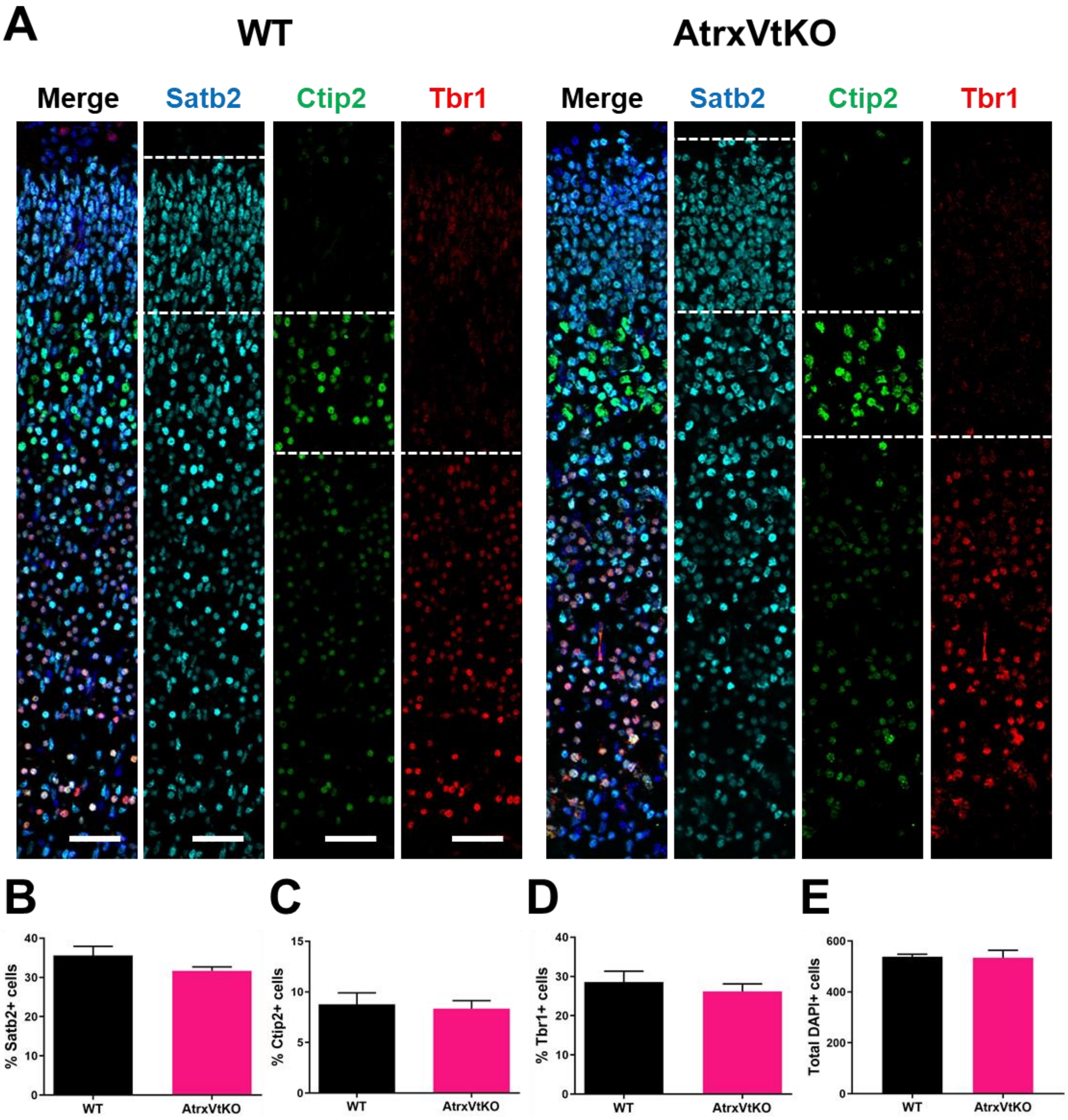

<u>**Figure 4.7: AtrxVtKO have no cortical lamination defects**</u>

A P0 coronal sections were used to perform immunofluorescence staining. Satb2 (cyan), CTIP2 (green) and Tbr1 (red) were used to label layer II-V, layer V and layer VI respectively. Quantification of **B** Satb2, **C** CTIP2, **D** Tbr1, and **E** DAPI+ cells. Scale bar, 50µm. Data represent means ± SEM. n=3.

4.6 AtrxVtKO mice have more mature neurons in the CA3 hippocampal region

Previous *Atrx* knockout mouse models have shown hippocampal defects [205]. Also, *Mecp2* deletion in inhibitory neurons leads to hippocampal learning and memory impairments [237]. Therefore, we examined the hippocampus of AtrxVtKO mice. We used P0 coronal sections to perform IF staining using the mature neuron marker NeuN, which was quantified in each hippocampal region (Figure 4.8). First, we found no change in the total number of cells (WT: CA1 559.250 cells ± 62.324, CA3 636.750 cells ± 94.491, DG 1060 cells ± 123.544; AtrxVtKO: CA1 539.500 cells ± 27.536, CA3 618.500 cells ± 51.741, DG 1100.500 cells ± 47.174; n=4). Interestingly, we found that the CA3 region had more mature neurons in AtrxVtKO mice (WT: CA1 46.355% ± 1.889, CA3 69.755% ± 1.211, DG 67.050% ± 3.727; AtrxVtKO: CA1 44.978% ± 3.794, CA3 85.768% ± 2.132, DG 69.150% ± 2.157; n=4). Contrary to the phenotype observed in AtrxVgKO, we saw no difference in the signal intensity and location of NeuN-stained cells in AtrxVtKO mice.

We continued the assessment of the hippocampus by assessing the number of progenitors in the DG. We performed IF staining on P0 coronal section using Pax6 and Tbr2 to label radial glial and intermediate progenitors respectively (Figure 4.9). We outlined the DG and quantified the number of positive cells within the region of interest. We found that AtrxVtKO mice had more Pax6+ and Tbr2+ cells in comparison to WT mice (Pax6: WT: 519.6 cells ± 48.98; AtrxVtKO: 683.0 cells ± 50.46; n=5) (Tbr2: WT: 213.3 cells ± 35.37; AtrxVtKO: 326.3 cells ± 17.38; n=5). Furthermore, we noticed that the progenitors were aggregating at the bottom blade of the DG.

Thus, *Atrx* deletion in inhibitory neurons caused an increase in the progenitor pool and percentage of mature neurons in the CA3 region.

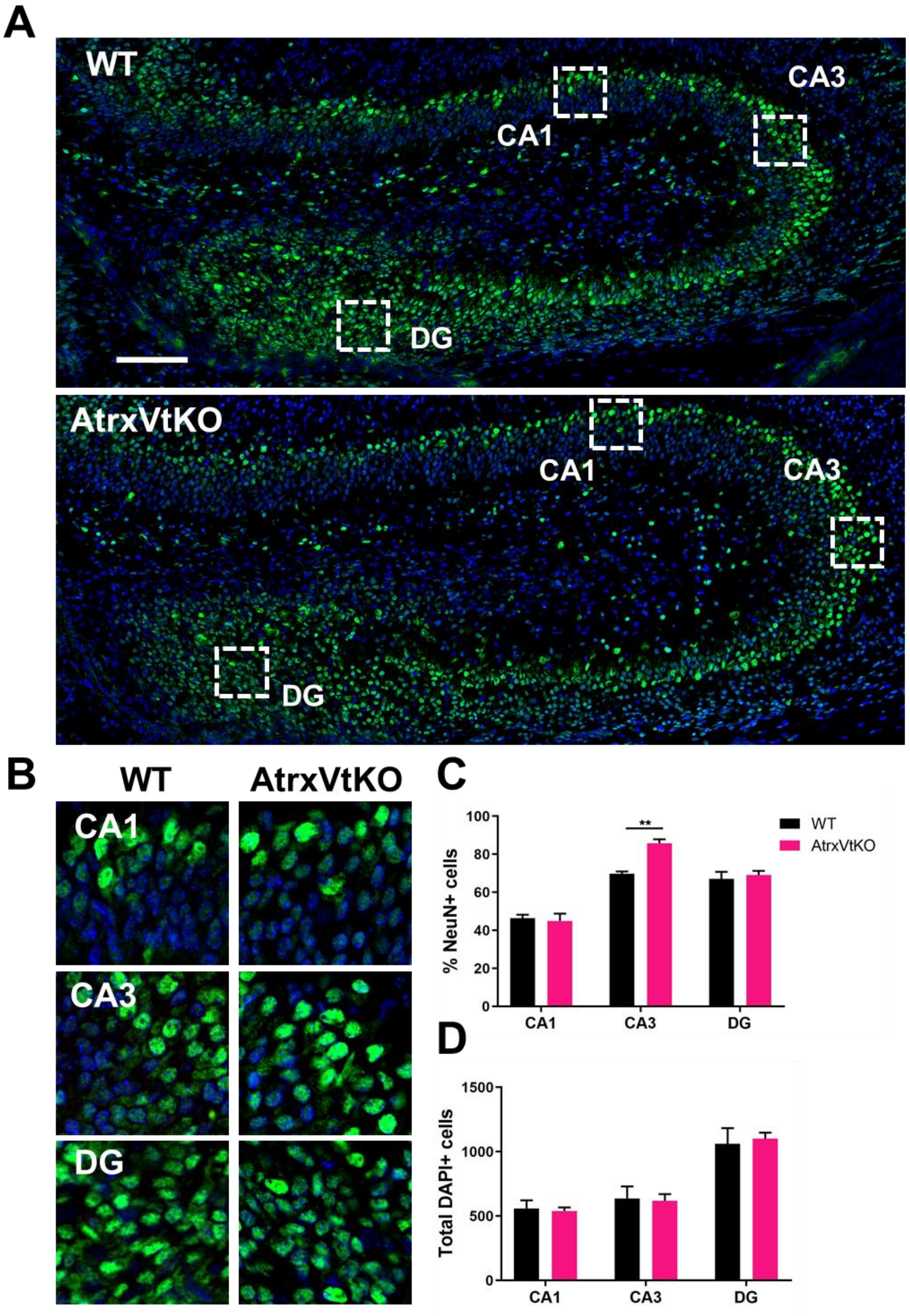
A
WT
CA1
CA3
DG
AtrxVtKO
CA1
CA3
DG
B
WT
AtrxVtKO
CA1
CA3
DG
C
% NeuN+ cells
100
80
60
40
20
0
**
WT
AtrxVtKO
CA1
CA3
DG
D
Total DAPI+ cells
1500
1000
500
0
CA1
CA3
DG

Figure 4.8: AtrxVtKO mice have more mature neurons in CA3 region

A P0 coronal sections were used to perform IF staining using NeuN (green) and DAPI (blue). **B** Magnified images of CA1, CA3 and DG (white squares) of WT and AtrxVtKO are shown. **C** Percentage of NeuN+ cells and **D** Number of DAPI+ cells were assessed. Scale bar, 100µm. Data represent means ± SEM. n=4. ** $p < 0.01$.

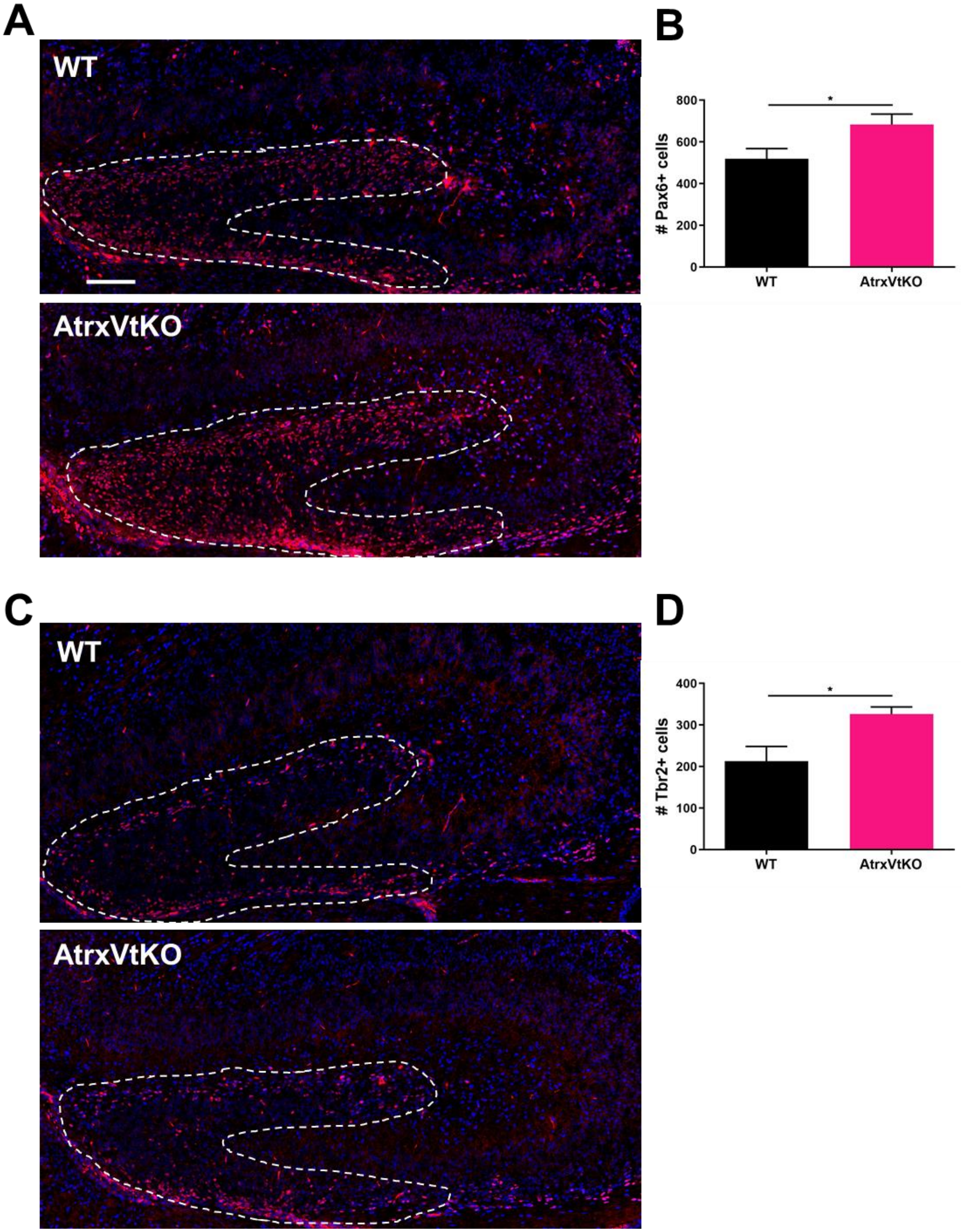
A
WT
AtrxVtKO
B
Pax6+ cells
800
600
400
200
0
*
WT
AtrxVtKO
C
WT
AtrxVtKO
D
Tbr2+ cells
400
300
200
100
0
*
WT
AtrxVtKO

Figure 4.9: AtrxVtKO mice have more progenitors in the hippocampus

P0 coronal sections were used to perform IF staining using **A** Pax6 (red), **C** Tbr2 (red) and DAPI (blue). The DG of WT and AtrxVtKO were outlined in white. **B** The number of Pax6+ cells and **D** Tbr2+ were assessed. Scale bar, 100µm. Data represent means ± SEM. n=4. * $p < 0.05$.

4.7 AtrxVtKO mice have defects in the dentate gyrus migratory path

The increase in progenitors observed in P0 AtrxVtKO mice led us to examine the formation of the DG through the DG migratory path. We injected pregnant females with EdU at gestational day 16.5 and collected the embryos one hour later. The fixed embryos were than sectioned and stained using Pax6 and EdU to label actively proliferating progenitors. The DG migratory path was divided into three sections, namely Matrix 1, Matrix 2 and Matrix 3. We quantified the percentage of Pax6+, EdU+ and double-labeled cells in each Matrix (Figure 4.10). First, we found that the percentage of Pax6+ cells in Matrix 1 and 2 were significantly lower in AtrxVtKO mice (WT: M1 94.940% ± 0.545, M2 60.800% ± 2.188, M3 55.530% ± 5.250; AtrxVtKO: M1 77.442% ± 1.910, M2 40.368% ± 1.445, M3 45.627% ± 3.153; n=5) (Figure 4.10B). We found no change in the percentage of EdU+ cells (WT: M1 35.895% ± 2.751, M2 11.505% ± 1.527, M3 7.335% ± 1.204; AtrxVtKO: M1 36.373% ± 3.002, M2 11.562% ± 0.739, M3 8.447% ± 0.763; n=5) (Figure 4.10C). When we quantified the percentage of Pax6/EdU double+ cells, we found no significant difference between the two groups (WT: M1 92.593% ± 1.620, M2 84.160% ± 3.735, M3 70.893% ± 3.545; AtrxVtKO: M1 90.300% ± 2.097, M2 85.102% ± 2.210, M3 73.297% ± 1.624; n=5) (Figure 4.10D). However, due to the small number of cells in each Matrix, the percentage of double-labeled cells was highly variable. Therefore, we plotted the number of Pax6+EdU+ cells (Figure 4.10E). Interestingly, there was a two-fold increase in the number of Pax6+EdU+ cells in Matrix 2 of AtrxVtKO mice (WT: M1 49.833 cells ± 4.078, M2 23.667 cells ± 1.801, M3 9.167 cells ± 1.579; AtrxVtKO: M1 51.667 cells ± 5.090, M2 39.167 cells ± 3.736, M3 13.000 cells ± 1.461; n=5). Furthermore, we noted that Matrix 2 was larger in AtrxVtKO mice in comparison to the WT.

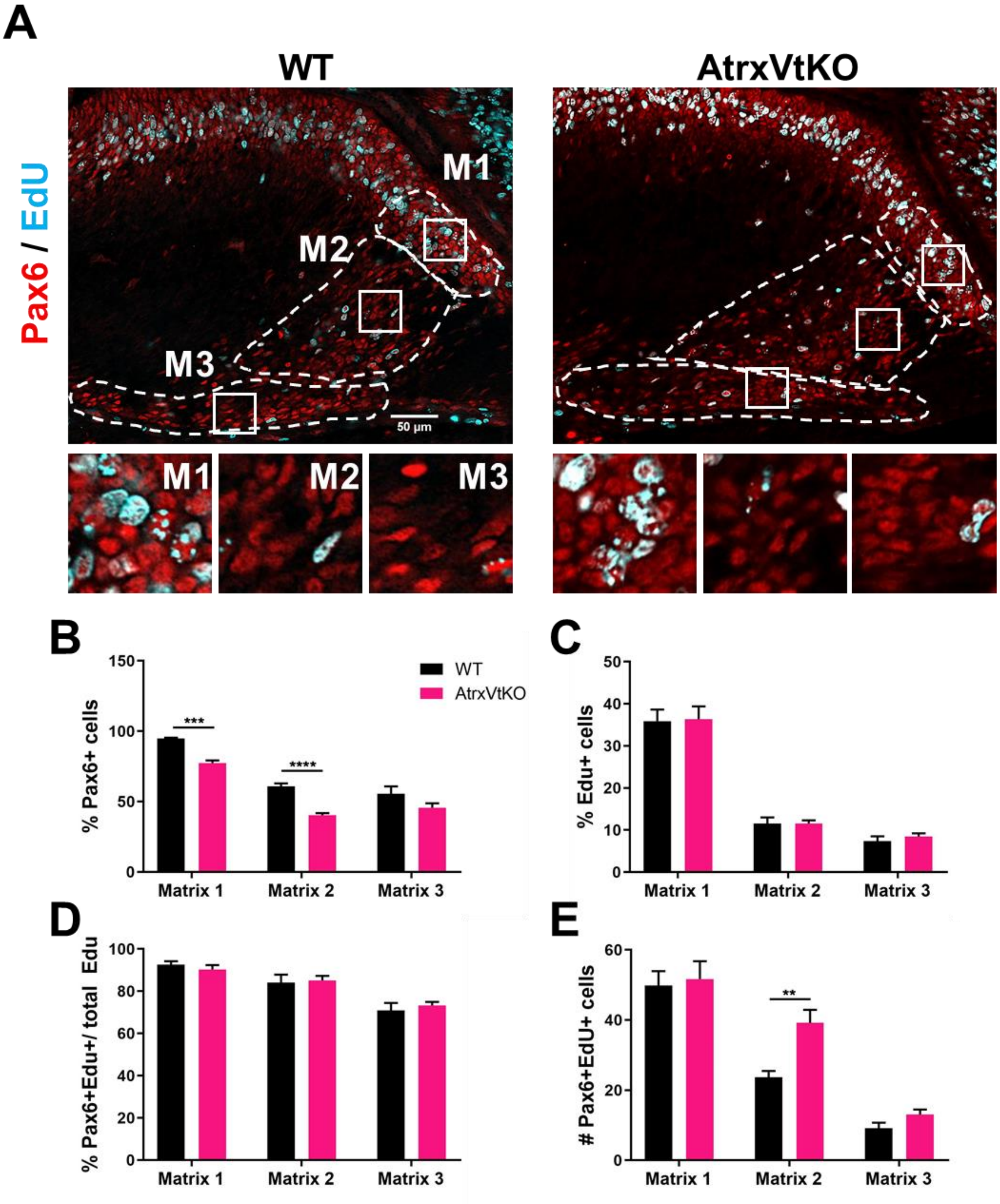
A
WT
AtrxVtKO
Pax6 / EdU
M1
M2
M3
50 µm
M1
M2
M3
B
% Pax6+ cells
150
100
50
0
WT
AtrxVtKO
***
****
Matrix 1
Matrix 2
Matrix 3
C
% Edu+ cells
50
40
30
20
10
0
Matrix 1
Matrix 2
Matrix 3
D
% Pax6+Edu+/ total Edu
100
80
60
40
20
0
Matrix 1
Matrix 2
Matrix 3
E
Pax6+EdU+ cells
60
40
20
0
**
Matrix 1
Matrix 2
Matrix 3

Figure 4.10: AtrxVtKO mice have a less radial glia progenitors in Matrix 1 and 2

Pregnant females were injected with EdU one hour prior to embryo dissection. **A** E16.5 coronal sections were used to perform IF staining using markers for Pax6 (red) and EdU (blue). The location of magnified images of Matrix 1 (M1), Matrix 2 (M2) and Matrix 3 (M3) are shown as white squares. **B** Percentage of Pax6+ cells, **C** EdU+ cells and **D** double-labeled cells were quantified. **E** The number of Pax6+EdU+ cells were assessed. Scale bar, 50µm. Data represent means ± SEM. n=5. ** $p < 0.01$, *** $p < 0.001$, **** $p < 0.0001$.

Next, we wanted to determine whether the intermediate progenitors were affected by *Atrx* deletion in inhibitory neurons. We repeated the same experiment but used Tbr2 to label the intermediate progenitors (Figure 4.11). We found no change in the percentage of Tbr2+ cells (WT: M1 35.904% ± 5.667, M2 45.882% ± 4.695, M3 46.140% ± 4.209; AtrxVtKO: M1 43.620% ± 2.742, M2 54.190% ± 4.211, M3 46.053% ± 2.658; n=5) (Figure 4.11B). Consistent with our previous findings, we showed no difference in the percentage of EdU+ cells (WT: M1 36.774% ± 2.535, M2 11.300% ± 1.491, M3 6.654% ± 1.401; AtrxVtKO: M1 41.258% ± 3.477, M2 12.165% ± 1.556, M3 8.195% ± 1.062; n=5) (Figure 4.11C). The percentage of double-labeled cells were similar in WT and AtrxVtKO mice (WT: M1 26.740% ± 9.819, M2 48.428% ± 3.029, M3 39.078% ± 4.928; AtrxVtKO: M1 38.678% ± 6.691, M2 51.527% ± 5.808, M3 42.385% ± 4.292; n=5) (Figure 4.11D). A high variability in the percentage of double-labeled cells between samples was observed due to the overall low number of Tbr2+EdU+ cells. Thus, we plotted the number of double-labeled cells and we found that AtrxVtKO mice had twice the quantity or number (WT: M1 7.750 cells ± 3.351, M2 6.800 cells ± 0.800, M3 5.000 cells ± 1.378; AtrxVtKO: M1 11.167 cells ± 1.721, M2 12.800 cells ± 1.158, M3 4.333 cells ± 1.116; n=5) (Figure 4.11E).

Taken together, *Atrx* deletion in inhibitory neurons lead to an increase of proliferating radial glia progenitors in Matrix 1 and 2 and intermediate progenitors in Matrix 2. At E16.5, Matrix 3 is not affected by *Atrx* removal. This increase in progenitor cells at E16.5 could account for the increase in progenitor cells observed at P0 (Figure 4.9).

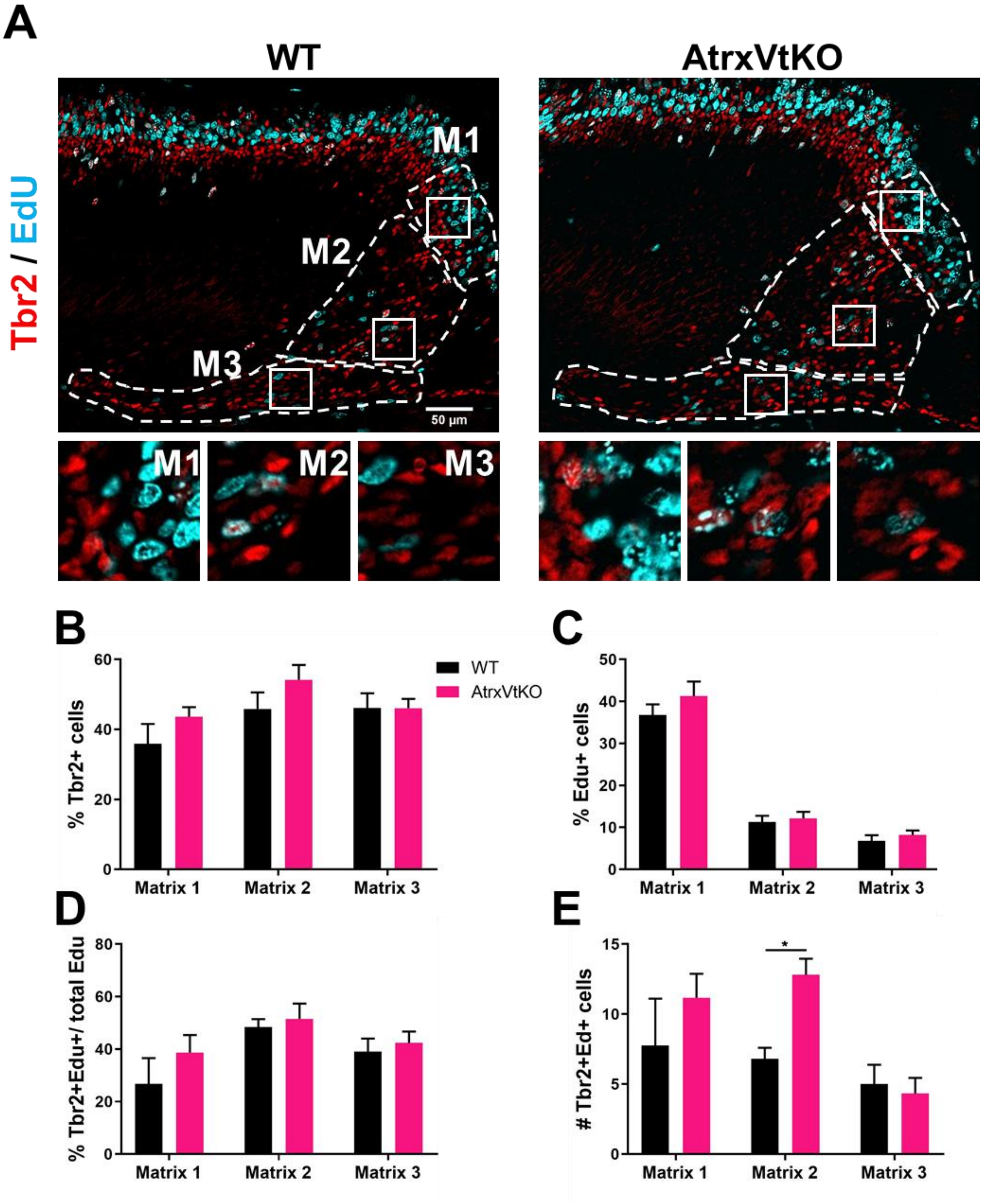
A
WT
AtrxVtKO
Tbr2 / EdU
M1
M2
M3
50 µm
M1
M2
M3
B
% Tbr2+ cells
60
40
20
0
Matrix 1
Matrix 2
Matrix 3
WT
AtrxVtKO
C
% Edu+ cells
50
40
30
20
10
0
Matrix 1
Matrix 2
Matrix 3
D
% Tbr2+Edu+/ total Edu
80
60
40
20
0
Matrix 1
Matrix 2
Matrix 3
E
Tbr2+Ed+ cells
15
10
5
0
*
Matrix 1
Matrix 2
Matrix 3

Figure 4.11: AtrxVtKO mice have more Tbr2+EdU+ cells in Matrix 2

Pregnant females were injected with EdU 1 hour prior to embryo dissection. **A** E16.5 coronal sections were used to perform IF staining using markers for Tbr2 (red) and EdU (blue). The location of magnified images of Matrix 1 (M1), Matrix 2 (M2) and Matrix 3 (M3) are shown as white squares. **B** Percentage of Tbr2+ cells, **C** EdU+ cells and **D** double-labeled cells were quantified. **E** The number of Tbr2+EdU+ cells were assessed. Scale bar, 50µm. Data represent means ± SEM. n=5. * $p < 0.05$.

4.8 Summary of Findings

In summary, we generated two mouse models to examine whether altering the equilibrium between the glutamatergic and GABAergic neurons recreates the pathogenesis of ATR-X syndrome. We used the *Atrx*; *Vglut2*-Cre to target *Atrx* loss in the excitatory neurons and *Atrx*; *Viaat*-Cre for *Atrx* excision in the inhibitory neurons. Upon breeding these two mouse lines, we found that both KOs were dying embryonically or at early postnatal ages. We saw no obvious cause of death for either AtrxVgKO or AtrxVtKO mice. Although the gross morphology of the whole brains was not different from WT mice, we found that both AtrxVgKO and AtrxVtKO mice had morphological defects in the hippocampus.

Surprisingly, we found no change in the cortical thickness and lamination of AtrxVgKO and AtrVtKO mice as was observed in other Atrx cKO mutants [205]. We examined the hippocampus of AtrxVgKO mice and found that the CA1 and CA3 regions had a reduction in mature neurons. Interestingly, the total number of cells in all the hippocampal regions were unchanged, indicating that further studies are required to define the fate of these cells. Furthermore, we found no difference in the number of intermediate progenitors in the DG of AtrxVgKO mice.

The hippocampal analysis of AtrxVtKO mice revealed an increase in the number of mature neurons in the CA3 region. We quantified the number of progenitors in the DG at P0 and found that both radial glial and intermediate progenitors were increased. However, the overall number of DG cells were unchanged. Further work is required to identify the cell type that is reduced in the DG. Next, we wanted to determine whether the defect originated from the proliferation or migration of progenitors in the dentate gyrus migratory path. We found less radial glial progenitors in Matrix 1 and 2 and the percentage of Pax6+EdU+ cells in Matrix 2 was significantly lower in AtrxVtKO mice. Although we found no change in the intermediate progenitors, we found that the percentage or EdU+Tbr2+ cells in Matrix 2 was higher in AtrxVtKO mice.

Chapter 5: Characterization of the forebrain-specific Atrx knockout mouse

5.1 Introduction and rational

Over the years, multiple *Atrx* mutant models have been generated to elucidate the function of Atrx in various contexts. Biochemical studies and characterization of *Atrx*-null mice have shown it is critical for the expansion of the neuroprogenitor pool [205]. Studies in the retina identified a post-mitotic role for Atrx as bipolar neurons show impaired axonal targeting and non-cell-autonomous effects on the survival of interconnected neurons [211]. Recently, *Atrx* inactivation in forebrain pyramidal neurons showed synaptic ultrastructural defects and male-specific memory deficits [213]. While these studies have helped clarify *Atrx* function, individually they do not represent strong models of the ATR-X syndrome.

Global and forebrain-specific deletion of *Atrx* as well as excitatory and inhibitory neurons cKOs resulted in embryonic and early postnatal lethality [205] (see Chapter 4), precluding the study of ATRX in postmitotic cells. To avoid this limitation, we generated a conditional *Atrx* knockout using the *Emx1*-Cre transgenic mouse line. Previous studies using *Emx1*-Cre driver showed milder progenitor expansion deficits with other chromatin remodeler knockouts, while maintaining widespread activity in developing excitatory neurons of the cortex and hippocampus. Here, we dissected the function of *Atrx* in the developing brain to provide a better understanding of the development of intellectual disabilities in ATR-X syndrome.

5.2 Generation and initial characterization of *Atrx*; *Emx1*-Cre mice

We generated the *Atrx*; *Emx1*-Cre mice by breeding the *Atrx*$^{fl/fl}$ mice with the *Emx1*-Cre mice. The *Atrx*$^{fl/fl}$ mice have two loxp sites flanking exon 18 of the *Atrx* gene, which correspond to the first of the 7 SNF2-like motifs of the ATPase domain (Figure 5.1A) [152, 205].

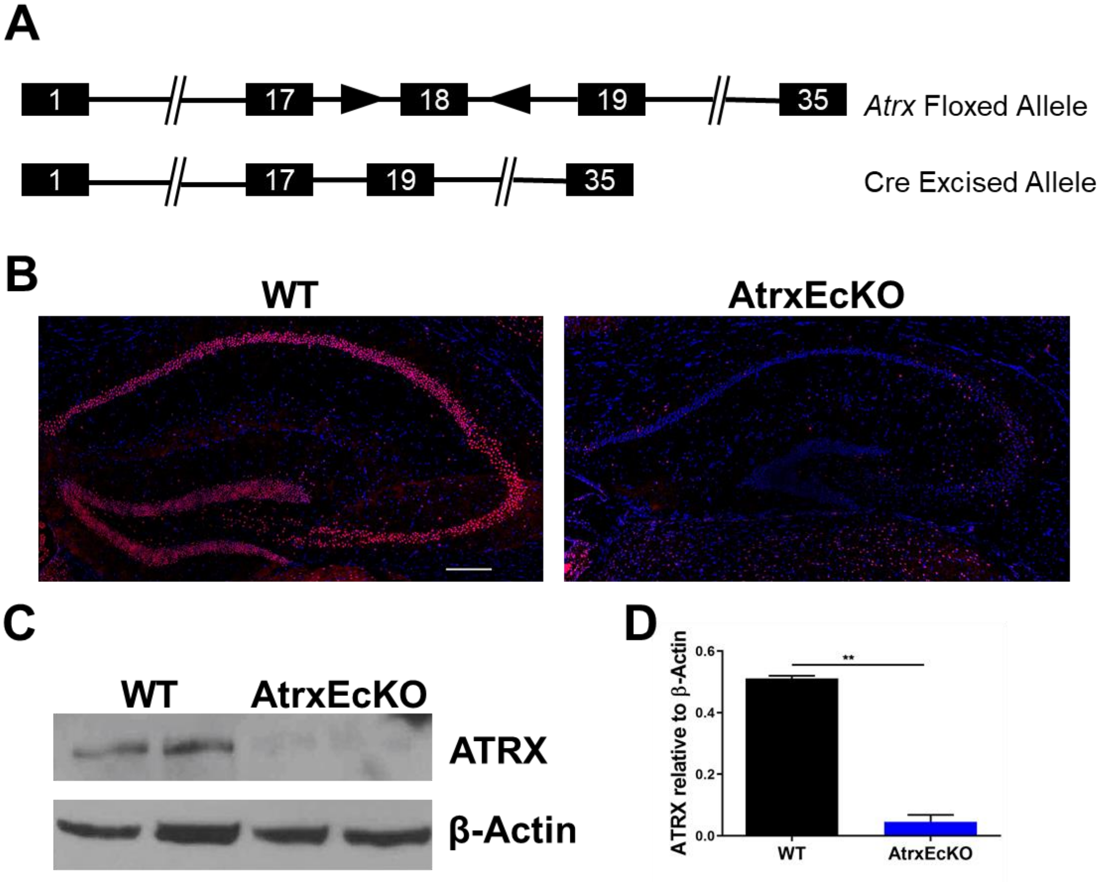

<u>Figure 5.1: Characterization of *Atrx*; *Emx1*-Cre mice</u>

A Schematic of the *Atrx* floxed allele and the *Cre* excised allele. **B** P60 coronal sections were used to do IF staining using Atrx (red) and DAPI (blue). **C** Atrx levels were assessed from cortical protein lysates by western blot analysis and **D** quantified. Scale bar, 200μm. Data represent means ± SEM. n=4. ** p < 0.01.

In the presence of Cre recombinase, the excision of exon 18 removes the ATP-binding pocket rendering the ATPase domain inactive. Also, it creates a reading frame shift leading to an unstable transcript that presumably undergoes nonsense mediated decay. We bred the *Atrx*$^{fl/fl}$ mice to the second mouse line, *Emx1*-Cre$^{+/-}$ mice, where the expression of Cre recombinase is driven by the *Emx1* promoter. We chose this forebrain-specific promoter due to its later expression (E10.5) [238], in comparison to *Foxg1* (E8.5) [267] and *Nestin* (E7.5) Cre driver lines [235], to potentially avoid inactivation of *Atrx* during peak progenitor proliferation that would result in perinatal lethality. We successfully generated a viable mouse line and confirmed the deletion of *Atrx* in AtrxEcKO male mice using immunofluorescence staining (Figure 5.1B). All studies compared male mice of WT and AtrxEcKO genotypes. We used P60 coronal sections of WT and AtrxEcKO hippocampi and we observed a striking reduction in *Atrx* expression in AtrxEcKO mice. Also, we extracted proteins from P60 cortices to quantify protein levels using immunoblotting (Figure 5.1C-D). We found that the *Atrx* levels in AtrxEcKO mice were significantly reduced in comparison to the WT (WT: 0.5106 ± 0.009; AtrxEcKO 0.04564 ± 0.02263; n=4). Next, we compared the body weight of AtrxEcKO mice to WT mice at P0 and found no significant difference (WT: 1.450g ± 0.05; AtrxEcKO 1.333g ± 0.08; n=10) (Figure 5.2A). We also did the comparison at P90 and found that AtrxEcKO mice are smaller than the WT mice (WT: 28.57g ± 0.5112; AtrxEcKO 23.76g ± 0.5686; n=10) (Figure 5.2B-C). We found that the brain width of AtrxEcKO mice at P90 was significantly smaller than the WT (WT: 10.71mm ± 0.08544; AtrxEcKO 9.390mm ± 0.0100; n=10) (Figure 5.2D). We sectioned the brains of both genotypes sagittally and observed that the size of the hippocampus was reduced in AtrxEcKO mice (Figure 5.2E dotted line).

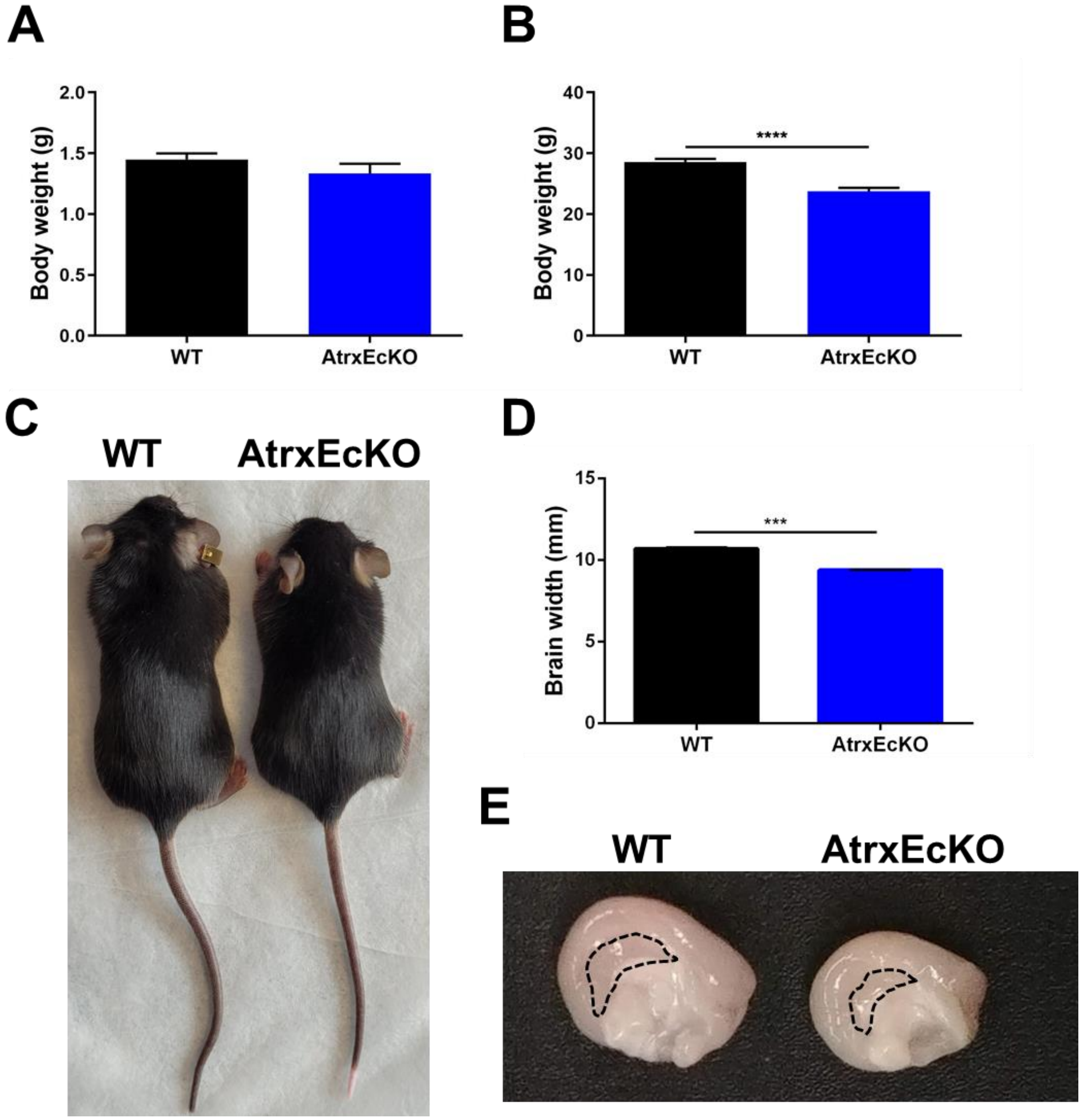

Figure 5.2: Morphology analysis of AtrxEcKO mice

The body weight of WT and AtrxEcKO mice was measured at **A** P0 and **B** P90. **C** Picture of P90 WT (left) and AtrxEcKO (right) mice. **D** Brain width was measured on P90 brains. **E** P90 sagittal sections exposing the hippocampus (dotted lines). Data represent means ± SEM. n=10. *** $p < 0.001$, **** $p < 0.0001$.

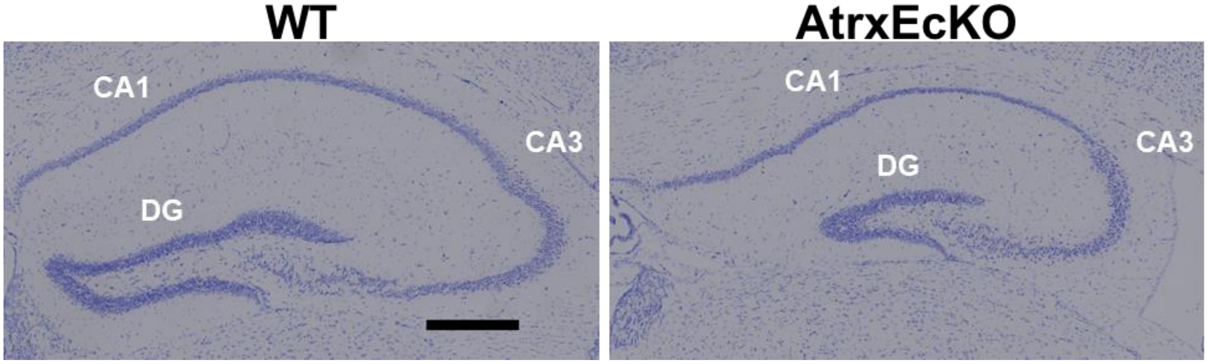

Figure 5.3: AtrxEcKO mice have severe structural defects in the hippocampus

Nissl stain was performed on P40 WT (left) and AtrxEcKO (right) coronal sections. Hippocampal regions (CA1, CA3 and dentate gyrus (DG)) are shown. Scale bars represent 300µm.

Subsequently, we performed a Nissl stain using brain sections of P40 animals to better visualize the hippocampi (Figure 5.3). We noted that AtrxEcKO mice had a striking reduction in the overall size of the hippocampus in comparison to the WT mice and we observed a reduction in the length of the DG. Thus, forebrain-specific Atrx ablation leads to structural defects in the hippocampus.

We collaborated with Dr. Binnaz Yalcin from the University of Bourgogne in France to perform a volumetric analysis to confirm the reduction of the hippocampus and examine other brain areas (Figure 5.4). Briefly, we extracted, fixed and sectioned the brains of 16-week old WT and AtrxEcKO mice. The sagittal sections were double-stained using Luxol fast blue to label myelin and Cresyl violet for neurons. Lastly, images were taken at the cell-level resolution and analyzed through Image J. First, the total brain area, brain height and brain width were not significantly different in AtrxEcKO mice in comparison to the WT mice (Figure 5.4A). The area of the temporal cortex was larger and the length of the secondary motor cortex was smaller in AtrxEcKO mice. Further, we confirmed that the area of the hippocampus was significantly reduced in AtrxEcKO as well as other hippocampus parameters such as the area and length of the pyramidal layer, and area and length of the granule layer of the DG (Figure 5.4B-C). We also found that the area of the stria medullaris and the anterior commissure were significantly increased in the AtrxEcKO brains. These regions are white matter tracks that relay information from the forebrain, more specifically the frontal, septal, striatal and hypothalamic areas, to the habenula, which is crucial for integrating motor, cognitive, emotional and sensory processing [268-270].

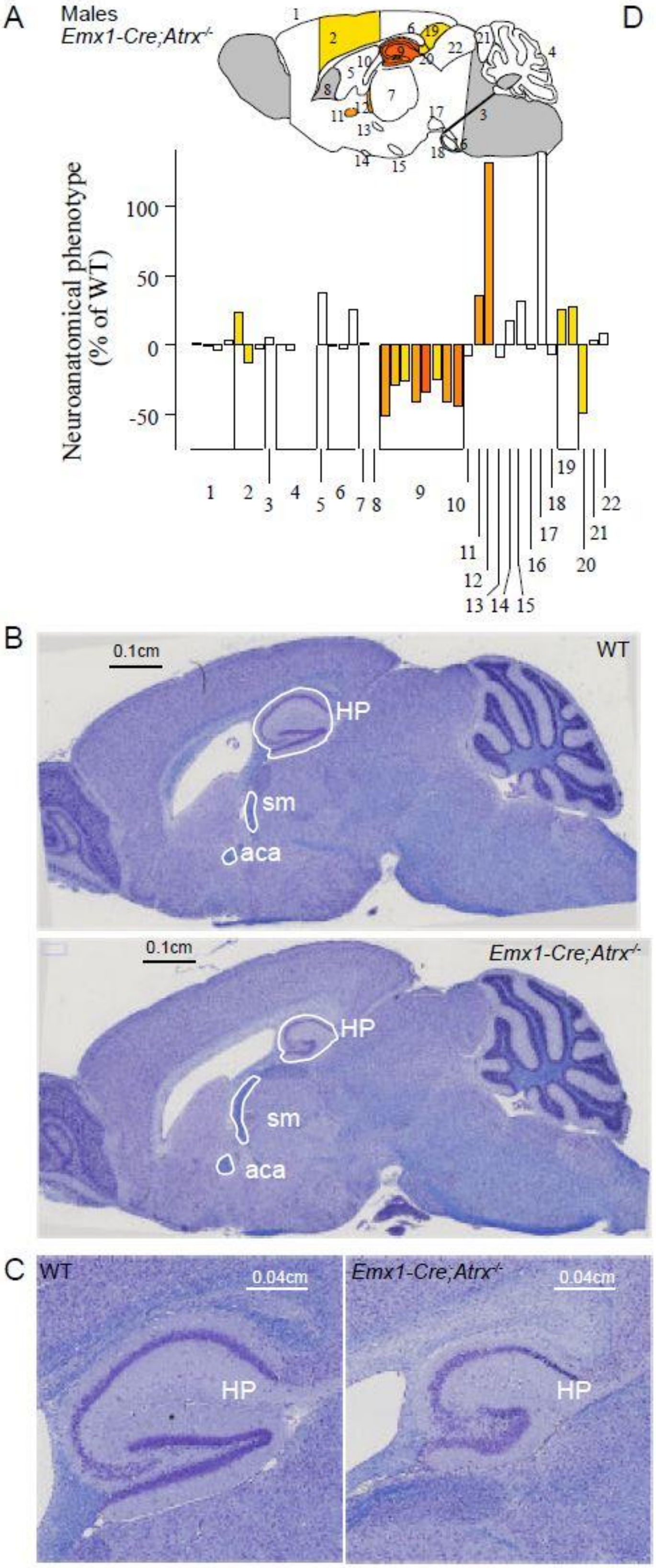

D

Areas and lengths

1	total brain - area
	brain - width
	brain - height 1
	brain - height 2
2	temporal cortex - area
	secondary motor cortex - length
	primary motor cortex - length
3	pons - height
4	cerebellum - area
	internal granule layer - area
	number of folia
	medial cerebellar nucleus - area
5	lateral ventricle - area
6	corpus callosum - area
	corpus callosum - length
	corpus callosum - height
7	thalamus - area
	caudate putamen - area
8	hippocampus - area
9	radiatum layer of the hippocampus - length
	oriens layer of the hippocampus - length
	pyramidal layers - area
	pyramidal layers - length
	lacunosum moleculare layer - length
	granule cell layer of dentate gyrus - area
	granule cell layer of dentate gyrus - length
10	Fimbria of the hippocampus - area
11	anterior commissure - area
12	stria medullaris - area
13	fornix - area
14	optic chiasm - area
15	ventromedial hypothalamus nucleus - area
16	pontine nuclei - area
17	substantia nigra - area
18	transverse fibers of the pons - area
19	cingulate cortex, area 29a - area
	cingulate cortex, area 29a - height
20	dorsal subiculum - area
21	inferior colliculus - area
22	superior colliculus - area

Figure 5.4: Neuroanatomical analysis of AtrxEcKO mice

WT and AtrxEcKO brains sections from 16-week old mice were stained using Luxol fast blue and Cresyl violet. **A** Schematic showing the sagittal section separated into 22 regions. Each analyzed parameter is shown as a percentage of the WT on the graph. **B** Sagittal sections of WT (top) and AtrxEcKO (bottom) showing the hippocampus (HP), stria medullaris (sm) and anterior commissure (aca). **C** Magnification of the hippocampus of WT (left) and AtrxEcKO (right) mice. **D** List of the 40 brain morphological parameters that were measured. Scale bars represent **B** 0.1cm and **C** 0.04cm.

Taken together, *Atrx* deletion in the forebrain causes severe morphological defects of the hippocampus and affects the tracks that relay and process critical information to different brain regions.

Lastly, previous *Atrx* conditional KO mouse models showed a reduction in cortical thickness associated with a disruption of the cortical layers [205]. Here, we wanted to determine whether this phenotype was present in AtrxEcKO mice. We performed IF staining on P0 coronal sections of WT and AtrxEcKO mice using Satb2, Ctip2 and Tbr1 to label layer II-III, layer IV and layer VI, respectively (Figure 5.5A). We found no significant difference in the percentage of Satb2+ cells (WT: 28.22% ± 2.327; AtrxEcKO 27.58% ± 1.855; n=4) (Figure 5.5B). We quantified the percentage of Ctip2+ cells and found a ~5% increase in AtrxEcKO mice (WT: 10.90% ± 0.5485; AtrxEcKO 15.27% ± 0.9427; n=4) (Figure 5.5C). The Ctip2+ cells of AtrxEcKO mice located near the layer VI delimitation appeared smaller in size compared to the Ctip2 population located near layer III. Furthermore, these positive cells expressed both the Ctip2 and Tbr1 markers. We did not observe any change in the percentage of Tbr1+ cells (WT: 30.49% ± 1.219; AtrxEcKO 26.84% ± 1.661; n=4) (Figure 5.5D) and total number of cells (WT: 522.5 cells ± 37.53; AtrxEcKO 470.4 cells ± 25.85; n=4) (Figure 5.5E). Thus, Atrx deletion using the *Emx1* Cre driver does not affect the cortical thickness but rather increases the layer VI population.

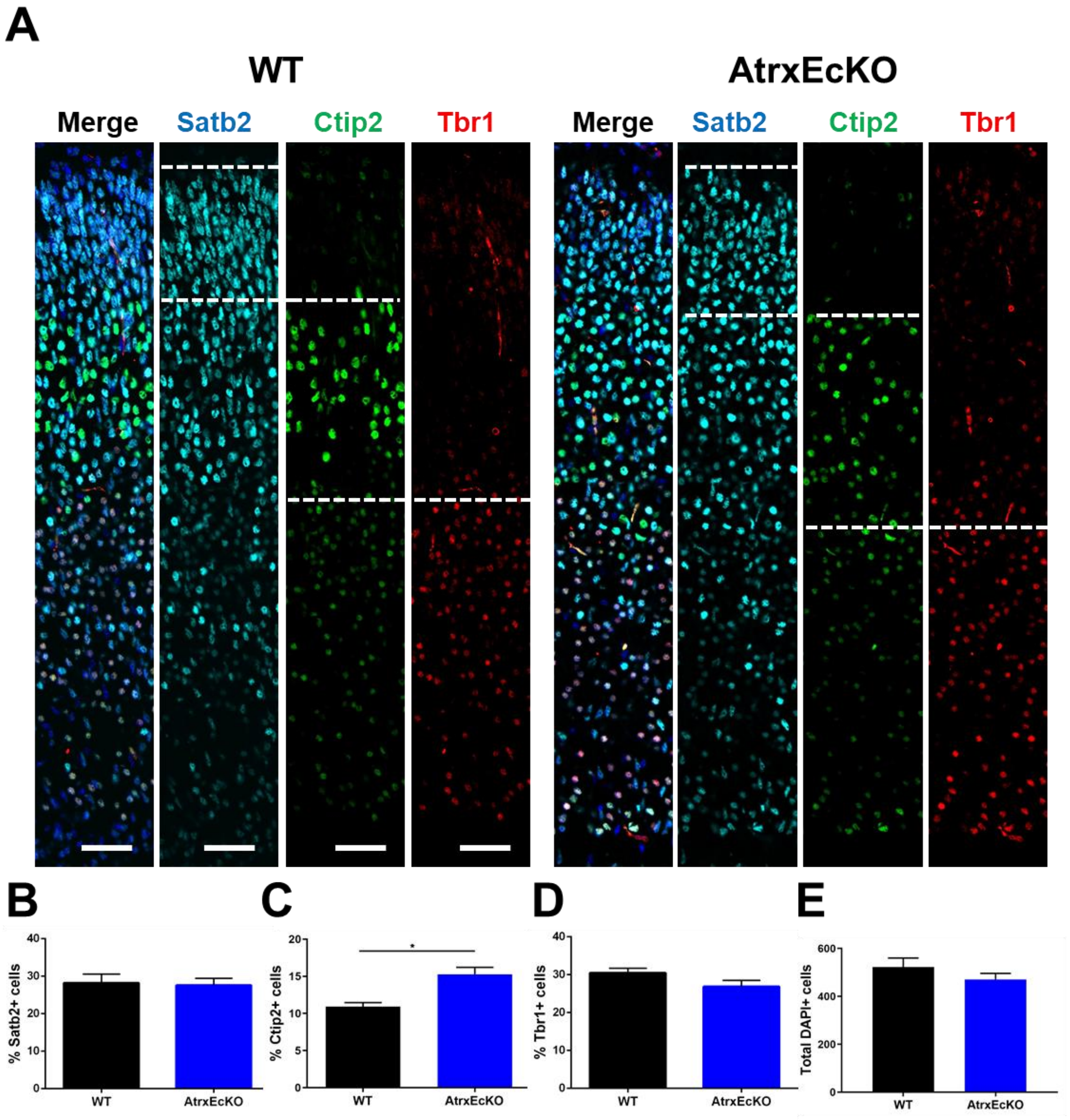

Figure 5.5: AtrxEcKO mice have more Ctip2+ cells

A P0 coronal sections were used to do immunofluorescence staining. Satb2 (blue), Ctip2 (green) and Tbr1 (red) were used to label layer II-IV, layer V and layer VI respectively. Quantification of **B** Satb2, **C** Ctip2, **D** Tbr1 and **E** DAPI are shown. Scale bar, 50µm. Data represent means ± SEM. n=3. * $p < 0.05$.

5.3 AtrxEcKO mice have myelination defects

A study used MRI and CT scans of ATR-X patients to classify their brain defects. They found white matter abnormalities and myelination defects [217]. They concluded that ATRX is involved in the myelination process. Another study reported partial or complete agenesis of the *corpus callosum* in ATR-X syndrome patients [226]. Coupled with the reduced size of some white matter tracts observed in the mice, we wanted to determine whether AtrxEcKO mice have myelin-related defects. We performed IF staining on P60 mice using the Myelin Associated Glycoprotein (MAG) marker to look at the myelin in the *corpus callosum* (CC). We measured the thickness of the rostral, medial and caudal CC (Figure 5.6). We found no change in the thickness of the rostral portion of the CC (WT: 400.5µm ± 39.35; AtrxEcKO 392.7µm ± 13.42; n=3) (Figure 5.6). However, we observed a significant reduction in the thickness of the medial CC (WT: 296.1µm ± 1.665; AtrxEcKO 193.0µm ± 14.00; n=3) (Figure 5.6) and the caudal CC (WT: 200.7µm ± 6.128; AtrxEcKO 159.8µm ± 5.299; n=3) (Figure 5.6). Interestingly, we noted that the density of the MAG+ fibers was reduced.

Next, we wanted to determine whether the myelination defects previously observed could be attributed to defects in the oligodendrocyte population. We used P60 coronal sections and performed IF staining. We used Olig2 to label the oligodendrocyte lineage and the myelin-producing oligodendrocytes were identified by their expression of Olig2 and CC1 (Figure 5.7A). We found a reduction in the total number of oligodendrocytes in the CC of AtrxEcKO mice (WT: 16.28 cells/10,000µm^2 ± 0.1852; AtrxEcKO 11.27 cells/10,000µm^2 ± 1.440; n=3) (Figure 5.7B).

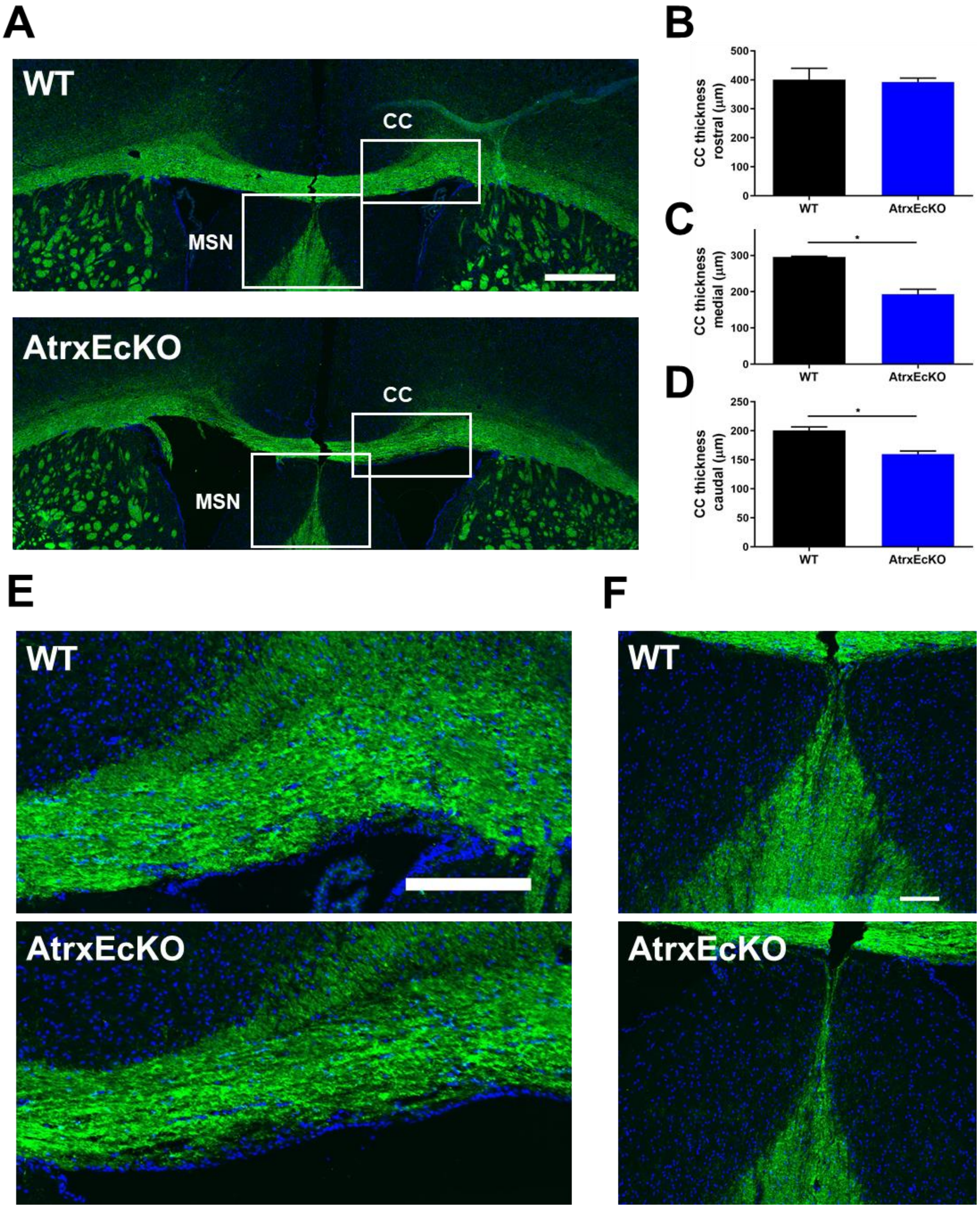
A
WT
CC
MSN
AtrxEcKO
CC
MSN
B
500
400
300
200
100
0
CC thickness rostral (μm)
WT
AtrxEcKO
C
*
300
200
100
0
CC thickness medial (μm)
WT
AtrxEcKO
D
*
250
200
150
100
50
0
CC thickness caudal (μm)
WT
AtrxEcKO
E
WT
AtrxEcKO
F
WT
AtrxEcKO

Figure 5.6: Myelination defects are observed in AtrxEcKO mice

A P60 coronal sections of WT (top) and AtrxEcKO (bottom) were stained using MAG (green) and DAPI (blue). The thickness of the **B** rostral, **C** medial and **D** caudal CC were measured. Magnification of the **E** *corpus callosum* (CC) and **F** medial septal nuclei (MSN) are shown. Scale represent **A** 500µm, **E** 200µm and **F** 100µm. Data represent means ± SEM. n=4. * $p < 0.05$.

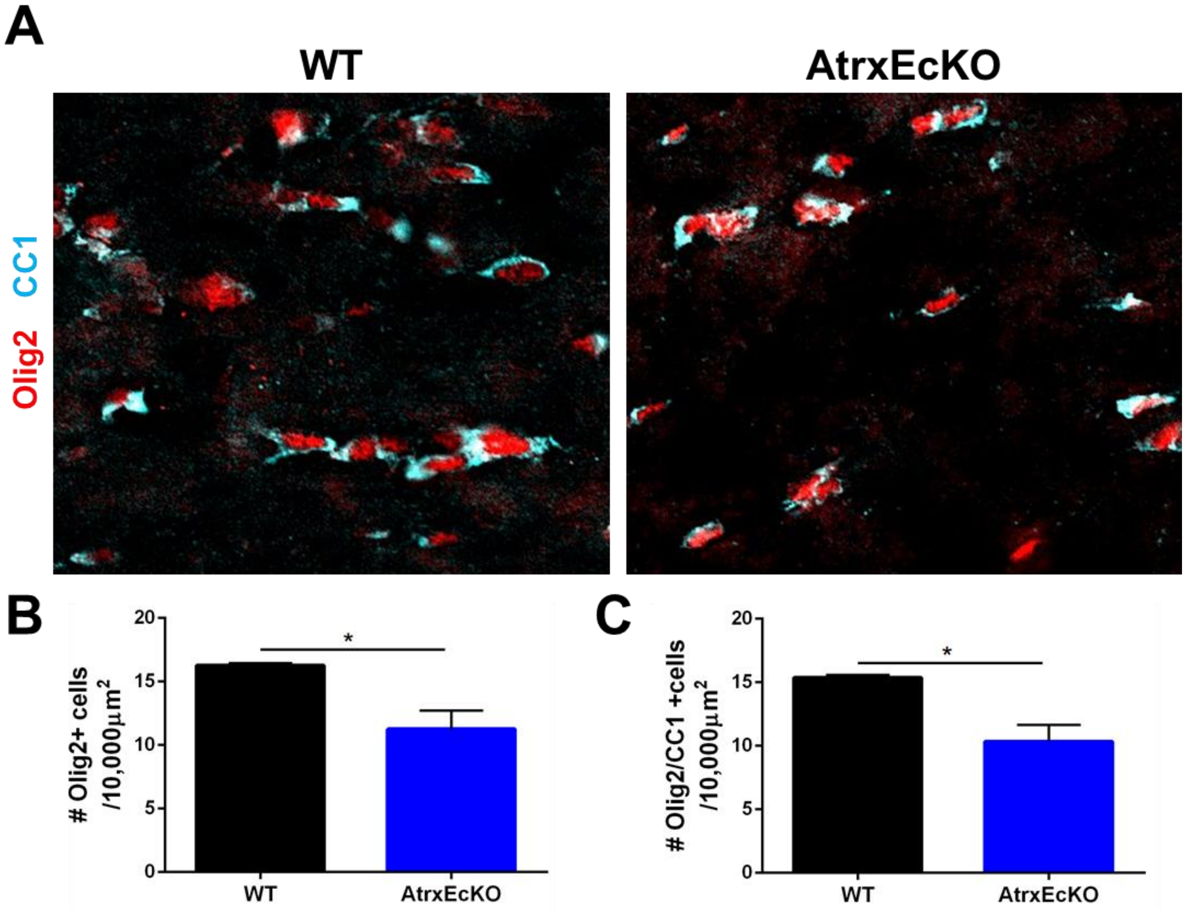

Figure 5.7: Altered number of oligodendrocyte lineage and mature cells in the CC of AtrxEcKO mice

A *Corpus callosum* of P60 WT and AtrxEcKO mice were stained using the Olig2 (red) and Cc1 (blue) antibodies. **B** Quantification of total oligodendrocytes per 10, 000µm^2. **C** Quantification of mature oligodendrocytes per 10, 000µm^2. Data represent means ± SEM. n=4. * $p < 0.05$.

Also, we observed a significant reduction in the number of double-labeled cells in AtrxEcKO mice (WT: 15.38 cells/10,000µm^2 ± 0.2048; AtrxEcKO 10.35 cells/10,000µm^2 ± 1.315; n=3) (Figure 5.7C). Interestingly, we noticed a qualitative difference in the Cc1 labeling on the oligodendrocytes in AtrxEcKO mice (Figure 5.7A). In the WT, Cc1 is located all around the nucleus and extends on both sides whereas in the AtrxEcKO mice, Cc1 is restricted to a small area surrounding the nucleus.

Lastly, we wanted to determine whether ATRX was expressed in myelin-producing oligodendrocytes. We used P60 coronal sections and stained them using Atrx and Cc1 (Figure 5.8). We noticed that ATRX was not expressed in the CC of the WT and AtrxEcKO animals (Figure 5.8A, B). Therefore, we looked at the cortex and showed that ATRX was not expressed in oligodendrocytes (Figure 5.8C-D), suggesting a non-cell autonomous effect. Another explanation could be that since the white track is thinner, it requires less oligodendrocytes to myelinate the axons. Therefore, it would be a direct consequence of losing *Atrx* rather than a non-cell autonomous effect.

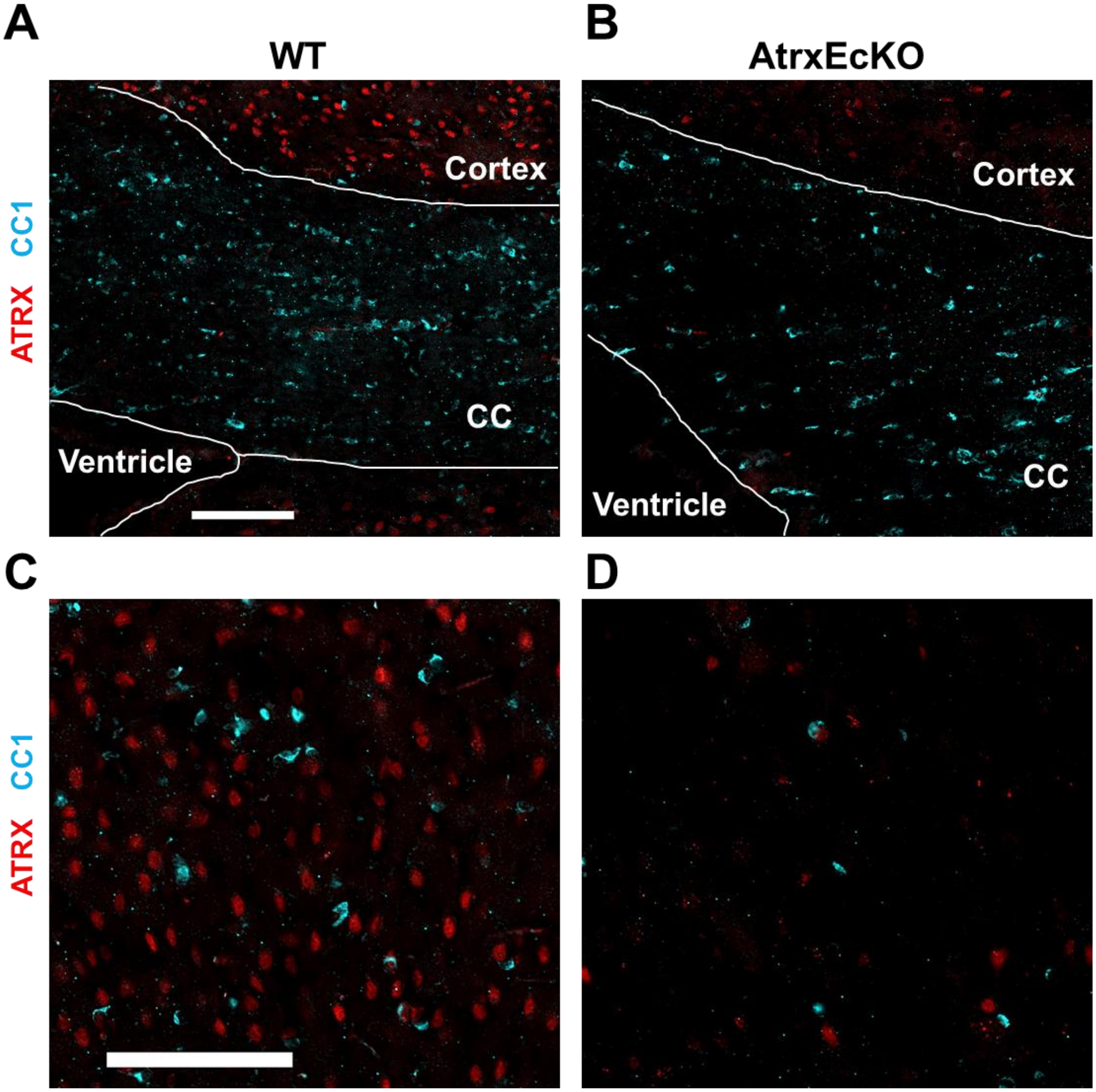

<u>**Figure 5.8: ATRX is not expressed in oligodendrocytes**</u>

P60 coronal sections of **A, C** WT and **B, D** AtrxEcKO mice were stained using the ATRX (red) and Cc1 (blue). **A-B** *Corpus callosum* (CC) and **C-D** cortex are shown. Scale represent 100µm.

5.4 AtrxEcKO mice have hyperactivity and seizure-like episodes

Next, we characterized the behaviour of AtrxEcKO mice to determine whether they harbored the key features of ATR-X syndrome. We evaluated the spontaneous activity using the BBK assay (Figure 5.9). In this test, the mouse is allowed to freely move in a home cage-like environment for 48 hours while its movements are recorded. We found that AtrxEcKO mice had significantly more beam breaks around 7am on both days (Figure 5.9A). This period correlated with the transition from dark to light in the 12-hour light cycle. Interestingly, the ambulatory time and the total movement were unchanged during the day and night (Figure 5.9B-C). Lastly, we found that AtrxEcKO mice travelled more distance at the beginning of the test and it took two hours for them to habituate to the new environment. The increased movement during the habituation period was also observed during the NOR test. Interestingly, this test takes place in a homecage environment under dark-light conditions, thus a stress-free environment. Using a heatmap that tracked the mouse's movements, we observed that the AtrxEcKO mice were significantly more active than the WT mice (Figure 5.9D). Also, we quantified the distance traveled during the habituation period and found that it was significantly higher in AtrxEcKO mice (WT: 1550 cm ± 137.8, n=21; AtrxEcKO 3541 cm ± 290.0; n=19) compared to WT littermates (Figure 5.9E).

Next, we investigated the spikes of movement seen during the BBK assay. We used the Phenotyper box to record the mice for 72 hours. This apparatus provides a home cage-like environment for video tracking research experiments. We observed seizure-like episodes in AtrxEcKO mice and the hyperactive phenotype previously described.

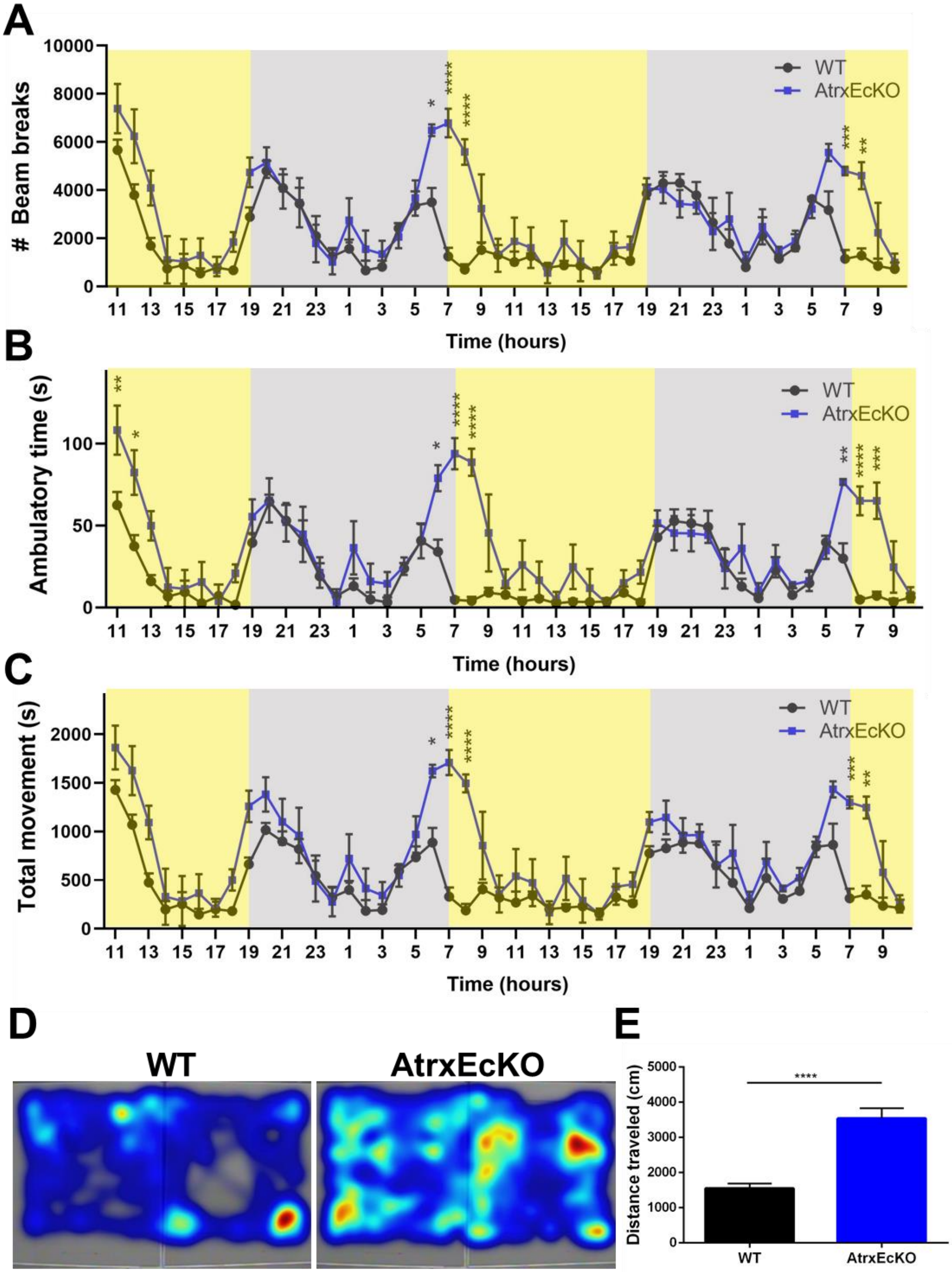
A
Beam breaks
0
2000
4000
6000
8000
10000
WT
AtrxEcKO
*
****
****
***
**
11 13 15 17 19 21 23 1 3 5 7 9 11 13 15 17 19 21 23 1 3 5 7 9
Time (hours)
B
Ambulatory time (s)
0
50
100
WT
AtrxEcKO
**
*
*
****
****
**
****
***
11 13 15 17 19 21 23 1 3 5 7 9 11 13 15 17 19 21 23 1 3 5 7 9
Time (hours)
C
Total movement (s)
0
500
1000
1500
2000
WT
AtrxEcKO
*
****
****
***
**
11 13 15 17 19 21 23 1 3 5 7 9 11 13 15 17 19 21 23 1 3 5 7 9
Time (hours)
D
WT
AtrxEcKO
E
Distance traveled (cm)
0
1000
2000
3000
4000
5000
****
WT
AtrxEcKO

Figure 5.9: AtrxEcKO mice display a hyperactivity phenotype

A The number of beam breaks, **B** ambulatory time and **C** total movement were measured during the beam break assay. The X axis represents the time of the day. The 12-hour light/dark cycle is depicted as the yellow and grey rectangles, respectively. Total movement during the novel object recognition test is shown in a **D** heat map and **E** graph. Data represent means ± SEM. * $p < 0.05$, ** $p < 0.01$, *** $p < 0.001$, **** $p < 0.0001$. n=10 (WT), n=10 (AtrxEcKO) for BBK and n=21 (WT), n=19 (AtrxEcKO) for NOR.

We found that AtrxEcKO mice experienced ~five seizure-like events during the 72-hour observational period whereas none of the WT experienced seizure-like episodes (WT: 0 seizure ± 0.000, n=10; AtrxEcKO 4.667 seizures ± 0.6667; n=10) (Figure 5.10A). The majority of these events presented themselves as absence seizures while a few of them resembled mild tonic/clonic seizures. Furthermore, the total distance traveled over 72-hours was significantly higher in AtrxEcKO mice in comparison to the WT mice (WT: 115 049 cm ± 12 043, n=10; AtrxEcKO 447 264 cm ± 56 942; n=10) (Figure 5.10B).

Lastly, repetitive behaviours have been documented in ATR-X syndrome patients. An equivalent behaviour in mice would be excessive grooming, so we examined grooming behaviours in WT and AtrxEcKO mice [226]. In this way, we observed abnormal grooming behaviour while the mice were singly housed during the behaviour tests. To quantify the grooming behaviour, we recorded the percentage of WT and AtrxEcKO mice with healthy coat, missing fur, open wounds and end-point wounds (Figure 5.11). We noted that only 25% of AtrxEcKO mice had a healthy coat. Interestingly, 40% of total AtrxEcKO mice had missing fur, 22% had open wounds and 15% had end-point wounds. This excessive grooming behaviour was also observed in other mouse models of neurodevelopmental disorders [271, 272].

Taken together, these results showed that AtrxEcKO mice had a hyperactivity phenotype that was observed in three independent tests. Unfortunately, it prevented the assessment of the learning/memory function since the majority of the behaviour tests are based on the movement of the animal. We also detected seizure-like events and excessive grooming behaviour in our ATR-X syndrome model, both features of ATR-X patients.

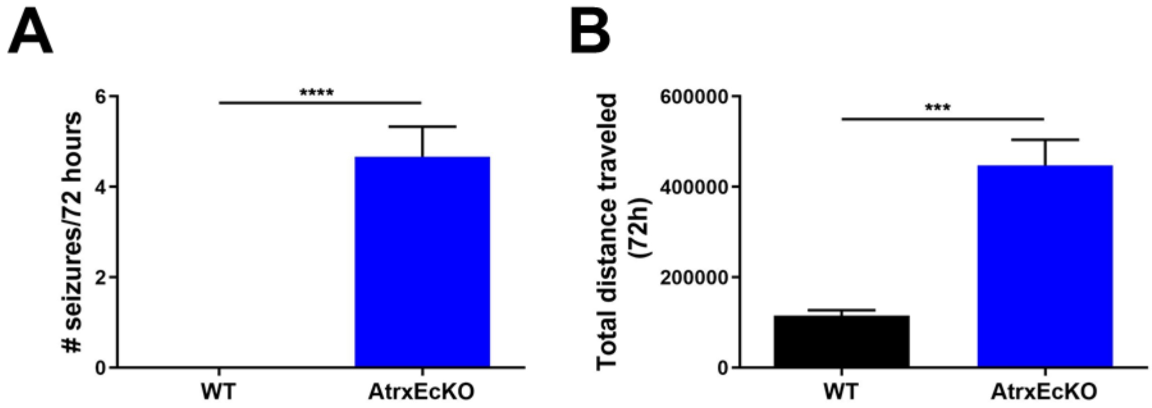

Figure 5.10: AtrxEcKO mice display episodic seizure-like events and present a hyperactive behaviour

A The number of seizure-like episodes for 72 hours and **B t**otal distance traveled were assessed during the Phenotyper box. Data represent means ± SEM. * $p < 0.05$, ** $p < 0.01$, *** $p < 0.001$, **** $p < 0.0001$. n=10 (WT), n=10 (AtrxEcKO).

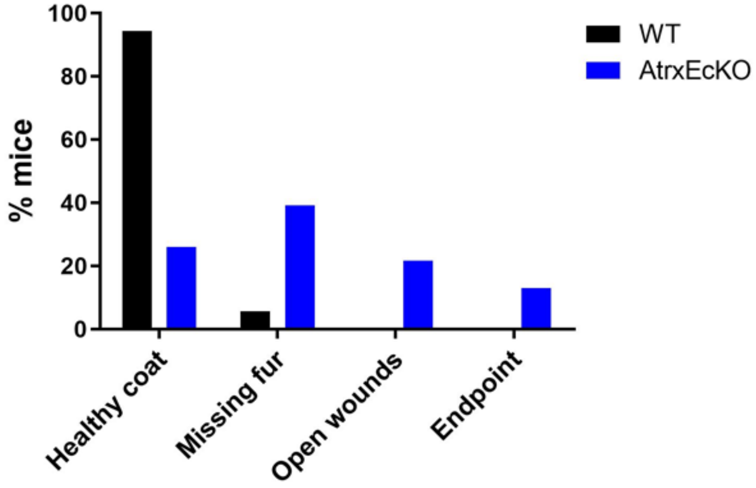

Figure 5.11: AtrxEcKO mice have excessive grooming behaviours

Each mouse was classified in a category based on the state of its coat; healthy coat, missing fur, open wounds and endpoint. Percentage of WT and AtrxEcKO mice are shown. n=35 (WT), n=32 (AtrxEcKO).

5.5 Transcriptional dysregulation of AtrxEcKO hippocampus

To gain insights on the potential genes causing the hippocampal defects, we performed an RNA-sequencing experiment. We extracted RNA from P60 hippocampus of WT and AtrxEcKO mice and purified it. Then, the isolated RNA was sent to Genome Quebec for bulk RNA sequencing. We found 1373 differentially expressed transcripts in our AtrxEcKO hippocampus samples ($\log_2$FC ± 0.25, qval < 0.05). Out of those, 656 were upregulated and 717 were downregulated. Volcano plots were used to show the distribution of differentially expressed transcripts and highlight the differential expression change of several genes of interest, namely Netrin 5 (Ntn5), Netrin-G1 (Ntng1), Netrin-G2 (Ntng2) and Unc13c (Figure 5.12).

Next, we performed Gene Ontology (GO) term enrichment analysis on the 656 upregulated and 717 downregulated transcripts (Figure 5.13). Looking at the upregulated transcripts, we found GO terms implicated in protein phosphorylation and well-known pathways including the ERK1 the ERK2 cascade. As for the downregulated transcripts, we found several clusters involved in cell adhesion, signal transduction and cell differentiation. Next, we used a different platform to determine the significant GO terms related to biological processes (Figure 5.14). We found that the interleukin-mediated pathway was the primary cluster identified for the upregulated transcripts. On the other hand, we identified multiple gene clusters implicated in the myelination process and ensheathment of neurons amongst the downregulated genes.

To validate the expression of some of our genes of interest, we performed quantitative RT-PCR (qRT-PCR) (Figure 5.15). We extracted the hippocampal RNA from another set of three WT and three AtrxEcKO mice to confirm the reproducibility of our results.

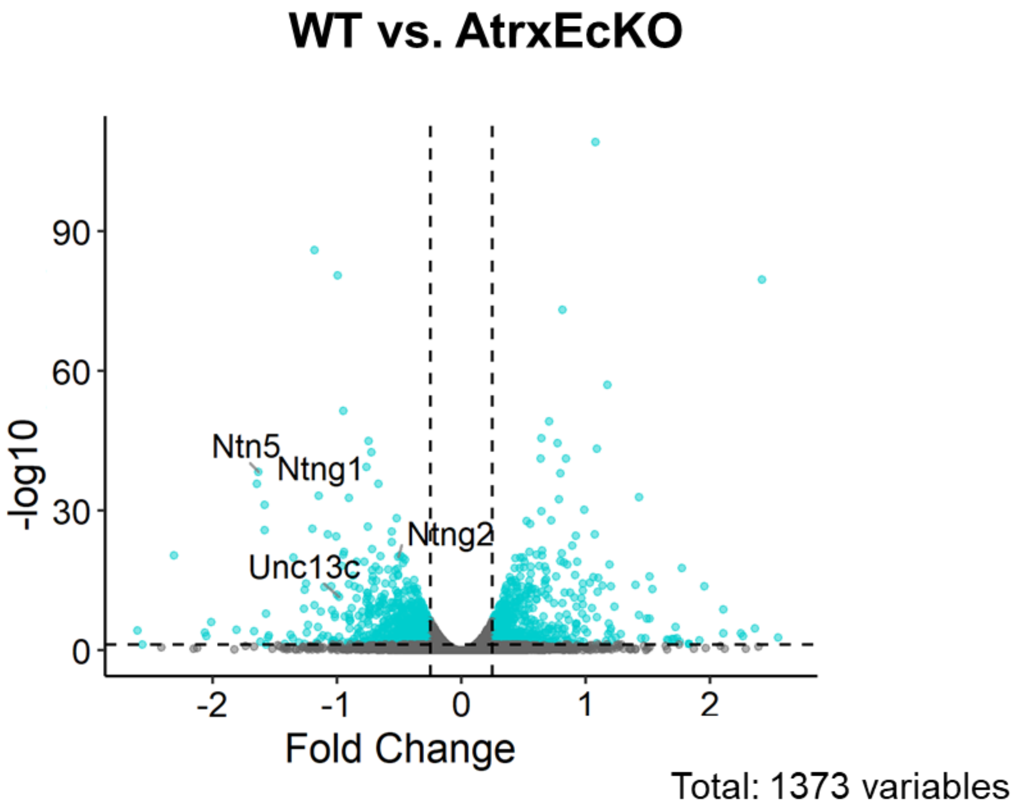

Figure 5.12: Volcano plot of the differentially expressed transcripts

Differentially expressed transcripts were determined using a fold change cut-off of 0.25 and a P value cut-off of 0.05. The blue dots represent transcripts that were significantly altered whereas the grey dots do not meet the statistical significance or fold change requirements. There were 1373 differentially expressed transcripts. Ntn5, Ntng1, Ntng2 and Unc13c were identified as potential genes of interest.

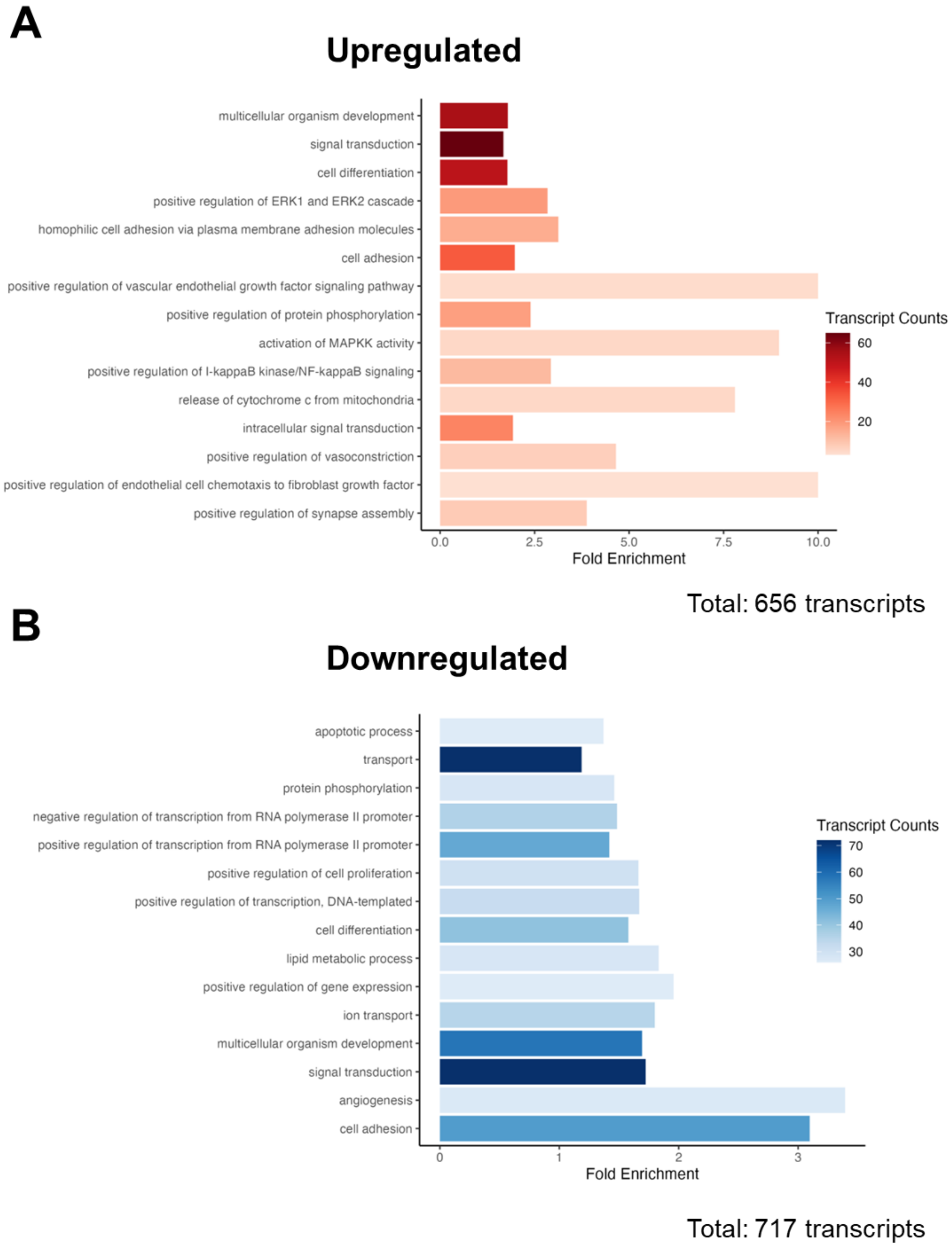
A
Upregulated
multicellular organism development
signal transduction
cell differentiation
positive regulation of ERK1 and ERK2 cascade
homophilic cell adhesion via plasma membrane adhesion molecules
cell adhesion
positive regulation of vascular endothelial growth factor signaling pathway
positive regulation of protein phosphorylation
activation of MAPKK activity
positive regulation of I-kappaB kinase/NF-kappaB signaling
release of cytochrome c from mitochondria
intracellular signal transduction
positive regulation of vasoconstriction
positive regulation of endothelial cell chemotaxis to fibroblast growth factor
positive regulation of synapse assembly
0.0
2.5
5.0
7.5
10.0
Fold Enrichment
Transcript Counts
60
40
20
Total: 656 transcripts
B
Downregulated
apoptotic process
transport
protein phosphorylation
negative regulation of transcription from RNA polymerase II promoter
positive regulation of transcription from RNA polymerase II promoter
positive regulation of cell proliferation
positive regulation of transcription, DNA-templated
cell differentiation
lipid metabolic process
positive regulation of gene expression
ion transport
multicellular organism development
signal transduction
angiogenesis
cell adhesion
0
1
2
3
Fold Enrichment
Transcript Counts
70
60
50
40
30
Total: 717 transcripts

Figure 5.13: Gene Ontology of the differentially expressed transcripts between WT and AtrxEcKO in hippocampus samples

Differentially expressed genes (DEGs) were determined using a fold change cut-off of 0.25 and a P value cut-off of 0.05. Enriched GO terms associated with the **A** upregulated and **B** downregulated transcripts were determined.

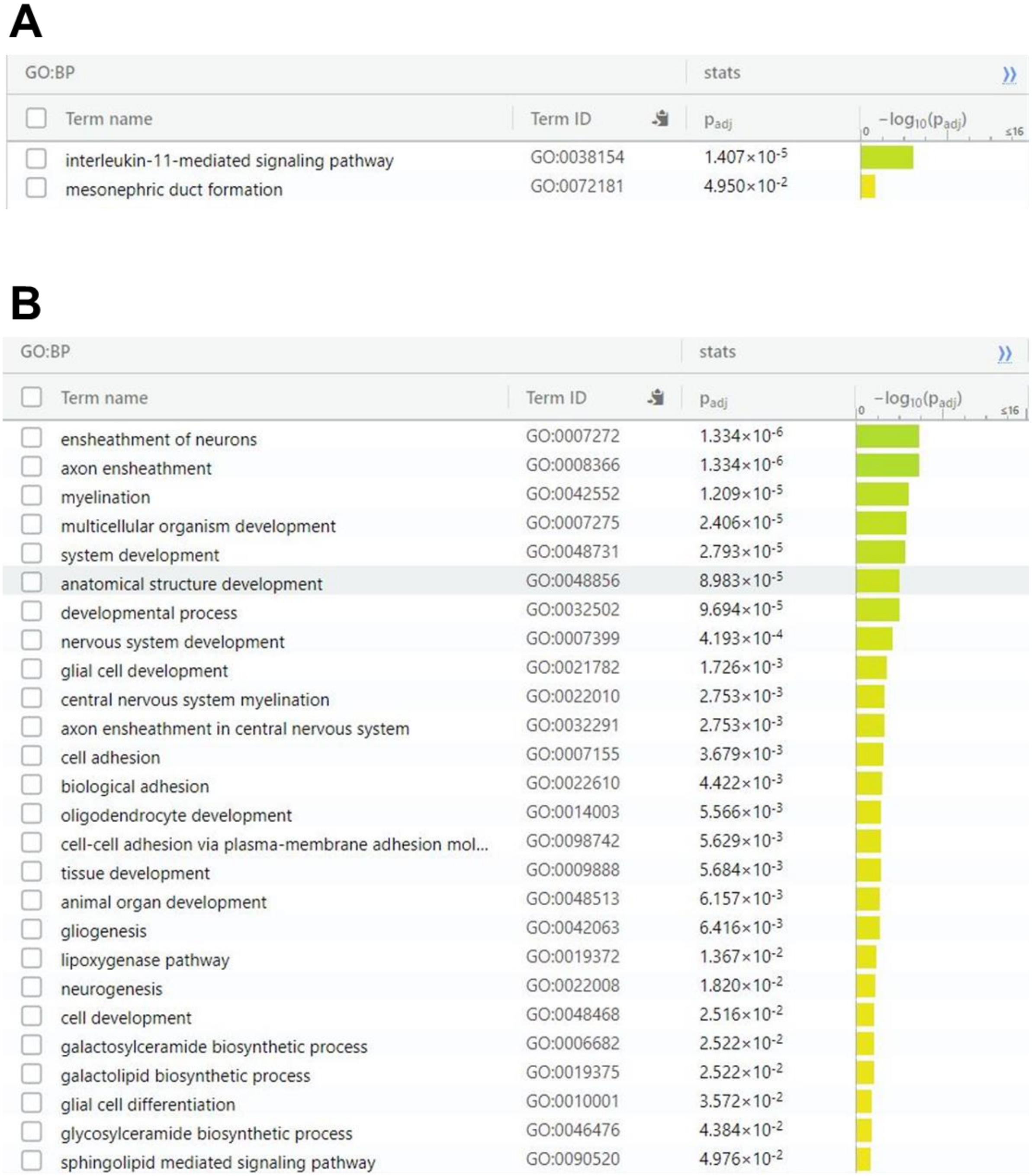

GO:BP			stats	
☐	Term name	Term ID	p_{adj}	$-\log_{10}(p_{adj})$
☐	interleukin-11-mediated signaling pathway	GO:0038154	1.407×10^{-5}	
☐	mesonephric duct formation	GO:0072181	4.950×10^{-2}	

GO:BP			stats	
☐	Term name	Term ID	p_{adj}	$-\log_{10}(p_{adj})$
☐	ensheathment of neurons	GO:0007272	1.334×10^{-6}	
☐	axon ensheathment	GO:0008366	1.334×10^{-6}	
☐	myelination	GO:0042552	1.209×10^{-5}	
☐	multicellular organism development	GO:0007275	2.406×10^{-5}	
☐	system development	GO:0048731	2.793×10^{-5}	
☐	anatomical structure development	GO:0048856	8.983×10^{-5}	
☐	developmental process	GO:0032502	9.694×10^{-5}	
☐	nervous system development	GO:0007399	4.193×10^{-4}	
☐	glial cell development	GO:0021782	1.726×10^{-3}	
☐	central nervous system myelination	GO:0022010	2.753×10^{-3}	
☐	axon ensheathment in central nervous system	GO:0032291	2.753×10^{-3}	
☐	cell adhesion	GO:0007155	3.679×10^{-3}	
☐	biological adhesion	GO:0022610	4.422×10^{-3}	
☐	oligodendrocyte development	GO:0014003	5.566×10^{-3}	
☐	cell-cell adhesion via plasma-membrane adhesion mol...	GO:0098742	5.629×10^{-3}	
☐	tissue development	GO:0009888	5.684×10^{-3}	
☐	animal organ development	GO:0048513	6.157×10^{-3}	
☐	gliogenesis	GO:0042063	6.416×10^{-3}	
☐	lipoxygenase pathway	GO:0019372	1.367×10^{-2}	
☐	neurogenesis	GO:0022008	1.820×10^{-2}	
☐	cell development	GO:0048468	2.516×10^{-2}	
☐	galactosylceramide biosynthetic process	GO:0006682	2.522×10^{-2}	
☐	galactolipid biosynthetic process	GO:0019375	2.522×10^{-2}	
☐	glial cell differentiation	GO:0010001	3.572×10^{-2}	
☐	glycosylceramide biosynthetic process	GO:0046476	4.384×10^{-2}	
☐	sphingolipid mediated signaling pathway	GO:0090520	4.976×10^{-2}	

<u>Figure 5.14: Gene Ontology of the biological process of upregulated and downregulated transcripts</u>

DEGs were determined using a fold change cut-off of 0.25 and a P value cut-off of 0.05. Enriched GO terms associated with the **A** upregulated and **B** downregulated transcripts were determined.

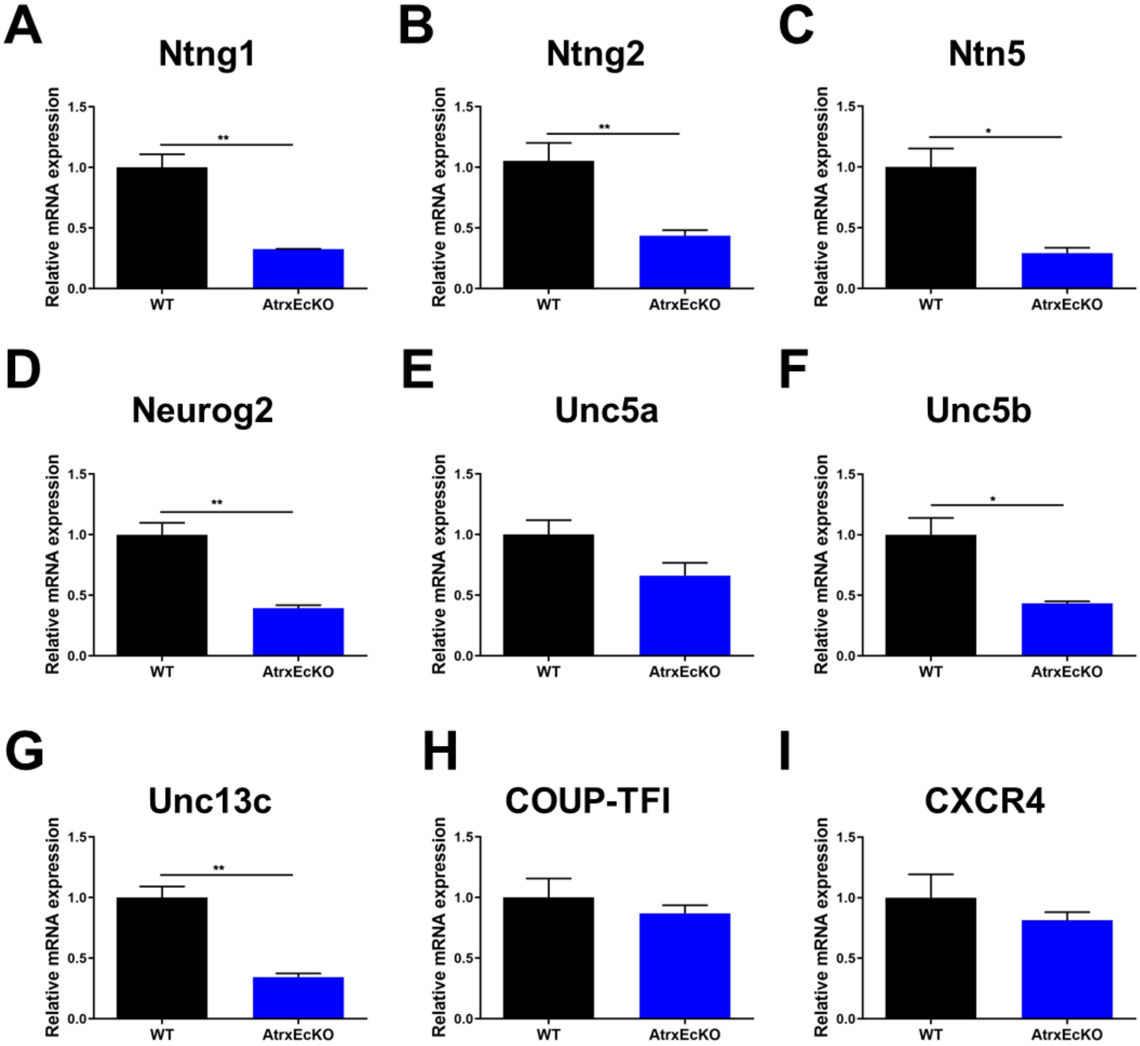

Figure 5.15: Validation of genes of interest found in the RNAseq

qRT-PCR quantification from P90 WT and AtrxEcKO hippocampus RNA extracts. Relative mRNA expression of **A** Ntng1, **B** Ntng2 **C** Ntn5**, D** Neurog2, **E** Unc5a**, F** Unc5b, **G** Unc13c**, H** COUP-TFI and **I** CXCR4 are shown. Data represent means ± SEM. n=3. * $p < 0.05$, ** $p < 0.01$.

We confirmed the significant reduction in Ntng1 (WT: 1.000 ± 0.1087, n=3; AtrxEcKO 0.3258 ± 0.002624; n=3), Ntng2 (WT: 1.000 ± 0.1482, n=3; AtrxEcKO 0.4366 ± 0.04485; n=3), Ntn5 (WT: 1.000 ± 0.1525, n=3; AtrxEcKO 0.2920 ± 0.04405; n=3), neurogenin 2 (WT: 1.000 ± 0.09805, n=3; AtrxEcKO 0.3928 ± 0.02506; n=3), Unc5b (WT: 1.000 ± 0.1399, n=3; AtrxEcKO 0.4340 ± 0.01699; n=3) and Unc13c (WT: 1.000 ± 0.09152, n=3; AtrxEcKO 0.3449 ± 0.02899; n=3) in AtrxEcKO mice. However, we did not find any differences in the expression of Unc5a (WT: 1.000 ± 0.1189, n=3; AtrxEcKO 0.6618 ± 0.1048; n=3). Also, we looked at COUP-TFI (WT: 1.000 ± 0.1567, n=3; AtrxEcKO 0.8699 ± 0.06521; n=3) and CXCR4 (WT: 1.000 ± 0.1935, n=3; AtrxEcKO 0.8131 ± 0.06750; n=3), which are proteins implicated in the formation of the dentate gyrus, and we did not find any significant change in their expression levels.

In sum, we used Next-Generation Sequencing on P60 hippocampus to gain insights into the molecular pathways that could be dysregulated in our mouse model. We identified key proteins that have a role in hippocampal development that were significantly altered. Also, GO term analysis revealed multiple clusters involved in cell adhesion, signal transduction, cell differentiation and myelination suggesting new possible roles for Atrx.

5.6 AtrxEcKO mice have severe hippocampal defects

We further characterized the hippocampal defects by examining different cell populations. First, we performed IF staining on P60 coronal sections of WT and AtrxEcKO mice using NeuN and doublecortin (DCX) to label mature and immature neurons respectively (Figure 5.16).

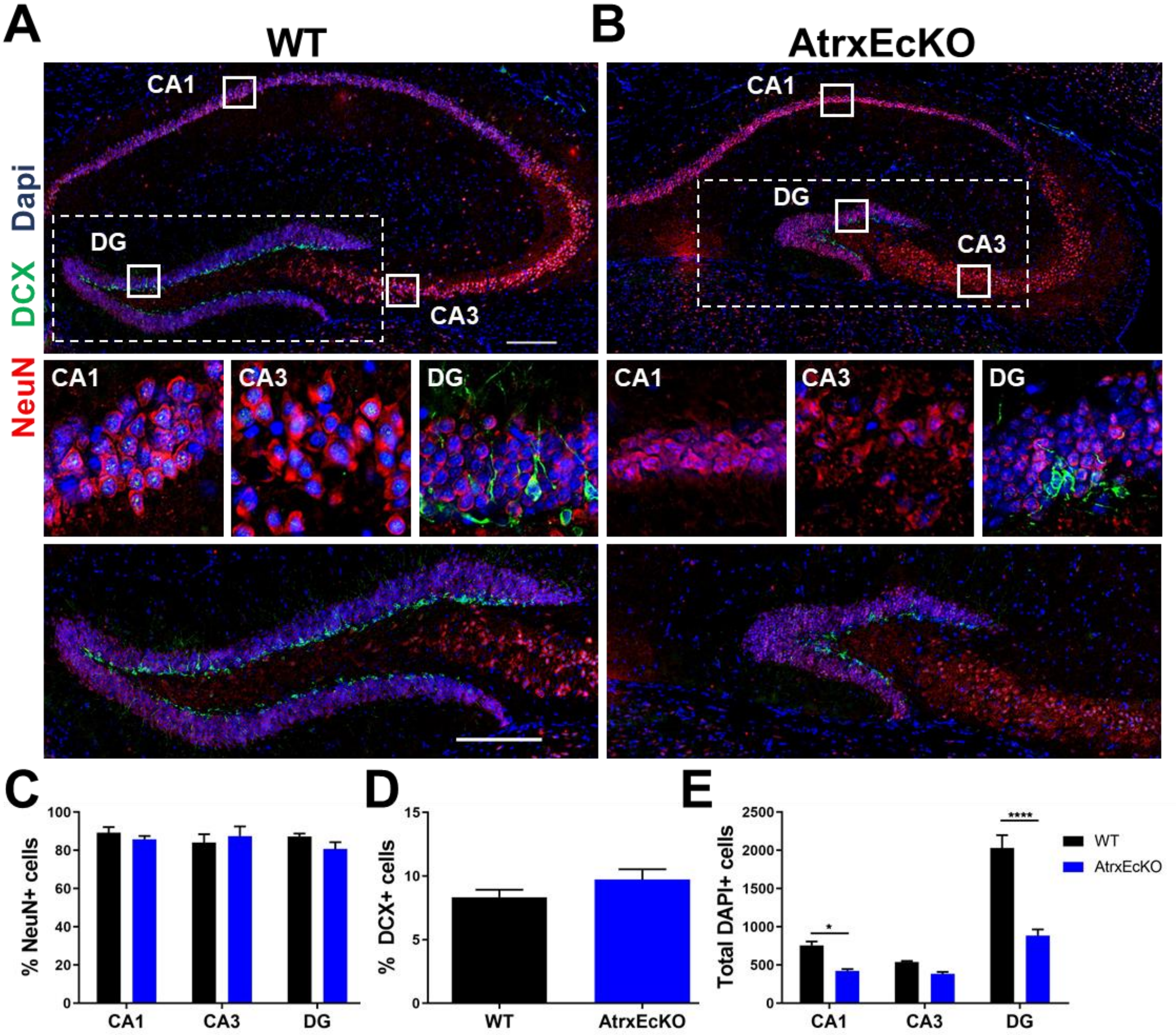

Figure 5.16: AtrxEcKO mice have a smaller hippocampus and disorganized DG

P60 coronal sections were used to do IF staining using NeuN (red), DCX (green) antibodies and a DAPI (blue) counterstain. The location of the magnified images (middle panels) of the CA1, CA3 and DG regions for **A** WT and **B** AtrxEcKO are indicated by white squares. **C** Percentage of NeuN+ cells, **D** DCX+ cells and **E** the number of DAPI cells were quantified. Scale bar, 200µm. Data represent means ± SEM. n=4. **** $p < 0.0001$.

We quantified the total number of NeuN+ cells in each hippocampal region, namely CA1, CA3 and DG and normalized it to the total number of cells within their respective regions. We did not find any difference in the percentage of NeuN+ cells in any of the hippocampal regions (WT: CA1 89.193% ± 3.006, CA3 84.110% ± 4.372, DG 87.233% ± 1.547; AtrxEcKO: CA1 85.827% ± 1.676, CA3 87.443% ± 5.085, DG 80.733% ± 3.588; n=4) (Figure 5.16C). Also, the percentage of DCX+ cells in the DG of AtrxEcKO mice was not significantly different than the WT (WT: 8.317% ± 0.5961; AtrxEcKO 9.717% ± 0.8121; n=4) (Figure 5.16D). However, the total number of cells in CA1 and DG of AtrxEcKO mice was significantly lower than the WT (WT: CA1 673.667 cells ± 43.594, CA3 454.333 cells ± 21.667, DG 1776.000 cells ± 173.995; AtrxEcKO: CA1 363.333 cells ± 23.183, CA3 333.000 cells ± 8.622, DG 720.333 cells ± 96.202; n=4) (Figure 5.16E). In fact, the DG of AtrxEcKO mice had 60% less cells, as clearly depicted in the representative images (Figure 5.16A-B). We also noted that the positioning and distribution of the DCX+ cells were altered in AtrxEcKO mice. Instead of being evenly distributed along the DG and projecting upwards for the top blade and downwards for the bottom blade, they were clustering and had the wrong orientation (Figure 5.16, DG magnified panel). In addition, we observed a reduction in the thickness of the CA1 region in the AtrxEcKO mice. The WT had approximately five cells in thickness whereas the AtrxEcKO only had three (Figure 5.16, CA1 magnified panel). Overall, *Atrx* deletion in the forebrain impaired the structure of the hippocampus and altered the immature and mature neuronal populations. The next cell population we investigated was the immature granule cells in the DG. We used P60 coronal sections for IF staining using the calcium-binding protein calretinin to label immature granule cells and the inner molecular layer (Figure 5.17). We found that the percentage of calretinin+ cells in AtrxEcKO mice was approximately 50% lower than in the WT animals

(WT: 5.810 % ± 0.4015; AtrxEcKO 2.313% ± 0.1961; n=4) (Figure 5.17C). Also, the total number of cells in the DG was significantly reduced in AtrxEcKO mice (WT: 2386 cells ± 125.1; AtrxEcKO 892 cells ± 75.01; n=4) (Figure 5.17D). This result was consistent with our previous finding (Figure 5.16E). Moreover, we saw that the inner molecular layer was missing in AtrxEcKO mice. In addition, we noted that the calretinin+ cells in AtrxEcKO appeared more immature than the ones in the WT. Indeed, the cell bodies were smaller and round without any projection, which was reminiscent of a progenitor-like shape. Furthermore, we noticed a population of calretinin+ cells located outside the DG close to the apex and in the outer molecular layer that was not observed in the WT mice (Figure 5.17B, white arrow). Interestingly, this cell population had complex dendrites that were intricately connected. This was surprising since the calretinin+ cells in the DG of the AtrxEcKO were immature. In the WT, the calretinin+ cells found in the DG and in the molecular layer were in the same developmental stages whereas in the AtrxEcKO this was not true. Indeed, the calretinin cell population in the molecular layer was significantly more mature than the one found in the DG.

Following the characterization of the hippocampus (HPC) at P60, we wanted to determine whether the defects observed would be present at an earlier time point. First, we performed IF staining on P40 coronal section using DCX and calretinin (Figure 5.18). We found no change in the percentage of DCX+ cells (WT: 12.60% ± 1.090; AtrxEcKO 11.20% ± 0.06245; n=4) (Figure 5.18E). Similar to the results observed in P60 mice (Figure 5.16), the DCX+ cells were forming clusters and most of the neurons had the wrong orientation.

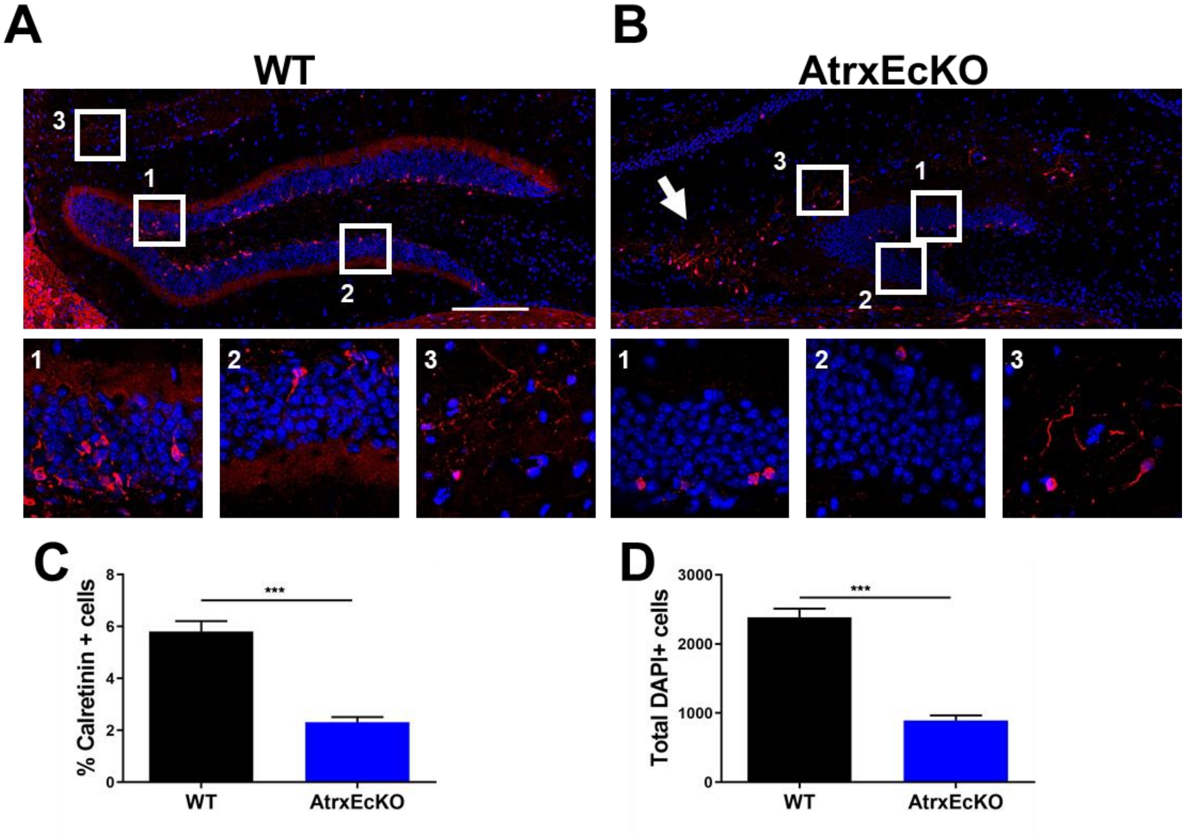

Figure 5.17: AtrxEcKO mice are missing the inner molecular layer

P60 coronal sections were used to do IF staining using calretinin (red) and DAPI (blue). Labeled white squares denote the three magnified images shown in the lower panels for **A** WT and **B** AtrxEcKO sections. **C** Percentage of calretinin+ cells and **D** the number of DAPI cells were quantified. Scale bar, 200μm. Data represent means ± SEM. n=4. *** $p < 0.001$.

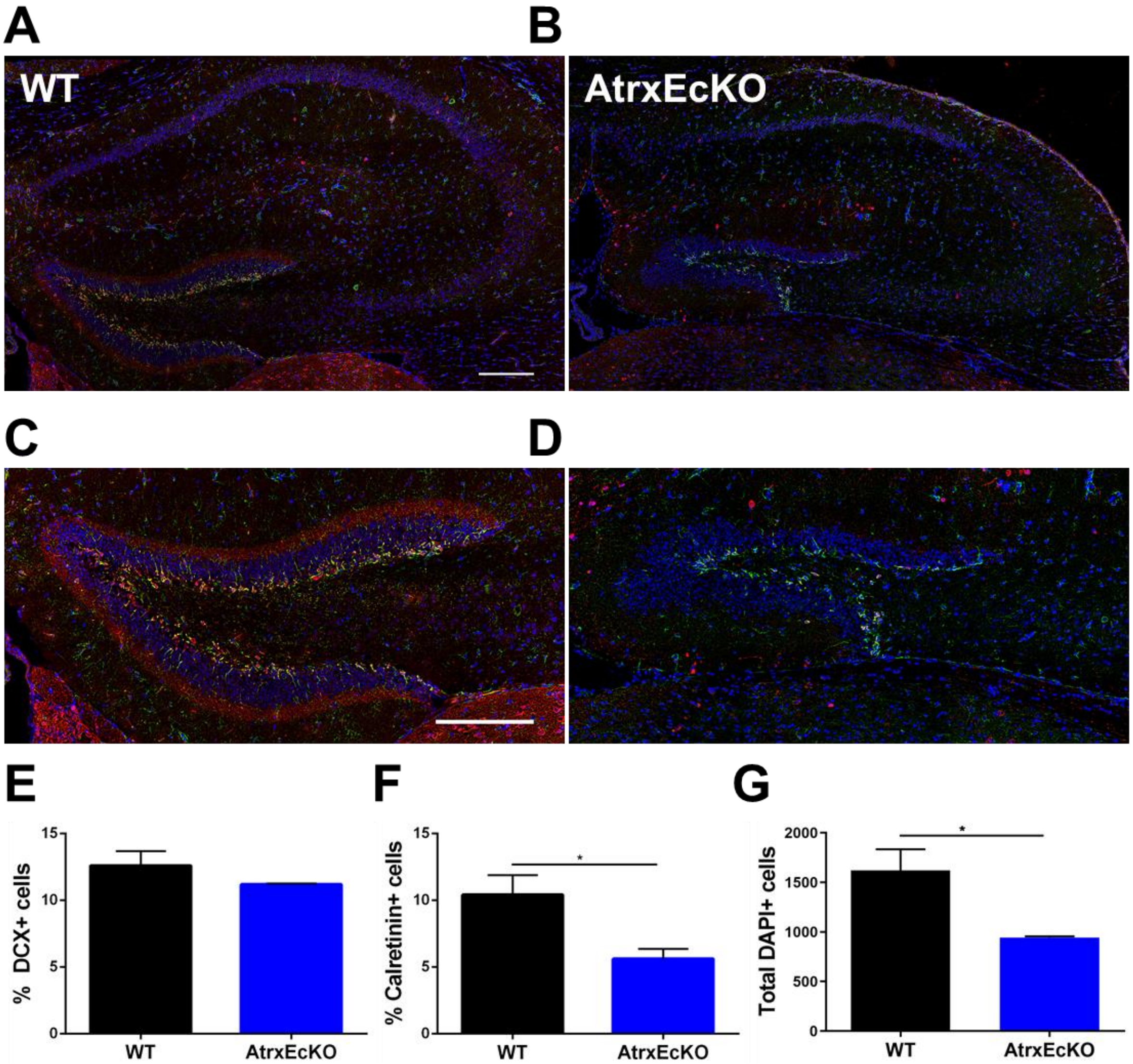

<u>**Figure 5.18: AtrxEcKO mice have defects in the dentate gyrus**</u>

A-D P40 coronal sections were used to do IF staining using calretinin (red), DCX (green) and DAPI (blue). Magnifications of the DG of **C** WT and **D** AtrxEcKO are shown. **E** Percentage of DCX+ cells, **F** Calretinin+ cells and **G** the number of DAPI cells were quantified. Scale bar, 200µm. Data represent means ± SEM. n=4. * $p < 0.05$.

Moreover, we saw a ~50% decrease in the percentage of calretinin+ cells in AtrxEcKO mice (WT: 10.42% ± 1.467; AtrxEcKO 5.620% ± 0.7465; n=4) (Figure 5.18F). Interestingly, the inner molecular layer was missing in AtrxEcKO mice, which was also observed in P60 mice. We quantified the total number of DAPI cells in the DG and found a striking reduction in AtrxEcKO mice (WT: 1620 cells ± 214.4; AtrxEcKO 943.3 cells ± 13.30; n=4) (Figure 5.18G). Furthermore, we noted that the HPC and the DG of AtrxEcKO mice are significantly smaller than the WT mice (Figure 5.18A-D). Next, we assessed whether the smaller DG of AtrxEcKO mice could be attributed to a reduction in the DG granule cell population. We used P40 coronal sections to perform IF staining using Prox1 to label the granule neurons (Figure 5.19A). We quantified the percentage of Prox1+ cells and found a ~15% reduction in AtrxEcKO mice (WT: 87.79% ± 1.948; AtrxEcKO 73.30% ± 1.833; n=3) (Figure 5.19B). Furthermore, we found a ~50% reduction in the total number of cells in the DG of AtrxEcKO mice (WT: 1770 cells ± 206.7; AtrxEcKO 1060 cells ± 123.3; n=3) (Figure 5.19C). We visually compared the images and we noticed that the intensity of the Prox1 staining was reduced in AtrxEcKO mice. Indeed, only a small proportion of Prox1-postive cells had a signal as strong as in the WT mice. Since Prox1 is a marker of granule cell fate, we can affirm that they are being generated but to a smaller extent. Thus, forebrain-specific deletion of *Atrx* affected the granule cell population.

We previously showed that the CA1 and CA3 regions of AtrxEcKO mice were thinner and the overall size of the HPC was reduced (Figure 5.16). Here, we examined whether the size reduction was due to a decrease in pyramidal neurons. We performed IF staining using Math2, also called NeuroD6, on P40 coronal sections (Figure 5.20A).

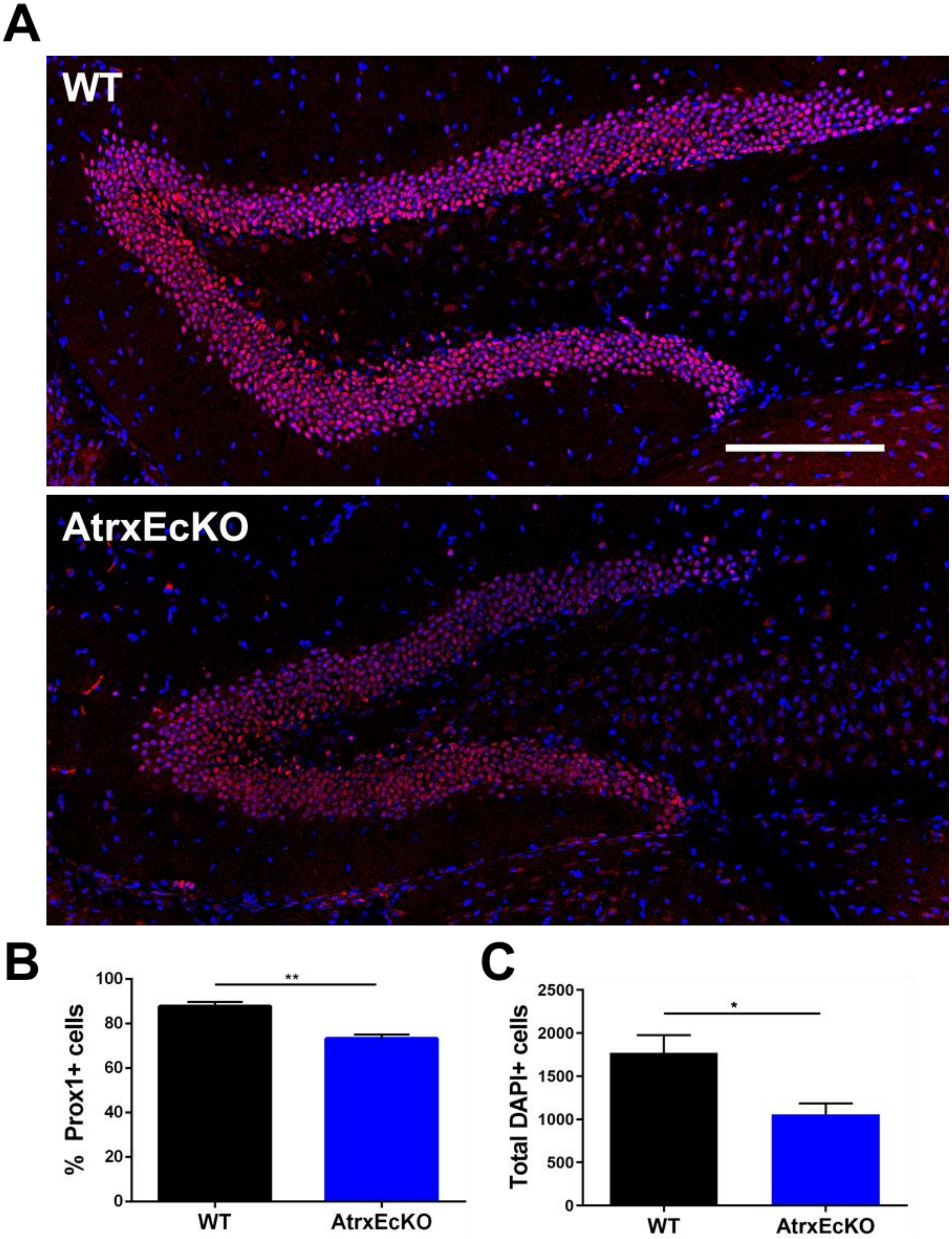
A
WT
AtrxEcKO
B
% Prox1+ cells
0
20
40
60
80
100
**
WT
AtrxEcKO
C
Total DAPI+ cells
0
500
1000
1500
2000
2500
*
WT
AtrxEcKO

Figure 5.19: *Atrx* loss in Emx1+ cells leads results in a reduction of granule cells in the DG

A P40 coronal section of WT (top) and AtrxEcKO (bottom) mice were used for IF staining using Prox1 (red) and DAPI (blue). **B** Percentage of Prox1+ cells and **C** the total number of cells were quantified in the DG. Data represent mean ± SEM. n=3. Scale bar is 200µm. * $p < 0.05$, ** $p < 0.01$.

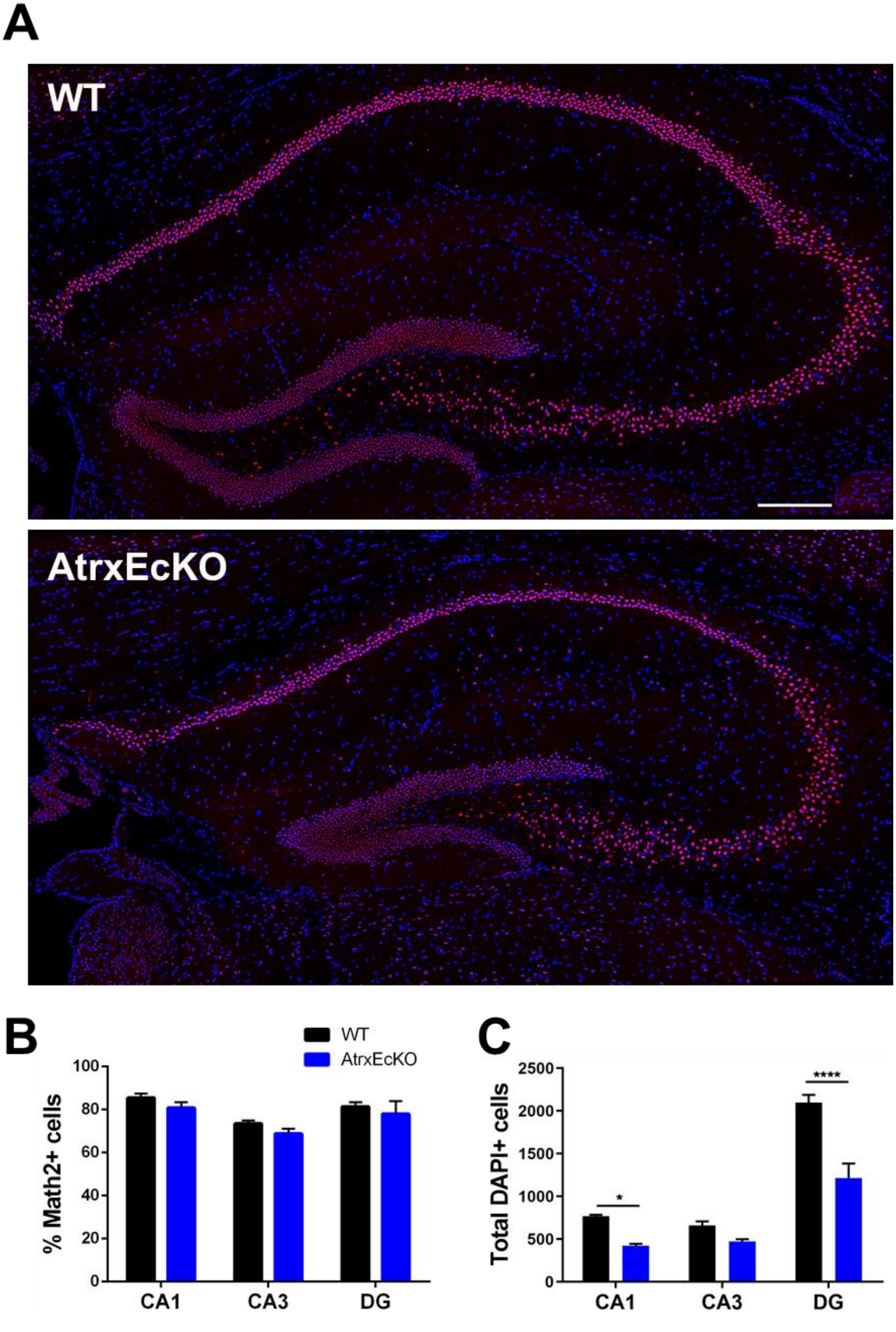
A
WT
AtrxEcKO
B
WT
AtrxEcKO
% Math2+ cells
100
80
60
40
20
0
CA1
CA3
DG
C
Total DAPI+ cells
2500
2000
1500
1000
500
0
*
****
CA1
CA3
DG

Figure 5.20: Pyramidal neurons in the HPC were not affected by the forebrain-specific *Atrx* deletion.

A P40 coronal section of WT (top) and AtrxEcKO (bottom) mice were used to do IF using Math2 (red) and DAPI (blue). **B** Percentage of Math2+ cells and **C** the total number of cells were quantified. Data represent mean ± SEM. n=4. Scale bar is 200µm. **** $p < 0.0001$.

We quantified Math2+ cells in each hippocampal region, namely CA1, CA3 and DG, and we found no change in the number of pyramidal neurons (WT: CA1 85.435% ± 1.914, CA3 73.483% ± 1.490, DG 81.3857% ± 1.968; AtrxEcKO: CA1 80.827% ± 2.601, CA3 68.757% ± 2.375, DG 77.983% ± 6.016; n=4) (Figure 5.20B). Consistent with the previous IF staining (Figure 5.19), we observed a 50% reduction in the total number of cells in the DG of AtrxEcKO mice (WT: CA1 768.250 cells ± 16.750, CA3 658.500 cells ± 48.926, DG 2097.000 cells ± 90.924; AtrxEcKO: CA1 421.000 cells ± 23.116, CA3 472.667 cells ± 26.735, DG 1216.333 cells ± 167.062; n=4) (Figure 5.20C). Thus, forebrain-specific deletion of *Atrx* did not alter the fate of pyramidal neurons in the HPC.

Following the characterization of the different cell populations in the HPC, we followed up on two genes of interest obtained in the RNAseq results, netrin G1 and netrin G2. Together, they play an important role in axon guidance and defects in these proteins have been linked to decreased dendritic arborization of hippocampal neurons and neurodevelopmental disorders [273, 274]. We performed IF staining on P40 coronal sections using netrin G1 and netrin G2 antibodies (Figure 5.21). In the WT mice, netrin G1 labeled the *stratum lacunosum-moleculare* (SLM) and the outer molecular layer (OML) and netrin G2 labeled the middle molecular layer (MML) (Figure 5.21A). We observed a significant reduction in thickness of netrin G1 staining in the AtrxEcKO mice (Figure 5.21C) and the netrin G2 layer was not detectable in the AtrxEcKO mice (Figure 5.21D).

Lastly, we wanted to determine whether there was a difference in the dendritic arborization in the AtrxEcKO mice. We performed Golgi Cox staining on P40 coronal sections to visualize the neurons (Figure 5.22A, B). We saw a striking difference in the staining pattern between the WT and AtrxEcKO mice.

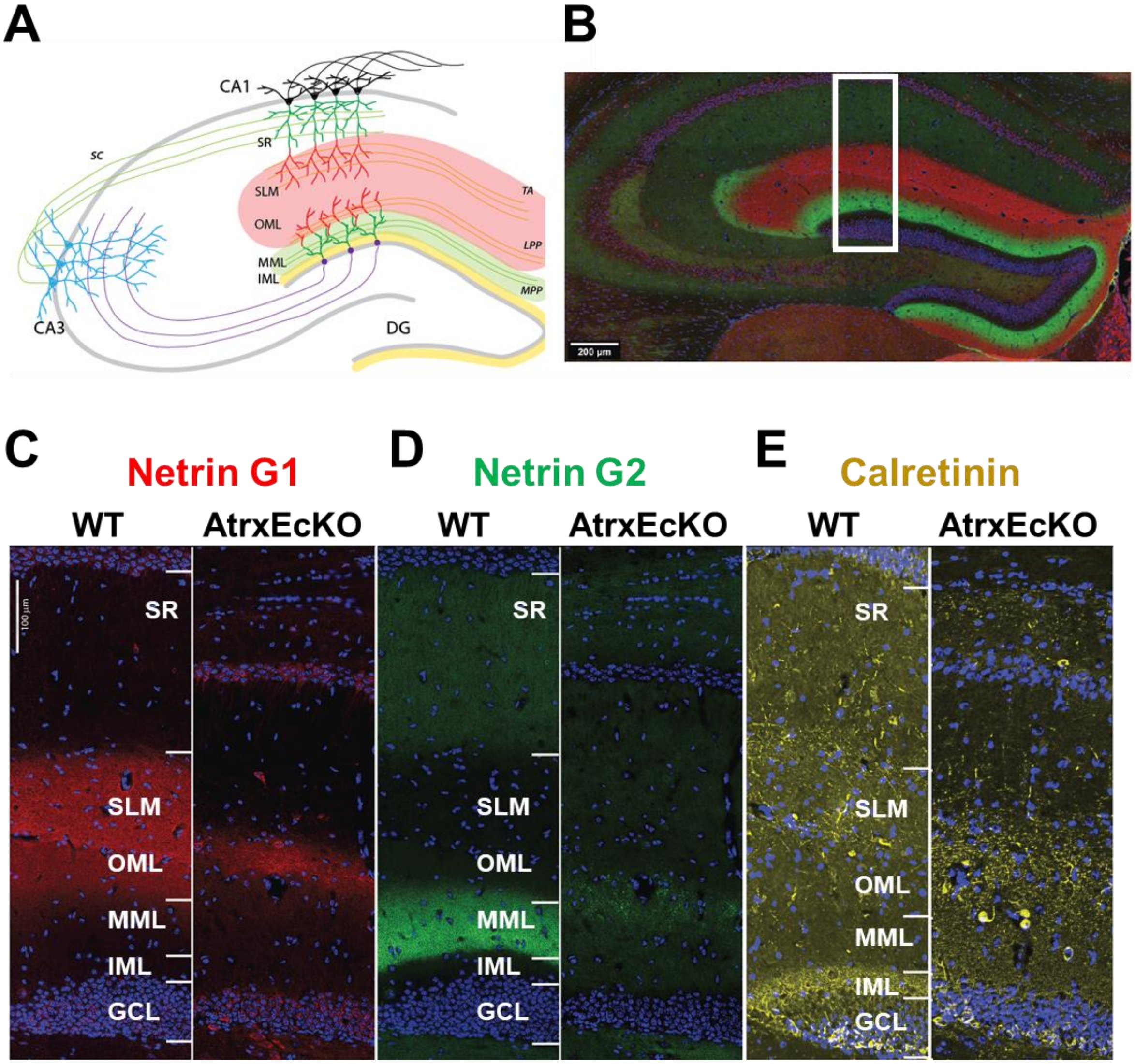
A
CA1
SR
SC
SLM
OML
MML
IML
TA
LPP
MPP
CA3
DG
B
200 µm
C
Netrin G1
WT
AtrxEcKO
100 µm
SR
SLM
OML
MML
IML
GCL
D
Netrin G2
WT
AtrxEcKO
SR
SLM
OML
MML
IML
GCL
E
Calretinin
WT
AtrxEcKO
SR
SLM
OML
MML
IML
GCL

Figure 5.21: AtrxEcKO mice have severe defects in hippocampal lamination.

A Schematic and **B** IF staining of a WT P40 coronal section using Netrin G1 (red), Netrin G2 (green) and DAPI (blue). Magnified image (white rectangle) of **C** Netrin G1 **D** Netrin G2 channels with DAPI. **E** A similar magnification was taken for calretinin (yellow). Scale bar is **B** 200µm and **C-E** 100µm. SR, *stratum radiatum*, SLM, *stratum lacunosum-moleculare*; OML, outer molecular layer; MML, middle molecular layer; IML, inner molecular layer; GCL, granule cell layer.

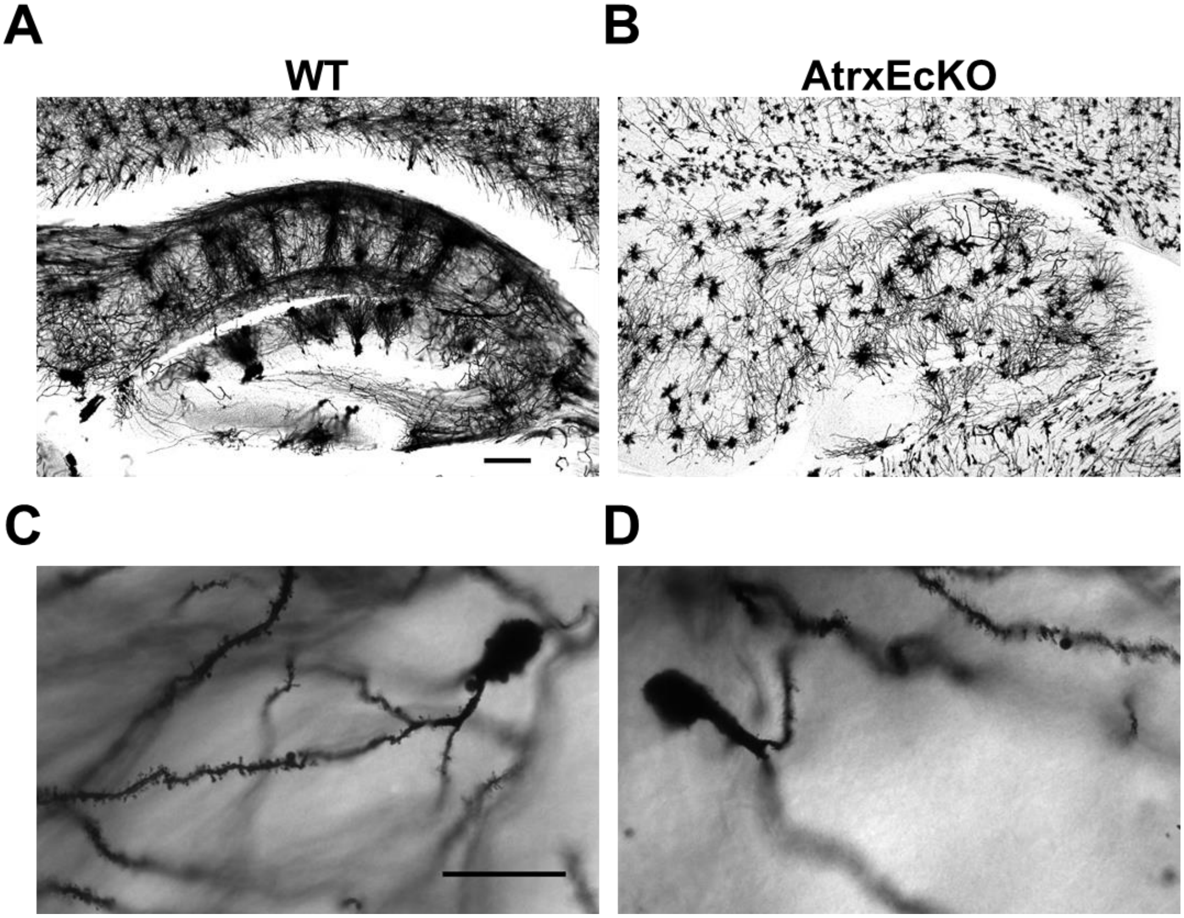

Figure 5.22: AtrxEcKO mice have less complex and disorganized neurons

Golgi Cox stained coronal sections of P40 hippocampus from WT (left) and AtrxEcKO (right) mice. Scale bar is 200µm.

We observed that the localization of the labeled neurons was altered and we noted differences in the dendritic arborization of AtrxEcKO mice, which appeared reduced and disorganized (Figure 5.22).

Taken together, these results revealed that *Atrx* deletion in *Emx1*+ cells significantly altered the hippocampal structure, multiple cell populations and the dendritic arborization. Thus, *Atrx* is crucial for proper hippocampal development.

5.7 Progenitors in the dentate gyrus migratory path

To explain the developmental defects observed in the DG of AtrxEcKO mice, we examined the proliferation, differentiation, and migration of granule cell progenitors in the dentate gyrus migratory path. We set up timed breeding and we injected the pregnant females with EdU at gestational day 16.5 and dissected the embryos one hour later. The heads were fixed in 4% PFA and sectioned coronally. We used those brain sections to do IF staining using Pax6 and EdU to label proliferating radial glial progenitors (Figure 5.23A-B). First, we quantified the percentage of Pax6+ cells within each Matrix and we found a reduction in Matrix 2 of AtrxEcKO mice (WT: M1 80.047% ± 4.642, M2 72.100% ± 2.906, M3 56.693% ± 0.918; AtrxEcKO: M1 81.610% ± 0.860, M2 49.355% ± 7.515, M3 42.975% ± 4.025; n=4) (Figure 5.23C). We assessed the percentage of EdU+ cells and found no change (WT: M1 34.997% ± 1.383, M2 8.620% ± 0.616, M3 4.193% ± 1.550; AtrxEcKO: M1 34.547% ± 2.541, M2 9.547% ± 1.174, M3 4.253% ± 0.057; n=4) (Figure 5.23D).

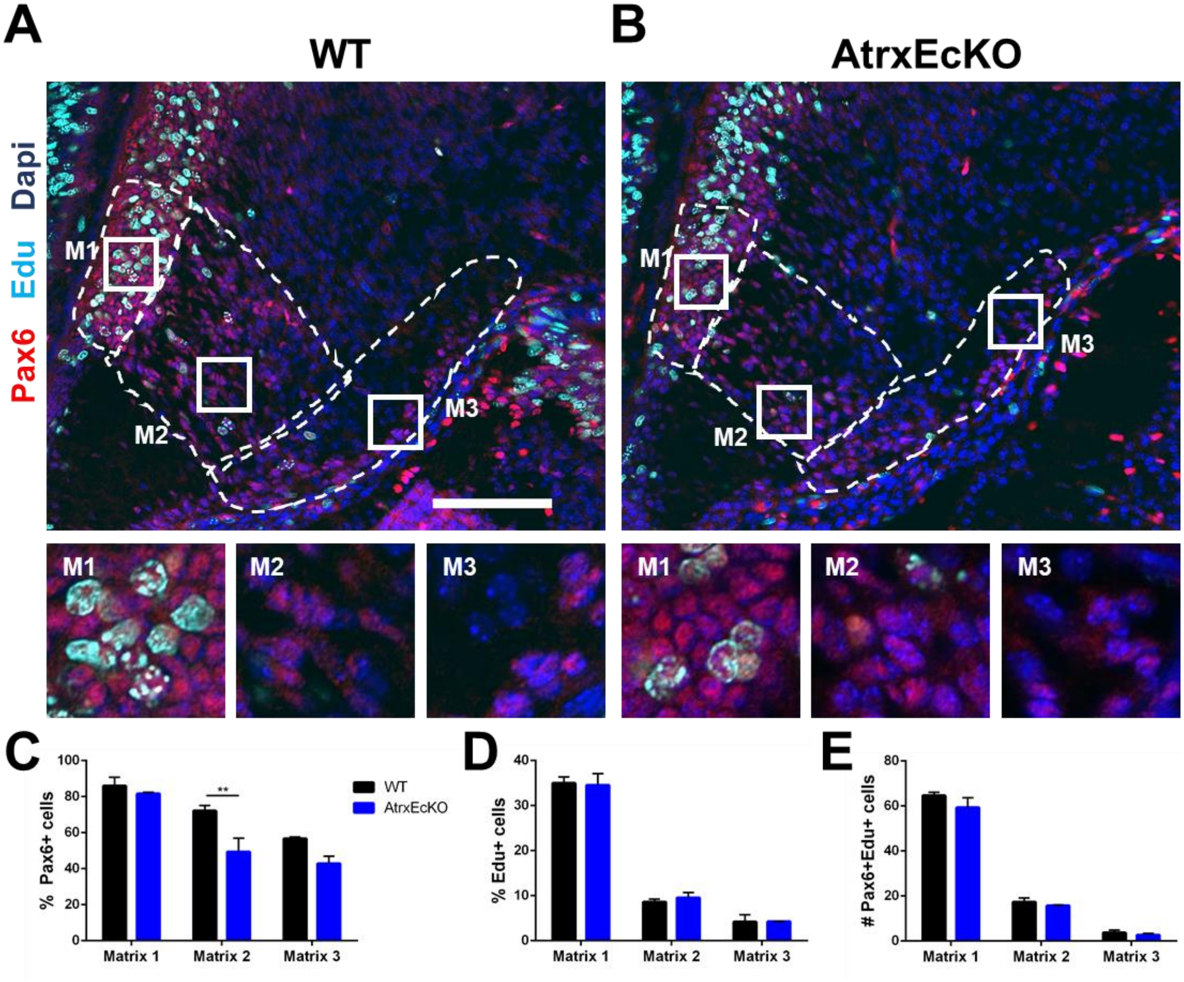

<u>Figure 5.23: *Atrx* loss affects the number of radial glial progenitors in the DG migratory path</u>

Pregnant females were injected with EdU one hour prior to embryo dissection. **A-B** E16.5 coronal sections were used to do IF staining using Pax6 (red), EdU (light blue) and DAPI (dark blue). Magnifications of Matrix 1 (M1), Matrix 2 (M2) and Matrix 3 (M3) are shown as white squares. **C** Percentage of Pax6+ cells, **D** EdU+ cells and **E** the number of double-labeled cells were quantified. Scale bar, 100µm. Data represent means ± SEM. n=4. ** $p < 0.01$.

Also, we found no difference in the number of double-labeled cells (WT: M1 64.667 cells ± 1.453, M2 17.33 cells ± 1.856, M3 3.667 cells ± 1.202; AtrxEcKO: M1 59.333 cells ± 4.333, M2 15.667 cells ± 0.333, M3 2.667 cells ± 0.667; n=4) (Figure 5.23E).

We repeated the experiment using Tbr2 and EdU to label proliferating intermediate progenitors in the matrices (Figure 5.24A-B). We found a significant decrease in the percentage of Tbr2+ cells in Matrix 2 of AtrxEcKO mice (WT: M1 28.340% ± 4.596, M2 38.243% ± 0.671, M3 53.477% ± 4.675; AtrxEcKO: M1 25.250% ± 2.962, M2 56.817% ± 1.516, M3 55.883% ± 8.854; n=5) (Figure 5.24C). Comparable to the results found in Figure 5.23D, we saw no change in the percentage of EdU+ cells (WT: M1 31.300% ± 0.125, M2 8.263% ± 1.610, M3 5.007% ± 0.585; AtrxEcKO: M1 32.863% ± 1.052, M2 5.790% ± 1.120, M3 3.227% ± 0.903; n=4) (Figure 5.24D). Moreover, we did not observe any change in the number of Tbr2+ EdU+ cells (WT: M1 7.000 cells ± 0.5777, M2 2.667 cells ± 0.333, M3 0.333 cells ± 0.333; AtrxEcKO: M1 7.000 cells ± 2.082, M2 4.000 cells ± 1.000, M3 0.667 cells ± 0.667; n=4) (Figure 5.24E)

The next set of experiments were performed on E17.5 embryos that received a 24-hour EdU pulse. First, we examined the proliferation rate of the cells in the matrices. We performed IF staining using brain sections that were co-labeled with Ki67 and EdU (Figure 5.25A-B). We quantified the percentage of Ki67+ cells in the matrices and found no difference between the WT and AtrxEcKO mice (WT: M1 49.423% ± 2.190, M2 34.023% ± 1.108, M3 28.103% ± 1.905; AtrxEcKO: M1 50.307% ± 0.612, M2 38.977% ± 1.989, M3 31.577% ± 2.060; n=4) (Figure 5.25C). Then we analyzed the percentage of EdU+ cells and found no change (WT: M1 44.340% ± 2.661, M2 21.310% ± 0.788, M3 15.570% ± 0.878; AtrxEcKO: M1 44.913% ± 2.627, M2 25.090% ± 0.748, M3 15.963% ± 0.355; n=4) (Figure 5.25D).

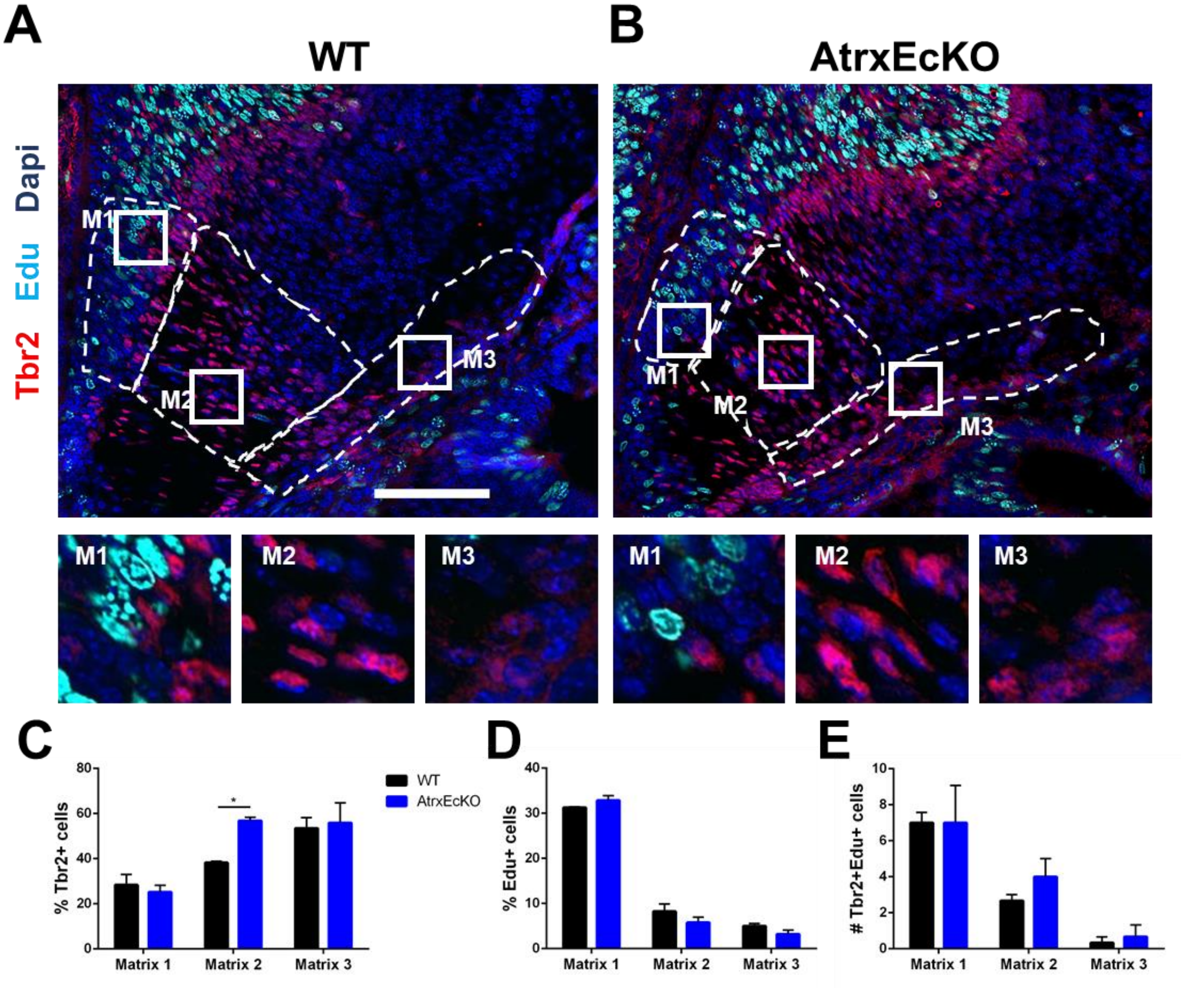

Figure 5.24: *Atrx* loss affects the number of intermediate progenitors in the DG migratory path

Pregnant females were injected with EdU one hour prior to embryo dissection. **A-B** E16.5 coronal sections were used to do IF staining using Tbr2 (red), EdU (light blue) and DAPI (dark blue). Magnifications of Matrix 1 (M1), Matrix 2 (M2) and Matrix 3 (M3) are shown as white squares. **C** Percentage of Tbr2+ cells, **D** EdU+ cells and **E** the number of double-labeled cells were quantified. Scale bar, 100µm. Data represent means ± SEM. n=4. * $p < 0.05$.

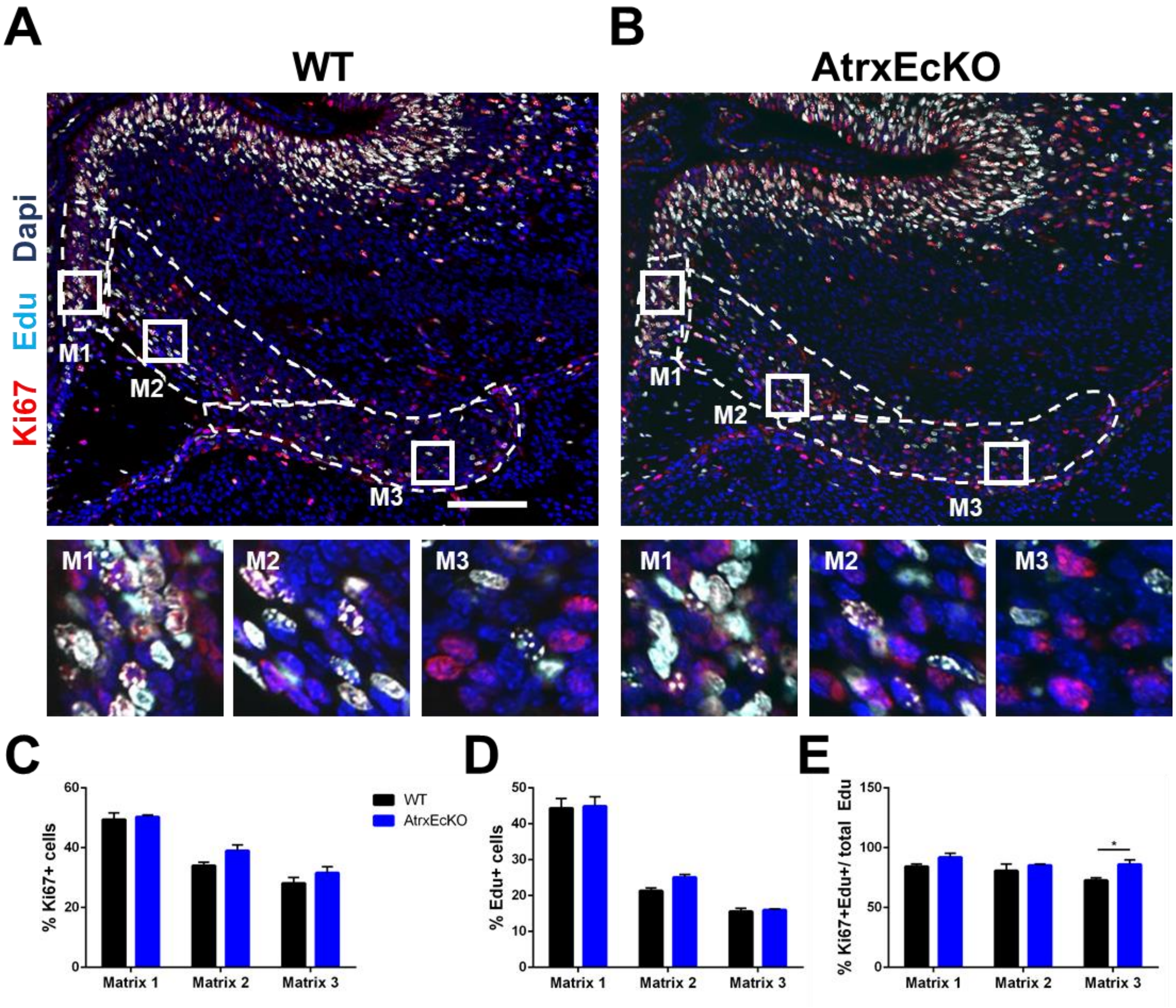

Figure 5.25: EdU labeled progenitors show similar progression through the different hippocampal matrices at E17.5

Pregnant females were injected with EdU 24 hour prior to embryo dissection. **A-B** E17.5 coronal sections were used to do IF staining using Ki67 (red), EdU (light blue) and DAPI (dark blue). Magnifications of Matrix 1 (M1), Matrix 2 (M2) and Matrix 3 (M3) are shown as white squares. **C** Percentage of Ki67+ cells, **D** EdU+ cells and **E** double-labeled cells were quantified. Scale bar, 100µm. Data represent means ± SEM. n=4. * $p < 0.05$.

Lastly, we saw an increase in the percentage of double-labeled cells in Matrix 3 of AtrxEcKO mice (WT: M1 84.257% ± 2.135, M2 80.640% ± 5.650, M3 72.657% ± 2.180; AtrxEcKO: M1 91.933% ± 3.347, M2 85.263% ± 1.151, M3 86.123% ± 3.821; n=4) (Figure 5.25E).

Next, we followed the progression of radial glial progenitors in the matrices at E17.5 after a 24-hour EdU pulse. Progenitors were labeled using Pax6 and EdU (Figure 5.26A-B). We quantified the percentage of Pax6+ cells in each Matrix and found no change between the WT and AtrxEcKO mice (WT: M1 33.185% ± 0.145, M2 15.665% ± 1.375, M3 10.225% ± 1.035; AtrxEcKO: M1 27.900% ± 1.090, M2 17.380% ± 2.550, M3 7.230% ± 1.420; n=4) (Figure 5.26C). Similar to the previous figure, we found no change in the percentage of EdU+ cells (WT: M1 47.125% ± 8.525, M2 21.725% ± 1.335, M3 16.865% ± 1.505; AtrxEcKO: M1 37.680% ± 4.350, M2 22.010% ± 4.570, M3 13075% ± 1.455; n=4) (Figure 5.26D). Also, we saw no significant difference in the percentage of double-labeled cells (WT: M1 73.225% ± 15.415, M2 72.355% ± 12.575, M3 61.005% ± 16.775; AtrxEcKO: M1 73.425% ± 11.355, M2 78.335% ± 6.665, M3 58.330% ± 1.190; n=4) (Figure 5.26E). However, we observed that the Pax6+ cells were dispersed in Matrix 2 of AtrxEcKO mice whereas in the WT, the cells were organized and the migration path was clearly visible.

Next, we quantified the percentage of intermediate progenitors using Tbr2 and EdU (Figure 5.27A-B). We observed no difference in the percentage of Tbr2+ cells (WT: M1 48.633% ± 0.340, M2 37.147% ± 3.943, M3 34.293% ± 0.534; AtrxEcKO: M1 47.950% ± 0.693, M2 33.580% ± 1.069, M3 32.690% ± 2.555; n=4) (Figure 5.27C).

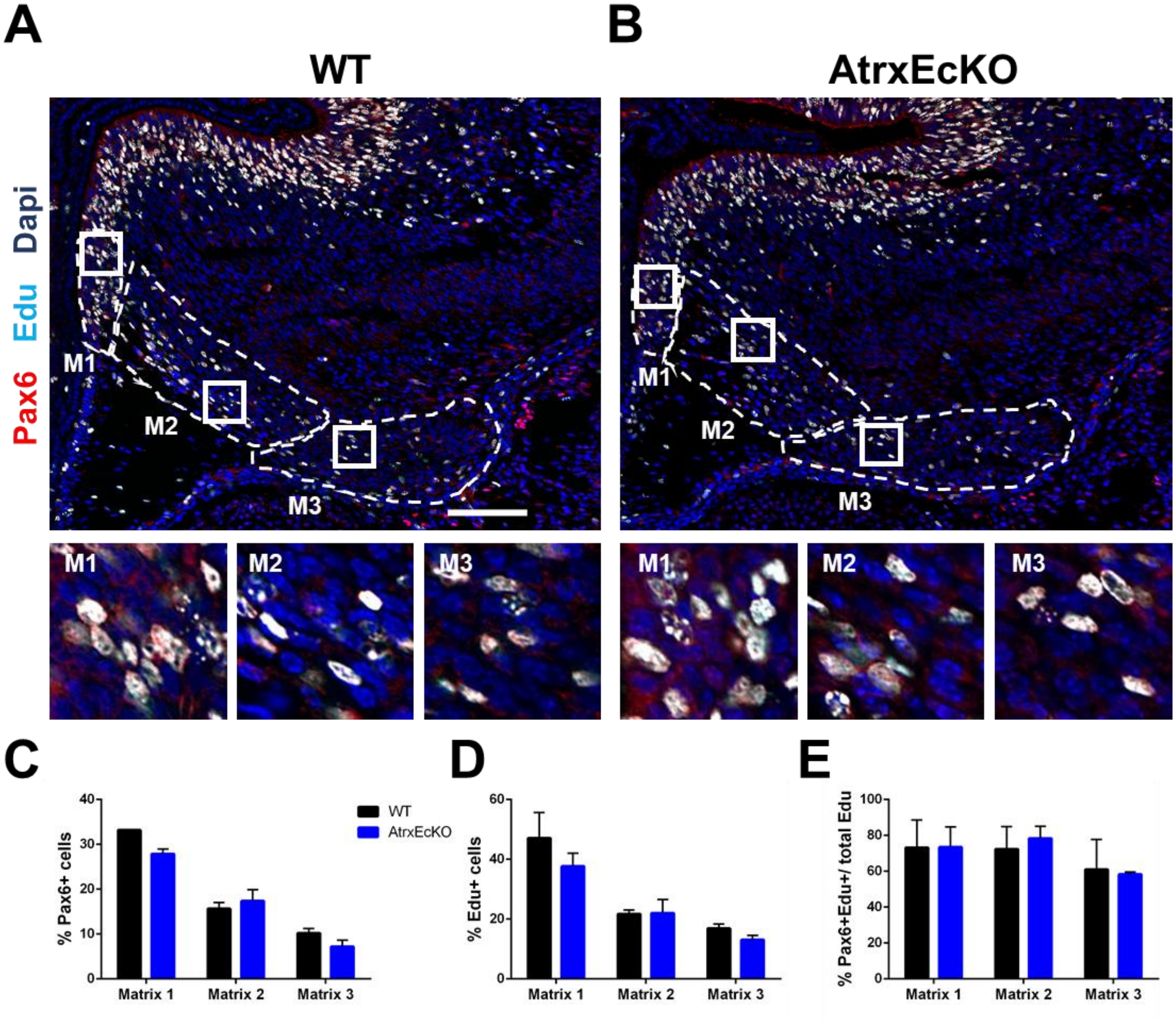

Figure 5.26: Progenitor pool in the DG migratory path are unaffected in E17.5 AtrxEcKO mice

Pregnant females were injected with EdU 24 hour prior to embryo dissection. **A-B** E17.5 coronal sections were used to do IF staining using Pax6 (red), EdU (light blue) and DAPI (dark blue). Magnifications of Matrix 1 (M1), Matrix 2 (M2) and Matrix 3 (M3) are shown as white squares. **C** Percentage of Pax6+ cells, **D** EdU+ cells and **E** double-labeled cells were quantified. Scale bar, 100µm. Data represent means ± SEM. n=4.

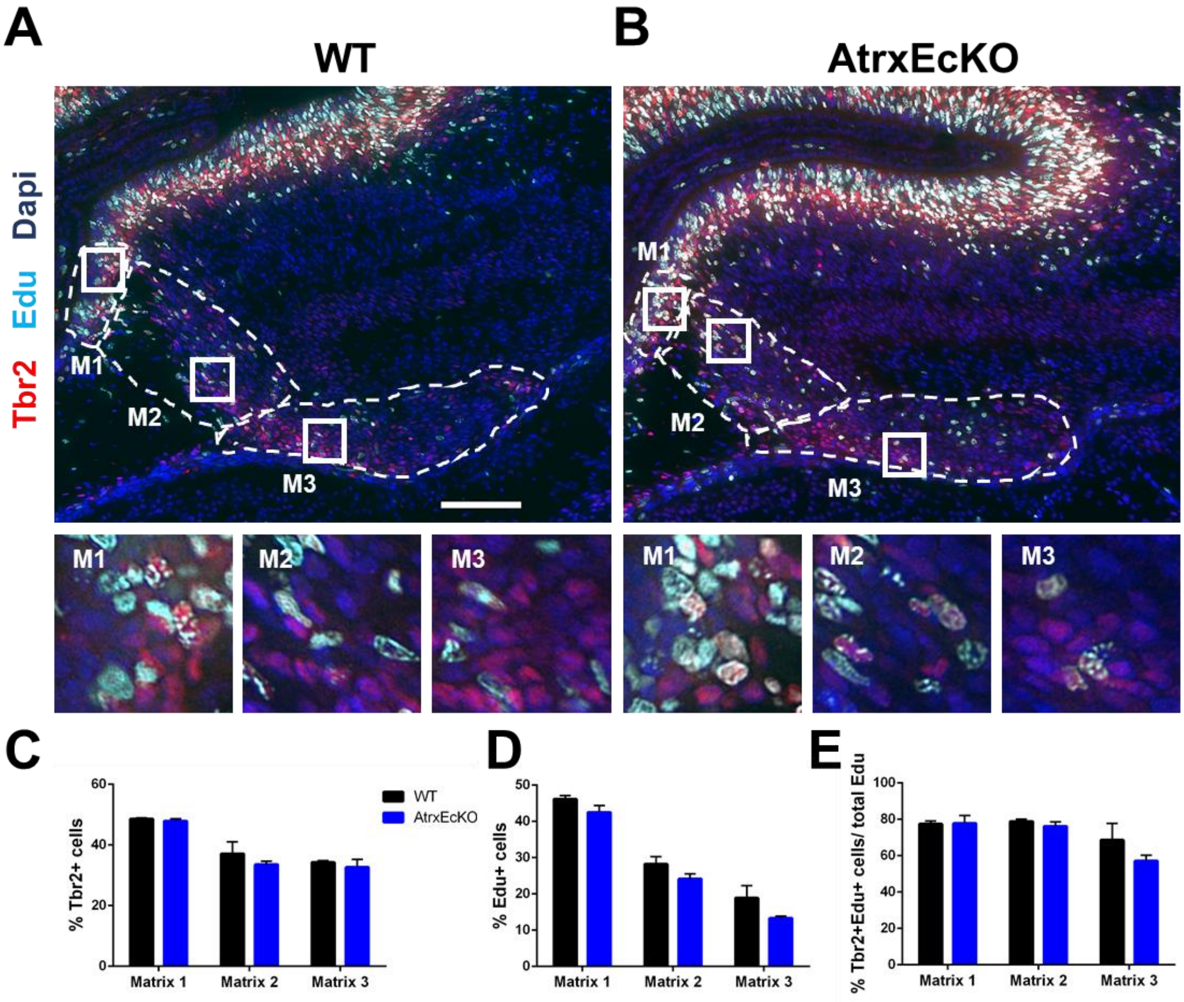

Figure 5.27: Intermediate progenitor pool in the DG migratory path are unaffected by *Atrx* deletion at E17.5

Pregnant females were injected with EdU 24 hour prior to embryo dissection. **A-B** E17.5 coronal sections were used to do IF staining using Tbr2 (red), EdU (light blue) and DAPI (dark blue). Magnifications of Matrix 1 (M1), Matrix 2 (M2) and Matrix 3 (M3) are shown as white squares. **C** Percentage of Tbr2+ cells, **D** EdU+ cells and **E** double-labeled cells were quantified. Scale bar, 100µm. Data represent means ± SEM. n=4.

Furthermore, we did not find any change in the percentage of EdU+ cells (WT: M1 16.150% ± 0.987, M2 28.210% ± 2.109, M3 18.900% ± 3.398; AtrxEcKO: M1 42.500% ± 1.866, M2 24.140% ± 1.407, M3 13.307% ± 0.562; n=4) (Figure 5.27D) and double-labeled cells (WT: M1 77.423% ± 1.660, M2 78.880% ± 1.220, M3 68.640% ± 9.068; AtrxEcKO: M1 77.830% ± 4.223, M2 76.183% ± 2.385, M3 57.133% ± 3.198; n=4) (Figure 5.27E).

Next, we examined the migration and proliferation of both populations of progenitors in the matrices following a 24-hour EdU pulse. We injected the pregnant females at gestational day 16.5 and collected the embryo at E17.5. We followed the progression of the dividing cells in the matrices by quantifying and comparing the location of the EdU+ cells at E16.5 that were labeled one hour and the EdU+ cells at E17.5 that were labeled for 24 hours (Figure 5.28). We generated the graphs from the E16.5 mice by pooling the results from the EdU- Pax6 and EdU-Tbr2 IF staining experiment presented in Figure 5.23 and 5.24. Similarly, the graphs for the E17.5 mice were done by merging the results from the EdU-Ki67, EdU-Pax6 and EdU-Tbr2 experiments (Figure 5.25-5.27). We visually compared the overall morphology of the DG migratory path at E16.5 and E17.5 for changes. At 16.5, the DG migratory path was smaller and more condensed. At 17.5, we observed that Matrix 2 expanded to almost twice its size and that Matrix 3 was pushed down by Matrix 2 and elongated.

We quantified the number of EdU+ cells within each Matrix and found no difference (WT: M1 67.167 cells ± 1.014, M2 15.167 cells ± 1.493, M3 3.667 cells ± 0.882; AtrxEcKO: M1 66.000 cells ± 1.317, M2 18.500 cells ± 2.277, M3 4.667 cells ± 0.882; n=8) (Figure 5.28C).

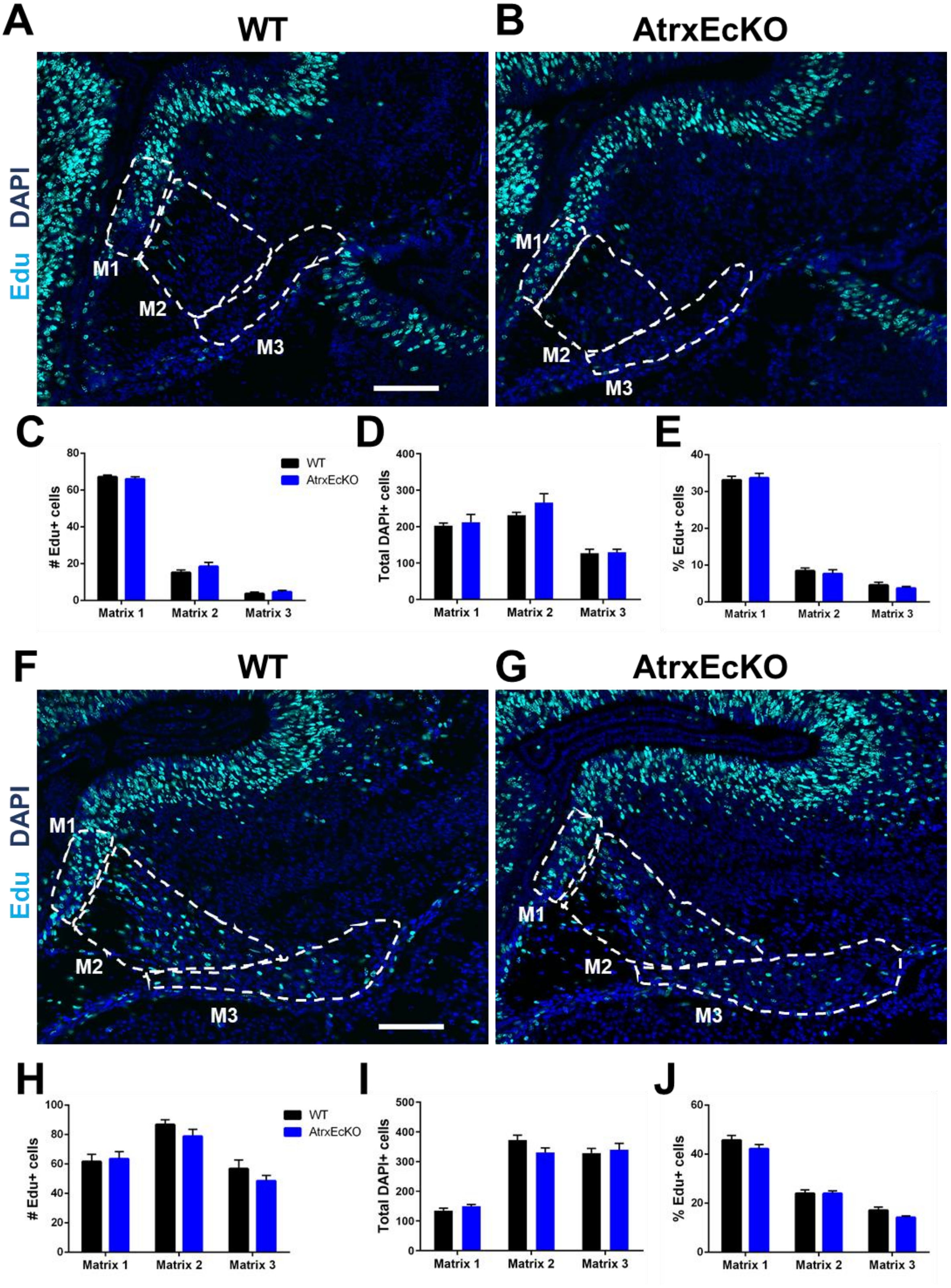
A
WT
B
AtrxEcKO
Edu DAPI
M1
M2
M3
C
Edu+ cells
0
20
40
60
80
Matrix 1
Matrix 2
Matrix 3
WT
AtrxEcKO
D
Total DAPI+ cells
0
100
200
300
400
Matrix 1
Matrix 2
Matrix 3
E
% Edu+ cells
0
10
20
30
40
Matrix 1
Matrix 2
Matrix 3
F
WT
G
AtrxEcKO
Edu DAPI
M1
M2
M3
H
Edu+ cells
0
20
40
60
80
100
Matrix 1
Matrix 2
Matrix 3
WT
AtrxEcKO
I
Total DAPI+ cells
0
100
200
300
400
500
Matrix 1
Matrix 2
Matrix 3
J
% Edu+ cells
0
20
40
60
Matrix 1
Matrix 2
Matrix 3

Figure 5.28: Progression of proliferating progenitors in DG migratory path at E16.5 and E17.5

A-E Pregnant females were injected with EdU one hour prior to embryo dissection. **A-B** E16.5 coronal sections were used to do IF staining using EdU (cyan) and DAPI (dark blue). **C** The number of EdU+ cells, **D** DAPI+ cells and **E** the percentage of EdU+ cells were quantified. **F-J** Pregnant females were injected with EdU 24 hour prior to embryo dissection. **F-G** E16.5 coronal sections were used to do IF staining using EdU (light blue) and DAPI (dark blue). **H** The number of EdU+ cells, **I** DAPI+ cells and **J** the percentage of EdU+ cells were quantified. Scale bar, 100µm. Data represent means ± SEM. n=8.

We assessed the total number of DAPI+ cells and saw no change (WT: M1 202.833 cells ± 6.930, M2 231.167 cells ± 7.918, M3 126.833 cells ± 11.173; AtrxEcKO: M1 212.200 cells ± 21.214, M2 265.800 cells ± 24.632, M3 129.600 cells ± 8.501; n=8) (Figure 5.28D). Lastly, we found no change in the percentage of EdU+ cells (WT: M1 33.148% ± 1.034, M2 8.442% ± 0.775, M3 4.600% ± 0.763; AtrxEcKO: M1 33.705% ± 1.286, M2 7.668% ± 1.129, M3 3.740% ± 0.465; n=8) (Figure 5.28E). At E16.5, we observed that the majority of the dividing cells were in Matrix 1 and only a few positive cells were in Matrix 3.

At 17.5, we found no significant difference in the number of EdU+ cells (WT: M1 61.625 cells ± 4.899, M2 86.750 cells ± 3.266, M3 56.750 cells ± 5.993; AtrxEcKO: M1 63.500 cells ± 4.979, M2 78.875 cells ± 4.760, M3 48.500 cells ± 3.775; n=8) (Figure 5.28H). However, we saw that the number of EdU+ cells in Matrix 2 was five times higher at E17.5 compared to E16.5 in AtrxEcKO mice. This suggested that the proliferating cells were migrating along the matrices. Next, we examined the number of DAPI cells and found no difference between AtrxEcKO and the WT mice (WT: M1 134.500 cells ± 8.679, M2 372.250 cells ± 16.545, M3 328.500 cells ± 15.726; AtrxEcKO: M1 149.250 cells ± 6.259, M2 330.500 cells ± 15.593, M3 339.625 cells ± 21.892; n=8) (Figure 5.28I). Also, we observed no change in the percentage of EdU+ cells in the matrices (WT: M1 45.715% ± 1.908, M2 24.001% ± 1.459, M3 17.143% ± 1.304; AtrxEcKO: M1 42.200% ± 1.708, M2 23.964% ± 1.106, M3 14.245% ± 0.614; n=8) (Figure 5.28J). These results suggested that the EdU+ cells of AtrxEcKO mice have a comparable migration pattern and proportion of proliferating cells to the WT animals. Moreover, this suggests that increased replication stress is not contributing significantly to the overall reduction in the size of the hippocampus and dentate gyrus, as has been shown in the VZ of the neocortex [205].

5.8 Summary of Findings

In sum, we successfully created a viable forebrain-specific Atrx knockout mouse to generate a model for the ATR-X syndrome that survives postnatally. AtrxEcKO mice are smaller at P90 and the brain width is also reduced in comparison to the WT mice. We found that the general morphology of the AtrxEcKO hippocampus is altered and the size is significantly smaller. Contrary to other Atrx knockout mouse models, AtrxEcKO mice had a similar cortical thickness to the WT mice. Also, there were no differences in the Satb2- and Tbr1+ neuronal populations. However, we found that the Ctip2+ cell population was increased and most of the cells were also expressing Tbr1.

We used multiple approaches to define myelination defects and white matter abnormalities in the AtrxEcKO mice, which is also found in ATR-X patients [217]. Indeed, the volumetric analysis revealed that the stria medullaris and the anterior commissure, which are white matter tracks, were altered in AtrxEcKO mice. IF staining of the CC showed a significant reduction in its thickness, morphology, and a reduction in the number of mature oligodendrocytes were identified. Lastly, we identified multiple GO terms associated with the myelination process in the downregulated transcripts.

Behavioural assessment of AtrxEcKO mice revealed a hyperactivity phenotype and seizure-like episodes. Also, we found that AtrxEcKO mice had excessive grooming behaviour, which can be observed in patients with autism spectrum disorders [275]. Unfortunately, we were not able to characterize the learning and memory ability of the mice due to the hyperactivity phenotype.

We identified multiple genes of interest that were dysregulated in the hippocampus of AtrxEcKO mice, namely netrin G1, netrin G2, netrin5 and neurogenin2. Also, Gene Ontology analysis revealed several clusters associated with cell adhesion, signal transduction and cell differentiation.

We characterized the hippocampal defects by examining different cell populations. We found that the DG of AtrxEcKO mice was ~60% smaller than the WT mice and that the number of granule cells was reduced by ~15%. Also, AtrxEcKO mice had significantly less calretinin+ cells and they were missing markers (Netrin G1/G2) of the inner and middle molecular layer suggesting that inputs to the DG may be compromised. The *stratum lacunosum-moleculare* layer, labeled by netrin G1, was thinner by ~70% in AtrxEcKO mice. Lastly, we noted a striking difference in the dendritic arborization of AtrxEcKO mice, which appeared reduced and disorganized.

Finally, we examined the proliferation, migration and localization of the DG progenitors to give us insights into the developmental defects previously observed. We found that Atrx loss affects the number of radial and intermediate progenitors at E16.5 but, by E17.5, the percentage of progenitors in each Matrix was comparable to the WT mice. Also, the migration of the proliferating progenitors at E16.5 and E17.5 was similar to the WT mice.

Chapter 6: Discussion

6.1 Summary of Findings – NEDDFL mouse model

Bptf is a large regulatory protein and part of the NURF chromatin remodeling complex [132]. Missense or loss-of-function mutations of one *BPTF* allele have been identified as the cause of the Neurodevelopmental Disorder with Dysmorphic Facies and distal Limb anomalies (NEDDFL) syndrome [110]. This recently identified syndrome is characterized by developmental, motor and speech delays, intellectual disability, brain abnormalities, dysmorphic features and seizures [149, 150]. Although recent studies have been conducted to elucidate the function of *Bptf* in various cell types, research on this disorder is only at the beginning and more characterization is needed to fully understand the extant of the phenotype.

The first part of this thesis was aimed at generating a mouse model with a greater coverage of *Bptf* deletion in the neural system to mimic NEDDFL. We conditionally inactivated *Bptf* in neural progenitors of the central and peripheral nervous system using the *Nestin*-Cre driver. We have shown that *Bptf* NcKO mice have major morphological brain defects, including an abnormal cortex and malformed hippocampus. Furthermore, assessment of *Bptf* NcKO mice revealed key behavioural features found in NEDDFL patients.

6.2 *Bptf* is essential to produce deep-layer cortical neurons

The neocortex is formed in an inside-out manner and can be divided into 6 layers. Interestingly, the uniqueness of each layer comes from its developmental timing, gene expression patterns, cell types and neuronal connections [3]. The deep layer cortical neurons are generated earlier than in the upper superficial layers [276]. We believe that *Bptf* is necessary to produce deep-layer neurons and is required for proper cortex formation. In our *Bptf*; *Nestin*-

Cre mouse model, we found several indications to support this claim. First, we found that the gross morphology and the size of the *Bptf* NcKO brains were significantly affected by *Bptf* deletion (Figure3.1D). This finding was also observed in another *Bptf* conditional KO model (*Bptf*; *Emx1*-Cre) [277]. In addition, we examined the cortical lamination and observed several alterations (Figure 3.3). We saw a significant reduction in the cortical thickness and in the number of layer VI neurons. There was no clear distinction between layer V and VI and almost all Tbr1+ cells were also expressing Ctip2 in the *Bptf* NcKO mice. In *Bptf*; *Emx1*-Cre mice, there was a 60% reduction in the number of low-expressing Ctip2 cells in layer VI [277]. Lastly, the cortical dysgenesis and the aberrant distribution of the cortical neurons strongly suggest that *Bptf* is crucial for cortical development.

One of the possible explanations is that the cortical neurons have migration defects. The total number of cells in the cortex of *Bptf* NcKO mice is comparable to the WT animal. Neurons from layer II to IV can migrate upward but perhaps not far enough resulting in thinner layers and a thinner cortex. Also, the thinning of the layers would explain why the neurons are densely packed and overlapping. Another possible explanation for the reduction in layer VI neurons is cell fate defects. Cortical neurons in layer VI reduce the expression of *Ctip2* to specify their identity [3]. In layer V, *Ctip2* represses the expression of *Tbr1* allowing for the production of the proper neuronal cell type. Since we observed that most of the Ctip2+ cells were also Tbr1+, it is possible that *Bptf* NcKO mice require more time to switch on and off certain cell markers. Indeed, it is possible that *Bptf* is required to silence *Ctip2* in layer VI, which would explain the high levels of Ctip2-expressing cells within that layer.

To validate one of these hypotheses, characterizing the cortex at P7 would give essential information. At P7, all the cortical layers are clearly separated, which means that the migration process is completed and that the cortical neurons acquire their final identity. The quantitation of each layer population would give us insights into the cell fate process. For example, we could determine whether the layer V and VI neurons are still expressing both Ctip2 and Tbr1 markers or if one of the 2 populations increased at the expense of the other population. In *Bptf*; *Emx1*-Cre mice, cell fate defects were affecting the deep layer neurons [151]. They also quantified the number of Ctip2+ cells located in other layers and found lamination defects as well as cell fate defects. This experiment could be repeated using our mouse model to determine whether some cortical cell populations are also located outside of their residing niche.

6.3 *Bptf* is necessary for the formation of the hippocampus

The majority of the brain characterization performed on NEDDFL patients and previous *Bptf* KO mice were focused on the cortex. Because of this, there are still no reports of hippocampal defects. Since it is known that NEDDFL patients have intellectual disabilities as well as learning and memory deficits, it would be fair to extrapolate and assume that they have some hippocampal alterations. In our *Bptf*; *Nestin*-Cre mouse model, we found that the hippocampus of *Bptf* NcKO mice was strikingly smaller than the WT mice and that all the sub-regions had hypocellularity (Figure 3.4). We also observed that the mature neurons were scattered throughout the hippocampus instead of lining the outside border.

In Smarca1 (Snf2L) and Smarca5 (Snf2H) conditional KO mice, no hippocampal defect was observed [104, 278]. It is interesting because both proteins can interact with BPTF in the NURF complex. On the other hand, the dysgenesis of the hippocampus was also observed in another neurodevelopmental disorder phenotypically similar to NEDDFL called the William-

Beuren syndrome (WBS). WBS is caused by deletions within the WSTF gene, a subunit of the WICH complex, a chromatin remodeler of the ISWI family [279]. In a WBS mouse model, it was discovered that the mutant mice exhibited neuroanatomical defects in hippocampus development [280]. More specifically, they found an increase in apoptotic cells and a reduction in the number of granule cells.

Other chromatin remodelers have been shown to play a critical role in the formation, development and maintenance of the hippocampus. Chromatin remodeler *CHD7* maintains neural stem cell quiescence preventing the premature depletion of the stem cell pool in the hippocampus [281]. On the other hand, conditional deletion of BAF170, a subunit of the BAF complex, depletes the pool of radial glial-like progenitors in the DG [282]. Behavioural analysis of these mice also revealed learning deficits during the MWM. Lastly, Bcl11b, a protein associated with the NuRD complex, regulates the proliferation of the progenitors by a feedback mechanism [283]. Deletion of Bcl11b leads to a reduction in proliferating progenitors and, ultimately, a reduction of dentate granule cells. Also, it was shown that the differentiation of postmitotic neurons is dependent on Bcl11b expression. In absence of Bcl11b, the neurons fail to integrate into de hippocampal circuitry, which leads to learning and memory impairments.

Although there are no previous studies linking *Bptf* deletion to hippocampal alterations, there are studies that showed its implication in progenitors. For example, *Bptf* is required for the self-renewal capacity of mammary stem cells [138]. Another study showed that in absence of *Bptf*, cortical progenitors have a prolonged cell cycle length [151]. Interestingly, it was also found that in a *Bptf* conditional KO mouse model, there was increased neuronal cell death associated with altered expression of fate-determining transcription factors and apoptotic signaling pathways.

Based on the previous findings, we believe the cause of the dysgenesis of the hippocampus is due to defects in the progenitors and/or increased cell death. To test this, we could examine the progenitor pool to determine whether the total number of radial glial and intermediate progenitors is decreased. We could also verify the number of proliferating progenitors, which would affect the size of the progenitor pool and, eventually, the number of postmitotic cells. Second, we could perform an immunostaining using cleaved caspase 3 and γ-H2AX antibodies to label apoptotic cells and DNA damage. This experiment would allow us to determine whether the loss of *Bptf* in progenitors leads to increased cell death resulting in hypocellularity and a smaller hippocampus.

6.4 Deletion of *Bptf* in neural progenitors recapitulates some behavioral features of NEDDFL patients

The behavioural characterization of NEDDFL patients is limited due to the low number of diagnosed individuals and the novelty of the syndrome. To date, we know that most patients experience developmental delay, intellectual disability and motor delay [110, 149]. However, those terms are vague, making it difficult to compare them with the behavioural phenotype we observed in our mouse model. To account for that, we compared the behavioural phenotype of *Bptf* NcKO mice with NEDDFL patients as well as patients with Williams-Beuren syndrome (WBS).

The first behavioural phenotype that we observed in the *Bptf* NcKO mice is the motor deficits. We performed the rotarod test to assess the coordination and endurance of the mice during a complex motor task. We saw that the *Bptf* NcKO mice were falling more quickly than the WT mice (Figure 3.5E). These results suggest that *Bptf* deletion in neural progenitors leads to locomotor deficits when presented with a complex motor function task. Most NEDDFL patients experience motor disabilities, some of which are attributed to skeletal abnormalities [110]. Also, gross motor skills defects are observed in WBS patients [284, 285]. The lack of endurance of *Bptf* NcKO mice on the rotarod could be explained by low muscle tone. Interestingly, hypotonia is observed in NEDDFL patients and it is associated with gait impairments in WBS patients [110, 286]. We assessed the gait of the *Bptf* NcKO mice and found significant impairments (Figure 3.6). We saw that the fore limb and hind limb paws had longer contact time with the belt and, inevitably, less time in the swinging and propulsion phase. These results suggest that *Bptf* NcKO mice are struggling to lift and swing their paws during a stride, which could be the result of hypotonia. In agreement with that, we saw that the *Bptf* NcKO mice made smaller strides and increase their stride frequency in order to keep up with the set belt speed. Interestingly, a decrease in the range of motion at the hips, knees and ankles was noted in some WBS patients [287]. Other patients reported limb and gait ataxia as well as a reduced stride length [288]. Unfortunately, there is no report of gait impairments yet for NEDDFL patients, which could be due to the early stage of characterization of the syndrome. Lastly, we observed fine motor skill defects in *Bptf* NcKO mice. These skills are innate daily activities that require several complex and coordinated actions. We found that *Bptf* NcKO mice were incapable of building a nest and were inefficient at grooming (Figure 3.9A, B, E, F). Although there is no data for NEDDFL patients, there are multiple reports of fine motor skills defects in patients with neurodevelopmental disorders, including WBS, Coffin-Siris syndrome and Rett syndrome [289-291].

One of the key characteristics of NEDDFL is intellectual disability. In our mouse model, we detected severe learning and memory deficits. We found that the *Bptf* NcKO mice were incapable of learning the location of a hidden platform using spatial cues (Figure 3.8A-C). We discovered that the associative memory was also affected in our mouse model (Figure 3.8D-G). Indeed, the *Bptf* NcKO mice were unable to associate an aversive stimulus to a neutral context and an aversive stimulus to neutral auditory cue. Learning and memory impairments or intellectual disabilities are commonly found in neurodevelopmental disorders.

Even though the behavioural data for NEDDFL patients is limited, we relied on other related neurodevelopmental disorders caused by mutation in chromatin remodelers to analyze the behaviour of our mouse model. We believe that our *Bptf*; *Nestin*-Cre mouse model mimic the behavioural phenotype of NEDDFL. As more information are gathered on this new syndrome, we will be able to further confirm the validity of our model.

6.5 Summary of Findings – Excitatory and inhibitory

A common cause of neurodevelopmental disorders are defects in epigenetic regulation. Mutations in the ATRX gene, an ATP-dependent chromatin remodeling protein, causes the ATR-X syndrome [129]. The ATR-X syndrome is a severe neurodevelopmental disorder affecting males characterized by intellectual disability and, sometimes, classified as an autism spectrum disorder (ASD). Often, ASD arise from single genes that are mutated which play complex roles in multiple cell types and can give rise to changes in excitation or inhibition altering network activity. The disturbance of the balance between the excitatory and inhibitory systems are thought to be implicated in the pathogenesis of numerous ASDs [233].

In the second part of this thesis, our goal was to determine the contributions of the glutamatergic and GABAergic neurons to the phenotype of the ATR-X syndrome. We conditionally removed *Atrx* in the excitatory and inhibitory neurons using the *Vglut2*-Cre and *Viaat*-Cre drivers, respectively. We have shown that both AtrxVgKO and AtrxVtKO mice die embryonically or shortly after birth. In addition, hippocampal assessment revealed distinct defects in both mouse models.

6.6 *Atrx* deletion in excitatory neurons

The glutamatergic system plays a significant role in neurodevelopmental disorders and autism spectrum disorders [292, 293]. An imbalance between the excitatory and inhibitory inputs was found in multiple patients and the glutamatergic system is often the target of drug treatments [294]. Animal studies of Rett syndrome found that deletion of *Mecp2* in *Vglut2*+ cells recapitulates part of the human phenotype [262]. Another group used *Vglut1*-Cre to remove *Mecp2* in excitatory neurons and found a 46% reduction in synaptic response in the hippocampus [295]. It was concluded that Mecp2 regulated the glutamatergic synapse formation and in its absence, the glutamatergic network is significantly altered.

Here, we wanted to determine the contribution of the excitatory neurons to the ATR-X syndrome's phenotype. We used *Vglut2*-Cre mice to specifically remove *Atrx* in excitatory neurons. Unfortunately, the AtrxVgKO mice died embryonically or shortly after birth. *VGLUT2* is mainly expressed in the spinal cord, brain stem and subcortical areas [296, 297]. The distribution of the vesicular transporter may account for the high lethality of our *Atrx* KO mouse model and, because of that, we were not able to perform behaviour tests or follow the evolution of the brain postnatally. We found no defect in the cortical layers but we did observe some hippocampal defects (Figure 4.4-4.5). The number of mature neurons in the CA1 and CA3 hippocampal regions were significantly reduced in AtrxVgKO mice. A recent study found that *VGLUT2* is strongly expressed in the subiculum, which is a structure positioned between the hippocampus, entorhinal cortex and other cortical areas [298]. The subicular pyramidal neurons mediate the hippocampal-cortical interactions although little is known about their function. It is possible that those neurons lacking *Atrx* are able to influence the inputs going to the hippocampus [299]. Therefore, the CA1 and CA3 neurons are not receiving the proper signals for localization and differentiation.

Unfortunately, AtrxVgKO mice are incompatible with life, which prevents the analysis of older mice. Interestingly, mice without MeCP2 can survive whereas ATRX deletion is lethal. This striking difference between MeCP2;*Vglut2* KO and AtrxVgKO mice may be the confounding factor that precluded a broader analysis. Perhaps by switching the Cre driver to *Vglut1,* which is predominantly expressed in the cortex and hippocampus, we would get a viable mouse model [300-302]. Furthermore, in Chapter 5, we generated a forebrain-specific mouse model using *Emx1* to drive the expression of Cre. Interestingly, one of the targets of *Emx1*-Cre is the excitatory neurons.

6.7 *Atrx* deletion in inhibitory neurons leads to progenitor pool defects

The involvement of the inhibitory system has been demonstrated in multiple ASDs. However, there are still no research studies that have been performed to assess its involvement in the ATR-X syndrome. In the second part of this thesis, we wanted to characterize a mouse model with an *Atrx* deletion in GABAergic neurons. We found that AtrxVtKO mice either died embryonically or survived for a few hours after birth. *Viaat*, also referred in the literature as vesicular GABA transporter (VGAT), was shown to have an important role in biological processes that support life [303]. During embryonic development, *Viaat* is vital for the release of GABA and glycine in the spinal cord. The absence of *Viaat* leads to severe defects in the muscles, lungs and liver of the developing embryos. Thus, it is possible that *Atrx* deletion in *Viaat*+ cells causes irreparable damages that cannot be compensated for and, ultimately, are incompatible with life.

The premature death of AtrxVtKO mice complicated our analysis of the P0 pups. However, we were able to determine that the cortical lamination and the gross morphology of the brain was unaffected by *Atrx* ablation (Figure 4.7). On the other hand, we noted mild hippocampal changes and defects in the progenitor pool (Figure 4.8-4.11). We observed a decrease in the number of radial glial progenitors at E16.5 in the dentate gyrus migratory stream (Figure 4.10). Surprisingly, we found an augmentation in the RGC population at P0 (Figure 4.9). With the limited amount of data we collected, it is difficult to find a conclusive explanation. It would be useful to have information regarding the proliferation rate, cell cycle length, number of apoptotic cells and quantify the number of cells with DNA damage. In addition, it would be interesting to investigate the firing patterns and the connections in the hippocampus. However, it would be complicated to conduct these experiments due to the early postnatal lethality of this mouse model. Similarly to the *Atrx*; *Nestin*-Cre mouse model, these results would only give us insights into the embryonic stage of AtrxVtKO mice [205]. To further investigate the implication of the GABAergic system in ATR-X syndrome, I would suggest using another Cre line that targets a smaller population of inhibitory neurons.

Somatostatin- and parvalbumin-positive neurons contribute for 30% and 40% respectively of the entire inhibitory cortical neurons' population [304]. Targeting one of these two cell populations may give us insights into the contribution of these inhibitory cells to the phenotype of ATR-X syndrome's patients.

6.8 Summary of Findings – ATR-X syndrome mouse model

ATR-X syndrome is a characterized by intellectual disability, skeletal abnormalities causing psychomotor deficits, genital abnormalities, seizures and hematological signs of α-thalassaemia [226]. Mutations in the chromatin remodeler ATRX have been reported to be central to the disease pathology [129]. However, it remains unclear how *ATRX* causes the various symptoms of this condition.

In the last section of this thesis, we investigated the function of *Atrx* in the developing brain to provide a better understanding of the development of intellectual disabilities in ATR-X syndrome. We successfully generated a viable forebrain-specific *Atrx* KO mouse model using the *Emx1*-Cre driver. The thinner *corpus callosum* and the defects observed in the oligodendrocyte population led us to conclude that AtrxEcKO mice had myelination defects. In addition, we revealed severe hippocampal impairments, both at the cellular and molecular levels. We believe that the mouse model we generated is a better representation of ATR-X syndrome and will be useful in the future to further assess the molecular pathways that are disrupted in this neurodevelopmental disorder.

6.9 *Atrx* is required during myelinogenesis

White matter abnormalities and myelination defects were identified in a study that used MRI and CT scans of ATR-X patients to classify their brain defects [36]. They concluded that ATRX is involved in the myelination process. Another study reported partial or complete agenesis of the *corpus callosum* (CC) in ATR-X syndrome patients [35].

In our new ATR-X syndrome mouse model, we found striking results confirming the importance of ATRX to the myelination process. First, we found a significant reduction in the thickness of the medial and caudal CC and noted that the density of the myelin fibers was reduced (Figure 5.6). This reduction was also observed in a Snf2h deletion model where partial agenesis of the CC and altered neuronal projections was reported [37]. Next, we found a significant decrease in the number of oligodendrocytes and myelin-producing oligodendrocytes of AtrxEcKO mice (Figure 5.7). In addition, we noted that the morphology of the oligodendrocytes was altered in comparison to the WT mice. These results suggest that ATRX is important for the myelination process.

Over the years, the INO80, SWI/SNF and CHD families of chromatin remodelers have been associated with the myelination process. For example, loss of Ep400 in oligodendrocytes leads to increased DNA damage and apoptosis as well as severe hypomyelination of the CNS [38]. In addition, it was found that Ep400 is functionally required for the onset of oligodendrocyte differentiation. Another study found that Chd7 cooperates with Sox10 to regulate the expression of genes important for the initiation of myelinogenesis and oligodendroglial maturation [39]. Lastly, Brg1 was reported to be indispensable and sufficient to initiate and promote the progression in the oligodendrocyte lineage [40]. RNA sequencing analysis of the optic nerves of Brg1 cKO mice showed enrichment of downregulated genes related to myelination and lipid-protein synthesis. Also, it was reported that Brg1 interacts with the Olig2 promoter in neural stem cells to regulate its expression during early development [40, 41].

The RNA sequencing analysis of the hippocampus of AtrxEcKO mice showed that multiple downregulated genes cited in the Brg1 studies, namely Olig2, Mbp, Plp1, Cnp, Sox10, Hes5 were also significantly decreased in the AtrxEcKO mice despite this analysis being performed on P60 mice. In mouse neuroprogenitors, Atrx binding sites were primarily found in gene bodies and promoter regions [42]. Taken together, Atrx may have a similar role to Brg1 in myelinogenesis and could interact with the Olig2 promoter to regulate its expression. Also, Atrx could cooperate with Sox10, similar to Chd7, and regulate crucial genes for the myelination process. Therefore, in the absence of Atrx, there would be a reduction in oligodendrocytes and hypomyelination in the CNS.

6.10 AtrxEcKO mice recapitulate some behavioural features of the ATR-X syndrome

Behavioural features for ATR-X syndrome patients include autistic-like behaviours, aggressive behaviours, seizures, emotional fluctuation episodes, hyperactivity episodes and severe anxiety (see section 1.4.5) [226]. However, not all these features can be tested in a mouse model. At first, we wanted to characterize the learning and memory ability of the AtrxEcKO mice as well as the anxiety and overall movements. We quickly discovered that the AtrxEcKO mice had a hyperactivity phenotype observable in multiple behaviour tests (Figure 5.9 and 5.10). To avoid this limitation, we attempted to increase the handling time, increase the habituation time prior to testing and changing the light intensity during each test but it was unsuccessful in helping the animals acclimatize to the testing protocols. Due to this very strong phenotype, we were unable to further assess the cognitive abilities of the AtrxEcKO mice. On the other hand, we were able to analyse the behaviour of the mice in an undisturbed home cage-like environment. We noted that AtrxEcKO mice had excessive grooming behaviour causing wounds and, occasionally, the severity of the injury led to the euthanasia of the mouse (Figure 5.11). Humans with autism spectrum disorders (ASD), and also ATR-X syndrome, exhibits repetitive behaviours [226, 305]. In mice, excessive self-grooming and barbering are considered the equivalent [275, 306]. Another feature we were able to recapitulate in our mouse model were the seizures. During the 72-hour observation period, we recorded ~5 seizure-like episodes in the AtrxEcKO mice (Figure 5.10). However, further studies such as an electroencephalogram would be necessary to confirm that these episodes are indeed seizures.

Other behavioural characterizations have been performed on other mouse models with *Atrx* deletion. A study used *Nestin*-Cre to target the deletion of *Atrx* in progenitors [206]. However, male homozygous die early postnatally, thus they used female Atrx-cHet mice to conduct their behavioural testing. They found that Atrx-cHet mice had deficits in contextual fear and spatial memory as well as in object recognition memory. Other studies used the *αCaMKII* gene promoter to delete *Atrx* in a population of excitatory neurons [214, 215]. These Atrx-cKO male and female mice only had minimal behavioural deficits related to autism. Also, only the Atrx-cKO male had spatial learning and memory deficits. A recent paper on the preprint server BioRxiv used Nex-Cre to inactivate Atrx and found similar handling difficulties, over-grooming and hyperactivity as we observed in our mice, thereby validating our findings. Taken together, none of the ATR-X syndrome mouse models were able to recapitulate entirely the human phenotype.

6.11 *Atrx* is crucial for the development of the hippocampus

The hippocampus is a complex structure containing a heterogeneous population of interconnected neurons that are involved in learning and memory processes [307]. It is also important for spatial navigation, emotional behaviours and regulating the hypothalamic functions [308-310]. ATR-X syndrome patients have severe intellectual disabilities and some of them suffer from seizures, which could indicate hippocampal deficits [218]. Other *Atrx* mouse models showed hippocampal impairments at the cellular and molecular levels [205, 212, 213, 215, 311].

In our new newly generated *Atrx* KO mouse model, we found striking results confirming the necessity of ATRX for hippocampal development and neuronal connections. First, volumetric analysis revealed a significant reduction in the hippocampus area, length of the pyramidal layer and the area and length of the granule cell layer of the dentate gyrus (DG) (Figure 5.4). The total number of cells in the CA1 region and DG was also reduced (Figure 5.16). Second, RNA sequencing analysis showed transcriptional dysregulation of AtrxEcKO hippocampus and identified netrin-G1 and netrin-G2 as genes of interest (Figure 5.12-5.15). Third, we found multiple deficits in the hippocampus neuronal populations. The positioning and distribution of DCX+ cells in the DG were altered, the number of DG granule cells was reduced by 15%, the population of calretinin+ cells were decreased by 50% and had a progenitor-like shape (Figure 5.16-5.17, 5.19). The layers of the hippocampus were also affected by *Atrx* deletion. The inner and middle molecular layer were missing and the *stratum lacunosum-moleculare* and the outer molecular layer were reduced by 70% (Figure 5.21). Lastly, the dendritic arborisation of hippocampal neurons appeared reduced and disorganized (Figure 5.22). Taken together, these results clearly show that *Atrx* deletion in *Emx1*+ cells significantly alters the hippocampal structure, transcriptional profile, cell population and dendritic arborisation.

The question that remains is: How can *Atrx* be causing all these hippocampal defects? We know that ATRX is a heterochromatin interacting protein and that it associates with histone chaperone DAXX to deposit histone H3.3 to pericentric and telomeric repeats [169]. Multiple studies have suggested that ATRX is implicated in gene regulation [184]. ATRX can bind to guanine-rich intragenic regions found within gene bodies to promote the incorporation of histone H3.3. In the absence of ATRX, G4 DNA quadruplexes are formed and the RNA polymerase II stalls at these intragenic regions. It is possible that in our mouse model the expression of specific genes needed for neuronal identity are reduced leading to impaired neuronal populations. For example, our RNA sequencing analysis revealed a significant reduction in the proneural protein Neurogenin 2 (Ngn2). Ngn2 is a transcription factor expressed in neural progenitor cells that regulates their commitment to a neuronal fate [312]. In the DG, Ngn2-expressing progenitors generate almost all the dentate granule cells [313]. In the absence of Ngn2, there is a significant reduction in DG granule cells and severe defects in DG morphogenesis. Therefore, it is possible that the reduction in Ngn2 expression in AtrxEcKO mice directly impaired the DG morphology and the number of granule cells.

A more general statement would be that changes in the chromatin landscape caused by *Atrx* deletion leads to the aberrant expression of several genes implicated in neurogenesis. It is more likely that the phenotype we observed in AtrxEcKO mice is a consequence of the accumulation of multiple defects including lower levels of cell-fate signals, axon guidance molecules and, potentially, increased DNA damage based on other *Atrx* knockout models.

6.12 Forebrain-deletion of *Atrx* leads to neural circuit defects

Any changes affecting the hippocampal network can have dramatic effects. A smaller hippocampus and decreased hippocampal function have been associated with autism spectrum disorders, Fragile X syndrome, Rett syndrome, Angelman Syndrome and Prader-Willi syndrome [314-318]. Patients with these syndromes share multiple features with ATR-X syndrome including cognitive deficits and intellectual disabilities.

A complex network of guidance signals regulates specific neuronal connections during brain development. They are molecules located in the extracellular Matrix or expressed on the cells along the route to guide the navigating axons [319]. Guiding cues are classified as attractive or repulsive molecules and they can have a short- or long-range effect. Axonal pathfinding is a crucial process during brain development to establish functional neuronal circuits. Netrins and their receptors are part of a family involved in axon guidance [320]. The attractive effect of netrins is mediated through the transmembrane receptor Deleted in Colorectal Cancer (DCC) whereas its repulsive effect is dependent on both DCC and Unc5 receptors [321, 322]. Unlike classic netrins, netrin-Gs are anchored to the plasma membrane surface and lack affinity to the known netrin receptors [323, 324]. Instead, Ntng1 and Ntng2 interact with the netrin-G1 ligand (NGL-1) and netrin-G2 ligand (NGL-2), respectively [325]. Ntng1 and Ntng2 are predominantly expressed in the brain on complimentary subsets of neurons in a laminated manner [323, 324, 326]. For example, Ntng1 is found in cortical layer I and IV, which correlates to the terminal arborisation of thalamocortical axons, and Ntng2 was detected in layer VI and IV as well as in the deeper layers of the piriform cortex suggesting a distribution in intracortical projections [325, 326]). In the hippocampus, Ntng1 expression is located in the outer molecular layer as well as the *stratum lacunosum moleculare* whereas

Ntng2 is strongly expressed in the inner molecular layer, *stratum radiatum* and *stratum oriens* [324]. Interestingly, these layers correspond to the termination of hippocampal circuits. The perforant pathway, sometimes referred to the entorhinal cortex-hippocampus pathway, is the major source of cortical inputs to the hippocampus (Figure 6.1) [327]. It originates in the entorhinal cortex (EC) and projects to the DG, CA1, CA3 and the subiculum [328].

The EC is divided into the medial entorhinal cortex (MEC) and lateral entorhinal cortex (LEC) giving rise to the medial perforant path (MPP) and lateral perforant path (LPP). The MPP and LPP that originate from layer II neurons of the MEC and LEC terminate on the middle third and the outer third of the molecular layer respectively [329]. Layer III neurons of the EC are part of the temporoammonic pathway and terminates on the *stratum lacunosum moleculare*. Schaffer collaterals are axon side branches, called collaterals, that originate from CA3 pyramidal neurons and project on the *stratum radiatum* and *stratum oriens* [330].

In our *Atrx* KO mouse model, we found that the transcript levels of Ntng1/Ntng2 and their expression in their respective hippocampal layers were severely affected by *Atrx* deletion. The RNA sequencing analysis revealed that other members of the netrin family were also significantly decreased in AtrxEcKO hippocampus. Therefore, it is highly likely that *Atrx* deletion leads to axonal pathfinding defects and that the MPP, LPP and Schaffer collaterals are impaired by *Atrx* deletion. Deficits to the perforant path is associated with poor learning and memory abilities [331]. In addition, decreased Ntng1/Ntng2 expression has been associated with neurodevelopmental disorders, neuropsychiatric disorders and intellectual disabilities [274, 332-336].

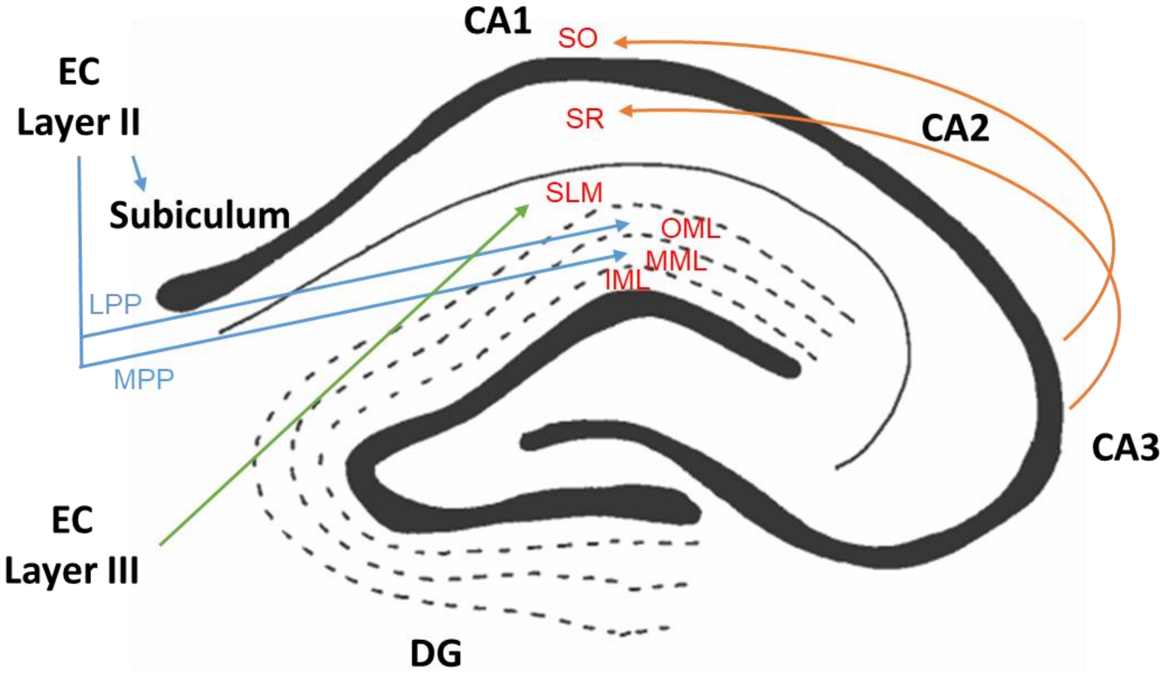

Figure 6.1: Schematic of the perforant path

Layer II of the entorhinal cortex (EC) projects to the subiculum, outer molecular layer (OML) and middle molecular layer (MML). Layer III of the EC projects to the *stratum lacunosum-moleculare* (SLM, green line). The Schaffer collaterals (orange lines) originate from the CA3 pyramidal neurons and project to the *stratum oriens* (SO) and *stratum radiatum* (SR).

In mice, defects in Ntng1/Ntng2 and NGL-1/NGL-2 are linked to reduced dendritic arborisation and spine density of hippocampal neurons, which is also an observation that we made in the AtrxEcKO mice (Figure 5.22) [326, 337, 338].

Another pathway that could be affected by *Atrx* deletion in *Emx1+* cells is the hippocampo-septal pathway (Figure 6.2A). This pathway is mostly composed of cholinergic, glutamatergic and GABAergic projections from the medial septum and the hippocampus [339]. The medial septum receives inputs from multiple brain regions including the amygdala, supramammillary nucleus (SuM), hippocampus, thalamus and ventral tegmental area [340].

In AtrxEcKO mice, we observed a reduction in the Myelin-associated glycoprotein (MAG) staining in the septum nuclei (Figure 5.6). This result suggests that there is a reduction in afferent and efferent neurons from the septum nuclei. This pathway is involved in memory function, regulating cholinergic inputs to the hippocampus and regulating CA1 neuron excitability [339, 341]. Cooperatively, the hippocampus, SuM and the medial septum are responsible for the rhythmic activity of the theta frequency band. Disturbance of the theta oscillation is associated with temporal lobe epilepsy and cognitive dysfunction [342, 343]. It is possible that the seizure-like episodes observed in our mouse model were caused by a disruption of the electrical activity between these brain structures.

The SuM is a hypothalamic structure that provides extensive innervation to the DG and the CA2 region [344, 345]. Its fibers terminate in the granule cell layer of the DG and within the *stratum oriens* and pyramidal cell layer (Figure 6.2B) [346]. Axons originating from the SuM make monosynaptic connections to granule cells and interneurons in the DG where they co-release glutamate and GABA at the synapses [347].

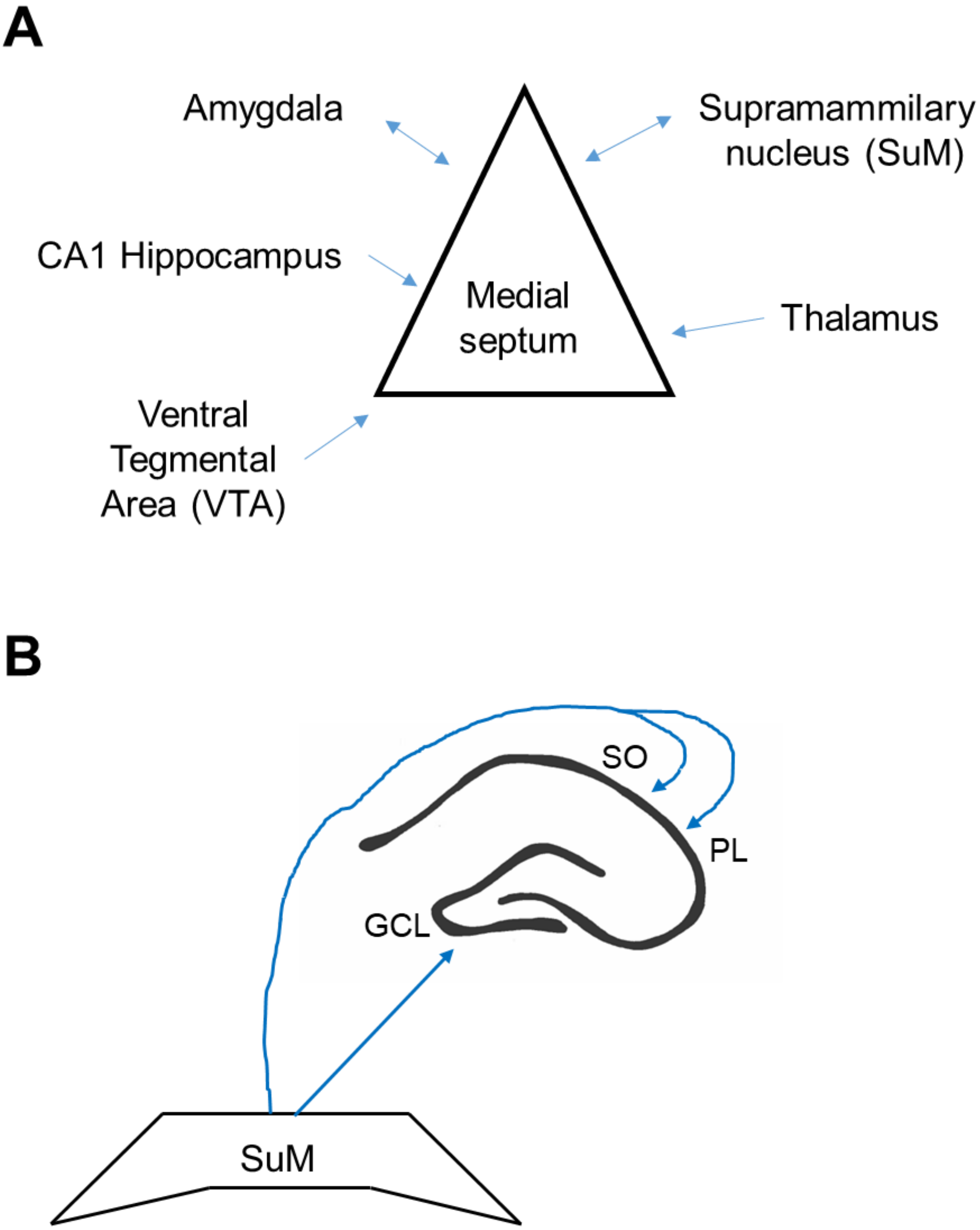
A
Amygdala
Supramammilary nucleus (SuM)
CA1 Hippocampus
Medial septum
Thalamus
Ventral Tegmental Area (VTA)
B
SO
PL
GCL
SuM

Figure 6.2: Schematic representing the hippocampo-septal pathway

A The medial septum receives input from the amygdala, supramammilary nucleus (SuM), CA1, thalamus and ventral tegmental area. **B** The SuM fibers terminate in the granule cell layer (GCL) of the dentate gyrus and within the the *stratum oriens* (SO) and pyramidal cell layer (PL) of the CA2 region.

SuM neurons and SuM to DG projections become more active during spatial memory retrieval and the release of glutamate from SuM neurons is crucial for this process [348]. Therefore, impairments in this neuronal circuit significantly affects the memory recovery process and could account for some of the learning and memory defects observed in ATR-X syndrome patients.

6.13 Future directions

The BPTF NcKO mice displayed a very strong behavioural phenotype regarding learning and memory, motor function and dyspraxia. It would be interesting to further the behavioural characterization by including tests to assess the social aspect of the animals. Mice are a social species that have reciprocal social interactions during nesting, parenting, territorial scent marking and more [349]. The adult social interaction test can be used to detect social abnormalities in mice. The ability to communicate could be assessed using the ultrasonic vocalization test [350]. Olfactory cues are important in the communication language of mice [351]. Therefore, the olfactory habituation/dishabituation test could be used to further assess the social ability of BPTF NcKO mice. Here, mice are presented with different odours, non-social and social odours, that elicit different levels of sniffing behaviour. The shape of the habituation and dishabituation curves reveal the mouse's ability to discriminate between the same and different non-social and social odours. With these three tests, the behavioural characterization of BPTF NcKO mice would be complete.

The early lethality of the AtrxVtKO and AtrxVgKO mice prevented us from completing a full characterization of these two models. In section 6.6 and 6.7, we discussed the possibility of using different Cre drivers targeting the excitatory and inhibitory systems. Another option would be to use the Vglut2-CreERT2 and Viaat-CreERT2, which are tamoxifen-inducible Cre drivers. This way, Atrx can be removed at a later time to, hopefully, avoid the early lethality phenotype.

In the AtrxEcKO mice, we observed that the communication between the supramammillary nucleus (SuM), entorhinal cortex (EC) and the hippocampus was severely affected. Therefore, it would be of interest to investigate these regions for possible alterations preventing axons from reaching the dentate gyrus. Anterograde labeling of the cell bodies of neurons located in the SuM and EC could be used to determine where the projections are going, since we observed that they are not reaching the hippocampus [352].

6.14 Chromatin remodelers and their effects on brain development

ATP-dependent chromatin remodelling is a process to modulate DNA accessibility by sliding, assembling or evicting nucleosomes [82]. As previously discussed, there are five different families of chromatin remodelling complexes that can be used for specific tasks. During brain development, they can have global roles to facilitate cellular processes or they can drastically influence the faith of specific progenitors or neuronal populations.

The subunit composition of the BAF chromatin remodelling complex determines the target specificity and its function within a specific cell type [90]. Mutations in the ARID1A subunit, also known as BAF250A, was identified in Coffin-Siris syndrome, a neurodevelopmental disorder characterized by agenesis of the *corpus callosum* (CC) [332]. During brain development, ARID1A has an essential non-cell autonomous role on intracortical axon track targeting and regulates the expression of a subset of subplate-specific genes [333]. ARID1A promotes the proliferation and differentiation of radial glial progenitors [334]. At the onset of differentiation, the BAF complex switches the ARID1A subunit for the ARID1B subunit triggering pluripotency exit and lineage commitment [335]. This dynamic process is crucial in generating appropriate cell populations and network connections.

Histone variant H3.3 has an important role during brain development. It is deposited to gene bodies, enhancers and promoters by chaperone complexes ATRX/DAXX or HIRA in a replication-independent manner suggesting a role in gene regulation [353-355]. The levels of H3.3 varies from cell type to cell type [356]. Cycling neural progenitor cells (NPCs) are characterized by a low level of histone variant H3.3 and high levels of H3.1 and H3.2. Oppositely, histone H3.3 accumulates rapidly in newly generated neurons post-mitotically. Co-deletion of the histone H3.3 genes, *H3f3a* and *H3f3b*, in cycling NPCs and newly postmitotic neurons prevents histone H3.3 synthesis and leads to loss of histone H3.3 [356]. In post-mitotic neurons, it also alters the distribution of post-translational modifications (PTMs), H3K4me3 and H3k27me3, causing widespread gene expression changes and a failure to establish the neuronal transcriptome. Interestingly, co-deletion of *H3f3a* and *H3f3b* in neurons several days after their final mitosis leads to progressive loss of histone H3.3 without disrupting the neuronal transcriptome. Therefore, histone H3.3 is critical in NPCs and postmitotic neurons for the acquisition of distinct neuronal identities but it is only required in terminally postmitotic neurons to maintain histone H3.3 levels over time.

ATRX is a great example of a chromatin remodeler with many roles depending on the cell type. In satellite cells, *Atrx* deletion causes a delayed progression through mid to late S phase of mitosis [198]. The replication-dependant chromatin defects led to fragmented and aberrant nuclei, increased genomic damage, telomeric fragility and activation of the DNA damage response. Thus, *Atrx* is required in satellite cells to sustain the rapid expansion of the population. In the retina, *Atrx* expression is required in bipolar cells for their morphology, function and circuitry [211]. It also has a non-cell autonomous effect on the survival of retinal interneurons. Oppositely, *Atrx* deletion in amacrine and horizontal progenitors has no effect on the size of both cell populations suggesting that *Atrx* expression is not necessary for their survival. Loss of *Atrx* in neuroprogenitors impairs chromosome segregation leading to mitotic dysfunction and reduction in the progenitor pool [197]. Defects in mitosis is also found in a forebrain-specific *Atrx* KO where an increase in cell cycle exit is observed during early neurogenesis [357]. This defect correlates with increased outer radial glial progenitors and basal progenitors leading to their premature differentiation into cortical neurons and precipitate depletion of the progenitor pool during late neurogenesis. ATRX has a transcriptional regulatory role in oligodendrocyte precursor cells (OPCs) [358]. Indeed, ATRX binds to and activates the *Olig2* gene and in its absence, OPCs revert to a more pluripotent state through chromatin landscape changes allowing for astrogliogenesis to occur. Finally, we can now add ATRX to the list of required proteins for myelinogenesis, axonogenesis, axonal pathfinding, cell differentiation and transcriptional regulation.

Taken together, these studies show that the chromatin landscape is highly malleable and that changes in its accessibility is required in different cell types and tissues but also during specific stages of neuronal development. Understanding the intricate functions of chromatin remodelers at multiple timepoints during neurogenesis will help us understand how the dysfunction of those complexes can cause neurodevelopment disorders. There is so much more to discover on ATRX and BPTF function in the brain but hopefully my work has contributed to elucidate part of their stories.

References

1. Rossant, J. and P.P. Tam, *Emerging asymmetry and embryonic patterning in early mouse development.* Dev Cell, 2004. **7**(2): p. 155-64.
2. Copp, A.J., N.D. Greene, and J.N. Murdoch, *The genetic basis of mammalian neurulation.* Nat Rev Genet, 2003. **4**(10): p. 784-93.
3. Adnani, L., et al., *Mechanisms of Cortical Differentiation.* Int Rev Cell Mol Biol, 2018. **336**: p. 223-320.
4. Shimamura, K., et al., *Longitudinal organization of the anterior neural plate and neural tube.* Development, 1995. **121**(12): p. 3923-33.
5. Azzarelli, R., L.J. Hardwick, and A. Philpott, *Emergence of neuronal diversity from patterning of telencephalic progenitors.* Wiley Interdiscip Rev Dev Biol, 2015. **4**(3): p. 197-214.
6. Armentano, M., et al., *COUP-TFI regulates the balance of cortical patterning between frontal/motor and sensory areas.* Nat Neurosci, 2007. **10**(10): p. 1277-86.
7. Bishop, K.M., G. Goudreau, and D.D. O'Leary, *Regulation of area identity in the mammalian neocortex by Emx2 and Pax6.* Science, 2000. **288**(5464): p. 344-9.
8. Chou, S.J., et al., *Lhx2 specifies regional fate in Emx1 lineage of telencephalic progenitors generating cerebral cortex.* Nat Neurosci, 2009. **12**(11): p. 1381-9.
9. Sahara, S., et al., *Sp8 exhibits reciprocal induction with Fgf8 but has an opposing effect on anterior-posterior cortical area patterning.* Neural Dev, 2007. **2**: p. 10.
10. Breunig, J.J., T.F. Haydar, and P. Rakic, *Neural stem cells: historical perspective and future prospects.* Neuron, 2011. **70**(4): p. 614-25.
11. Tan, X. and S.H. Shi, *Neocortical neurogenesis and neuronal migration.* Wiley Interdiscip Rev Dev Biol, 2013. **2**(4): p. 443-59.
12. Estivill-Torrus, G., et al., *Pax6 is required to regulate the cell cycle and the rate of progression from symmetrical to asymmetrical division in mammalian cortical progenitors.* Development, 2002. **129**(2): p. 455-66.
13. Britz, O., et al., *A role for proneural genes in the maturation of cortical progenitor cells.* Cereb Cortex, 2006. **16 Suppl 1**: p. i138-51.
14. Ochiai, W., et al., *Periventricular notch activation and asymmetric Ngn2 and Tbr2 expression in pair-generated neocortical daughter cells.* Mol Cell Neurosci, 2009. **40**(2): p. 225-33.
15. Brazel, C.Y., et al., *Roles of the mammalian subventricular zone in brain development.* Prog Neurobiol, 2003. **69**(1): p. 49-69.
16. Wilkinson, G., D. Dennis, and C. Schuurmans, *Proneural genes in neocortical development.* Neuroscience, 2013. **253**: p. 256-73.
17. Schuurmans, C., et al., *Sequential phases of cortical specification involve Neurogenin-dependent and -independent pathways.* EMBO J, 2004. **23**(14): p. 2892-902.
18. Casarosa, S., C. Fode, and F. Guillemot, *Mash1 regulates neurogenesis in the ventral telencephalon.* Development, 1999. **126**(3): p. 525-34.
19. Molyneaux, B.J., et al., *Neuronal subtype specification in the cerebral cortex.* Nat Rev Neurosci, 2007. **8**(6): p. 427-37.
20. Frotscher, M., *Role for Reelin in stabilizing cortical architecture.* Trends Neurosci, 2010. **33**(9): p. 407-14.

21. Kwan, K.Y., N. Sestan, and E.S. Anton, *Transcriptional co-regulation of neuronal migration and laminar identity in the neocortex.* Development, 2012. **139**(9): p. 1535-46.
22. Kanold, P.O., *Subplate neurons: crucial regulators of cortical development and plasticity.* Front Neuroanat, 2009. **3**: p. 16.
23. Briggs, F., *Organizing principles of cortical layer 6.* Front Neural Circuits, 2010. **4**: p. 3.
24. Chen, B., L.R. Schaevitz, and S.K. McConnell, *Fezl regulates the differentiation and axon targeting of layer 5 subcortical projection neurons in cerebral cortex.* Proc Natl Acad Sci U S A, 2005. **102**(47): p. 17184-9.
25. Fame, R.M., J.L. MacDonald, and J.D. Macklis, *Development, specification, and diversity of callosal projection neurons.* Trends Neurosci, 2011. **34**(1): p. 41-50.
26. Staiger, J.F., et al., *Functional diversity of layer IV spiny neurons in rat somatosensory cortex: quantitative morphology of electrophysiologically characterized and biocytin labeled cells.* Cereb Cortex, 2004. **14**(6): p. 690-701.
27. Li, X., et al., *Foxp1 regulates cortical radial migration and neuronal morphogenesis in developing cerebral cortex.* PLoS One, 2015. **10**(5): p. e0127671.
28. Srinivasan, K., et al., *A network of genetic repression and derepression specifies projection fates in the developing neocortex.* Proc Natl Acad Sci U S A, 2012. **109**(47): p. 19071-8.
29. Florio, M. and W.B. Huttner, *Neural progenitors, neurogenesis and the evolution of the neocortex.* Development, 2014. **141**(11): p. 2182-94.
30. Tremblay, R., S. Lee, and B. Rudy, *GABAergic Interneurons in the Neocortex: From Cellular Properties to Circuits.* Neuron, 2016. **91**(2): p. 260-92.
31. Anderson, S.A., et al., *Distinct cortical migrations from the medial and lateral ganglionic eminences.* Development, 2001. **128**(3): p. 353-63.
32. Miyoshi, G., et al., *Genetic fate mapping reveals that the caudal ganglionic eminence produces a large and diverse population of superficial cortical interneurons.* J Neurosci, 2010. **30**(5): p. 1582-94.
33. Colasante, G. and A. Sessa, *Last but not least: cortical interneurons from caudal ganglionic eminence.* J Neurosci, 2010. **30**(22): p. 7449-50.
34. Ciceri, G., et al., *Lineage-specific laminar organization of cortical GABAergic interneurons.* Nat Neurosci, 2013. **16**(9): p. 1199-210.
35. Miyoshi, G. and G. Fishell, *GABAergic interneuron lineages selectively sort into specific cortical layers during early postnatal development.* Cereb Cortex, 2011. **21**(4): p. 845-52.
36. Bortone, D. and F. Polleux, *KCC2 expression promotes the termination of cortical interneuron migration in a voltage-sensitive calcium-dependent manner.* Neuron, 2009. **62**(1): p. 53-71.
37. Hayashi, K., et al., *Cellular dynamics of neuronal migration in the hippocampus.* Front Neurosci, 2015. **9**: p. 135.
38. Insausti, R., M. Munoz-Lopez, and A.M. Insausti, *The CA2 hippocampal subfield in humans: A review.* Hippocampus, 2023. **33**(6): p. 712-729.
39. Kitazawa, A., et al., *Hippocampal pyramidal neurons switch from a multipolar migration mode to a novel "climbing" migration mode during development.* J Neurosci, 2014. **34**(4): p. 1115-26.

40. Nakahira, E. and S. Yuasa, *Neuronal generation, migration, and differentiation in the mouse hippocampal primoridium as revealed by enhanced green fluorescent protein gene transfer by means of in utero electroporation.* J Comp Neurol, 2005. **483**(3): p. 329-40.
41. Tole, S. and E.A. Grove, *Detailed field pattern is intrinsic to the embryonic mouse hippocampus early in neurogenesis.* J Neurosci, 2001. **21**(5): p. 1580-9.
42. Altman, J. and S.A. Bayer, *Prolonged sojourn of developing pyramidal cells in the intermediate zone of the hippocampus and their settling in the stratum pyramidale.* J Comp Neurol, 1990. **301**(3): p. 343-64.
43. Bayer, S.A., *Development of the hippocampal region in the rat. I. Neurogenesis examined with 3H-thymidine autoradiography.* J Comp Neurol, 1980. **190**(1): p. 87-114.
44. Altman, J. and S.A. Bayer, *Migration and distribution of two populations of hippocampal granule cell precursors during the perinatal and postnatal periods.* J Comp Neurol, 1990. **301**(3): p. 365-81.
45. Seki, T., et al., *Distinctive population of Gfap-expressing neural progenitors arising around the dentate notch migrate and form the granule cell layer in the developing hippocampus.* J Comp Neurol, 2014. **522**(2): p. 261-83.
46. Frotscher, M., S. Zhao, and E. Forster, *Development of cell and fiber layers in the dentate gyrus.* Prog Brain Res, 2007. **163**: p. 133-42.
47. Piovesan, A., et al., *On the length, weight and GC content of the human genome.* BMC Res Notes, 2019. **12**(1): p. 106.
48. Saha, A., J. Wittmeyer, and B.R. Cairns, *Chromatin remodelling: the industrial revolution of DNA around histones.* Nat Rev Mol Cell Biol, 2006. **7**(6): p. 437-47.
49. Oberdoerffer, P. and D.A. Sinclair, *The role of nuclear architecture in genomic instability and ageing.* Nat Rev Mol Cell Biol, 2007. **8**(9): p. 692-702.
50. Nielsen, A.L., et al., *Heterochromatin formation in mammalian cells: interaction between histones and HP1 proteins.* Mol Cell, 2001. **7**(4): p. 729-39.
51. Kornberg, R.D., *Chromatin structure: a repeating unit of histones and DNA.* Science, 1974. **184**(4139): p. 868-71.
52. Venkatesh, S. and J.L. Workman, *Histone exchange, chromatin structure and the regulation of transcription.* Nat Rev Mol Cell Biol, 2015. **16**(3): p. 178-89.
53. Talbert, P.B. and S. Henikoff, *Histone variants--ancient wrap artists of the epigenome.* Nat Rev Mol Cell Biol, 2010. **11**(4): p. 264-75.
54. Pruss, D., et al., *An asymmetric model for the nucleosome: a binding site for linker histones inside the DNA gyres.* Science, 1996. **274**(5287): p. 614-7.
55. Zhou, B.R., et al., *Structural insights into the histone H1-nucleosome complex.* Proc Natl Acad Sci U S A, 2013. **110**(48): p. 19390-5.
56. Smolle, M. and J.L. Workman, *Transcription-associated histone modifications and cryptic transcription.* Biochim Biophys Acta, 2013. **1829**(1): p. 84-97.
57. Gillette, T.G. and J.A. Hill, *Readers, writers, and erasers: chromatin as the whiteboard of heart disease.* Circ Res, 2015. **116**(7): p. 1245-53.
58. Rossetto, D., N. Avvakumov, and J. Cote, *Histone phosphorylation: a chromatin modification involved in diverse nuclear events.* Epigenetics, 2012. **7**(10): p. 1098-108.
59. Sawicka, A. and C. Seiser, *Sensing core histone phosphorylation - a matter of perfect timing.* Biochim Biophys Acta, 2014. **1839**(8): p. 711-8.

60. Haberland, M., R.L. Montgomery, and E.N. Olson, *The many roles of histone deacetylases in development and physiology: implications for disease and therapy.* Nat Rev Genet, 2009. **10**(1): p. 32-42.
61. Kouzarides, T., *Acetylation: a regulatory modification to rival phosphorylation?* EMBO J, 2000. **19**(6): p. 1176-9.
62. Xu, F., et al., *Sir2 deacetylates histone H3 lysine 56 to regulate telomeric heterochromatin structure in yeast.* Mol Cell, 2007. **27**(6): p. 890-900.
63. Shi, Y., *Histone lysine demethylases: emerging roles in development, physiology and disease.* Nat Rev Genet, 2007. **8**(11): p. 829-33.
64. Xu, F., K. Zhang, and M. Grunstein, *Acetylation in histone H3 globular domain regulates gene expression in yeast.* Cell, 2005. **121**(3): p. 375-85.
65. Ozdemir, A., et al., *Characterization of lysine 56 of histone H3 as an acetylation site in Saccharomyces cerevisiae.* J Biol Chem, 2005. **280**(28): p. 25949-52.
66. Ng, S.S., et al., *Dynamic protein methylation in chromatin biology.* Cell Mol Life Sci, 2009. **66**(3): p. 407-22.
67. Bedford, M.T. and S.G. Clarke, *Protein arginine methylation in mammals: who, what, and why.* Mol Cell, 2009. **33**(1): p. 1-13.
68. Bannister, A.J. and T. Kouzarides, *Reversing histone methylation.* Nature, 2005. **436**(7054): p. 1103-6.
69. Martin, C. and Y. Zhang, *The diverse functions of histone lysine methylation.* Nat Rev Mol Cell Biol, 2005. **6**(11): p. 838-49.
70. Peters, A.H., et al., *Partitioning and plasticity of repressive histone methylation states in mammalian chromatin.* Mol Cell, 2003. **12**(6): p. 1577-89.
71. Plath, K., et al., *Role of histone H3 lysine 27 methylation in X inactivation.* Science, 2003. **300**(5616): p. 131-5.
72. Black, J.C., C. Van Rechem, and J.R. Whetstine, *Histone lysine methylation dynamics: establishment, regulation, and biological impact.* Mol Cell, 2012. **48**(4): p. 491-507.
73. Oh, E., D. Akopian, and M. Rape, *Principles of Ubiquitin-Dependent Signaling.* Annu Rev Cell Dev Biol, 2018. **34**: p. 137-162.
74. Lee, J.S., et al., *Histone crosstalk between H2B monoubiquitination and H3 methylation mediated by COMPASS.* Cell, 2007. **131**(6): p. 1084-96.
75. Wang, H., et al., *Role of histone H2A ubiquitination in Polycomb silencing.* Nature, 2004. **431**(7010): p. 873-8.
76. Mevissen, T.E.T. and D. Komander, *Mechanisms of Deubiquitinase Specificity and Regulation.* Annu Rev Biochem, 2017. **86**: p. 159-192.
77. Nayak, A. and S. Muller, *SUMO-specific proteases/isopeptidases: SENPs and beyond.* Genome Biol, 2014. **15**(7): p. 422.
78. Hammond, C.M., et al., *Histone chaperone networks shaping chromatin function.* Nat Rev Mol Cell Biol, 2017. **18**(3): p. 141-158.
79. Ahmad, K. and S. Henikoff, *The histone variant H3.3 marks active chromatin by replication-independent nucleosome assembly.* Mol Cell, 2002. **9**(6): p. 1191-200.
80. Ray-Gallet, D., et al., *Functional activity of the H3.3 histone chaperone complex HIRA requires trimerization of the HIRA subunit.* Nat Commun, 2018. **9**(1): p. 3103.
81. Lewis, P.W., et al., *Daxx is an H3.3-specific histone chaperone and cooperates with ATRX in replication-independent chromatin assembly at telomeres.* Proc Natl Acad Sci U S A, 2010. **107**(32): p. 14075-80.

82. Tyagi, M., et al., *Chromatin remodelers: We are the drivers!!* Nucleus, 2016. **7**(4): p. 388-404.
83. Becker, P.B. and W. Horz, *ATP-dependent nucleosome remodeling.* Annu Rev Biochem, 2002. **71**: p. 247-73.
84. Zhang, P., et al., *An Overview of Chromatin-Regulating Proteins in Cells.* Curr Protein Pept Sci, 2016. **17**(5): p. 401-10.
85. Hota, S.K. and B.G. Bruneau, *ATP-dependent chromatin remodeling during mammalian development.* Development, 2016. **143**(16): p. 2882-97.
86. Clapier, C.R., et al., *Mechanisms of action and regulation of ATP-dependent chromatin-remodelling complexes.* Nat Rev Mol Cell Biol, 2017. **18**(7): p. 407-422.
87. Cenik, B.K. and A. Shilatifard, *COMPASS and SWI/SNF complexes in development and disease.* Nat Rev Genet, 2021. **22**(1): p. 38-58.
88. Kasten, M., et al., *Tandem bromodomains in the chromatin remodeler RSC recognize acetylated histone H3 Lys14.* EMBO J, 2004. **23**(6): p. 1348-59.
89. Narayanan, R., et al., *Loss of BAF (mSWI/SNF) Complexes Causes Global Transcriptional and Chromatin State Changes in Forebrain Development.* Cell Rep, 2015. **13**(9): p. 1842-54.
90. Phelan, M.L., et al., *Reconstitution of a core chromatin remodeling complex from SWI/SNF subunits.* Mol Cell, 1999. **3**(2): p. 247-53.
91. Wilson, B.G. and C.W. Roberts, *SWI/SNF nucleosome remodellers and cancer.* Nat Rev Cancer, 2011. **11**(7): p. 481-92.
92. Ho, L., et al., *An embryonic stem cell chromatin remodeling complex, esBAF, is essential for embryonic stem cell self-renewal and pluripotency.* Proc Natl Acad Sci U S A, 2009. **106**(13): p. 5181-6.
93. Bossen, C., et al., *The chromatin remodeler Brg1 activates enhancer repertoires to establish B cell identity and modulate cell growth.* Nat Immunol, 2015. **16**(7): p. 775-84.
94. Wang, X., et al., *SMARCB1-mediated SWI/SNF complex function is essential for enhancer regulation.* Nat Genet, 2017. **49**(2): p. 289-295.
95. Ho, L., et al., *An embryonic stem cell chromatin remodeling complex, esBAF, is an essential component of the core pluripotency transcriptional network.* Proc Natl Acad Sci U S A, 2009. **106**(13): p. 5187-91.
96. Hirabayashi, Y. and Y. Gotoh, *Epigenetic control of neural precursor cell fate during development.* Nat Rev Neurosci, 2010. **11**(6): p. 377-88.
97. Kosho, T., N. Miyake, and J.C. Carey, *Coffin-Siris syndrome and related disorders involving components of the BAF (mSWI/SNF) complex: historical review and recent advances using next generation sequencing.* Am J Med Genet C Semin Med Genet, 2014. **166C**(3): p. 241-51.
98. Wieczorek, D., et al., *A comprehensive molecular study on Coffin-Siris and Nicolaides-Baraitser syndromes identifies a broad molecular and clinical spectrum converging on altered chromatin remodeling.* Hum Mol Genet, 2013. **22**(25): p. 5121-35.
99. Sokpor, G., et al., *Chromatin Remodeling BAF (SWI/SNF) Complexes in Neural Development and Disorders.* Front Mol Neurosci, 2017. **10**: p. 243.
100. Tsukiyama, T. and C. Wu, *Purification and properties of an ATP-dependent nucleosome remodeling factor.* Cell, 1995. **83**(6): p. 1011-20.

101. Tsukiyama, T., et al., *ISWI, a member of the SWI2/SNF2 ATPase family, encodes the 140 kDa subunit of the nucleosome remodeling factor.* Cell, 1995. **83**(6): p. 1021-6.
102. Grune, T., et al., *Crystal structure and functional analysis of a nucleosome recognition module of the remodeling factor ISWI.* Mol Cell, 2003. **12**(2): p. 449-60.
103. Clapier, C.R., et al., *Critical role for the histone H4 N terminus in nucleosome remodeling by ISWI.* Mol Cell Biol, 2001. **21**(3): p. 875-83.
104. Goodwin, L.R. and D.J. Picketts, *The role of ISWI chromatin remodeling complexes in brain development and neurodevelopmental disorders.* Mol Cell Neurosci, 2018. **87**: p. 55-64.
105. Lazzaro, M.A. and D.J. Picketts, *Cloning and characterization of the murine Imitation Switch (ISWI) genes: differential expression patterns suggest distinct developmental roles for Snf2h and Snf2l.* J Neurochem, 2001. **77**(4): p. 1145-56.
106. Oppikofer, M., et al., *Expansion of the ISWI chromatin remodeler family with new active complexes.* EMBO Rep, 2017. **18**(10): p. 1697-1706.
107. Sokpor, G., et al., *ATP-Dependent Chromatin Remodeling During Cortical Neurogenesis.* Front Neurosci, 2018. **12**: p. 226.
108. Barak, O., et al., *Isolation of human NURF: a regulator of Engrailed gene expression.* EMBO J, 2003. **22**(22): p. 6089-100.
109. Fusco, C., et al., *Smaller and larger deletions of the Williams Beuren syndrome region implicate genes involved in mild facial phenotype, epilepsy and autistic traits.* Eur J Hum Genet, 2014. **22**(1): p. 64-70.
110. Stankiewicz, P., et al., *Haploinsufficiency of the Chromatin Remodeler BPTF Causes Syndromic Developmental and Speech Delay, Postnatal Microcephaly, and Dysmorphic Features.* Am J Hum Genet, 2017. **101**(4): p. 503-515.
111. Woodage, T., et al., *Characterization of the CHD family of proteins.* Proc Natl Acad Sci U S A, 1997. **94**(21): p. 11472-7.
112. Marfella, C.G. and A.N. Imbalzano, *The Chd family of chromatin remodelers.* Mutat Res, 2007. **618**(1-2): p. 30-40.
113. Hall, J.A. and P.T. Georgel, *CHD proteins: a diverse family with strong ties.* Biochem Cell Biol, 2007. **85**(4): p. 463-76.
114. Murawska, M. and A. Brehm, *CHD chromatin remodelers and the transcription cycle.* Transcription, 2011. **2**(6): p. 244-53.
115. Kasah, S., C. Oddy, and M.A. Basson, *Autism-linked CHD gene expression patterns during development predict multi-organ disease phenotypes.* J Anat, 2018. **233**(6): p. 755-769.
116. Kim, H.G., et al., *Mutations in CHD7, encoding a chromatin-remodeling protein, cause idiopathic hypogonadotropic hypogonadism and Kallmann syndrome.* Am J Hum Genet, 2008. **83**(4): p. 511-9.
117. Jongmans, M.C., et al., *CHD7 mutations in patients initially diagnosed with Kallmann syndrome--the clinical overlap with CHARGE syndrome.* Clin Genet, 2009. **75**(1): p. 65-71.
118. Bouazoune, K. and R.E. Kingston, *Chromatin remodeling by the CHD7 protein is impaired by mutations that cause human developmental disorders.* Proc Natl Acad Sci U S A, 2012. **109**(47): p. 19238-43.
119. Mizuguchi, G., et al., *ATP-driven exchange of histone H2AZ variant catalyzed by SWR1 chromatin remodeling complex.* Science, 2004. **303**(5656): p. 343-8.

120. Udugama, M., A. Sabri, and B. Bartholomew, *The INO80 ATP-dependent chromatin remodeling complex is a nucleosome spacing factor.* Mol Cell Biol, 2011. **31**(4): p. 662-73.
121. van Attikum, H., O. Fritsch, and S.M. Gasser, *Distinct roles for SWR1 and INO80 chromatin remodeling complexes at chromosomal double-strand breaks.* EMBO J, 2007. **26**(18): p. 4113-25.
122. Shen, X., et al., *A chromatin remodelling complex involved in transcription and DNA processing.* Nature, 2000. **406**(6795): p. 541-4.
123. Papamichos-Chronakis, M., et al., *Global regulation of H2A.Z localization by the INO80 chromatin-remodeling enzyme is essential for genome integrity.* Cell, 2011. **144**(2): p. 200-13.
124. Halkidou, K., et al., *Putative involvement of the histone acetyltransferase Tip60 in ribosomal gene transcription.* Nucleic Acids Res, 2004. **32**(5): p. 1654-65.
125. Sapountzi, V., I.R. Logan, and C.N. Robson, *Cellular functions of TIP60.* Int J Biochem Cell Biol, 2006. **38**(9): p. 1496-509.
126. Kusch, T., et al., *Acetylation by Tip60 is required for selective histone variant exchange at DNA lesions.* Science, 2004. **306**(5704): p. 2084-7.
127. Humbert, J., et al., *De Novo KAT5 Variants Cause a Syndrome with Recognizable Facial Dysmorphisms, Cerebellar Atrophy, Sleep Disturbance, and Epilepsy.* Am J Hum Genet, 2020. **107**(3): p. 564-574.
128. Hood, R.L., et al., *Mutations in SRCAP, encoding SNF2-related CREBBP activator protein, cause Floating-Harbor syndrome.* Am J Hum Genet, 2012. **90**(2): p. 308-13.
129. Gibbons, R.J., et al., *Mutations in a putative global transcriptional regulator cause X-linked mental retardation with alpha-thalassemia (ATR-X syndrome).* Cell, 1995. **80**(6): p. 837-45.
130. Picketts, D.J., et al., *ATRX encodes a novel member of the SNF2 family of proteins: mutations point to a common mechanism underlying the ATR-X syndrome.* Hum Mol Genet, 1996. **5**(12): p. 1899-907.
131. Xiao, H., et al., *Dual functions of largest NURF subunit NURF301 in nucleosome sliding and transcription factor interactions.* Mol Cell, 2001. **8**(3): p. 531-43.
132. Jones, M.H., N. Hamana, and M. Shimane, *Identification and characterization of BPTF, a novel bromodomain transcription factor.* Genomics, 2000. **63**(1): p. 35-9.
133. Zahid, H., N.M. Olson, and W.C.K. Pomerantz, *Opportunity knocks for uncovering the new function of an understudied nucleosome remodeling complex member, the bromodomain PHD finger transcription factor, BPTF.* Curr Opin Chem Biol, 2021. **63**: p. 57-67.
134. Doerks, T., R. Copley, and P. Bork, *DDT -- a novel domain in different transcription and chromosome remodeling factors.* Trends Biochem Sci, 2001. **26**(3): p. 145-6.
135. Li, H., et al., *Molecular basis for site-specific read-out of histone H3K4me3 by the BPTF PHD finger of NURF.* Nature, 2006. **442**(7098): p. 91-5.
136. Ruthenburg, A.J., et al., *Recognition of a mononucleosomal histone modification pattern by BPTF via multivalent interactions.* Cell, 2011. **145**(5): p. 692-706.
137. Perell, G.T., et al., *Specific Acetylation Patterns of H2A.Z Form Transient Interactions with the BPTF Bromodomain.* Biochemistry, 2017. **56**(35): p. 4607-4615.
138. Frey, W.D., et al., *BPTF Maintains Chromatin Accessibility and the Self-Renewal Capacity of Mammary Gland Stem Cells.* Stem Cell Reports, 2017. **9**(1): p. 23-31.

139. Landry, J.W., et al., *Chromatin remodeling complex NURF regulates thymocyte maturation.* Genes Dev, 2011. **25**(3): p. 275-86.
140. Wu, B., et al., *BPTF Is Essential for T Cell Homeostasis and Function.* J Immunol, 2016. **197**(11): p. 4325-4333.
141. Dai, M., et al., *BPTF promotes tumor growth and predicts poor prognosis in lung adenocarcinomas.* Oncotarget, 2015. **6**(32): p. 33878-92.
142. Xiao, S., et al., *BPTF Associated with EMT Indicates Negative Prognosis in Patients with Hepatocellular Carcinoma.* Dig Dis Sci, 2015. **60**(4): p. 910-8.
143. Lee, J.H., et al., *BPTF, a chromatin remodeling-related gene, exhibits frameshift mutations in gastric and colorectal cancers.* APMIS, 2016. **124**(5): p. 425-7.
144. Dar, A.A., et al., *The role of BPTF in melanoma progression and in response to BRAF-targeted therapy.* J Natl Cancer Inst, 2015. **107**(5).
145. Richart, L., et al., *BPTF is required for c-MYC transcriptional activity and in vivo tumorigenesis.* Nat Commun, 2016. **7**: p. 10153.
146. Green, A.L., et al., *BPTF regulates growth of adult and pediatric high-grade glioma through the MYC pathway.* Oncogene, 2020. **39**(11): p. 2305-2327.
147. Richart, L., F.X. Real, and V.J. Sanchez-Arevalo Lobo, *c-MYC partners with BPTF in human cancer.* Mol Cell Oncol, 2016. **3**(3): p. e1152346.
148. Landry, J., et al., *Essential role of chromatin remodeling protein Bptf in early mouse embryos and embryonic stem cells.* PLoS Genet, 2008. **4**(10): p. e1000241.
149. Midro, A.T., et al., *Neurodevelopmental disorder with dysmorphic facies and distal limb anomalies syndrome due to disruption of BPTF in a 35-year-old man initially diagnosed with Silver-Russell syndrome.* Clin Genet, 2019. **95**(4): p. 534-536.
150. Glinton, K.E., et al., *Phenotypic expansion of the BPTF-related neurodevelopmental disorder with dysmorphic facies and distal limb anomalies.* Am J Med Genet A, 2021. **185**(5): p. 1366-1378.
151. Zapata, G., K. Yan, and D.J. Picketts, *Generation of a mouse model of the neurodevelopmental disorder with dysmorphic facies and distal limb anomalies (NEDDFL) syndrome.* Hum Mol Genet, 2022.
152. Garrick, D., et al., *A conserved truncated isoform of the ATR-X syndrome protein lacking the SWI/SNF-homology domain.* Gene, 2004. **326**: p. 23-34.
153. Timpano, S. and D.J. Picketts, *Neurodevelopmental Disorders Caused by Defective Chromatin Remodeling: Phenotypic Complexity Is Highlighted by a Review of ATRX Function.* Front Genet, 2020. **11**: p. 885.
154. Xue, Y., et al., *The ATRX syndrome protein forms a chromatin-remodeling complex with Daxx and localizes in promyelocytic leukemia nuclear bodies.* Proc Natl Acad Sci U S A, 2003. **100**(19): p. 10635-40.
155. Jaskelioff, M. and C.L. Peterson, *Chromatin and transcription: histones continue to make their marks.* Nat Cell Biol, 2003. **5**(5): p. 395-9.
156. Omichinski, J.G., et al., *NMR structure of a specific DNA complex of Zn-containing DNA binding domain of GATA-1.* Science, 1993. **261**(5120): p. 438-46.
157. Argentaro, A., et al., *Structural consequences of disease-causing mutations in the ATRX-DNMT3-DNMT3L (ADD) domain of the chromatin-associated protein ATRX.* Proc Natl Acad Sci U S A, 2007. **104**(29): p. 11939-44.
158. Valenzuela, M., et al., *The Multiple Facets of ATRX Protein.* Cancers (Basel), 2021. **13**(9).

159. Iwase, S., et al., *ATRX ADD domain links an atypical histone methylation recognition mechanism to human mental-retardation syndrome.* Nat Struct Mol Biol, 2011. **18**(7): p. 769-76.
160. Eustermann, S., et al., *Combinatorial readout of histone H3 modifications specifies localization of ATRX to heterochromatin.* Nat Struct Mol Biol, 2011. **18**(7): p. 777-82.
161. Noh, K.M., et al., *ATRX tolerates activity-dependent histone H3 methyl/phos switching to maintain repetitive element silencing in neurons.* Proc Natl Acad Sci U S A, 2015. **112**(22): p. 6820-7.
162. Berube, N.G., C.A. Smeenk, and D.J. Picketts, *Cell cycle-dependent phosphorylation of the ATRX protein correlates with changes in nuclear matrix and chromatin association.* Hum Mol Genet, 2000. **9**(4): p. 539-47.
163. Kourmouli, N., et al., *Epigenetic regulation of mammalian pericentric heterochromatin in vivo by HP1.* Biochem Biophys Res Commun, 2005. **337**(3): p. 901-7.
164. Nan, X., et al., *Interaction between chromatin proteins MECP2 and ATRX is disrupted by mutations that cause inherited mental retardation.* Proc Natl Acad Sci U S A, 2007. **104**(8): p. 2709-14.
165. McDowell, T.L., et al., *Localization of a putative transcriptional regulator (ATRX) at pericentromeric heterochromatin and the short arms of acrocentric chromosomes.* Proc Natl Acad Sci U S A, 1999. **96**(24): p. 13983-8.
166. Kernohan, K.D., et al., *ATRX partners with cohesin and MeCP2 and contributes to developmental silencing of imprinted genes in the brain.* Dev Cell, 2010. **18**(2): p. 191-202.
167. Law, M.J., et al., *ATR-X syndrome protein targets tandem repeats and influences allele-specific expression in a size-dependent manner.* Cell, 2010. **143**(3): p. 367-78.
168. Valton, A.L. and M.N. Prioleau, *G-Quadruplexes in DNA Replication: A Problem or a Necessity?* Trends Genet, 2016. **32**(11): p. 697-706.
169. Voon, H.P. and L.H. Wong, *New players in heterochromatin silencing: histone variant H3.3 and the ATRX/DAXX chaperone.* Nucleic Acids Res, 2016. **44**(4): p. 1496-501.
170. Tang, J., et al., *A novel transcription regulatory complex containing death domain-associated protein and the ATR-X syndrome protein.* J Biol Chem, 2004. **279**(19): p. 20369-77.
171. Udugama, M., et al., *Histone variant H3.3 provides the heterochromatic H3 lysine 9 tri-methylation mark at telomeres.* Nucleic Acids Res, 2015. **43**(21): p. 10227-37.
172. He, Q., et al., *The Daxx/Atrx Complex Protects Tandem Repetitive Elements during DNA Hypomethylation by Promoting H3K9 Trimethylation.* Cell Stem Cell, 2015. **17**(3): p. 273-86.
173. Lovejoy, C.A., et al., *Loss of ATRX, genome instability, and an altered DNA damage response are hallmarks of the alternative lengthening of telomeres pathway.* PLoS Genet, 2012. **8**(7): p. e1002772.
174. Heaphy, C.M., et al., *Altered telomeres in tumors with ATRX and DAXX mutations.* Science, 2011. **333**(6041): p. 425.
175. Abedalthagafi, M., et al., *The alternative lengthening of telomere phenotype is significantly associated with loss of ATRX expression in high-grade pediatric and adult astrocytomas: a multi-institutional study of 214 astrocytomas.* Mod Pathol, 2013. **26**(11): p. 1425-32.

176. Kurihara, S., et al., *Clinical features of ATRX or DAXX mutated neuroblastoma.* J Pediatr Surg, 2014. **49**(12): p. 1835-8.
177. Johnson, J.E. and D. Broccoli, *Telomere maintenance in sarcomas.* Curr Opin Oncol, 2007. **19**(4): p. 377-82.
178. Voon, H.P., et al., *ATRX Plays a Key Role in Maintaining Silencing at Interstitial Heterochromatic Loci and Imprinted Genes.* Cell Rep, 2015. **11**(3): p. 405-18.
179. Baumann, C. and R. De La Fuente, *ATRX marks the inactive X chromosome (Xi) in somatic cells and during imprinted X chromosome inactivation in trophoblast stem cells.* Chromosoma, 2009. **118**(2): p. 209-22.
180. Kernohan, K.D., et al., *Analysis of neonatal brain lacking ATRX or MeCP2 reveals changes in nucleosome density, CTCF binding and chromatin looping.* Nucleic Acids Res, 2014. **42**(13): p. 8356-68.
181. Butler, M.G., *Genomic imprinting disorders in humans: a mini-review.* J Assist Reprod Genet, 2009. **26**(9-10): p. 477-86.
182. Shioda, N., et al., *Targeting G-quadruplex DNA as cognitive function therapy for ATR-X syndrome.* Nat Med, 2018. **24**(6): p. 802-813.
183. Cubelos, B., et al., *Cux1 and Cux2 regulate dendritic branching, spine morphology, and synapses of the upper layer neurons of the cortex.* Neuron, 2010. **66**(4): p. 523-35.
184. Levy, M.A., et al., *ATRX promotes gene expression by facilitating transcriptional elongation through guanine-rich coding regions.* Hum Mol Genet, 2015. **24**(7): p. 1824-35.
185. Boyer, L.A., et al., *Core transcriptional regulatory circuitry in human embryonic stem cells.* Cell, 2005. **122**(6): p. 947-56.
186. Bunina, D., et al., *Genomic Rewiring of SOX2 Chromatin Interaction Network during Differentiation of ESCs to Postmitotic Neurons.* Cell Syst, 2020. **10**(6): p. 480-494 e8.
187. Guion, L.G. and M. Sapp, *The Role of Promyelocytic Leukemia Nuclear Bodies During HPV Infection.* Front Cell Infect Microbiol, 2020. **10**: p. 35.
188. Ishov, A.M., et al., *PML is critical for ND10 formation and recruits the PML-interacting protein daxx to this nuclear structure when modified by SUMO-1.* J Cell Biol, 1999. **147**(2): p. 221-34.
189. Delbarre, E., et al., *PML protein organizes heterochromatin domains where it regulates histone H3.3 deposition by ATRX/DAXX.* Genome Res, 2017. **27**(6): p. 913-921.
190. Bernardi, R. and P.P. Pandolfi, *Structure, dynamics and functions of promyelocytic leukaemia nuclear bodies.* Nat Rev Mol Cell Biol, 2007. **8**(12): p. 1006-16.
191. Wong, L.H., et al., *Histone H3.3 incorporation provides a unique and functionally essential telomeric chromatin in embryonic stem cells.* Genome Res, 2009. **19**(3): p. 404-14.
192. Meng, T.G., et al., *PRC2 and EHMT1 regulate H3K27me2 and H3K27me3 establishment across the zygote genome.* Nat Commun, 2020. **11**(1): p. 6354.
193. Juhasz, S., et al., *ATRX Promotes DNA Repair Synthesis and Sister Chromatid Exchange during Homologous Recombination.* Mol Cell, 2018. **71**(1): p. 11-24 e7.
194. Clynes, D., et al., *ATRX dysfunction induces replication defects in primary mouse cells.* PLoS One, 2014. **9**(3): p. e92915.
195. Leung, J.W., et al., *Alpha thalassemia/mental retardation syndrome X-linked gene product ATRX is required for proper replication restart and cellular resistance to replication stress.* J Biol Chem, 2013. **288**(9): p. 6342-50.

196. Qiu, S. and J. Huang, *MRN complex is an essential effector of DNA damage repair.* J Zhejiang Univ Sci B, 2021. **22**(1): p. 31-37.
197. Ritchie, K., et al., *Loss of ATRX leads to chromosome cohesion and congression defects.* J Cell Biol, 2008. **180**(2): p. 315-24.
198. Huh, M.S., et al., *Compromised genomic integrity impedes muscle growth after Atrx inactivation.* J Clin Invest, 2012. **122**(12): p. 4412-23.
199. Watson, L.A., et al., *Atrx deficiency induces telomere dysfunction, endocrine defects, and reduced life span.* J Clin Invest, 2013. **123**(5): p. 2049-63.
200. Huh, M.S., et al., *Stalled replication forks within heterochromatin require ATRX for protection.* Cell Death Dis, 2016. **7**: p. e2220.
201. Sarma, K., et al., *ATRX directs binding of PRC2 to Xist RNA and Polycomb targets.* Cell, 2014. **159**(4): p. 869-83.
202. Ren, W., et al., *Disruption of ATRX-RNA interactions uncovers roles in ATRX localization and PRC2 function.* Nat Commun, 2020. **11**(1): p. 2219.
203. Berube, N.G., et al., *Patient mutations alter ATRX targeting to PML nuclear bodies.* Eur J Hum Genet, 2008. **16**(2): p. 192-201.
204. Garrick, D., et al., *Loss of Atrx affects trophoblast development and the pattern of X-inactivation in extraembryonic tissues.* PLoS Genet, 2006. **2**(4): p. e58.
205. Berube, N.G., et al., *The chromatin-remodeling protein ATRX is critical for neuronal survival during corticogenesis.* J Clin Invest, 2005. **115**(2): p. 258-67.
206. Tamming, R.J., et al., *Mosaic expression of Atrx in the mouse central nervous system causes memory deficits.* Dis Model Mech, 2017. **10**(2): p. 119-126.
207. Seah, C., et al., *Neuronal death resulting from targeted disruption of the Snf2 protein ATRX is mediated by p53.* J Neurosci, 2008. **28**(47): p. 12570-80.
208. Hebert, J.M. and S.K. McConnell, *Targeting of cre to the Foxg1 (BF-1) locus mediates loxP recombination in the telencephalon and other developing head structures.* Dev Biol, 2000. **222**(2): p. 296-306.
209. London, A., I. Benhar, and M. Schwartz, *The retina as a window to the brain-from eye research to CNS disorders.* Nat Rev Neurol, 2013. **9**(1): p. 44-53.
210. Medina, C.F., et al., *Altered visual function and interneuron survival in Atrx knockout mice: inference for the human syndrome.* Hum Mol Genet, 2009. **18**(5): p. 966-77.
211. Lagali, P.S., et al., *Retinal interneuron survival requires non-cell-autonomous Atrx activity.* Hum Mol Genet, 2016. **25**(21): p. 4787-4803.
212. Shioda, N., et al., *Aberrant calcium/calmodulin-dependent protein kinase II (CaMKII) activity is associated with abnormal dendritic spine morphology in the ATRX mutant mouse brain.* J Neurosci, 2011. **31**(1): p. 346-58.
213. Gugustea, R., et al., *Inactivation of ATRX in forebrain excitatory neurons affects hippocampal synaptic plasticity.* Hippocampus, 2020. **30**(6): p. 565-581.
214. Martin-Kenny, N. and N.G. Berube, *Effects of a postnatal Atrx conditional knockout in neurons on autism-like behaviours in male and female mice.* J Neurodev Disord, 2020. **12**(1): p. 17.
215. Tamming, R.J., et al., *Atrx Deletion in Neurons Leads to Sexually Dimorphic Dysregulation of miR-137 and Spatial Learning and Memory Deficits.* Cell Rep, 2020. **31**(13): p. 107838.
216. Weatherall, D.J., et al., *Hemoglobin H disease and mental retardation: a new syndrome or a remarkable coincidence?* N Engl J Med, 1981. **305**(11): p. 607-12.

217. Wada, T., et al., *Neuroradiologic features in X-linked alpha-thalassemia/mental retardation syndrome.* AJNR Am J Neuroradiol, 2013. **34**(10): p. 2034-8.
218. Gibbons, R.J., et al., *Clinical and hematologic aspects of the X-linked alpha-thalassemia/mental retardation syndrome (ATR-X).* Am J Med Genet, 1995. **55**(3): p. 288-99.
219. Thienpont, B., et al., *Partial duplications of the ATRX gene cause the ATR-X syndrome.* Eur J Hum Genet, 2007. **15**(10): p. 1094-7.
220. Wada, T., S. Suzuki, and N. Shioda, *5-Aminolevulinic acid can ameliorate language dysfunction of patients with ATR-X syndrome.* Congenit Anom (Kyoto), 2020. **60**(5): p. 147-148.
221. Leahy, R.T., et al., *Asplenia in ATR-X syndrome: a second report.* Am J Med Genet A, 2005. **139**(1): p. 37-9.
222. Ogle, R., et al., *X linked mental retardation with non-deletional alpha thalassaemia (ATR-X): further delineation of the phenotype.* J Med Genet, 1994. **31**(3): p. 245-7.
223. Giacomini, T., et al., *Epileptic Encephalopathy, Myoclonus-Dystonia, and Premature Pubarche in Siblings with a Novel C-Terminal Truncating Mutation in ATRX Gene.* Neuropediatrics, 2019. **50**(5): p. 327-331.
224. Yun, K.W., et al., *The first case of X-linked Alpha-thalassemia/mental retardation (ATR-X) syndrome in Korea.* J Korean Med Sci, 2011. **26**(1): p. 146-9.
225. Moncini, S., et al., *ATRX mutation in two adult brothers with non-specific moderate intellectual disability identified by exome sequencing.* Meta Gene, 2013. **1**: p. 102-8.
226. Gibbons, R., *Alpha thalassaemia-mental retardation, X linked.* Orphanet J Rare Dis, 2006. **1**: p. 15.
227. Wilkie, A.O., et al., *Clinical features and molecular analysis of the alpha thalassemia/mental retardation syndromes. I. Cases due to deletions involving chromosome band 16p13.3.* Am J Hum Genet, 1990. **46**(6): p. 1112-26.
228. Kurosawa, K., et al., *Self-induced vomiting in X-linked alpha-thalassemia/mental retardation syndrome.* Am J Med Genet, 1996. **63**(3): p. 505-6.
229. Wada, T., et al., *[Three Japanese children with X-linked alpha-thalassemia/mental retardation syndrome (ATR-X)].* No To Hattatsu, 1998. **30**(4): p. 283-9.
230. Martucciello, G., et al., *Gastrointestinal phenotype of ATR-X syndrome.* Am J Med Genet A, 2006. **140**(11): p. 1172-6.
231. Lee, E., J. Lee, and E. Kim, *Excitation/Inhibition Imbalance in Animal Models of Autism Spectrum Disorders.* Biol Psychiatry, 2017. **81**(10): p. 838-847.
232. Cellot, G. and E. Cherubini, *GABAergic signaling as therapeutic target for autism spectrum disorders.* Front Pediatr, 2014. **2**: p. 70.
233. Rubenstein, J.L. and M.M. Merzenich, *Model of autism: increased ratio of excitation/inhibition in key neural systems.* Genes Brain Behav, 2003. **2**(5): p. 255-67.
234. Nelson, S.B. and V. Valakh, *Excitatory/Inhibitory Balance and Circuit Homeostasis in Autism Spectrum Disorders.* Neuron, 2015. **87**(4): p. 684-98.
235. Dahlstrand, J., M. Lardelli, and U. Lendahl, *Nestin mRNA expression correlates with the central nervous system progenitor cell state in many, but not all, regions of developing central nervous system.* Brain Res Dev Brain Res, 1995. **84**(1): p. 109-29.
236. Vong, L., et al., *Leptin action on GABAergic neurons prevents obesity and reduces inhibitory tone to POMC neurons.* Neuron, 2011. **71**(1): p. 142-54.

237. Chao, H.T., et al., *Dysfunction in GABA signalling mediates autism-like stereotypies and Rett syndrome phenotypes.* Nature, 2010. **468**(7321): p. 263-9.
238. Gorski, J.A., et al., *Cortical excitatory neurons and glia, but not GABAergic neurons, are produced in the Emx1-expressing lineage.* J Neurosci, 2002. **22**(15): p. 6309-14.
239. Crawley, J.N., *What's Wrong With My Mouse?: Behavioral Phenotyping of Transgenic and Knockout Mice*. 2007: Wiley.
240. Brooks, S.P. and S.B. Dunnett, *Tests to assess motor phenotype in mice: a user's guide.* Nat Rev Neurosci, 2009. **10**(7): p. 519-29.
241. Shiotsuki, H., et al., *A rotarod test for evaluation of motor skill learning.* J Neurosci Methods, 2010. **189**(2): p. 180-5.
242. Bailey, K.R. and J.N. Crawley, *Anxiety-Related Behaviors in Mice*, in *Methods of Behavior Analysis in Neuroscience,* nd and J.J. Buccafusco, Editors. 2009: Boca Raton (FL).
243. Seibenhener, M.L. and M.C. Wooten, *Use of the Open Field Maze to measure locomotor and anxiety-like behavior in mice.* J Vis Exp, 2015(96): p. e52434.
244. Pellow, S., et al., *Validation of open:closed arm entries in an elevated plus-maze as a measure of anxiety in the rat.* J Neurosci Methods, 1985. **14**(3): p. 149-67.
245. Treit, D., J. Menard, and C. Royan, *Anxiogenic stimuli in the elevated plus-maze.* Pharmacol Biochem Behav, 1993. **44**(2): p. 463-9.
246. Carobrez, A.P. and L.J. Bertoglio, *Ethological and temporal analyses of anxiety-like behavior: the elevated plus-maze model 20 years on.* Neurosci Biobehav Rev, 2005. **29**(8): p. 1193-205.
247. Komada, M., K. Takao, and T. Miyakawa, *Elevated plus maze for mice.* J Vis Exp, 2008(22).
248. Jirkof, P., *Burrowing and nest building behavior as indicators of well-being in mice.* J Neurosci Methods, 2014. **234**: p. 139-46.
249. Deacon, R., *Assessing burrowing, nest construction, and hoarding in mice.* J Vis Exp, 2012(59): p. e2607.
250. Collins, S.C., et al., *A Method for Parasagittal Sectioning for Neuroanatomical Quantification of Brain Structures in the Adult Mouse.* Curr Protoc Mouse Biol, 2018. **8**(3): p. e48.
251. Bray, N.L., et al., *Near-optimal probabilistic RNA-seq quantification.* Nat Biotechnol, 2016. **34**(5): p. 525-7.
252. Yu, G., et al., *DOSE: an R/Bioconductor package for disease ontology semantic and enrichment analysis.* Bioinformatics, 2015. **31**(4): p. 608-9.
253. Bernal, A. and L. Arranz, *Nestin-expressing progenitor cells: function, identity and therapeutic implications.* Cell Mol Life Sci, 2018. **75**(12): p. 2177-2195.
254. Gibbs, J., J. Appleton, and R. Appleton, *Dyspraxia or developmental coordination disorder? Unravelling the enigma.* Arch Dis Child, 2007. **92**(6): p. 534-9.
255. Foundas, A.L., et al., *Gesture laterality in aphasic and apraxic stroke patients.* Brain Cogn, 1995. **29**(2): p. 204-13.
256. Stamenova, V., E.A. Roy, and S.E. Black, *A model-based approach to understanding apraxia in Corticobasal Syndrome.* Neuropsychol Rev, 2009. **19**(1): p. 47-63.
257. Dziuk, M.A., et al., *Dyspraxia in autism: association with motor, social, and communicative deficits.* Dev Med Child Neurol, 2007. **49**(10): p. 734-9.

258. Lopez-Garrido, M.P., et al., *Brief Report: Evidence of Autism Spectrum Disorder Caused by a Mutation in ATRX Gene: A Case Report.* J Autism Dev Disord, 2022.
259. Gong, X., et al., *Analysis of X chromosome inactivation in autism spectrum disorders.* Am J Med Genet B Neuropsychiatr Genet, 2008. **147B**(6): p. 830-5.
260. Brett, M., et al., *Massively parallel sequencing of patients with intellectual disability, congenital anomalies and/or autism spectrum disorders with a targeted gene panel.* PLoS One, 2014. **9**(4): p. e93409.
261. Amir, R.E., et al., *Rett syndrome is caused by mutations in X-linked MECP2, encoding methyl-CpG-binding protein 2.* Nat Genet, 1999. **23**(2): p. 185-8.
262. Meng, X., et al., *Manipulations of MeCP2 in glutamatergic neurons highlight their contributions to Rett and other neurological disorders.* Elife, 2016. **5**.
263. Boulland, J.L., et al., *Expression of the vesicular glutamate transporters during development indicates the widespread corelease of multiple neurotransmitters.* J Comp Neurol, 2004. **480**(3): p. 264-80.
264. Fremeau, R.T., Jr., et al., *Vesicular glutamate transporters 1 and 2 target to functionally distinct synaptic release sites.* Science, 2004. **304**(5678): p. 1815-9.
265. Oh, W.J., et al., *The mouse vesicular inhibitory amino acid transporter gene: expression during embryogenesis, analysis of its core promoter in neural stem cells and a reconsideration of its alternate splicing.* Gene, 2005. **351**: p. 39-49.
266. Ure, K., et al., *Restoration of Mecp2 expression in GABAergic neurons is sufficient to rescue multiple disease features in a mouse model of Rett syndrome.* Elife, 2016. **5**.
267. Dou, C.L., S. Li, and E. Lai, *Dual role of brain factor-1 in regulating growth and patterning of the cerebral hemispheres.* Cereb Cortex, 1999. **9**(6): p. 543-50.
268. Gardon, O., et al., *Expression of mu opioid receptor in dorsal diencephalic conduction system: new insights for the medial habenula.* Neuroscience, 2014. **277**: p. 595-609.
269. Sutherland, R.J., *The dorsal diencephalic conduction system: a review of the anatomy and functions of the habenular complex.* Neurosci Biobehav Rev, 1982. **6**(1): p. 1-13.
270. Roman, E., et al., *Untangling the dorsal diencephalic conduction system: a review of structure and function of the stria medullaris, habenula and fasciculus retroflexus.* Brain Struct Funct, 2020. **225**(5): p. 1437-1458.
271. King, L.B., et al., *Developmental loss of neurofibromin across distributed neuronal circuits drives excessive grooming in Drosophila.* PLoS Genet, 2020. **16**(7): p. e1008920.
272. Kim, H., C.S. Lim, and B.K. Kaang, *Neuronal mechanisms and circuits underlying repetitive behaviors in mouse models of autism spectrum disorder.* Behav Brain Funct, 2016. **12**(1): p. 3.
273. Moore, S.W., M. Tessier-Lavigne, and T.E. Kennedy, *Netrins and their receptors.* Adv Exp Med Biol, 2007. **621**: p. 17-31.
274. Heimer, G., et al., *Netrin-G2 dysfunction causes a Rett-like phenotype with areflexia.* Hum Mutat, 2020. **41**(2): p. 476-486.
275. Arakawa, H., *Implication of the social function of excessive self-grooming behavior in BTBR T(+)ltpr3(tf)/J mice as an idiopathic model of autism.* Physiol Behav, 2021. **237**: p. 113432.
276. Leone, D.P., et al., *The determination of projection neuron identity in the developing cerebral cortex.* Curr Opin Neurobiol, 2008. **18**(1): p. 28-35.

277. Zapata, G., K. Yan, and D.J. Picketts, *Generation of a mouse model of the neurodevelopmental disorder with dysmorphic facies and distal limb anomalies syndrome.* Hum Mol Genet, 2022. **31**(20): p. 3405-3421.
278. Alvarez-Saavedra, M., et al., *Snf2h Drives Chromatin Remodeling to Prime Upper Layer Cortical Neuron Development.* Front Mol Neurosci, 2019. **12**: p. 243.
279. Poot, R.A., et al., *The Williams syndrome transcription factor interacts with PCNA to target chromatin remodelling by ISWI to replication foci.* Nat Cell Biol, 2004. **6**(12): p. 1236-44.
280. Zhao, C., et al., *Hippocampal and visuospatial learning defects in mice with a deletion of frizzled 9, a gene in the Williams syndrome deletion interval.* Development, 2005. **132**(12): p. 2917-27.
281. Jones, K.M., et al., *CHD7 maintains neural stem cell quiescence and prevents premature stem cell depletion in the adult hippocampus.* Stem Cells, 2015. **33**(1): p. 196-210.
282. Tuoc, T., et al., *Ablation of BAF170 in Developing and Postnatal Dentate Gyrus Affects Neural Stem Cell Proliferation, Differentiation, and Learning.* Mol Neurobiol, 2017. **54**(6): p. 4618-4635.
283. Simon, R., et al., *A dual function of Bcl11b/Ctip2 in hippocampal neurogenesis.* EMBO J, 2012. **31**(13): p. 2922-36.
284. Davies, M., O. Udwin, and P. Howlin, *Adults with Williams syndrome. Preliminary study of social, emotional and behavioural difficulties.* Br J Psychiatry, 1998. **172**: p. 273-6.
285. Francke, U., *Williams-Beuren syndrome: genes and mechanisms.* Hum Mol Genet, 1999. **8**(10): p. 1947-54.
286. Chapman, C.A., A. du Plessis, and B.R. Pober, *Neurologic findings in children and adults with Williams syndrome.* J Child Neurol, 1996. **11**(1): p. 63-5.
287. Morris, C.A., et al., *Natural history of Williams syndrome: physical characteristics.* J Pediatr, 1988. **113**(2): p. 318-26.
288. Hocking, D.R., et al., *Gait function in adults with Williams syndrome.* Exp Brain Res, 2009. **192**(4): p. 695-702.
289. Berencsi, A., F. Gombos, and I. Kovacs, *Capacity to improve fine motor skills in Williams syndrome.* J Intellect Disabil Res, 2016. **60**(10): p. 956-68.
290. Fleck, B.J., et al., *Coffin-Siris syndrome: review and presentation of new cases from a questionnaire study.* Am J Med Genet, 2001. **99**(1): p. 1-7.
291. Neul, J.L., et al., *Developmental delay in Rett syndrome: data from the natural history study.* J Neurodev Disord, 2014. **6**(1): p. 20.
292. Choudhury, P.R., S. Lahiri, and U. Rajamma, *Glutamate mediated signaling in the pathophysiology of autism spectrum disorders.* Pharmacol Biochem Behav, 2012. **100**(4): p. 841-9.
293. Moretto, E., et al., *Glutamatergic synapses in neurodevelopmental disorders.* Prog Neuropsychopharmacol Biol Psychiatry, 2018. **84**(Pt B): p. 328-342.
294. Canitano, R., *New experimental treatments for core social domain in autism spectrum disorders.* Front Pediatr, 2014. **2**: p. 61.
295. Chao, H.T., H.Y. Zoghbi, and C. Rosenmund, *MeCP2 controls excitatory synaptic strength by regulating glutamatergic synapse number.* Neuron, 2007. **56**(1): p. 58-65.

296. Landry, M., et al., *Expression of vesicular glutamate transporters in rat lumbar spinal cord, with a note on dorsal root ganglia.* J Comp Neurol, 2004. **468**(3): p. 380-94.
297. Fremeau, R.T., Jr., et al., *VGLUTs define subsets of excitatory neurons and suggest novel roles for glutamate.* Trends Neurosci, 2004. **27**(2): p. 98-103.
298. Wozny, C., et al., *VGLUT2 Functions as a Differential Marker for Hippocampal Output Neurons.* Front Cell Neurosci, 2018. **12**: p. 337.
299. O'Mara, S.M., et al., *The subiculum: a review of form, physiology and function.* Prog Neurobiol, 2001. **64**(2): p. 129-55.
300. Fremeau, R.T., Jr., et al., *The expression of vesicular glutamate transporters defines two classes of excitatory synapse.* Neuron, 2001. **31**(2): p. 247-60.
301. Varoqui, H., et al., *Identification of the differentiation-associated Na+/PI transporter as a novel vesicular glutamate transporter expressed in a distinct set of glutamatergic synapses.* J Neurosci, 2002. **22**(1): p. 142-55.
302. Herzog, E., et al., *The existence of a second vesicular glutamate transporter specifies subpopulations of glutamatergic neurons.* J Neurosci, 2001. **21**(22): p. RC181.
303. Saito, K., et al., *The physiological roles of vesicular GABA transporter during embryonic development: a study using knockout mice.* Mol Brain, 2010. **3**: p. 40.
304. Rudy, B., et al., *Three groups of interneurons account for nearly 100% of neocortical GABAergic neurons.* Dev Neurobiol, 2011. **71**(1): p. 45-61.
305. Szatmari, P., et al., *Investigating the structure of the restricted, repetitive behaviours and interests domain of autism.* J Child Psychol Psychiatry, 2006. **47**(6): p. 582-90.
306. Feusner, J.D., E. Hembacher, and K.A. Phillips, *The mouse who couldn't stop washing: pathologic grooming in animals and humans.* CNS Spectr, 2009. **14**(9): p. 503-13.
307. Anand, K.S. and V. Dhikav, *Hippocampus in health and disease: An overview.* Ann Indian Acad Neurol, 2012. **15**(4): p. 239-46.
308. Stella, F., et al., *Self-organization of multiple spatial and context memories in the hippocampus.* Neurosci Biobehav Rev, 2012. **36**(7): p. 1609-25.
309. Toyoda, H., et al., *Interplay of amygdala and cingulate plasticity in emotional fear.* Neural Plast, 2011. **2011**: p. 813749.
310. Koehl, M. and D.N. Abrous, *A new chapter in the field of memory: adult hippocampal neurogenesis.* Eur J Neurosci, 2011. **33**(6): p. 1101-14.
311. Nogami, T., et al., *Reduced expression of the ATRX gene, a chromatin-remodeling factor, causes hippocampal dysfunction in mice.* Hippocampus, 2011. **21**(6): p. 678-87.
312. Mizuguchi, R., et al., *Combinatorial roles of olig2 and neurogenin2 in the coordinated induction of pan-neuronal and subtype-specific properties of motoneurons.* Neuron, 2001. **31**(5): p. 757-71.
313. Galichet, C., F. Guillemot, and C.M. Parras, *Neurogenin 2 has an essential role in development of the dentate gyrus.* Development, 2008. **135**(11): p. 2031-41.
314. Brambilla, P., et al., *Brain anatomy and development in autism: review of structural MRI studies.* Brain Res Bull, 2003. **61**(6): p. 557-69.
315. Greicius, M.D., et al., *Reduced basal forebrain and hippocampal activation during memory encoding in girls with fragile X syndrome.* Neuroreport, 2004. **15**(10): p. 1579-83.
316. Carter, J.C., et al., *Selective cerebral volume reduction in Rett syndrome: a multiple-approach MR imaging study.* AJNR Am J Neuroradiol, 2008. **29**(3): p. 436-41.

317. Aghakhanyan, G., et al., *From Cortical and Subcortical Grey Matter Abnormalities to Neurobehavioral Phenotype of Angelman Syndrome: A Voxel-Based Morphometry Study*. PLoS One, 2016. **11**(9): p. e0162817.
318. Honea, R.A., et al., *The neuroanatomy of genetic subtype differences in Prader-Willi syndrome.* Am J Med Genet B Neuropsychiatr Genet, 2012. **159B**(2): p. 243-53.
319. Stoeckli, E., *Where does axon guidance lead us?* F1000Res, 2017. **6**: p. 78.
320. Livesey, F.J., *Netrins and netrin receptors.* Cell Mol Life Sci, 1999. **56**(1-2): p. 62-8.
321. Keino-Masu, K., et al., *Deleted in Colorectal Cancer (DCC) encodes a netrin receptor.* Cell, 1996. **87**(2): p. 175-85.
322. Hamelin, M., et al., *Expression of the UNC-5 guidance receptor in the touch neurons of C. elegans steers their axons dorsally.* Nature, 1993. **364**(6435): p. 327-30.
323. Nakashiba, T., et al., *Complementary expression and neurite outgrowth activity of netrin-G subfamily members.* Mech Dev, 2002. **111**(1-2): p. 47-60.
324. Nakashiba, T., et al., *Netrin-G1: a novel glycosyl phosphatidylinositol-linked mammalian netrin that is functionally divergent from classical netrins.* J Neurosci, 2000. **20**(17): p. 6540-50.
325. Lin, J.C., et al., *The netrin-G1 ligand NGL-1 promotes the outgrowth of thalamocortical axons.* Nat Neurosci, 2003. **6**(12): p. 1270-6.
326. Nishimura-Akiyoshi, S., et al., *Axonal netrin-Gs transneuronally determine lamina-specific subdendritic segments.* Proc Natl Acad Sci U S A, 2007. **104**(37): p. 14801-6.
327. Scharfman, H.E. and M.V. Chao, *The entorhinal cortex and neurotrophin signaling in Alzheimer's disease and other disorders.* Cogn Neurosci, 2013. **4**(3-4): p. 123-35.
328. Witter, M.P., et al., *Functional organization of the extrinsic and intrinsic circuitry of the parahippocampal region.* Prog Neurobiol, 1989. **33**(3): p. 161-253.
329. Witter, M.P., *The perforant path: projections from the entorhinal cortex to the dentate gyrus.* Prog Brain Res, 2007. **163**: p. 43-61.
330. Steward, O., *Topographic organization of the projections from the entorhinal area to the hippocampal formation of the rat.* J Comp Neurol, 1976. **167**(3): p. 285-314.
331. Ferbinteanu, J., R.M. Holsinger, and R.J. McDonald, *Lesions of the medial or lateral perforant path have different effects on hippocampal contributions to place learning and on fear conditioning to context.* Behav Brain Res, 1999. **101**(1): p. 65-84.
332. Dias, C.M., et al., *Homozygous Missense Variants in NTNG2, Encoding a Presynaptic Netrin-G2 Adhesion Protein, Lead to a Distinct Neurodevelopmental Disorder.* Am J Hum Genet, 2019. **105**(5): p. 1048-1056.
333. Borg, I., et al., *Disruption of Netrin G1 by a balanced chromosome translocation in a girl with Rett syndrome.* Eur J Hum Genet, 2005. **13**(8): p. 921-7.
334. Eastwood, S.L. and P.J. Harrison, *Decreased mRNA expression of netrin-G1 and netrin-G2 in the temporal lobe in schizophrenia and bipolar disorder.* Neuropsychopharmacology, 2008. **33**(4): p. 933-45.
335. Aoki-Suzuki, M., et al., *A family-based association study and gene expression analyses of netrin-G1 and -G2 genes in schizophrenia.* Biol Psychiatry, 2005. **57**(4): p. 382-93.
336. Wei, G., et al., *Patient Mutations of the Intellectual Disability Gene KDM5C Downregulate Netrin G2 and Suppress Neurite Growth in Neuro2a Cells.* J Mol Neurosci, 2016. **60**(1): p. 33-45.
337. DeNardo, L.A., et al., *NGL-2 regulates input-specific synapse development in CA1 pyramidal neurons.* Neuron, 2012. **76**(4): p. 762-75.

338. Matsukawa, H., et al., *Netrin-G/NGL complexes encode functional synaptic diversification.* J Neurosci, 2014. **34**(47): p. 15779-92.
339. Khakpai, F., et al., *Septo-hippocampo-septal loop and memory formation.* Basic Clin Neurosci, 2013. **4**(1): p. 5-23.
340. Swanson, L.W. and W.M. Cowan, *The connections of the septal region in the rat.* J Comp Neurol, 1979. **186**(4): p. 621-55.
341. Muller, C. and S. Remy, *Septo-hippocampal interaction.* Cell Tissue Res, 2018. **373**(3): p. 565-575.
342. Sip, V., et al., *Evidence for spreading seizure as a cause of theta-alpha activity electrographic pattern in stereo-EEG seizure recordings.* PLoS Comput Biol, 2021. **17**(2): p. e1008731.
343. Shuman, T., B. Amendolara, and P. Golshani, *Theta Rhythmopathy as a Cause of Cognitive Disability in TLE.* Epilepsy Curr, 2017. **17**(2): p. 107-111.
344. Haglund, L., L.W. Swanson, and C. Kohler, *The projection of the supramammillary nucleus to the hippocampal formation: an immunohistochemical and anterograde transport study with the lectin PHA-L in the rat.* J Comp Neurol, 1984. **229**(2): p. 171-85.
345. Vertes, R.P., *PHA-L analysis of projections from the supramammillary nucleus in the rat.* J Comp Neurol, 1992. **326**(4): p. 595-622.
346. Vertes, R.P., *Major diencephalic inputs to the hippocampus: supramammillary nucleus and nucleus reuniens. Circuitry and function.* Prog Brain Res, 2015. **219**: p. 121-44.
347. Hashimotodani, Y., et al., *Supramammillary Nucleus Afferents to the Dentate Gyrus Co-release Glutamate and GABA and Potentiate Granule Cell Output.* Cell Rep, 2018. **25**(10): p. 2704-2715 e4.
348. Li, Y., et al., *Supramammillary nucleus synchronizes with dentate gyrus to regulate spatial memory retrieval through glutamate release.* Elife, 2020. **9**.
349. Silverman, J.L., et al., *Behavioural phenotyping assays for mouse models of autism.* Nat Rev Neurosci, 2010. **11**(7): p. 490-502.
350. Caruso, A., L. Ricceri, and M.L. Scattoni, *Ultrasonic vocalizations as a fundamental tool for early and adult behavioral phenotyping of Autism Spectrum Disorder rodent models.* Neurosci Biobehav Rev, 2020. **116**: p. 31-43.
351. Carter, C.S., et al., *Oxytocin and social bonding.* Ann N Y Acad Sci, 1992. **652**: p. 204-11.
352. Amaral, D.G., H. Kondo, and P. Lavenex, *An analysis of entorhinal cortex projections to the dentate gyrus, hippocampus, and subiculum of the neonatal macaque monkey.* J Comp Neurol, 2014. **522**(7): p. 1485-505.
353. Jin, C. and G. Felsenfeld, *Nucleosome stability mediated by histone variants H3.3 and H2A.Z.* Genes Dev, 2007. **21**(12): p. 1519-29.
354. Mito, Y., J.G. Henikoff, and S. Henikoff, *Genome-scale profiling of histone H3.3 replacement patterns.* Nat Genet, 2005. **37**(10): p. 1090-7.
355. Chen, P., et al., *H3.3 actively marks enhancers and primes gene transcription via opening higher-ordered chromatin.* Genes Dev, 2013. **27**(19): p. 2109-24.
356. Funk, O.H., et al., *Postmitotic accumulation of histone variant H3.3 in new cortical neurons establishes neuronal chromatin, transcriptome, and identity.* Proc Natl Acad Sci U S A, 2022. **119**(32): p. e2116956119.

357. Ritchie, K., et al., *ATRX is required for maintenance of the neuroprogenitor cell pool in the embryonic mouse brain.* Biol Open, 2014. **3**(12): p. 1158-63.
358. Rowland, M.E., et al., *Systemic and intrinsic functions of ATRX in glial cell fate and CNS myelination.* bioRxiv, 2022.

Appendix

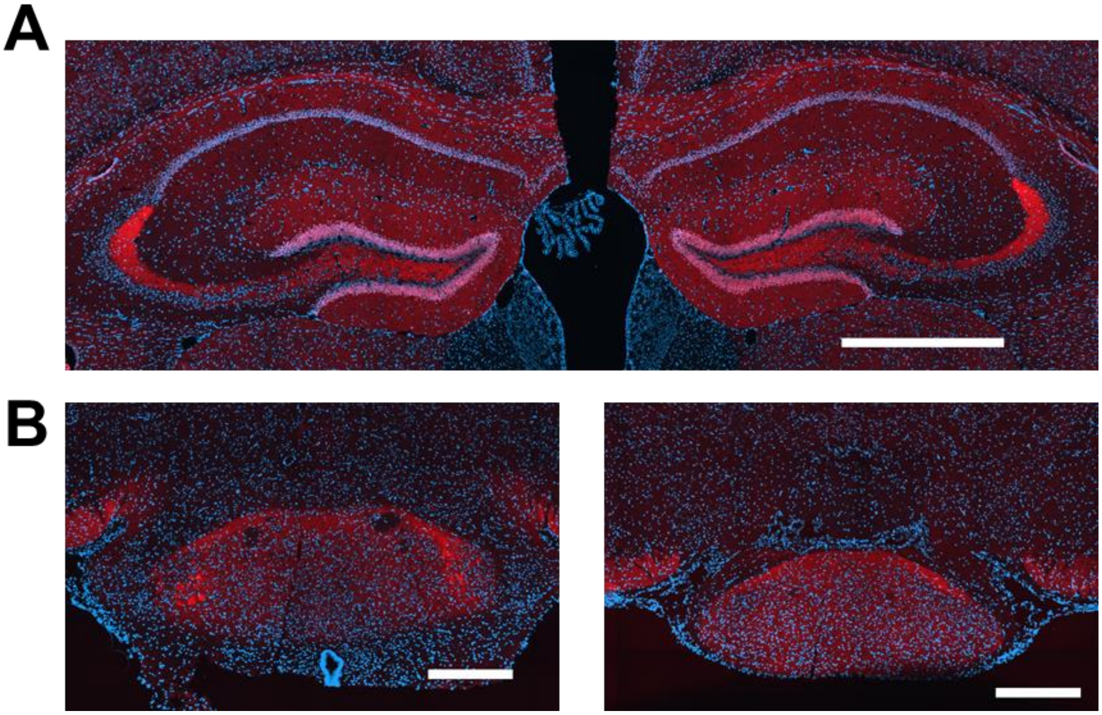

<u>Figure 7.1: Expression of tdtomato reporter in *Ai14; Emx1*-Cre mice.</u>

P40 coronal sections of Ai14; *Emx1*-Cre mice were labeled with DAPI (blue) to visualize the cells and the expression of the tdtomato (red) reporter in **A** the hippocampus and **B** supramammillary nucleus. Scale bar, **A** 500µm and **B** 200µm